Dissertation

Filter Bank Multicarrier Modulation for Future Wireless Systems

Ronald Nissel
Born December 16, 1985
Student ID: 0551696

Faculty of Electrical Engineering and Information Technology
TU Wien

This dissertation is submitted for the degree of
"Doktor der Technischen Wissenschaften".

December 2017

Advisor

Univ. Prof. **Markus Rupp**
Institute of Telecommunications
TU Wien, Austria

Examiners

Dr. **Stephan Weiss**
Department of Electronic and Electrical Engineering
University of Strathclyde, United Kingdom

Prof. **Maurice Bellanger**
Conservatoire national des arts et métiers (CNAM), France

Abstract

Future wireless systems will be characterized by a large range of possible use cases. This requires a flexible allocation of the available time-frequency resources, which is difficult in conventional Orthogonal Frequency Division Multiplexing (OFDM). Thus, modifications of OFDM, such as windowing or filtering, become necessary. Alternatively, one can employ a different modulation scheme, such as Filter Bank Multicarrier Modulation (FBMC). In this thesis, I provide a unifying framework, discussion and performance evaluation of FBMC and compare it to OFDM based schemes. My investigations are not only based on simulations, but are substantiated by real-world testbed measurements and trials, where I show that multiple antennas and channel estimation, two of the main challenges associated with FBMC, can be efficiently dealt with. Additionally, I derive closed-form solutions for the signal-to-interference ratio in doubly-selective channels and show that in many practical cases, one-tap equalizers are sufficient. For the rare cases where this is not true, I propose enhanced methods to deal with such harsh environments, including channel estimation and equalization. Finally, on top of a conventional FBMC system, I develop a novel precoding method based on a pruned Discrete Fourier Transform (DFT) in combination with one-tap scaling. This scheme offers a low peak-to-average power ratio, enables low latency transmissions and has a high spectral efficiency.

Kurzfassung

Zukünftige drahtlose Kommunikationssysteme sollten in der Lage sein, eine Vielzahl an unterschiedlichen Anwendungen zu unterstützen. Dies erfordert eine flexible Zeit und Frequenz Zuteilung der vorhandenen Ressourcen. Das derzeit vorherrschende Übertragungsverfahren, Orthogonal Frequency Division Multiplexing (OFDM), ist dafür nicht optimal geeignet. Es werden somit Modifikationen von OFDM notwendig, oder gänzlich neue Übertragungsverfahren müssen zum Einsatz kommen. In dieser Dissertation untersuche ich Filter Bank Multicarrier Modulation (FBMC), ein solch neues Übertragungsverfahren, und stelle es OFDM basierten Systemen gegenüber. Meine Untersuchungen basieren nicht nur auf theoretischen Überlegungen und Simulationen, sondern werden anhand realer Messungen validiert. Insbesondere zeige ich, dass viele Herausforderungen die üblicherweise mit FBMC assoziiert werden, vor allem in Bezug auf mehrere Antennen und Kanalschätzung, effizient gelöst werden können. Ich leite geschlossene Lösungen für das Signal-zu-Interferenz Verhältnis her und zeige, dass in den meisten Fällen eine einfache, symbolweise, Multiplikation ausreicht, um einen Zeit- und Frequenz-Selektiven Kanal zu entzerren. Für die seltenen Fälle wo dies nicht möglich ist, entwickle ich neue Schätzverfahren und Entzerrungsmethoden. Im letzten Kapitel präsentiere ich eine Erweiterung von FBMC welche Daten mithilfe einer modifizierten diskreten Fourier-Transformation spreizt, bevor sie übertragen werden. Diese neue Methode weist einen reduzierten Scheitelfaktor auf, erlaubt niedrige Latenzzeiten und besitzt eine hohe spektrale Effizienz.

Acknowledgements

First and foremost, I want to thank my advisor, Prof. Markus Rupp, for offering me the opportunity to conduct research under his guidance and for giving me the necessary freedom to pursue my own ideas, which eventually led to this thesis. I am also thankful to Dr. Stephan Weiss and Prof. Maurice Bellanger who agreed to review this thesis.

My thesis would not have been possible without the financial support of the Christian Doppler Laboratory and some outstanding companies such as Nokia (special thanks goes to Birger Haetty and Gottfried Schnabl), A1 (special thanks goes to Waltraud Müllner) and Kathrein (special thanks goes to Alexander Seeor).

Throughout my doctoral studies, I had the opportunity to attend eleven conferences, all over the world, ranging from Vancouver over Rio de Janeiro and Sydney to Hokkaido. On those conferences, I met many wonderful people. I want to thank them all, for making every single conference a unique experience.

I also want to thank Sebastian Caban for offering some unique insights and for building the Vienna Wireless Testbed. Being able to test theoretical concepts over true physical channels was very helpful, especially at the beginning of my study. In this context, I also want to thank Martin Lerch for keeping the testbed running and Erich Zöchmann for building a new mmWave testbed. Besides those three, I also want to thank all the other, former and current, members of the MIMO lab, that is, Martin Müller and Stefan Pratschner, for making the lab a much nicer place to work at.

Last but not least, I want to thank my parents. I owe them everything.

Table of Contents

Chapter 1

Introduction

1.1 Why Filter Bank Multicarrier Modulation?

Future mobile systems will be characterized by a large range of possible use cases, ranging from enhanced Mobile Broadband (eMBB) over enhanced Machine Type Communications (eMTC) to Ultra-Reliable Low Latency Communications (URLLC) [2–6]. To efficiently support such diverse use cases, a flexible time-frequency resource allocation becomes necessary, as illustrated in Figure 1.1. In such a multicarrier system, symbols are transmitted over a rectangular time-frequency grid. Note that the subcarrier spacing determines the shape in frequency and, correspondingly, in time. A high subcarrier spacing allows for low latency transmissions while a small subcarrier spacing increases the bandwidth efficiency. Furthermore, different subcarrier spacings allow to match the transmission system to specific channel conditions. A user at high velocities should employ a high subcarrier spacing. On the other hand, if multipath delay spread is the limiting factor, a small subcarrier spacing is the better choice. As illustrated in Figure 1.1, the Fifth Generation (5G) of mobile systems will indeed employ such flexible subcarrier spacings [7].

There has been a lively discussion both, within the scientific community as well as within standardizations, which modulation format should be used for 5G [8–11]. Eventually, the 3rd Generation Partnership Project (3GPP) decided that they will stick to Orthogonal Frequency Division Multiplexing (OFDM) for 5G [7, 12]. While such decision makes sense in terms of backwards compatibility to Fourth Generation (4G) wireless systems, it is not the most efficient technique for all possible use cases.

In this thesis, I investigate an alternative modulation technique, namely Filter Bank Multicarrier Modulation (FBMC), and show its benefits over OFDM based schemes. Two key observations make FBMC a viable choice for future wireless systems:

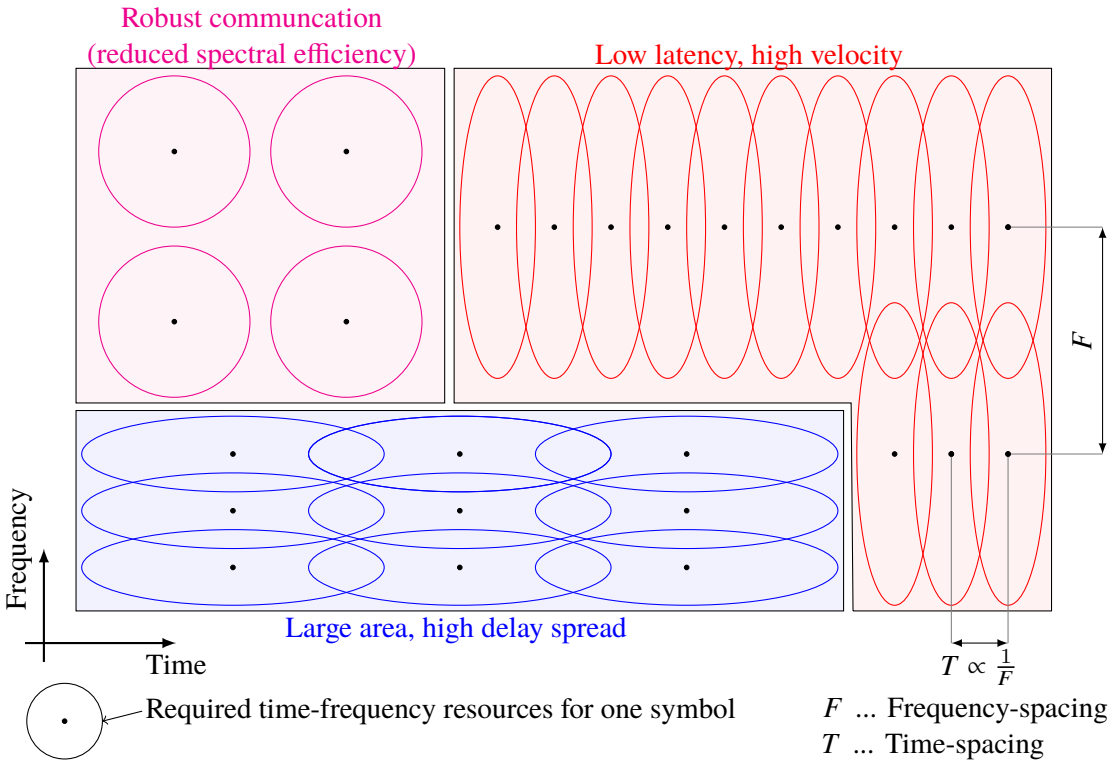

Figure 1.1. Future wireless systems will have to support a large range of possible use cases, requiring a flexible assignment of the available time-frequency resources. ©2017 IEEE, [1].

1. Flexible time-frequency allocation to efficiently support diverse user requirements and channel characteristics.

2. Low channel delay spread, especially in dense heterogeneous networks utilizing Multiple-Input and Multiple-Output (MIMO) beamforming and high carrier frequencies.

The first observation relates to Figure 1.1. In particular, low Out-Of-Band (OOB) emissions are required, so that the guard band between different use cases is relatively small. Conventional OFDM is not suited for that. 3GPP is therefore considering windowing and filtering in OFDM [5, 13, 14]. The windowed OFDM scheme is called OFDM with Weighted Overlap and Add (WOLA) and the filter based methods are called Universal Filtered Multi-Carrier (UFMC) and filtered-OFDM (f-OFDM). While windowing and filtering can indeed reduce the OOB emissions of pure OFDM, FBMC still performs much better, as shown in Figure 1.2. Additionally, FBMC has a maximum symbol density of $TF = 1$ while in OFDM based schemes the symbol density is lower, as indicated by $TF > 1$, additionally worsening the spectral efficiency.

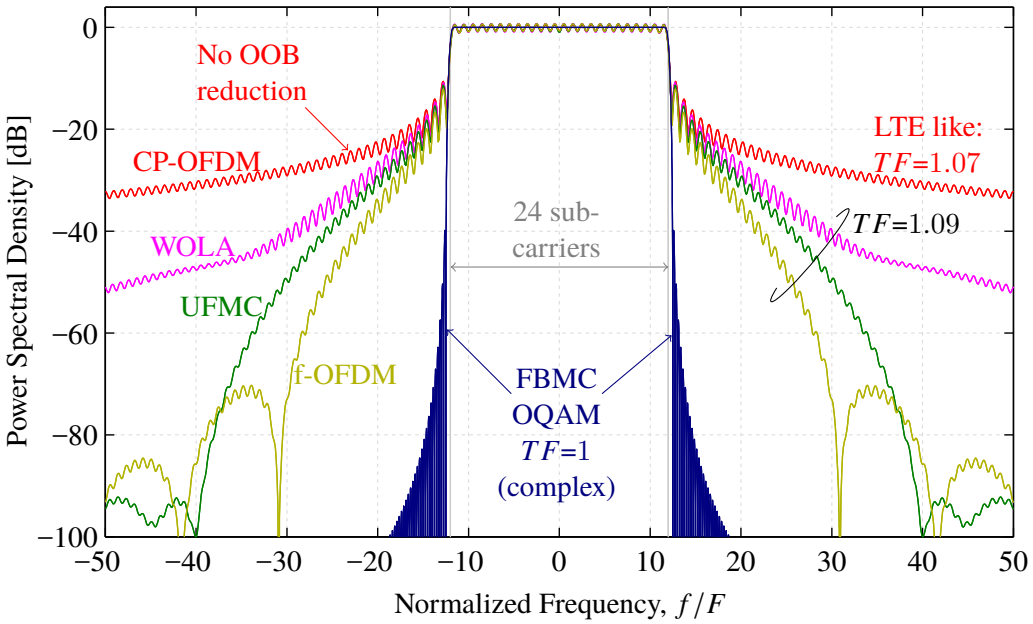

Figure 1.2. FBMC has much better spectral properties than CP-OFDM. Windowing (WOLA) and filtering (UFMC, f-OFDM) can improve the spectral properties of CP-OFDM, but FBMC still performs much better and has the additional advantage of a maximum symbol density, $TF = 1$ (complex). ©2017 IEEE, [1].

The second key observations relates to recent measurements. In [15], the authors present real-world measurement results for Third Generation (3G) systems and found that the measured delay spread is much smaller than "typically" assumed in simulations. They also provide convincing arguments for the lower delay spread, such as, decreasing cell sizes and "spatial filtering" of the environment through beamforming; these arguments will become even more significant in future mobile networks because of an increased network densification, application of massive two-dimensional antenna arrays and the push towards higher carrier frequencies, implying larger propagation path losses. A low delay spread was also observed by other measurements [16, 17]. The low delay spread guarantees that low-complexity one-tap equalizers are sufficient in FBMC to achieve a close to optimal performance. Thus, complicated and computationally demanding receiver structures, as for example proposed in [18], are not necessary in most cases.

There exist different variants of FBMC, but I will mainly focus on Offset Quadrature Amplitude Modulation (OQAM) [19] based schemes because they provide the highest spectral efficiency. Different names are used to describe OQAM, such as, OFDM/OQAM, FBMC-Pulse-Amplitude Modulation (PAM) [20–22], Staggered Multitone (SMT) or Cosine Modulated Multitone (CMT) [23, 24], which, however, are essentially all the same. One can

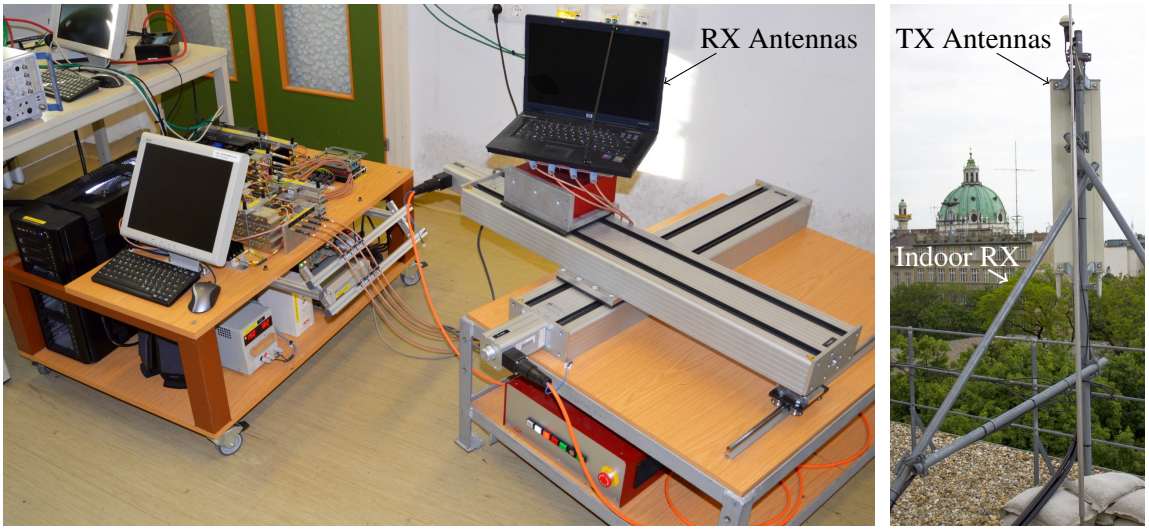

Figure 1.3. The Vienna Wireless Testbed operates at a carrier frequency of 2.5 GHz. The link distance between TX and RX is approximately 150 m. The RX antenna is mounted on a xyϕ-table, allowing to measure at different RX positions. This leads to Rayleigh fading.

easily transform one of those schemes into another by appropriately tuning the underlying parameters. For example, FBMC-PAM is a conventional FBMC-OQAM system where the subcarrier spacing is reduced by a factor of two, the number of subcarriers is increased by two, and the offset is applied in the frequency domain instead of the time domain. Unfortunately, all the nice features of FBMC-OQAM come at a price: the complex orthogonality condition is replaced by the less strict real orthogonality condition. While this limitation has in many cases either no, or only a minor influence on the performance, some important methods, such as, channel estimation or some MIMO techniques, become more challenging.

In this thesis, I provide a unifying framework, discussion and performance evaluation of FBMC and compare it to OFDM based schemes. I enhance existing methods of channel estimation and equalization. Furthermore, I provide novel insights into spread FBMC-OQAM systems. Finally, I propose a novel pruned Discrete Fourier Transform (DFT) spread FBMC transmission scheme with superior properties over legacy Single Carrier - Frequency-Division Multiple Access (SC-FDMA). Testbed measurements validate many of my proposed solutions.

1.2 Testbed Measurements

While most papers related to FBMC are purely based on simulations, I additionally perform real-world testbed measurements at a carrier frequency of 2.5 GHz, outdoor-to-indoor, 150 m

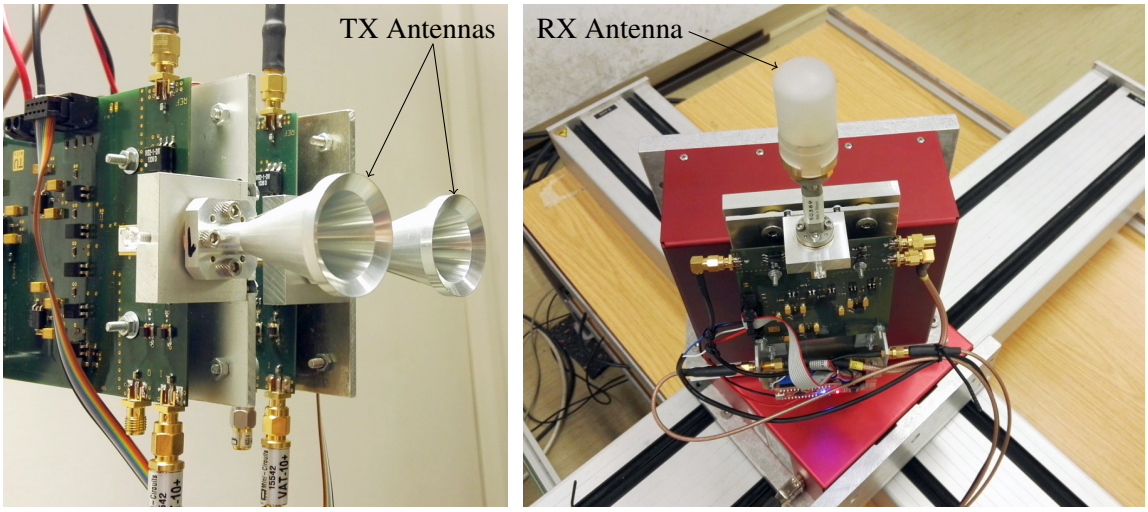

Figure 1.4. The indoor mmWave testbed operates at a carrier frequency of 60 GHz. The link distance between TX and RX is approximately 5 m, see also [25]. Again, the RX can be relocated, leading to Rician fading in case of LOS. Once the LOS component is blocked, the Rician K factor becomes very low, close to Rayleigh fading.

link distance, see Figure 1.3, and 60 GHz, indoor-to-indoor, 5 m link distance, see Figure 1.4. My measurements support the claim that FBMC is a viable choice for future mobile systems. I follow the measurement methodology presented in [26]. FBMC and OFDM signals are pre-generated off-line in MATLAB and the samples are saved on a hard disk. Then, a Digital-to-Analog-Converter (DAC) together with a radio frequency hardware up-converts the signal to 2.5 GHz, respectively 60 GHz. Furthermore, I relocate the receive antennas within an area of a few wavelengths, resulting in Rayleigh or Rician fading. Figure 1.5 shows a possible channel realization, measured at 60 GHz in case of NLOS. Different Signal-to-Noise Ratio (SNR) values are obtained by a stepwise attenuator at the transmitter. Time and frequency synchronization is guaranteed by a rubidium frequency standard, a GPS reference clock and a backbone network to exchanging time-stamps [28]. The receiver itself down-converts the signal and saves the samples on a hard disk. After the measurement, I evaluate the received samples again off-line in MATLAB. Such off-line evaluation represents a cost efficient way of emulating real world transmissions. Throughout all my measurements, simple one-tap equalizers were sufficient in FBMC. Thus, computationally demanding receiver structures, see Section 3.2, are in many cases not necessary.

In my 2.5 GHz measurement setup, see Figure 1.3, the transmit antenna points directly to the receiver but objects within the Fresnel zone cause diffraction and scattering. I measure approximately Rayleigh fading, that is, my measurement results in [29–31] are in agreement with the theoretical predictions of Rayleigh fading. All multipath components

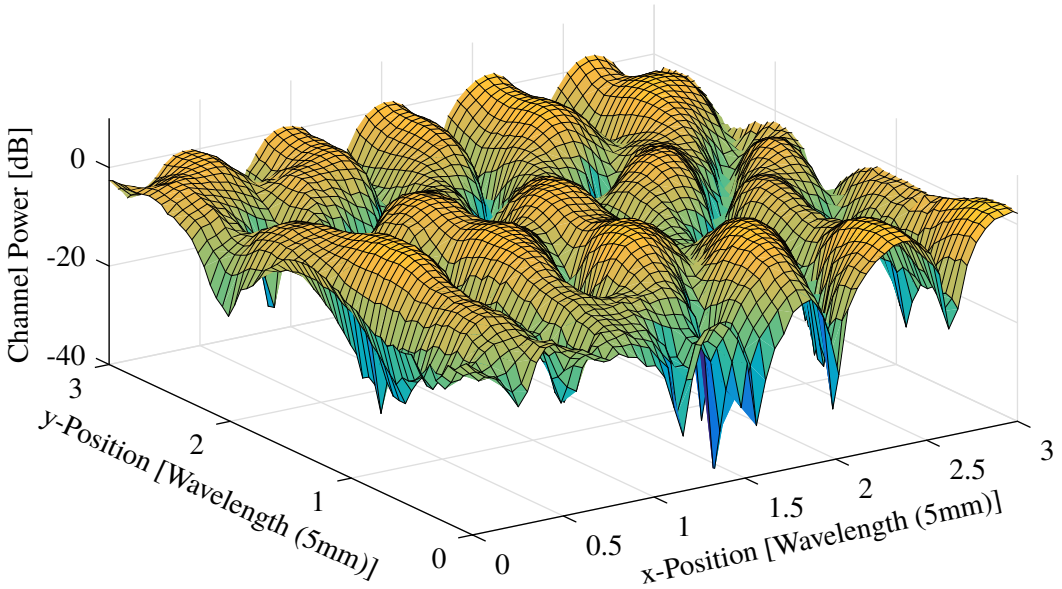

Figure 1.5. The measured channel at a carrier frequency of 60 GHz (averaged over 6 MHz and 300 μs, possible because of a high correlation in time and frequency) shows large fading dips in case of NLOS (low Rician K factor). For LOS, smaller fluctuations are observed due to a higher Rician K factor (not shown here). ©2017 IEEE, [27].

arrive approximately at the same time, so that the channel is relatively flat in frequency. Rayleigh fading is mainly observed by relocating the receive antennas within a few wavelength but not over the frequency domain (for the small bandwidth I usually consider). For my 60 GHz measurement setup, I observe a relatively high Rician K-factor in case of LOS, which can be explained by highly directional horn antennas and a small wavelength. Once the LOS path is blocked, however, the Rican K-factor becomes very small, close to Rayleigh fading.

While a testbed is very useful for proof-of-concept measurements and performance evaluations over true physical channels, it does not necessarily reflect real world systems. For example, my testbed does not operate in real time, higher layers are ignored, time-frequency synchronization is not an issue and I only measure two specific channel scenarios, see Figure 1.3 and Figure 1.4. Those drawbacks, however, could be mitigated by spending more money and more man-power into the testbed. Nonetheless, one of the most important aspects of a testbed is that it forces one to think about the true physical meaning behind certain transmission techniques. Very often, people forget the underlying assumptions of their simulation models and ignore crucial practical aspects. Some common physical misinterpretations for OFDM and FBMC included:

- Only the subcarrier spacing and the channel statistics determine the performance over a doubly-selective channel. The Fast Fourier Transform (FFT) size has no direct

influence. The relationship between FFT size N_{FFT}, subcarrier spacing F and sampling rate f_{s} is given by:

$$N_{\mathrm{FFT}} = \frac{f_{\mathrm{s}}}{F}. \tag{1.1}$$

- Practical systems will never operate at a critical sampling rate, that is, the FFT size will alway be larger than the number of active subcarriers. The remaining FFT points are set to zero. This has many important implications, especially for channel estimation. The channel impulse response cannot be accurately estimated because there is no information available at the zero subcarriers. Fortunately, the impulse response is not needed for equalization. Also, FFT interpolation will perform poorly because of errors at the edges.

- The FFT size must not necessarily be a power of two (in simulations). Instead, the FFT size should be chosen so that the sampling rate, see (1.1), fits approximately the predefined delay taps of the power delay profile (assuming that transmit filtering can be neglected). Alternatively, one could choose an FFT size that is a power of two but must later up-sample the transmit signal. The first approach is more convenient.

- One should always check the feasibility of parameters. An SNR of 70 dB can easily be achieved in MATLAB, but not so much in reality. Also, the maximum Doppler-shift and delay spread are often chosen too high.

- The usage of $\mathrm{E_b/N_0}$ instead of (receive) SNR might lead to the wrong conclusions, see Appendix A.2.

1.3 Scientific Contributions and Outline

As a doctoral candidate, I first-authored three journals papers [1, 32, 33], 13 high quality conference papers [27, 29–31, 34–42], one book chapter [43] and one master thesis in economics [44]. Furthermore, I coauthored several other papers [45–49]. In my first-authored papers, I investigated a large range of different topics, ranging from OFDM [34, 29, 30, 43] over information theory [31] and queuing theory [35] to the economic aspects of dynamic spectrum allocation [44]. However, for this thesis, I will mainly focus on FBMC because it was my main research topic over the last two years [1, 27, 32, 33, 36–42]. To be specific, my thesis is based on the following papers[1]:

[1] All those papers were accepted at the first go; none was ever truly rejected, indicating the high quality. The decision of (ii) and (iii) was reject - resubmission allowed, essentially a major revision. With respect to (iii), the editor and the reviewers encouraged us to transform the initial letter submission into a full paper.

(i) R. Nissel, S. Schwarz, and M. Rupp, "Filter bank multicarrier modulation schemes for future mobile communications," *IEEE Journal on Selected Areas in Communications*, vol. 35, no. 8, pp. 1768–1782, 2017

(ii) R. Nissel and M. Rupp, "OFDM and FBMC-OQAM in doubly-selective channels: Calculating the bit error probability," *IEEE Communications Letters*, vol. 21, no. 6, pp. 1297–1300, 2017

(iii) R. Nissel and M. Rupp, "Pruned DFT spread FBMC-OQAM: Low-PAPR, low latency, high spectral efficiency," *Submitted to IEEE Transactions on Communications*, 2018

(iv) R. Nissel, J. Blumenstein, and M. Rupp, "Block frequency spreading: A method for low-complexity MIMO in FBMC-OQAM," in *IEEE Workshop on Signal Processing Advances in Wireless Communications (SPAWC)*, Hokkaido, Japan, July 2017

(v) R. Nissel, M. Rupp, and R. Marsalek, "FBMC-OQAM in doubly-selective channels: A new perspective on MMSE equalization," in *IEEE Workshop on Signal Processing Advances in Wireless Communications (SPAWC)*, Hokkaido, Japan, July 2017

(vi) R. Nissel, E. Zöchmann, M. Lerch, S. Caban, and M. Rupp, "Low-latency MISO FBMC-OQAM: It works for millimeter waves!," in *IEEE International Microwave Symposium*, Honolulu, Hawaii, June 2017

(vii) R. Nissel, E. Zöchmann, and M. Rupp, "On the influence of doubly-selectivity in pilot-aided channel estimation for FBMC-OQAM," in *IEEE Vehicular Technology Conference (VTC Spring)*, Sydney, Australia, June 2017

(viii) R. Nissel and M. Rupp, "Enabling low-complexity MIMO in FBMC-OQAM," in *IEEE Globecom Workshops (GC Wkshps)*, Washington DC, USA, Dec 2016

(ix) R. Nissel, S. Caban, and M. Rupp, "Experimental evaluation of FBMC-OQAM channel estimation based on multiple auxiliary symbols," in *IEEE Sensor Array and Multichannel Signal Processing Workshop (SAM)*, Rio de Janeiro, Brazil, July 2016

(x) R. Nissel and M. Rupp, "Bit error probability for pilot-symbol aided channel estimation in FBMC-OQAM," in *IEEE International Conference on Communications (ICC)*, Kuala Lumpur, Malaysia, May 2016

(xi) R. Nissel and M. Rupp, "On pilot-symbol aided channel estimation in FBMC-OQAM," in *IEEE International Conference on Acoustics, Speech and Signal Processing (ICASSP)*, pp. 3681–3685, Shanghai, China, March 2016

In the following paragraphs, I will give a short overview of the individual chapters. A more detailed description can be found at the beginning of each chapter, where also the novel contributions are explicitly stated.

In **Chapter 2**, I provide a detailed description of FBMC and OFDM, propose a novel matrix based system model, and show that FBMC can be interpreted as a special case of windowed OFDM. Furthermore, I discuss possible use-cases for FBMC and show that it outperforms OFDM in terms of time-frequency efficiency.

In **Chapter 3**, I discuss channel equalization in FBMC. Firstly, I derive closed-form Bit Error Probability (BEP) and Signal-to-Interference Ratio (SIR) expressions and show that, in many practical cases, one-tap equalizers are sufficient. This is particularly true for an optimal subcarrier spacing. Secondly, for the few rare cases where one-tap equalizers are not sufficient, I propose a novel Minimum Mean Squared Error (MMSE) multi-tap equalizer and a low-complexity interference cancellation scheme. Additionally, I show how those two methods can be extended to MIMO systems.

In **Chapter 4**, I investigate pilot-aided channel estimation in FBMC. To cancel the imaginary interference at the pilot positions, I enhance two existing methods, namely the auxiliary symbol method and the data spreading method. Furthermore, I compare these two methods in terms of throughput, measured with my testbed, and in terms of BEP, based on closed-form expressions, allowing me also to find an optimal pilot-to-data power offset. Finally, I propose a novel channel estimation method for doubly-selective channels, purely based on correlations and not relying on clustered pilots or any basis expansion model.

In **Chapter 5**, I discuss block spread FBMC-OQAM. Here, data symbols are spread in time or frequency, allowing to restore complex orthogonality in FBMC-OQAM. I propose two different interpretations of such spreading (code dimension, transforming the basis pulses) and derive the optimal spreading matrix. I then investigate Walsh-Hadamard spreading in more detail, focusing on the effects of block interference and doubly-selective channels. In case of spreading in time, real world testbed measurements validate the feasibility of my approach.

In **Chapter 6**, I propose a novel modulation scheme which combines the advantages of FBMC and SC-FDMA. On top of a conventional FBMC system, I develop a novel precoding method based on a pruned DFT in combination with one-tap scaling. The proposed technique has the same Peak-to-Average Power Ratio (PAPR) as SC-FDMA but requires no CP and has much better spectral properties. Furthermore, my method restores complex orthogonality and allows for low latency transmissions. Compared to pure SC-FDMA, the computational complexity is only two times higher. MIMO simulations over doubly-selective channels validate my claims.

In **Appendix A**, I compare my matrix notation with the commonly used discrete-time filter representation. I also discuss the problem of $\mathrm{E_b}/\mathrm{N_0}$ when comparing different modulation schemes and provide a compact overview of my closed form BEP expressions.

Reproducibility

In my opinion, one the most important aspects of scientific work is reproducibility. Indeed, many journals encourage authors to make their publications reproducible by publishing the underlying code on a website [50]. Unfortunately, this important aspect is often neglected in research [51]. It is therefore very hard, sometimes even impossible, to reproduce certain results. This unfortunate situation should be changed. To set a good example, my MATLAB code can be downloaded at

https://www.nt.tuwien.ac.at/downloads/

and allows to reproduce the results of [1, 33, 36, 39, 42]. In particular, the following important contributions can be easily reproduced:

- Effect of different subcarrier spacings within the same band, see Section 2.4, [1].
- Closed-form BEP calculations, see Section 3.1.1, [32].
- SIR calculations, see Section 3.1.2, [1].
- Channel estimation, including throughput simulations, see Section 4.1-4.3.1, [1, 42].
- Block spread FBMC-OQAM, see Section 5.2-5.3, [1, 36, 39].
- Pruned DFT spread FBMC-OQAM, see Section 6.2-6.3, [33].

A publishable code should always be well documented, leading to an additional workload. Thus, not all my papers are supported by a downloadable MATLAB code. Instead, I focused on those papers which are, in my opinion, more relevant. Nonetheless, it is relatively easy to reproduce also the other papers because I consistently employ the same matrix notation. This allows to reused the same basic elements with only minor modifications which are described in the corresponding papers. Note that, providing a downloadable MATLAB code, is well received within the community, as indicated by more than 1300 downloads within one year.

Chapter 2

Filter Bank Multicarrier Modulation

In this chapter, I provide a comprehensive overview of multicarrier systems and compare FBMC to OFDM in the context of the Balian-Low theorem. The three basic versions of FBMC, that is, FBMC-Quadrature Amplitude Modulation (QAM), FBMC-OQAM and block spread FBMC-OQAM, as well as conventional OFDM, are explained in detail. I also show that FBMC is better suited than OFDM for supporting different subcarrier spacings within the same band. This chapter is mainly based on my publications [1, 36, 42] and includes the following novel contributions:

- In Section 2.2, I propose a novel, matrix-based, transmission system model with many beneficial properties over the commonly used discrete-time filter bank description [1, 42].

- In Section 2.3, I show that, from a conceptional point of view, there is little difference in the modulation and demodulation step between FBMC and windowed OFDM. Thus, many hardware components can be reused [1].

- In Section 2.4, I show that FBMC allows for an efficient co-existence between different use cases within the same band and that, in contrast to common believe, FBMC can also be efficiently used in low-latency transmissions [1].

2.1 Multicarrier Modulation

Multicarrier modulation has a long-standing history in wireless communications [52–54]; however, widespread practical applications have only been realized in the latest versions of wireless systems in the form of OFDM, enabled by advances in integrated circuits. Current

applications of OFDM include, for example, Long Term Evolution (LTE), WiFi and Digital Video Broadcasting - Terrestrial (DVB-T).

In multicarrier systems, information is commonly transmitted over orthogonal pulses which overlap in time and frequency, see Figure 1.1. The big advantage is that these pulses usually occupy only a small bandwidth, so that frequency selective broadband channels transform into multiple, virtually frequency flat, sub-channels (subcarriers) with negligible interference, see Section 3.1.2. This enables the application of low-complexity one-tap equalizers which correspond to the maximum likelihood symbol detection in case of Gaussian noise, see Section 3.1. Furthermore, in many cases, the channel estimation process is simplified, adaptive modulation and coding techniques become applicable and MIMO can be straightforwardly employed [55]. Mathematically, the transmitted signal, $s(t)$, of a multicarrier system in the time domain can be expressed as

$$s(t) = \sum_{k=1}^{K} \sum_{l=1}^{L} g_{l,k}(t)\, x_{l,k}, \tag{2.1}$$

where $x_{l,k}$ denotes the transmitted symbol at subcarrier-position l and time-position k, and is chosen from a symbol alphabet $\mathcal{X}$, often a QAM or a PAM signal constellation. The transmitted basis pulse, $g_{l,k}(t)$ in (2.1), is defined as

$$g_{l,k}(t) = p_{\mathrm{TX}}(t - kT)\ \mathrm{e}^{\mathrm{j}2\pi\, lF\,(t-kT)}\ \mathrm{e}^{\mathrm{j}\theta_{l,k}}, \tag{2.2}$$

and is, essentially, a time and frequency shifted version of the prototype filter $p_{\mathrm{TX}}(t)$ with T denoting the time spacing and F the frequency spacing (subcarrier spacing). The choice of the phase shift, $\theta_{l,k}$, becomes relevant later in the context of FBMC-OQAM. After transmission over a channel, the received symbols are decoded by projecting the received signal, $r(t)$, onto the receive basis pulses, $q_{l,k}(t)$, that is,

$$y_{l,k} = \langle r(t), q_{l,k}(t) \rangle = \int_{-\infty}^{\infty} r(t)\, q_{l,k}^{*}(t)\, \mathrm{d}t, \tag{2.3}$$

where $q_{l,k}(t)$ is similarly defined as $g_{l,k}(t)$, except that a different prototype filter might be used:

$$q_{l,k}(t) = p_{\mathrm{RX}}(t - kT)\ \mathrm{e}^{\mathrm{j}2\pi\, lF\,(t-kT)}\ \mathrm{e}^{\mathrm{j}\theta_{l,k}}. \tag{2.4}$$

In an Additive White Gaussian Noise (AWGN) channel, a matched filter maximizes the SNR, that is, $q_{l,k}(t) = g_{l,k}(t)$ and thus $p_{\mathrm{RX}}(t) = p_{\mathrm{TX}}(t)$. In a doubly-selective channel, on the other hand, it might better to choose the TX prototype filter and the RX prototype filter slightly

differently, $p_{\mathrm{RX}}(t) \neq p_{\mathrm{TX}}(t)$, as for example done in pulse-shaped multicarrier transmissions [56] or in the practically more relevant case of CP-OFDM, see Section 2.1.1. Throughout this thesis, I assume an AWGN matched filter for FBMC, that is, $p(t) = p_{\mathrm{RX}}(t) = p_{\mathrm{TX}}(t)$. Only for CP-OFDM, I allow different transmit and receive filters.

As indicated in (2.1)-(2.4), multicarrier systems are mainly characterized by the prototype filters, $p_{\mathrm{TX}}(t)$ and $p_{\mathrm{RX}}(t)$, as well as time spacing T and frequency spacing F, so that the ambiguity function, defined as [23, 55]:

$$A(\tau, \nu) = \int_{-\infty}^{\infty} p_{\mathrm{TX}}\left(t - \frac{\tau}{2}\right) p_{\mathrm{RX}}^{*}\left(t + \frac{\tau}{2}\right) \mathrm{e}^{\mathrm{j}2\pi\nu t}\, \mathrm{d}t, \tag{2.5}$$

captures the main properties of a multicarrier system in a compact way. In contrast to [23, 55], I flip the sign of τ and ν, leading to a more intuitive description of time and frequency offsets. The projection of the transmitted basis pulse onto the received basis pulse can then be expressed by the ambiguity function according to

$$\langle g_{l_1,k_1}(t), q_{l_2,k_2}(t)\rangle = \underbrace{\mathrm{e}^{-\mathrm{j}\pi TF(l_1+l_2)(k_1-k_2)}\, \mathrm{e}^{\mathrm{j}(\theta_{l_1,k_1}-\theta_{l_2,k_2})}}_{\text{only a phase shift}}\ \underbrace{A(T(k_1-k_2), F(l_1-l_2))}_{\text{ambiguity function}}. \tag{2.6}$$

Moreover, the SIR in a doubly-selective channel can be computed by the ambiguity function [55, 57].

There exist fundamental limitations for multicarrier systems, as formulated by the Balian-Low theorem [58], which states that it is mathematically impossible that the following four desired properties are fulfilled at the same time:

1. Maximum symbol density,
$$TF = 1, \tag{2.7}$$

2. Time-localization,
$$\sigma_t = \sqrt{\int_{-\infty}^{\infty} (t-\bar{t})^2\, |p(t)|^2\, \mathrm{d}t} \ < \infty, \tag{2.8}$$

3. Frequency-localization,
$$\sigma_f = \sqrt{\int_{-\infty}^{\infty} (f-\bar{f})^2\, |P(f)|^2\, \mathrm{d}f} \ < \infty, \tag{2.9}$$

Table 2.1. Comparison of different multicarrier schemes (for AWGN), ©2017 IEEE, [1]

	Maximum Symbol Density	Time-Localization	Frequency-Localization	(Bi)-Orthogonal	Independent Transmit Symbols
OFDM (without CP)	yes	yes	no	yes	yes
Windowed/Filtered OFDM	no	yes	yes	yes	yes
FBMC-QAM[1]	no	yes	yes	yes	yes
FBMC-OQAM	yes	yes	yes	real only	yes
Block Spread FBMC-OQAM	yes	yes	yes	yes, after de-spreading	no

[1] There does not exist a unique definition

4. (Bi)-orthogonality,

$$\langle g_{l_1,k_1}(t), q_{l_2,k_2}(t)\rangle = \delta_{(l_1-l_2),(k_1-k_2)} \tag{2.10}$$

$$A(T(k_1-k_2), F(l_1-l_2)) = \delta_{(l_1-l_2),(k_1-k_2)}, \tag{2.11}$$

with δ denoting the Kronecker delta function. The pulse $P(f) = \int_{-\infty}^{\infty} p(t)\,\mathrm{e}^{-\mathrm{j}2\pi ft}\mathrm{d}t$ in (2.9) represents the Fourier transform of $p(t)$ while $\bar{t} = \int_{-\infty}^{\infty} t\,|p(t)|^2\,\mathrm{d}t$ corresponds to the mean time and $\bar{f} = \int_{-\infty}^{\infty} f\,|P(f)|^2\,\mathrm{d}f$ the mean frequency of the pulse. Furthermore, I assume that $p(t)$ is normalized to preserve unit energy. The localization measures in (2.8) and (2.9) can be interpreted as standard deviation with $|p(t)|^2$ and $|P(f)|^2$ representing the probability density function (pdf). This relates the Balian-Low condition to the Heisenberg uncertainty relationship [59, Chapter 7].

The Balian-Low theorem implies that at least one of the desired properties has to be sacrificed when designing multicarrier waveforms. Table 2.1 compares different modulation schemes in the context of the Balian-Low theorem. The different techniques are explained in more detail in the following subsections.

2.1.1 CP-OFDM

CP-OFDM is the most prominent multicarrier scheme and is applied, for example, in Wireless LAN and LTE [60, 61]. CP-OFDM employs rectangular transmit and receive pulses, which greatly reduce the computational complexity. Furthermore, the CP guarantees orthogonality

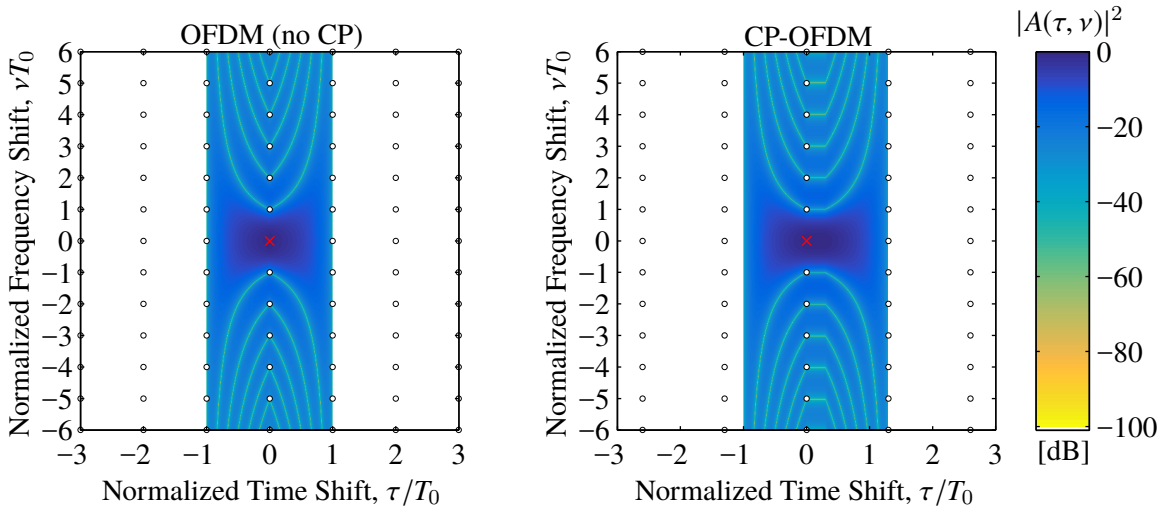

Figure 2.1. The ambiguity function $20\log_{10}|A(\tau,\nu)|$ in case of CP-OFDM, see (2.12) and (2.13). The right figure illustrates the case of $T_{\mathrm{CP}} = 0.3\,T_0$. In particular, a time-offset and multipath delays do not destroy orthogonality (as long as they are smaller than the CP). Unfortunately, the rectangular prototype filter leads to a poor localization in the frequency domain.

in frequency selective channels. The TX and RX prototype filters are given by

$$p_{\mathrm{TX}}(t) = \begin{cases} \frac{1}{\sqrt{T_0}} & \text{if } -\left(\frac{T_0}{2}+T_{\mathrm{CP}}\right) \le t < \frac{T_0}{2} \\ 0 & \text{otherwise} \end{cases} \tag{2.12}$$

$$p_{\mathrm{RX}}(t) = \begin{cases} \frac{1}{\sqrt{T_0}} & \text{if } \frac{T_0}{2} \le t < \frac{T_0}{2} \\ 0 & \text{otherwise} \end{cases} \tag{2.13}$$

for which

$$\begin{aligned} &\textbf{(Bi)-Orthogonal}: \quad T = T_0 + T_{\mathrm{CP}}; \quad F = 1/T_0 \quad \rightarrow TF = 1 + \tfrac{T_{\mathrm{CP}}}{T_0} \\ &\textbf{Localization}: \qquad \sigma_t = \tfrac{T_0+T_{\mathrm{CP}}}{2\sqrt{3}}; \quad \sigma_f = \infty \end{aligned}, \tag{2.14}$$

with T_0 representing a time-scaling parameter, which depends on the desired subcarrier spacing (or time-spacing).

Figure 2.1 shows the ambiguity function, see (2.5), for CP-OFDM. The left part of the figure represents the case if no CP is employed. Orthogonality is then guaranteed for a time spacing of $T = T_0$ and a frequency spacing of $F = 1/T_0$, leading to $TF = 1$. This is also indicated by the rectangular grid (the small circles) inside of Figure 2.1. Furthermore, one recognizes that the ambiguity function decays very slowly in frequency because of the rectangular pulse. The right part of Figure 2.1 assumes a CP length of $T_{\mathrm{CP}} = 0.3\,T_0$, leading

to an orthogonal time-frequency spacing of $TF = 1.3$. It can easily be checked that the system preserves orthogonality even if a time-offset (or multipath delay) occurs, simply by shifting the time-frequency grid by some additional time-offset. This works as long as the time-offset is smaller than the length of the CP.

One of the biggest disadvantages of OFDM is its poor spectral behavior, caused by the underlying rectangular prototype filters, see Figure 1.2 and Figure 2.1. Additionally, the CP simplifies equalization in frequency-selective channels but also reduces the spectral efficiency $TF > 1$; in an AWGN channel, no CP is needed. In order to reduce the OOB emissions in OFDM, 3GPP is currently considering windowing [13] and filtering [5, 14]. The windowed OFDM scheme is called OFDM with WOLA [13]. At the transmitter, the edges of the rectangular pulse are replaced by smoother functions (windowing) and neighboring WOLA symbols overlap in time. The receiver also applies windowing but the overlapping and add operation is performed within the same WOLA symbol which reduces the inter-band interference. To guarantee orthogonality, the CP must be long enough to account for both, windowing at the transmitter and windowing at the receiver (even in an AWGN channel). For the filter based OFDM schemes, two methods are proposed. Firstly, UFMC [14] which applies subband wise filtering based on a Dolph-Chebyshev window. Orthogonality is guaranteed by either Zero-Padding (ZP) or a conventional CP. The performance differences between CP and ZP are rather small, so that I will consider only the CP version here to be consistent with the other proposed schemes. The filter parameters are chosen similarly as suggested in [14]. This leads to 12 subcarriers per subband and, if no receive filter is employed, to an orthogonal time-frequency spacing of $TF = 1.07$ (same as in LTE). However, the receive filter is as important as the transmit filter, see Section 2.4. Thus, I also apply subband-wise filtering at the receiver. Orthogonality is then guaranteed for a time-frequency spacing of $TF = 1.14$. To improve the spectral efficiency, however, I decrease the time-frequency spacing to $TF = 1.09$ and allow some small self-interference ($\approx$65 dB). The second filter-based OFDM scheme considered within 3GPP is f-OFDM [5]. Here, the number of subcarriers for one subband is usually much higher than in UFMC and often includes all subcarriers belonging to a specific use case. The filter itself is based on a sinc pulse (perfect rectangular filter) which is multiplied by a Hann window; other filters are also possible [5]. For a fair comparison, I consider the same time-frequency spacing as in UFMC, that is, $TF = 1.09$ and increase the length of the transmit and receive filters so that self interference is approximately 65 dB. The filters in f-OFDM are usually longer than in UFMC.

As shown in Figure 1.2, windowing and filtering can reduce the high OOB emissions of CP-OFDM. However, this comes at the price of reduced spectral efficiency, as indicated by the product of $TF > 1$, and lower robustness in frequency selective channels. Furthermore,

filtering and windowing still do not provide as low OOB emissions as FBMC, which can additionally achieve a maximum symbol density of $TF = 1$.

2.1.2 FBMC-QAM

There does not exist a unique definition for FBMC-QAM. Some authors [62] sacrifice frequency localization, making the modulation scheme even worse than OFDM in terms of OOB emissions. Others [63, 64] sacrifice orthogonality in order to have a time-frequency spacing of $TF \approx 1$ and time-frequency localization. I, on the other hand, consider for FBMC-QAM a time-frequency spacing of $TF = 2$, thus sacrifice spectral efficiency to fulfill all other desired properties; see Table 2.1. Such large time-frequency spacing increases the overall robustness in a doubly-selective channel, see Section 3.1.2. However, the main reason for choosing $TF = 2$ is the straightforward application in FBMC-OQAM, described in Section 2.1.3.

A possible prototype filter for FBMC-QAM is based on Hermite polynomials $H_n(\cdot)$, as proposed in [65]:

$$p(t) = \frac{1}{\sqrt{T_0}} \mathrm{e}^{-2\pi\left(\frac{t}{T_0}\right)^2} \sum_{\substack{i=\{0,4,8,\\ 12,16,20\}}} a_i H_i\left(2\sqrt{\pi}\frac{t}{T_0}\right), \tag{2.15}$$

for which the coefficients can be found to be [42]

$$\begin{aligned} a_0 &= 1.412692577 & a_{12} &= -2.2611 \cdot 10^{-9} \\ a_4 &= -3.0145 \cdot 10^{-3} & a_{16} &= -4.4570 \cdot 10^{-15} \\ a_8 &= -8.8041 \cdot 10^{-6} & a_{20} &= 1.8633 \cdot 10^{-16}. \end{aligned} \tag{2.16}$$

This leads to the following properties of (2.15),

$$\begin{aligned} &\textbf{Orthogonal}: \quad T = T_0; && F = 2/T_0 && \rightarrow TF = 2 \\ &\textbf{Localization}: \quad \sigma_t = 0.2015\, T_0; && \sigma_f = 0.403/T_0. \end{aligned} \tag{2.17}$$

The left part of Figure 2.2 shows the ambiguity function for the Hermite prototype filter. Orthogonality is observed for a time spacing of $T = T_0$ and a frequency spacing of $F = 2/T_0$. Compared to OFDM, the frequency localization is much better. Note that the Hermite pulse has the same shape in time and frequency, allowing to exploit symmetries. Furthermore, it is based on a Gaussian function and therefore has a good joint time-frequency localization of $\sigma_t\sigma_f = 1.02 \times 1/4\pi$, almost as good as the bound of $\sigma_t\sigma_f \geq 1/4\pi \approx 0.08$ (attained by the Gaussian pulse), making it relatively robust to doubly-selective channels, see Section 3.1.2.

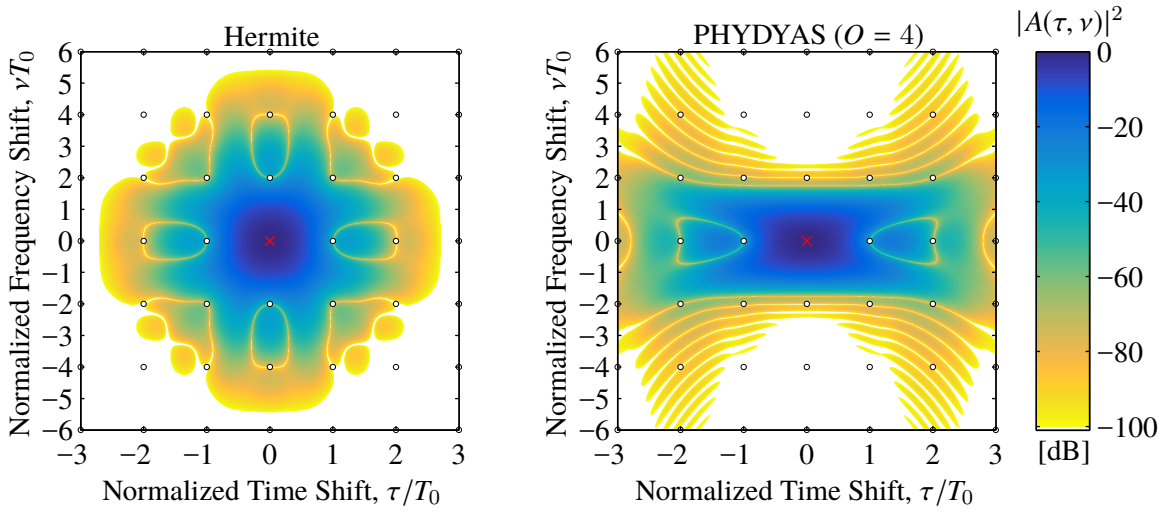

Figure 2.2. The ambiguity function $20 \log_{10} |A(\tau, \nu)|$, see (2.5), in case of FBMC-OQAM. In contrast to OFDM, the Hermite and the PHYDYAS pulses are localization in both, time and frequency. Orthogonality is guaranteed for $T = T_0$ and $F = \frac{2}{T_0}$, leading to $TF = 2$.

Note that no on-line evaluation of the Hermite polynomials is necessary because the sampled version of (2.15) can be pre-calculated.

Another prominent filter is the so called PHYDYAS prototype filter [66, 67], constructed by:

$$p(t) = \begin{cases} \dfrac{1+2\sum\limits_{i=1}^{O-1} b_i \cos\left(\frac{2\pi t}{OT_0}\right)}{O\sqrt{T_0}} & \text{if } -\frac{OT_0}{2} < t \leq \frac{OT_0}{2} \\ 0 & \text{otherwise} \end{cases}. \tag{2.18}$$

The coefficients b_i were calculated in [68] and depend on overlapping factor O (the interpretation of the overlapping factor will be more clear in Section 2.3). For example, for an overlapping factor of $O = 4$, the coefficients become:

$$b_1 = 0.97195983; \quad b_2 = \sqrt{2}/2; \quad b_3 = 0.23514695. \tag{2.19}$$

which leads to

$$\begin{array}{lllll} \textbf{Orthogonal}: & T = T_0; & F = 2/T_0 & \rightarrow TF = 2 \\ \textbf{Localization}: & \sigma_t = 0.2745\, T_0; & \sigma_f = 0.328/T_0. & \end{array} \tag{2.20}$$

The right part of Figure 2.2 shows the ambiguity function for the PHYDYAS filter ($O = 4$). Compared to the Hermite prototype filter, the PHYDYAS filter has better frequency-

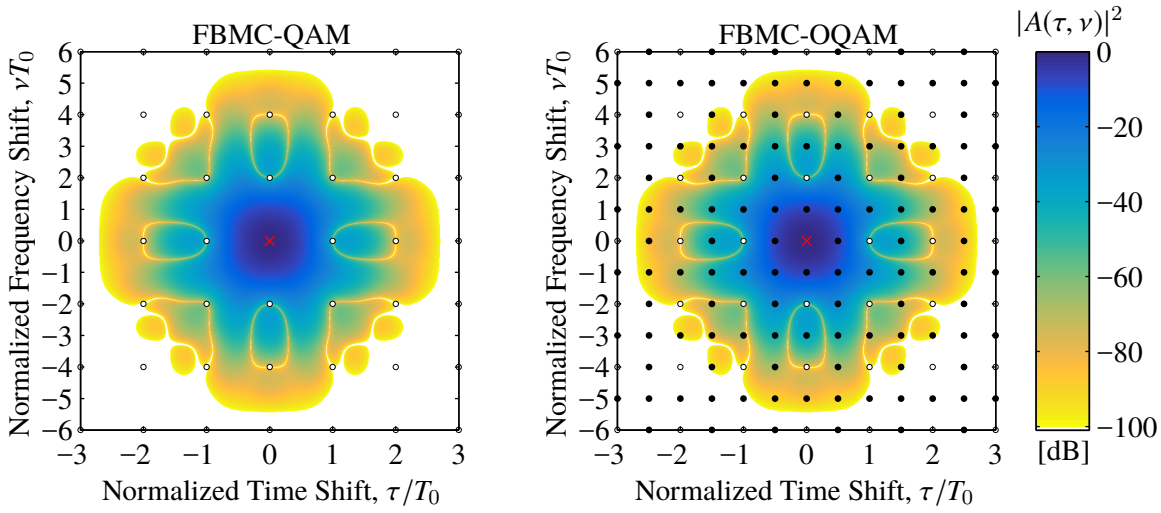

Figure 2.3. Illustration of FBMC-OQAM. Starting from an FBMC-QAM system (left), the time spacing and the frequency spacing are both reduced by a factor of two, leading to a time spacing of $T = T_0/2$ and a frequency spacing of $F = 1/T_0$ (right). The so induced interference (black markers) is shifted to the purely imaginary domain by the phase shift $\theta_{l,k} = \frac{\pi}{2}(l + k)$ and can easily be canceled by taking the real part.

localization but worse time-localization. The joint time-frequency localization of $\sigma_t\sigma_f = 1.13 \times 1/4\pi$ is also worse.

2.1.3 FBMC-OQAM

FBMC-OQAM is related to FBMC-QAM but has the same symbol density as OFDM without CP. To satisfy the Balian-Low theorem, the complex orthogonality condition $\langle g_{l_1,k_1}(t), g_{l_2,k_2}(t)\rangle = \delta_{(l_2-l_1),(k_2-k_1)}$ is replaced by the less strict real orthogonality condition $\Re\{\langle g_{l_1,k_1}(t), g_{l_2,k_2}(t)\rangle\} = \delta_{(l_2-l_1),(k_2-k_1)}$. FBMC-OQAM works, in principle, as follows:

1. Design a prototype filter with $p(t) = p(-t)$ which is orthogonal for a time spacing of $T = T_0$ and a frequency spacing of $F = 2/T_0$, leading to $TF = 2$, see (2.15) or (2.18).

2. Reduce the (orthogonal) time-frequency spacing by a factor of two each, that is, $T = T_0/2$ and $F = 1/T_0$.

3. The induced interference, caused by the time-frequency squeezing, is shifted to the purely imaginary domain by the phase shift $\theta_{l,k} = \frac{\pi}{2}(l + k)$ in (2.2).

The described process is illustrated in Figure 2.3. Starting from an FBMC-QAM system (left) the orthogonal time-frequency spacing of $T = T_0$ and $F = 2/T_0$ is reduced to $T = T_0/2$ and

$F = 1/T_0$ (right). This causes interference, indicated by the black markers. To be specific, for $\theta_{l,k} = \frac{\pi}{2}(l + k)$ and $TF = 0.5$, the inner product of (2.6), can be expressed as

$$\langle g_{l+\Delta l,k+\Delta k}(t), q_{l,k}(t)\rangle = \underbrace{\mathrm{e}^{\mathrm{j}\frac{\pi}{2}(\Delta l+\Delta k)}\mathrm{e}^{-\mathrm{j}\frac{\pi}{2}\Delta k(2l+\Delta l)}}_{\text{purely imaginary for odd } \Delta\mathrm{k},\, \Delta\mathrm{l}} \quad \underbrace{A(\Delta k\, T, \Delta l\, F)}_{0 \text{ if both } \Delta k\neq 0,\, \Delta l\neq 0 \text{ are even}} \quad . \tag{2.21}$$

The ambiguity function in (2.21) guarantees orthogonality if both, Δk and Δl, are even. On the other hand, if either Δk or Δl is odd, $A(\cdot)$ no longer becomes zero. Then, the overall phase of (2.21) is purely determined by the exponential function since the ambiguity function is always real-valued because of $p(t) = p(-t)$. In particular, the exponential function becomes purely imaginary if either Δk or Δl is odd. Thus, the real orthogonality condition is satisfied.

Although the time-frequency spacing of FBMC-OQAM is equal to $TF = 0.5$, only real-valued information symbols can be transmitted in such a system, leading to an equivalent time-frequency spacing of $TF = 1$ for complex-valued symbols. Very often, the real-part of a complex-valued symbol is mapped to the first time slot and the imaginary-part to the second time slot, thus the name offset-QAM. However, such self-limitation is not necessary.

The main disadvantage of FBMC-OQAM is the loss of complex orthogonality. This implies particularities for some MIMO techniques, such as space-time block codes [69] or maximum likelihood symbol detection [70], as well as for channel estimation [41].

2.1.4 Block Spread FBMC-OQAM

To overcome the problems related to FBMC-OQAM, one has to restore complex orthogonality. This can be achieved by spreading symbols in time or frequency. In [70] the authors utilize FFT spreading, while the authors of [69, 71] employ Walsh–Hadamard spreading. The latter can be implemented by a fast Walsh-Hadamard transform and has almost no additional complexity. Although block spread FBMC is similar to Code Division Multiple Access (CDMA), employed in 3G, it is also different in the sense that no rake receiver and no root-raised-cosine filter is necessary. Instead, simple one-tap equalizers can be employed, which is possible as long as the channel is approximately flat in time (for spreading in time) or in frequency (for spreading in frequency). Because wireless channels are highly underspread [72], such assumption is true in many scenarios. Furthermore, the good time-frequency localization of FBMC allows to efficiently separate blocks by only one guard symbol and no additional filtering is necessary. Figure 2.4 illustrates the concept of block spread FBMC-OQAM for spreading in the frequency domain, although one could equivalently spread in time. The left part of Figure 2.4 represents conventional FBMC-OQAM. Because each time-frequency position can only carry real-valued symbols, two subcarriers are required to transmit one

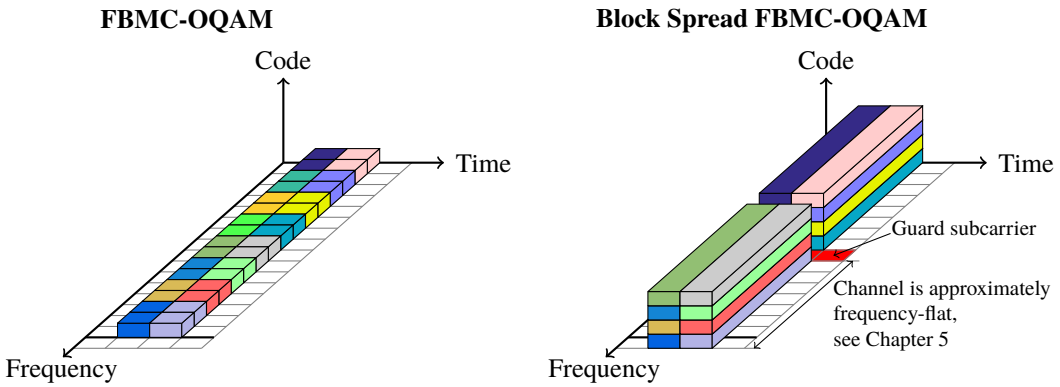

Figure 2.4. In conventional FBMC-OQAM (left), real valued symbols are transmitted over a rectangular time-frequency grid ($TF = 0.5$). Two real-valued symbols are required to transmit one complex-valued symbol. Thus, the name "offset"-QAM, where the offset is not in time (as often in literature) but in frequency to be consistent with block spread FBMC-OQAM (right). In block spread FBMC-OQAM, complex-valued symbols are spread over several subcarriers (or time positions). This restores complex orthogonality. To improve the SIR between different blocks, a guard symbol might be necessary. ©2017 IEEE, [36].

complex-valued data symbol, indicated by the color. In block spread FBMC-OQAM, on the other hand, data symbols no longer belong to a specific time-frequency position, but are rather spread over several subcarriers. To keep the spectral efficiency the same as in FBMC-OQAM (ignoring possible guard symbols), several data symbols are transmitted over the same time-frequency resources, but differentiated by the spreading/coding sequence. To be specific, $L/2$ complex-valued data symbols are spread over L subcarriers, leading to the same infomation rate as conventional FBMC-OQAM (again, ignoring possible guard symbols). Another advantage of block spread FBMC-OQAM can be found in the uplink. Conventional FBMC-OQAM requires phase synchronous transmissions ($\theta_{l,k} = \frac{\pi}{2}(l + k)$) which is problematic in the uplink (but not in the downlink) [14]. In block spread FBMC, this is no longer an issue because complex orthogonality is restored. The main disadvantage, on the other hand, is the increased sensitivity to doubly-selective channels. This, however, was never an issue in my real world testbed measurements. A more detailed discussion of block spread FBMC-OQAM can be found in Chapter 5.

2.2 Matrix-Based System Model

The continuous-time representation, presented in Section 2.1, provides analytical insights and gives physical meaning to multicarrier systems. However, such representation becomes analytically hard to track in doubly-selective channels because double integrals have to be

solved. Furthermore, in practice, the signal is generated in the discrete-time domain. Thus, I will switch from the continuous-time domain to the discrete-time domain. Additionally, I propose a novel matrix description, simplifying analytical calculations and allowing to utilize well-known matrix algebra. A more detailed discussion on the advantages of my matrix notation compared with the commonly used discrete-time filter description can be found in Appendix A.1.

I denote the sampling rate by $f_\mathrm{s} = 1/\Delta t = FN_\mathrm{FFT}$, where $N_\mathrm{FFT} \geq L$ represents the size of the FFT; see Section 2.3. For the time interval $-OT_0/2 + T \leq t < OT_0/2 + KT$, the sampled basis pulse $g_{l,k}(t)$, see (2.2), can be written in a basis pulse vector $\mathbf{g}_{l,k} \in \mathbb{C}^{N\times 1}$, that is,

$$[\mathbf{g}_{l,k}]_i = \sqrt{\Delta t}\; g_{l,k}(t)\Big|_{t=(i-1)\,\Delta t-\frac{OT_0}{2}+T} \quad \text{for} \quad i = 1, 2, \ldots, N \tag{2.22}$$

$$\text{with} \quad N = (OT_0 + T(K-1))f_\mathrm{s}. \tag{2.23}$$

By stacking all those basis pulse vectors in a large transmit matrix $\mathbf{G} \in \mathbb{C}^{N\times LK}$,

$$\mathbf{G} = \begin{bmatrix} \mathbf{g}_{1,1} & \cdots & \mathbf{g}_{L,1} & \mathbf{g}_{1,2} & \cdots & \mathbf{g}_{L,K} \end{bmatrix}, \tag{2.24}$$

and all data symbols in a large transmit symbol vector $\mathbf{x} \in \mathbb{C}^{LK\times 1}$,

$$\mathbf{x} = \mathrm{vec}\left\{ \begin{bmatrix} x_{1,1} & \cdots & x_{1,K} \\ \vdots & \ddots & \vdots \\ x_{L,1} & \cdots & x_{L,K} \end{bmatrix} \right\} \tag{2.25}$$

$$= \begin{bmatrix} x_{1,1} & \cdots & x_{L,1} & x_{1,2} & \cdots & x_{L,K} \end{bmatrix}^\mathsf{T}, \tag{2.26}$$

I can express the sampled transmit signal $\mathbf{s} \in \mathbb{C}^{N\times 1}$ in (2.1) by:

$$\mathbf{s} = \mathbf{G}\mathbf{x}. \tag{2.27}$$

Because of linearity, matrix $\mathbf{G}$ can easily be found even if the underlying modulation format is not known in detail. For that, all transmitted symbols have to be set to zero, except $x_{l,k} = 1$. Vector $\mathbf{s}$ then provides immediately the $l + L(k-1)$-th column vector of $\mathbf{G}$. Repeating this step for each time-frequency position delivers transmit matrix $\mathbf{G}$.

Similar as in (2.22)-(2.24), the sampled receive basis pulses $\mathbf{q}_{l,k} \in \mathbb{C}^{N\times 1}$, see (2.4), can also be stacked in a matrix according to,

$$\mathbf{Q} = \begin{bmatrix} \mathbf{q}_{1,1} & \cdots & \mathbf{q}_{L,1} & \mathbf{q}_{1,2} & \cdots & \mathbf{q}_{L,K} \end{bmatrix}. \tag{2.28}$$

By allowing a different transmit and receive matrix, I obtain a more general description of multicarrier systems that covers, for example, CP-OFDM and its derivatives (windowing/filtering). However, one should keep in mind that FBMC employs an AWGN matched filter, that is, $\mathbf{Q} = \mathbf{G}$.

Multipath propagation over time-variant channels is modeled by a time-variant impulse response $h[m_\tau, n]$, where m_τ represents the delay and n the time position [61]. By writing the impulse response in a time-variant convolution matrix $\mathbf{H} \in \mathbb{C}^{N\times N}$, defined as,

$$[\mathbf{H}]_{i,j} = h[i-j, i], \tag{2.29}$$

I can reformulate the received symbols in (2.3) by

$$\mathbf{y} = \mathbf{Q}^{\mathsf{H}}\,\mathbf{r} = \mathbf{Q}^{\mathsf{H}}\,\mathbf{H}\,\mathbf{G}\,\mathbf{x} + \mathbf{n}, \tag{2.30}$$

where $\mathbf{r} \in \mathbb{C}^{N\times 1}$ represents the sampled received signal and $\mathbf{n} \sim \mathcal{CN}(\mathbf{0}, P_\mathrm{n}\,\mathbf{Q}^{\mathsf{H}}\mathbf{Q})$ the Gaussian distributed noise, with P_n the white Gaussian noise power in the time domain. Because wireless channels are highly underspread, the channel induced interference can often be neglected compared to the noise. This means that the off-diagonal elements of $\mathbf{Q}^{\mathsf{H}}\mathbf{H}\mathbf{G}$ are so small, that they are dominated by noise; see Section 3.1 for more details. Thus, only the diagonal elements of $\mathbf{Q}^{\mathsf{H}}\mathbf{H}\mathbf{G}$ remain, allowing me to factor out the channel according to

$$\mathbf{y} \approx \mathrm{diag}\{\mathbf{h}\}\,\mathbf{Q}^{\mathsf{H}}\mathbf{G}\,\mathbf{x} + \mathbf{n}, \tag{2.31}$$

with $\mathbf{h} \in \mathbb{C}^{LK\times 1}$ describing the one-tap channel, that is, the diagonal elements of $\mathbf{Q}^{\mathsf{H}}\mathbf{H}\mathbf{G}$. The operator $\mathrm{diag}\{\cdot\}$ generates a diagonal matrix out of a vector. In OFDM and FBMC-QAM, the orthogonality condition implies that $\mathbf{Q}^{\mathsf{H}}\mathbf{G} = \mathbf{I}_{LK}$, while in FBMC-OQAM only real orthogonality holds true, that is, $\Re\{\mathbf{Q}^{\mathsf{H}}\mathbf{G}\} = \Re\{\mathbf{G}^{\mathsf{H}}\mathbf{G}\} = \mathbf{I}_{LK}$. The imaginary interference in FBMC-OQAM can be canceled by phase equalization of (2.31) followed by taking the real part. Note that, discarding the imaginary interference does not remove any useful information in an AWGN channel. To show that, I utilize a similar approach as for the derivation of the MIMO channel capacity [73], that is, I perform an eigendecomposition of $\mathbf{Q}^{\mathsf{H}}\mathbf{G}$ and employ water-filling. Figure 2.5 shows the corresponding eigenvalues of $\mathbf{Q}^{\mathsf{H}}\mathbf{G}$ and how they depend on the number of sucarriers, L, and the number of time symbols, K. I get rid of border effects (which become negligible for a large number of subcarriers and time symbols) by cyclically extending the pulses in time and frequency (which is equivalent to $K \to \infty$ and $L \to \infty$). Then $\mathbf{Q}^{\mathsf{H}}\mathbf{G}$ has exactly $LK/2$ non-zero eigenvalues, each having a value of two.

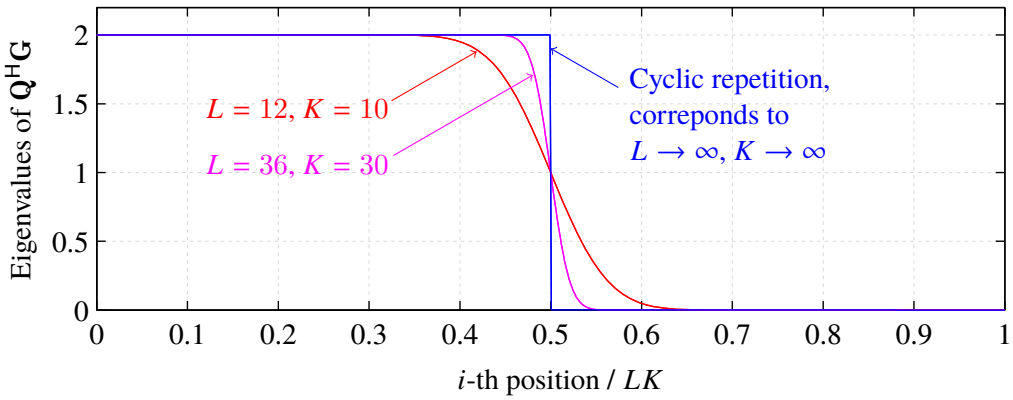

Figure 2.5. The eigenvalues of $\mathbf{Q}^H\mathbf{G}$ for an FBMC-OQAM system. Similar as for the derivation of the MIMO channel capacity, the eigenvalues in combination with eigenvector precoding can be utilized to determine the information rate. In particular, for a large number of subcarriers and time symbols, $\mathbf{Q}^H\mathbf{G}$ has exactly $LK/2$ nonzero eigenvalues. This is the same information rate as in FBMC-OQAM (LK real-valued symbols), implying that, by taking the real part, no useful information is lost.

This corresponds to the same information rate one can transmit with LK real-valued symbols (the SNR is also the same), so that, by taking the real part, no useful information is lost.

One advantage of my matrix notation is the straightforward equalization of the channel in OFDM and FBMC-QAM, for example, by a zero-forcing equalizer $(\mathbf{Q}^H\mathbf{H}\mathbf{G})^{-1}$, or an MMSE equalizer. In FBMC-OQAM, such direct inversion is not possible because $\mathbf{Q}^H\mathbf{H}\mathbf{G}$ has not full rank. Even more problematic is the inherent imaginary interference which influences the performance, so that a simple matrix inversion is overall a bad choice. Some of these problems can be avoided by stacking real and imaginary part into a supervector, see Section 3.2. However, as I have already elaborated and will further discuss throughout this thesis, in almost all practical cases one-tap equalizers are sufficient.

Another advantage of my matrix representation is the straightforward calculation of the expected transmit power in time, $\mathbf{P}_S \in \mathbb{R}^{N\times 1}$:

$$\mathbf{P}_S = \mathrm{diag}\{\mathbf{G}\,\mathbf{R}_\mathbf{x}\,\mathbf{G}^H\}, \tag{2.32}$$

where $\mathbf{R}_\mathbf{x} = \mathbb{E}\{\mathbf{x}\mathbf{x}^H\}$ describes the correlation matrix of the transmitted symbols, often an identity matrix. The Power Spectral Density (PSD), $\mathbf{PSD} \in \mathbb{R}^{N\times 1}$, can also be easily calculated by

$$[\mathbf{PSD}]_j = \sum_{i=0}^{KL-1} \left|[\mathbf{W}_N\,\mathbf{G}\,\mathbf{U}\,\sqrt{\mathbf{\Lambda}}]_{j,i}\right|^2, \tag{2.33}$$

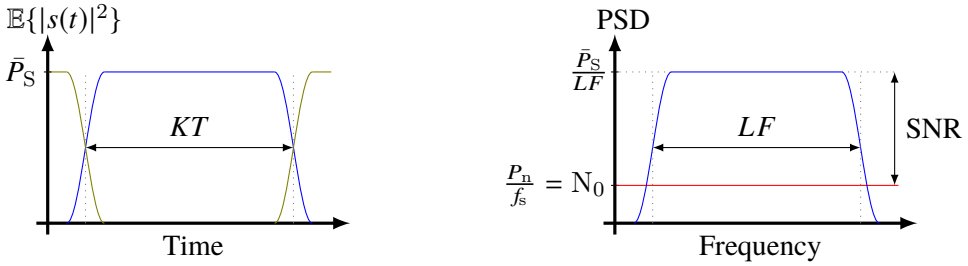

Figure 2.6. When comparing different modulation schemes, I always consider the same average transmit power (left part of the figure). Different transmission blocks may overlap in time, allowing to emulate the case of infinitely many blocks. The right part of the figure illustrates the SNR definition for FBMC-OQAM and OFDM.

where $\mathbf{W}_N$ is a DFT matrix of size N while $\mathbf{U}$ and $\mathbf{\Lambda}$ are obtained by an eigendecomposition of $\mathbf{R_x} = \mathbf{U}\mathbf{\Lambda}\mathbf{U}^\mathsf{H}$. Again, in many cases, $\mathbf{R_x}$ is an identity matrix, leading to $\mathbf{U}\sqrt{\mathbf{\Lambda}} = \mathbf{I}_{LK}$. Note that the index j in (2.33) represents the frequency index with resolution $\Delta f = \frac{f_\mathrm{s}}{N}$. Furthermore, (2.33) represents a scaled PSD. This scaling, however, does not matter because I usually normalize the PSD to 0 dB, see Figure 1.2, in order to improve readability.

When comparing different modulation schemes, I always consider the same average transmit power, defined as

$$\bar{P}_\mathrm{S} = \frac{1}{KT}\int_{-\infty}^{\infty} \mathbb{E}\{|s(t)|^2\}\,\mathrm{d}t \tag{2.34}$$

$$= \frac{1}{KT}\mathrm{tr}\{\mathbf{G}\,\mathbf{R_x}\,\mathbf{G}^\mathsf{H}\}\frac{1}{f_\mathrm{s}}. \tag{2.35}$$

This leads to a certain per symbol SNR, which determines the performance. For FBMC-OQAM and CP-OFDM, the SNR can be expressed by:

$$\mathrm{SNR} = \frac{\bar{P}_\mathrm{S}}{LF}\frac{1}{\mathrm{N}_0}, \tag{2.36}$$

with $\mathrm{N}_0 = \frac{P_\mathrm{n}}{f_\mathrm{s}}$ being the noise power spectral density. The SNR concept is illustrated in Figure 2.6. A fixed transmit power $\bar{P}_\mathrm{S}$ is equally spread over the transmission band. Furthermore, the left part of Figure 2.6 shows that different transmit blocks may overlap in time. Under the assumption of uncorrelated data symbols of equal power power, $P_x = \mathbb{E}\{|x_{l,k}|^2\}$, the SNR for OFDM and FBMC-OQAM can be expressed by

$$\mathrm{SNR} = \frac{P_x^{\mathrm{CP-OFDM}}}{P_\mathrm{n}} = \frac{P_x^{\mathrm{FBMC-OQAM}}}{\frac{1}{2}P_\mathrm{n}}. \tag{2.37}$$

For the same bandwidth FL, setting $P_x^{\mathrm{FBMC-OQAM}} = \frac{1}{2} P_x^{\mathrm{CP-OFDM}}$, see (2.37), implies that the average transmit power $P_{\mathrm{S}} = \frac{1}{KT} \int_{-\infty}^{\infty} \mathbb{E}\{|s(t)|^2\} \, \mathrm{d}t$ is the same for CP-OFDM and FBMC, allowing a fair comparison. FBMC only experiences half the noise power due to "taking the real part", which explains the factor of $\frac{1}{2}$ in (2.37). Furthermore, interpreting (2.37), one has to keep in mind that the channel has, on average, unit power and that the basis pulses are (real) orthonormal. In FBMC-QAM, the SNR definition changes because of a lower symbol density. To be specific, for the same bandwidth FL and the same average transmit power $\bar{P}_{\mathrm{S}}$, the SNR for FBMC-QAM ($TF = 2$) is 3 dB higher than for CP-OFDM and FBMC-OQAM. However, the data rate is also reduced by a factor of two.

2.3 IFFT Implementation

Practical systems must be much more efficient than the simple matrix multiplication in (2.27) and (2.30). It was shown in [74], for example, that FBMC-OQAM can be efficiently implemented by an Inverse Fast Fourier Transform (IFFT) together with a polyphase network. However, the authors of [74] do not provide an intuitive explanation of their implementation. I therefore investigate an alternative, intuitive, interpretation for such efficient FBMC-OQAM implementation. A similar interpretation was suggested, for example, in [56] for pulse-shaping multicarrier systems, or in [75] for FBMC-OQAM (without theoretical justification). However, most papers still refer to [74] when it comes to an efficient FBMC-OQAM implementation. It is thus worth to show that the modulation and demodulation step in FBMC is very simple and actually the same as in windowed OFDM.

To simplify the exposition and without losing generality, I consider only time-position $k = 0$. Any other time-position can easily be obtained by time-shifting this special case. The main idea is to factor out prototype filter $p(t)$ from (2.1),

$$s_0(t) = p(t) \sum_{l=1}^{L} \mathrm{e}^{\mathrm{j}2\pi \, lF \, t} \, \mathrm{e}^{\mathrm{j}\theta_{l,0}} \, x_{l,0}. \tag{2.38}$$

The exponential function in (2.38) is periodic in T_0 because of $F = \frac{1}{T0}$, so that the exponential summation has to be calculated only for the time interval $-T_0/2 \leq t < T_0/2$. Furthermore, with the sampling rate $f_{\mathrm{s}} = 1/\Delta t = FN_{\mathrm{FFT}}$, I deduce that the exponential summation corresponds to an N_{FFT} point inverse DFT. Thus, the sampled version of (2.38), $\mathbf{s}_0 \in \mathbb{C}^{ON_{\mathrm{FFT}} \times 1}$, can be

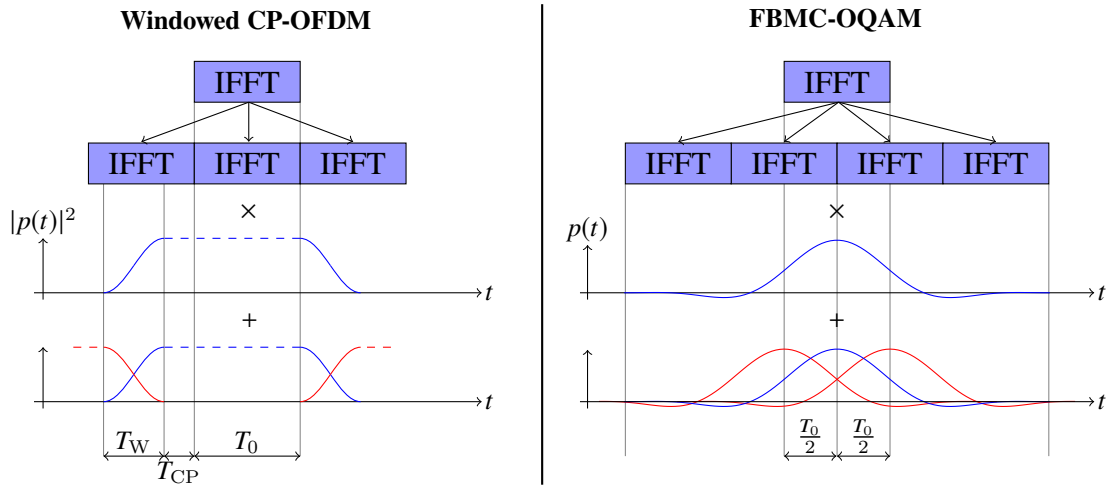

Figure 2.7. From a conceptional point of view, the signal generation in windowed OFDM and FBMC-OQAM requires the same basic operations, namely, an IFFT, copying the IFFT output, element wise multiplication with the prototype filter and, finally, overlapping. ©2017 IEEE, [1]

expressed by ($\mathrm{e}^{\mathrm{j}\theta_{l,0}} = \mathrm{j}^{l+0}$):

$$\mathbf{s}_0 = \mathbf{p} \circ \underbrace{\left(\mathbf{1}_{O\times 1} \otimes \underbrace{\mathbf{W}_{N_{\mathrm{FFT}}}^{\mathsf{H}} \underbrace{\begin{bmatrix} 0 \\ x_{1,0}\,\mathrm{j}^{1+0} \\ \vdots \\ x_{L,0}\,\mathrm{j}^{L+0} \\ 0 \\ \vdots \end{bmatrix}}_{\text{IFFT}}}_{\text{repeat } O\text{-times}} \right)}_{\text{element-wise multiplication}}, \tag{2.39}$$

where $\circ$ denotes the element-wise Hadamard product and $\otimes$ the Kronecker product. The sampled prototype filter $\mathbf{p} \in \mathbb{C}^{ON_{\mathrm{FFT}}\times 1}$ in (2.39) is given by:

$$[\mathbf{p}]_i = \sqrt{\Delta t}\; p(t)\Big|_{t=(i-1)\,\Delta t - \frac{O\,T_0}{2}} \quad \text{for} \quad i = 1, 2, \ldots, O\,N_{\mathrm{FFT}}. \tag{2.40}$$

Figure 2.7 illustrates such low-complexity implementation and compares FBMC-OQAM to windowed OFDM. Both modulation schemes apply the same basic steps, that is, IFFT, repeating and element-wise multiplications. However, windowed OFDM has overall a lower

complexity because the element-wise multiplication is limited to a window of size $2T_{\mathrm{W}}$ and time symbols are further apart, that is, $T = T_{\mathrm{W}} + T_{\mathrm{CP}} + T_0$ in windowed OFDM versus $T = T_0/2$ in FBMC-OQAM. Thus, FBMC needs to apply the IFFT more than two times (exactly two times if $T_{\mathrm{W}} = T_{\mathrm{CP}} = 0$). Of course, the overhead $T_{\mathrm{W}} + T_{\mathrm{CP}}$ in windowed OFDM reduces the spectral efficiency. Because the signal generation for both modulation schemes is very similar, FBMC-OQAM can utilize the same hardware components as windowed OFDM.

The receiver works in a similar way, but in reversed order, that is, element-wise multiplication, reshaping the received symbol vector to $N_{\mathrm{FFT}} \times O$, followed by a row-wise summation and, finally, an FFT. Note that the same operations are also required in WOLA. In contrast to FBMC, however, the transmit and receive prototype filters are different in WOLA.

2.4 Possible Use Cases

I will now investigate possible use cases for FBMC and discuss why it outperforms OFDM based schemes in many cases. Let me define the time-frequency efficiency as

$$\rho = \frac{KL}{(KT + T_{\mathrm{G}})(FL + F_{\mathrm{G}})}, \tag{2.41}$$

where T_{G} represents the required guard time and F_{G} the required guard band. The time-frequency efficiency helps to answer the question which modulation format utilizes available time-frequency resources best. Note that in the limit case of $K \to \infty$ and $L \to \infty$, the time-frequency efficiency depends only on the symbol density, that is, $\rho = \frac{1}{TF}$.

Figure 2.8 compares the time-frequency efficiency of FBMC-OQAM with that of f-OFDM. Guard time T_{G} is chosen so that 99.99% (= 40 dB) of the transmitted energy, see (2.32), is within the time interval $KT + T_{\mathrm{G}}$. Similarly, 99.99% of the transmitted energy (utilizing the PSD in (2.33)) is within the bandwidth $FL + F_{\mathrm{G}}$. Depending on the specific use case, one might want to apply different thresholds. However, the basic statements will stay the same. If only a few time symbols are used, for example $K = 1$ for f-OFDM and $K = 2$ for FBMC, f-OFDM shows a better performance than FBMC because of a larger guard time required in FBMC (only if no overlapping between blocks is possible). Approximately $K = 5$ complex-valued time symbols ($K = 10$ real-valued symbols) are required to make the time-frequency efficiency of FBMC better than that of f-OFDM, although this depends strongly on the number of subcarriers. Once the number of time symbols approaches infinity, which is approximately true in many cases because blocks (subframes) can easily overlap, only OOB emissions are relevant and FBMC strongly outperforms f-OFDM. Already $K = 15$

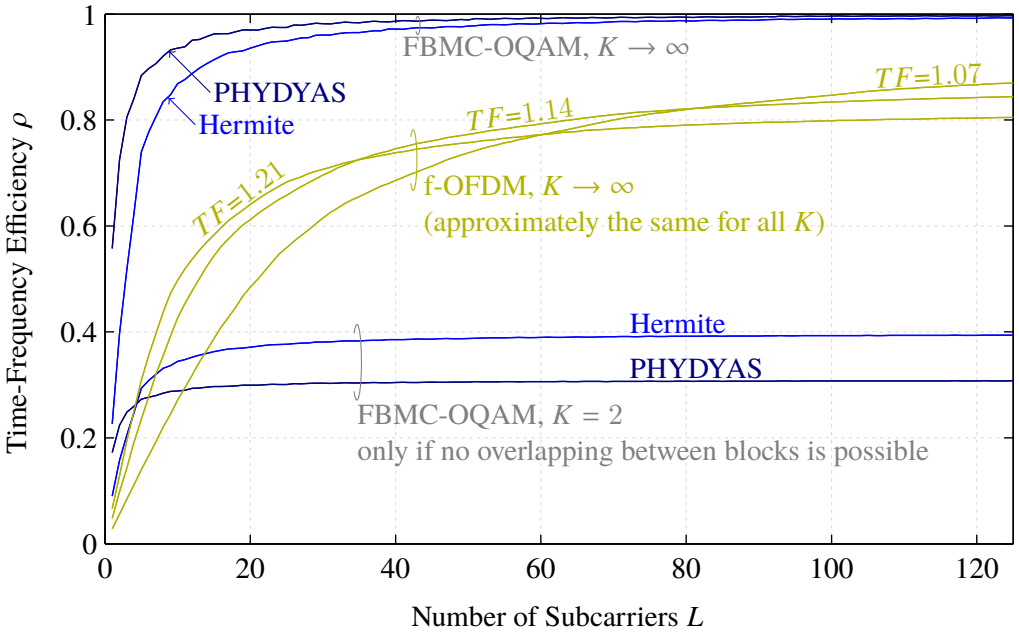

Figure 2.8. The time-frequency efficiency, see (2.41), depends on the number of subcarriers and the number of time symbols. If overlapping between transmit blocks is possible or if the number of time symbols is high, FBMC-OQAM strongly outperforms f-OFDM in terms of time-frequency efficiency. ©2017 IEEE, [1].

complex-valued time symbols are sufficient to come close to the limit of $K \to \infty$ for the Hermite pulse (95% threshold); for the PHYDYAS filter it is $K = 30$.

I will now take a closer look at how FBMC can efficiently support different use cases within the same band, as illustrated in Figure 1.1. For that, I assume two users. User 1 employs a subcarrier spacing of $F_1 = 15\,\text{kHz}$ and user 2 employs $F_2 = 120\,\text{kHz}$. Such different subcarrier spacings will be included in 5G [7] and allow, for example, to deal with different channel conditions, see Section 3.1.2. Another reason for different subcarrier spacings are different performance requirements. For example, a high subcarrier spacing allows low latency transmissions whereas a low subcarrier spacing increases the bandwidth efficiency and makes the system more robust to delays.

My metric of interest here is the SIR. To keep the analysis simple, I ignore the channel (although it could be included similar as later in Section 3.1.2). The transmitted signal of the first user is characterized by $\mathbf{G}_1$, see (2.27), and employs $L_1 = 96$ subcarriers with a subcarrier spacing of $F_1 = 15\,\text{kHz}$, leading to a transmission bandwidth of $F_1 L_1 = 1.44\,\text{MHz}$. Similarly, the second user is characterized by $\mathbf{G}_2$, employs $L_2 = 12$ subcarriers with a subcarrier spacing of $F_2 = 120\,\text{kHz}$, leading to the same bandwidth as before, that is, $L_2 F_2 = 1.44\,\text{MHz}$. Additionally, $\mathbf{G}_2$ is shifted in frequency by $F_1 L_1 + F_\text{G}$. Figure 2.9 shows the PSD, see (2.33),

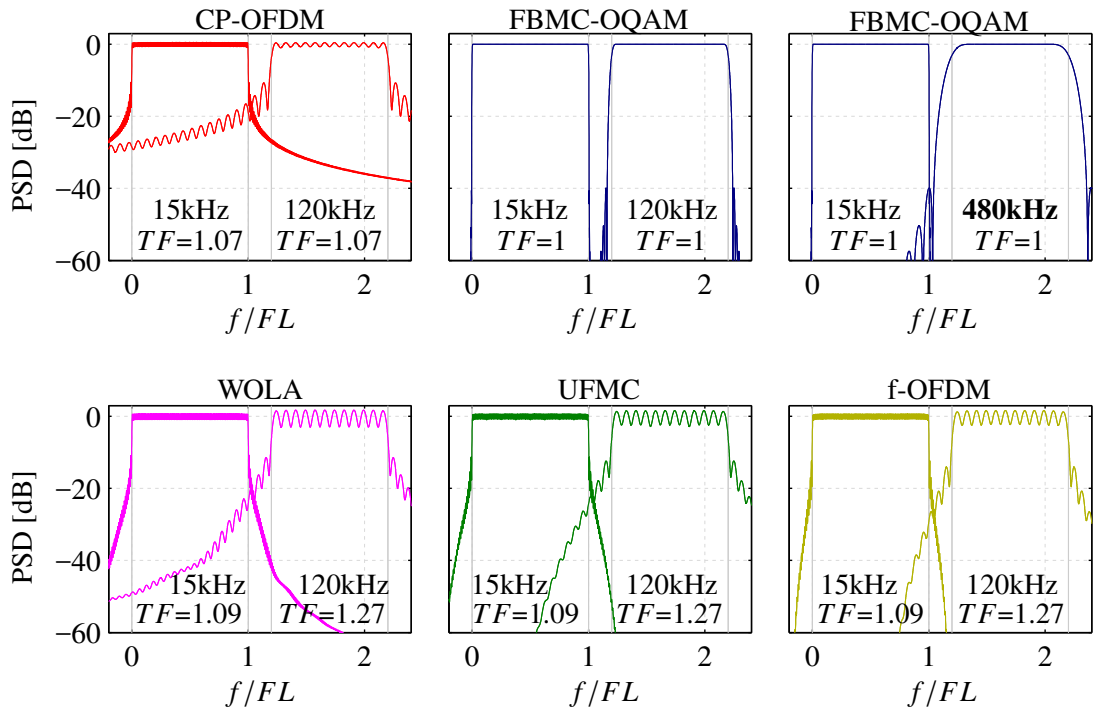

Figure 2.9. The PSD in case that two users with different subcarrier spacings ($F_1 = 15\,\text{kHz}$, $F_2 = 120\,\text{kHz}$) share the same band. The transmission bandwidth is the same for both users $F_1 L_1 = F_2 L_2 = 1.44\,\text{MHz}$. In case of FBMC, a subcarrier spacing of $F_2 = 480\,\text{kHz}$ is also considered, leading to approximately the same latency as for OFDM with $F_2 = 120\,\text{kHz}$. In this example, the guard band is set to $F_\text{G} = 0.2\,F_1 L_1$. ©2017 IEEE, [1].

for both users and a guard band of $F_\text{G} = 0.2\,F_1 L_1$. For WOLA, UFMC and f-OFDM, I assume a time-frequency spacing of $T_1 F_1 = 1.09$ for the first user, same as in Figure 1.2. For the second user, on the other hand, I assume a time-frequency spacing of $T_2 F_2 = 1.27$ to reduce the OOB emissions further. My proposed matrix notation again simplifies the analytical calculation of the total SIR, defined for FBMC-OQAM as:

$$\text{SIR}_{\text{total,2-use-case}} = \frac{L_1 K_1 + L_2 K_2}{||\Re\{\mathbf{Q}_1^\text{H}\mathbf{G}_2\}||_\text{F}^2 + ||\Re\{\mathbf{Q}_2^\text{H}\mathbf{G}_1\}||_\text{F}^2}, \tag{2.42}$$

where $||\cdot||_\text{F}$ represents the Frobenius norm. To keep the notation in (2.42) simple, I ignore self interference (≈65 dB for the PHYDYAS prototype filter, $O = 4$), that is, the off-diagonal elements of $\mathbf{Q}_1^\text{H}\mathbf{G}_1$ and $\mathbf{Q}_2^\text{H}\mathbf{G}_2$ are ignored. In CP-OFDM, WOLA, UFMC and f-OFDM, the $\Re\{\}$ in (2.42) disappears because they operate in the complex domain. In (2.42), I consider the sum interference power but one should keep in mind that subcarriers close to the other user experience a higher interference than subcarriers farther away. Furthermore, to keep the notation simple, (2.42) does not account for different receive power levels caused by different

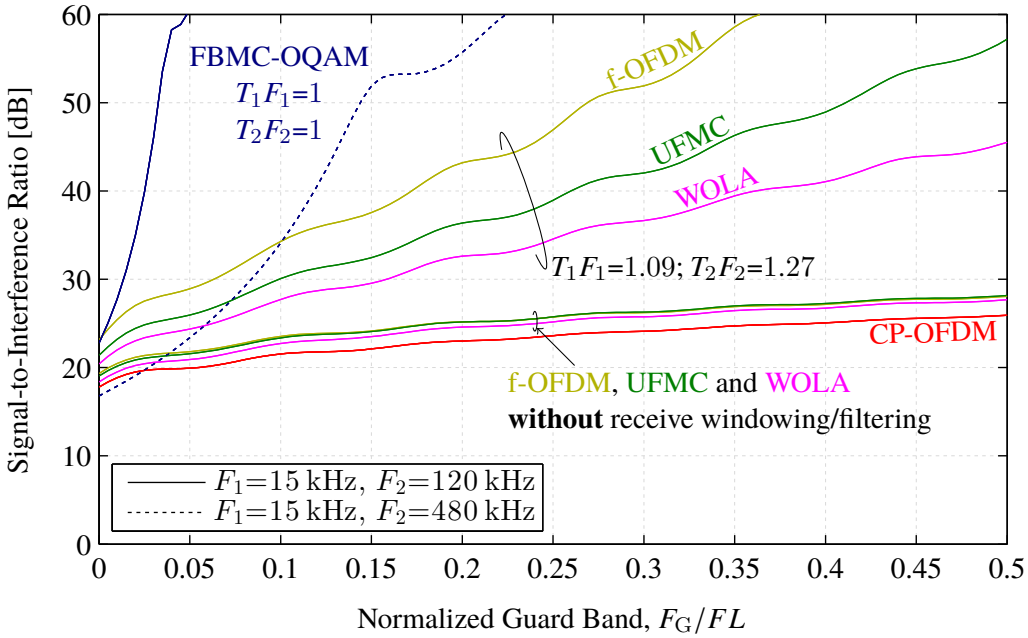

Figure 2.10. FBMC has a higher SIR than OFDM, so that the required guard band is much smaller. Compared with the channel induced inference, which will be discussed in Section 3.1.2, one often requires a much higher SIR because of different receive power levels (not included in (2.42) to keep the notation simple). Windowed and filtered OFDM only perform well if windowing and filtering is also applied at the receiver. ©2017 IEEE, [1].

transmit power levels and different path losses. Thus, compared to the channel induced interference, a higher SIR is often required to account for those factors. Figure 2.10 shows how the SIR, see (2.42), depends on the normalized guard band, where I assume $K \gg 1$, so that $T + \frac{T_G}{K} \approx T$. The higher the guard band, the less interference is observed. As illustrated in Figure 2.10, receive windowing and filtering are of utmost importance. Without it, there is not much difference between WOLA, UFMC, f-OFDM and conventional CP-OFDM. The importance of receive windowing and filtering was also observed in [76]. Additionally, one should keep in mind that, without receive windowing and filtering, the interference from user 1 to user 2 is higher than the interference from user 2 to user 1, which can also be deduced from Figure 2.9. Once windowing and filtering is applied at the receiver, both users experience approximately the same interference power. As shown in Figure 2.10, WOLA, UFMC and f-OFDM can improve the SIR but the performance is still not as good as in FBMC. Assuming an SIR of 45 dB is required, f-OFDM needs a guard band of $F_G = 0.24\,FL$. Thus, the time-frequency efficiency for user 2 becomes $\rho = \frac{1}{1.24 \times 1.27} = 0.64$. In contrast to that, FBMC has a much higher efficiency of $\rho = 0.97$. Therefore, the data rate in FBMC is approximately 50 % higher than in f-OFDM. One reason for the high subcarrier spacing

of user 2 ($F_2 = 120\,\mathrm{kHz}$) is to enable low latency transmissions. For a fair comparison in terms of latency, the subcarrier spacing in FBMC has to be further increased by a factor of four ($O = 4$), leading to $F = 480\,\mathrm{kHz}$ and thus approximately the same latency as in OFDM. The number of subcarriers in FBMC then decreases from $L = 12$ to only $L = 3$. As shown in Figure 2.10, a higher subcarrier spacing ($F = 480\,\mathrm{kHz}$) requires a larger guard band ($F_\mathrm{G} = 0.13\,FL$ for a 45 dB SIR threshold), but the time-frequency efficiency ($\rho = 0.88$) is still approximately 40% higher than in f-OFDM. Thus, the statement that FBMC is not suited for low-latency transmissions is not true in general. One only has to increase the subcarrier spacing. Of course, this further increases the sensitivity to time-offsets and delay spreads (but decreases the sensitivity to frequency-offsets and Doppler spreads). Note that the superior spectral properties of FBMC also simplify frequency synchronization [77].

For a higher bandwidth per user, say 10.08 MHz instead of 1.44 MHz, the possible improvement of FBMC compared to f-OFDM reduces to only 15% (45 dB SIR threshold). Thus, if the number of subcarriers is high, OFDM has a relatively high spectral efficiency. This will usually be the case in eMBB. However, other use cases, such as eMTC, might not always employ a high number of subcarriers (per user/machine). FBMC then becomes much more efficient, as discussed in this section. If only one subcarrier is active, FBMC can even act as a single carrier scheme with the advantage of a reduced PAPR. The time-frequency efficiency then decreases but is still much higher than in OFDM. If the bandwidth is sufficiently small, simple one-tap equalizers can still be employed and the SNR will be high. Of course, a small bandwidth implies low data rates but many use cases do not require high data rates.

Another important use case is URLLC. I have already shown that FBMC has a higher spectral efficiency than OFDM in low latency scenarios. For that, the subcarrier spacing needs to be increased. For example, I was able to transmit a 2×1 Alamouti FBMC and OFDM signal (one subframe) within less than 40 μs [27], thus satisfying the low latency condition [78] (the evaluation was performed off-line to keep hardware costs reasonable low). High reliability can also be achieved in FBMC by switching from an FBMC-OQAM transmission to an FBMC-QAM transmission. Thus, deliberately sacrificing spectral efficiency but improving robustness in doubly-selective channels and with respect to time-frequency offsets, see Section 3.1.2. Of course, one has to include additional steps, such as diversity (frequency, space), to guarantee high reliability.

Chapter 3

Equalization

As already mentioned in Section 2.2, time-variant multipath propagation causes distortions of the transmitted signal, so that equalization becomes necessary. Important questions are then what kind of equalization is needed and how computational demanding it is. To answer those questions, I start with a simple, yet effective, one-tap equalizer. I provide closed-form solutions for the BEP and calculate the SIR. The performance depends strongly on the subcarrier spacing. By considering an optimal subcarrier spacing, I eliminate this dependency. Numerical evaluations reveal that in most practical cases, one-tap equalizers are sufficient. Nonetheless, in a few rare cases, advanced equalization methods might be necessary. I thus propose a novel MMSE equalizer as well as a simple interference cancellation scheme. This chapter is mainly based on my publications [1, 32, 37] and includes the following novel contributions:

- In Section 3.1.1, I derive a closed-form BEP expression for arbitrary linear modulation methods based on one-tap equalizers, with OFDM and FBMC being special cases, covered by my general expression [32].
- In Section 3.1.2, I propose a novel method to calculate the SIR for doubly-selective channels and show that in many cases, one-tap equalizers are sufficient, especially if an optimal subcarrier spacing is considered [1].
- In Section 3.2, I propose a novel n-tap MMSE equalizer which not only takes neighboring time symbols into account, as usually done in literature, but also includes neighboring subcarriers into the equalization process. Furthermore, I propose a full block MMSE equalizer and a simple interference cancellation scheme [37].

Throughout this chapter, I assume perfect channel knowledge. The challenge of channel estimation for FBMC systems is discussed in Chapter 4.

3.1 Are One-Tap Equalizer Sufficient?

Equalization has always been one of the key challenges in wireless communications [79–84]. In multicarrier transmissions, however, equalization becomes in many cases a lot easier because (2.31) can be decomposed according to:

$$y_{l,k} = h_{l,k} x_{l,k} + n_{l,k}. \tag{3.1}$$

Here, I ignore the imaginary interference of FBMC, that is, $\mathbf{Q}^{\mathsf{H}}\mathbf{G} = \mathbf{I}_{LK}$. This is feasible because the imaginary interference is orthogonal to the useful signal, so that it has no influence on the performance. I further assume that the channel induced interference is dominated by the noise, so that (3.1) accurately describes the transmission system, and that the noise is Gaussian distributed, that is, $n_{l,k} \sim \mathcal{CN}(0, P_{\mathrm{n}})$. The Maximum Likelihood (ML) symbol detection for (3.1) can then be found by:

$$\hat{x}_{l,k} = \arg\max_{x_{l,k}\in\mathcal{X}} \left\{\mathrm{pdf}(y_{l,k}|x_{l,k})\right\} \tag{3.2}$$

$$= \arg\max_{x_{l,k}\in\mathcal{X}} \left\{\frac{1}{\pi P_{\mathrm{n}}} \exp\left(-\frac{|y_{l,k} - h_{l,k}x_{l,k}|^2}{P_{\mathrm{n}}}\right)\right\} \tag{3.3}$$

$$= \arg\min_{x_{l,k}\in\mathcal{X}} \left\{\left|\frac{y_{l,k}}{h_{l,k}} - x_{l,k}\right|\right\}. \tag{3.4}$$

In particular, (3.4) is nothing else than a simple one-tap Zero-Forcing (ZF) equalizer followed by nearest neighbor detection and can thus be expressed by

$$\hat{x}_{l,k} = Q\left\{\frac{y_{l,k}}{h_{l,k}}\right\}, \tag{3.5}$$

where $Q\{\cdot\}$ represents nearest neighbor detection. That a simple one-tap equalizer corresponds to the ML symbol detection is one of the biggest advantages of multicarrier systems. Of course, once the channel induced interference becomes relevant, one-tap equalization no longer corresponds to the ML symbol detection. The effect of doubly-selective channels on one-tap equalizers is discussed in this section.

3.1.1 Bit Error Probability

I start my analysis by calculating the BEP, an important metric in wireless communications. While many authors have already investigated the BEP in OFDM from an analytical point of view, such as [85] for a time-invariant channel and [86] for a doubly-selective channel,

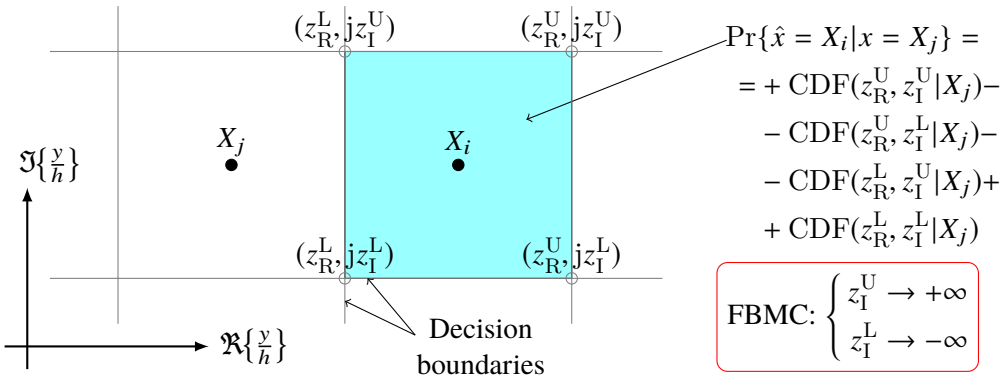

Figure 3.1. For a given symbol alphabet $\mathcal{X}$, Lemma 1 and (3.10)-(3.13) are applied to calculate the probability that $\hat{x}_{l,k} = X_i$ is detected, conditioned that $x_{l,k} = X_j$ was sent, allowing to calculate the BEP in (3.14). ©2017 IEEE, [32].

FBMC is still missing in literature. I therefore propose a general method to calculate the BEP in doubly-selective channels for arbitrary linear modulation techniques based on one-tap equalization, such as OFDM and FBMC. I assume Rayleigh fading, perfect channel knowledge at the receiver and that the data symbols are statistically independent. Furthermore, I limit myself to m-QAM and $\sqrt{m}$-PAM signal constellations because they lead to vertical and horizontal decision boundaries, see Figure 3.1, allowing me to use the following lemma to calculate the BEP:

Lemma 1 *Let y and h be zero mean, correlated, complex-valued, Gaussian random variables, then the Cumulative Distribution Function (CDF) of the complex Gaussian ratio $\frac{y}{h}$ reads*

$$\begin{aligned} CDF_{y/h}(z_R, z_I) &= \Pr\left\{\left(\Re\left\{\frac{y}{h}\right\} < z_R\right) \wedge \left(\Im\left\{\frac{y}{h}\right\} < z_I\right)\right\} = \\ &= \frac{1}{4} + \frac{(z_R - \Re\{\alpha\})\left(2\tan^{-1}\left(\frac{z_I - \Im\{\alpha\}}{\sqrt{(z_R - \Re\{\alpha\})^2 + \beta - |\alpha|^2}}\right) + \pi\right)}{4\pi\sqrt{(z_R - \Re\{\alpha\})^2 + \beta - |\alpha|^2}} + \\ &\quad + \frac{(z_I - \Im\{\alpha\})\left(2\tan^{-1}\left(\frac{z_R - \Re\{\alpha\}}{\sqrt{(z_I - \Im\{\alpha\})^2 + \beta - |\alpha|^2}}\right) + \pi\right)}{4\pi\sqrt{(z_I - \Im\{\alpha\})^2 + \beta - |\alpha|^2}}, \end{aligned} \tag{3.6}$$

with

$$\alpha = \frac{\mathbb{E}\{yh^*\}}{\mathbb{E}\{|h|^2\}} \quad \textit{and} \quad \beta = \frac{\mathbb{E}\{|y|^2\}}{\mathbb{E}\{|h|^2\}}. \tag{3.7}$$

Lemma 1 is obtained by reformulating and combining Equations (10)-(15) of [87]. In many cases, only the projection onto the real axis is needed, $z_{\mathrm{I}} \to \infty$, simplifying (3.6) according to [41],

$$\Pr\left(\Re\left\{\frac{y}{h}\right\} < z_{\mathrm{R}}\right) = \frac{1}{2} - \frac{\Re\{\alpha\} - z_{\mathrm{R}}}{2\sqrt{(\Re\{\alpha\} - z_{\mathrm{R}})^2 + \beta - |\alpha|^2}}. \tag{3.8}$$

By reformulating (2.30), I am able to express the received symbol at subcarrier position l and time position k by

$$y_{l,k} = \mathbf{q}_{l,k}^{\mathsf{H}}\,\mathbf{H}\,\mathbf{G}\,\mathbf{x} + n_{l,k} = \left((\mathbf{G}\,\mathbf{x})^{\mathsf{T}} \otimes \mathbf{q}_{l,k}^{\mathsf{H}}\right)\mathrm{vec}\{\mathbf{H}\} + n_{l,k}, \tag{3.9}$$

where I utilize the Kronecker product in (3.9) to simplify statistical investigations, see (3.10)-(3.12). To apply Lemma 1 in my transmission system, the received symbols $y_{l,k}$ have to be Gaussian distributed, which is only true conditioned on the transmitted data symbols $\mathbf{x}$. By employing (3.9), I straightforwardly calculate the required expectations in (3.7), conditioned on $\mathbf{x}$, according to

$$\mathbb{E}\left\{|y_{l,k}|^2\middle|\mathbf{x}\right\} = \mathbf{x}^{\mathsf{T}}\left(\mathbf{G}^{\mathsf{T}} \otimes \mathbf{q}_{l,k}^{\mathsf{H}}\right)\mathbf{R}_{\mathrm{vec}\{\mathbf{H}\}}\left(\mathbf{G}^{\mathsf{T}} \otimes \mathbf{q}_{l,k}^{\mathsf{H}}\right)^{\mathsf{H}}\mathbf{x}^{*} + P_{\mathrm{n}}, \tag{3.10}$$

$$\mathbb{E}\left\{|h_{l,k}|^2\right\} = \left(\mathbf{g}_{l,k}^{\mathsf{T}} \otimes \mathbf{q}_{l,k}^{\mathsf{H}}\right)\mathbf{R}_{\mathrm{vec}\{\mathbf{H}\}}\left(\mathbf{g}_{l,k}^{\mathsf{T}} \otimes \mathbf{q}_{l,k}^{\mathsf{H}}\right)^{\mathsf{H}}, \tag{3.11}$$

$$\mathbb{E}\left\{y_{l,k}h_{l,k}^{*}\middle|\mathbf{x}\right\} = \mathbf{x}^{\mathsf{T}}\left(\mathbf{G}^{\mathsf{T}} \otimes \mathbf{q}_{l,k}^{\mathsf{H}}\right)\mathbf{R}_{\mathrm{vec}\{\mathbf{H}\}}\left(\mathbf{g}_{l,k}^{\mathsf{T}} \otimes \mathbf{q}_{l,k}^{\mathsf{H}}\right)^{\mathsf{H}}, \tag{3.12}$$

where $\mathbf{R}_{\mathrm{vec}\{\mathbf{H}\}} = \mathbb{E}\{\mathrm{vec}\{\mathbf{H}\}\mathrm{vec}\{\mathbf{H}\}^{\mathsf{H}}\}$ represents the correlation matrix of the vectorized time-variant convolution matrix and depends on the underlying power delay profile and the Doppler spectral density. I normalize the channel so that it has unit power, that is, the taps of the power delay profile sum up to one. Combining Lemma 1 and (3.10)-(3.12) allows me to express the CDF, conditioned on $\mathbf{x}$, of my transmission system in (3.5), $\mathrm{CDF}_{y_{l,k}/h_{l,k}}(z_{\mathrm{R}}, z_{\mathrm{I}}|\mathbf{x})$. To calculate the overall BEP, however, I need the CDF conditioned solely on $x_{l,k}$. With a permutation matrix $\mathbf{P}$, I split the transmitted symbols $\mathbf{x}$ into interfering symbols $\mathbf{x}_{\mathrm{I}_{l,k}} \in \mathcal{X}^{(LK-1)\times 1}$ and the symbol of interest, $x_{l,k}$, according to $\mathbf{x} = \mathbf{P}\,[\mathbf{x}_{\mathrm{I}_{l,k}}^{\mathsf{T}}, x_{l,k}]^{\mathsf{T}}$. The required CDF can then be calculated with the law of total probability according to

$$\mathrm{CDF}_{y_{l,k}/h_{l,k}}(z_{\mathrm{R}}, z_{\mathrm{I}}|x_{l,k}) = \frac{1}{M}\sum_{\mathbf{x}_{\mathrm{I}_{l,k}} \in \mathcal{X}^{LK-1}} \mathrm{CDF}_{y_{l,k}/h_{l,k}}(z_{\mathrm{R}}, z_{\mathrm{I}}|\mathbf{x}_{\mathrm{I}_{l,k}}, x_{l,k}), \tag{3.13}$$

with $M = |\mathcal{X}^{LK-1}|$ denoting the cardinality of $\mathcal{X}^{LK-1}$. Note that (3.13) is required to model the interference influence correctly. Many papers, such as [88], assume that the interference

is Gaussian distributed, arguing that the central limit theorem can be applied. This is wrong because only a few symbols have a significant contribution to the interference, as also shown in [86]. For a small symbol alphabet, (3.13) can be calculated analytically, because only a few interferers have a significant contribution which makes the number of summations reasonable small. For higher modulation orders, on the other hand, this is no longer possible because too many summations are required. Then, numerical approximations, such as Monte Carlo evaluation, become necessary. Nonetheless, compared to pure simulations one has the advantages of analytical insights and a highly reduced evaluation time.

Finally, with Lemma 1 and (3.10)-(3.13), all the necessary tools are available to calculate the BEP of transmitted symbol $x_{l,k}$, given by:

$$\mathrm{BEP}_{l,k} = \frac{1}{\log_2|\mathcal{X}|} \sum_{p=1}^{\log_2|\mathcal{X}|} \frac{1}{|\mathcal{X}|} \sum_{j=1}^{|\mathcal{X}|} \sum_{X_i \in \mathcal{E}_j^p} \Pr\left\{\hat{x}_{l,k} = X_i | x_{l,k} = X_j\right\}. \tag{3.14}$$

Set $\mathcal{X} = \{X_1, \cdots, X_{|\mathcal{X}|}\}$ describes the symbol alphabet where each symbol is mapped to a unique bit sequence of size $\log_2|\mathcal{X}|$. Set $\mathcal{E}_j^p$, on the other hand, represents all those elements of $\mathcal{X}$ for which the bit-value at bit-position $p \in \mathbb{N}$ is different from the corresponding bit-value of X_j. Note that the cardinality of $\mathcal{E}_j^p$ is $\frac{|\mathcal{X}|}{2}$. As illustrated in Figure 3.1, the probability expression $\Pr\{\cdot\}$ in (3.14) can be straightforwardly calculated by the CDF, see (3.13).

Usually, the BEP expression in (3.14) consists of many terms, mainly because of the inference term described in (3.13). For the important special case of doubly-flat Rayleigh fading, that is, $\mathbf{H} = \bar{h}\,\mathbf{I}_N$ with $\bar{h} \sim \mathcal{CN}(0,1)$, however, I find compact expressions. For OFDM, the required expectations in (3.10)-(3.12) simplify to $\mathbb{E}\{|y_{l,k}|^2\,|\mathbf{x}\} = |x_{l,k}|^2 + P_n$, $\mathbb{E}\{|h_{l,k}|^2\} = 1$ and $\mathbb{E}\{y_{l,k}h_{l,k}^*\,|\mathbf{x}\} = x_{l,k}$. Note that those expressions no longer depend on the surrounding data symbols $\mathbf{x}_{\mathrm{I}_{l,k}}$, simplifying (3.13). For Gray-coded 4-QAM, symmetries allow me to rewrite (3.14) by $\mathrm{BEP}_{l,k} = \mathrm{CDF}_{y_{l,k}/h_{l,k}}\left(0, \infty\,\middle|\,\sqrt{P_x}\,\frac{1+\mathrm{j}}{\sqrt{2}}\right)$ which, together with Lemma 1 leads to

$$\mathrm{BEP}_{\text{4-(O)QAM}}^{\mathrm{OFDM,FBMC}} = \frac{1}{2} - \frac{1}{2\sqrt{1 + 2\frac{1}{\mathrm{SNR}}}}, \tag{3.15}$$

identical for each transmit symbol. FBMC experiences imaginary interference. However, this does not influence the BEP for a doubly-flat channel, so that (3.15) also describes the BEP for a 2-PAM (4-OQAM) FBMC system. Similar as before, I find the BEP for 16-QAM respectively 4-PAM (16-OQAM) by:

$$\mathrm{BEP}_{\text{16-(O)QAM}}^{\mathrm{OFDM,FBMC}} = \frac{1}{2} - \frac{3}{8\sqrt{1 + 10\frac{1}{\mathrm{SNR}}}} - \frac{6}{8\sqrt{9 + 10\frac{1}{\mathrm{SNR}}}} + \frac{5}{8\sqrt{25 + 10\frac{1}{\mathrm{SNR}}}}. \tag{3.16}$$

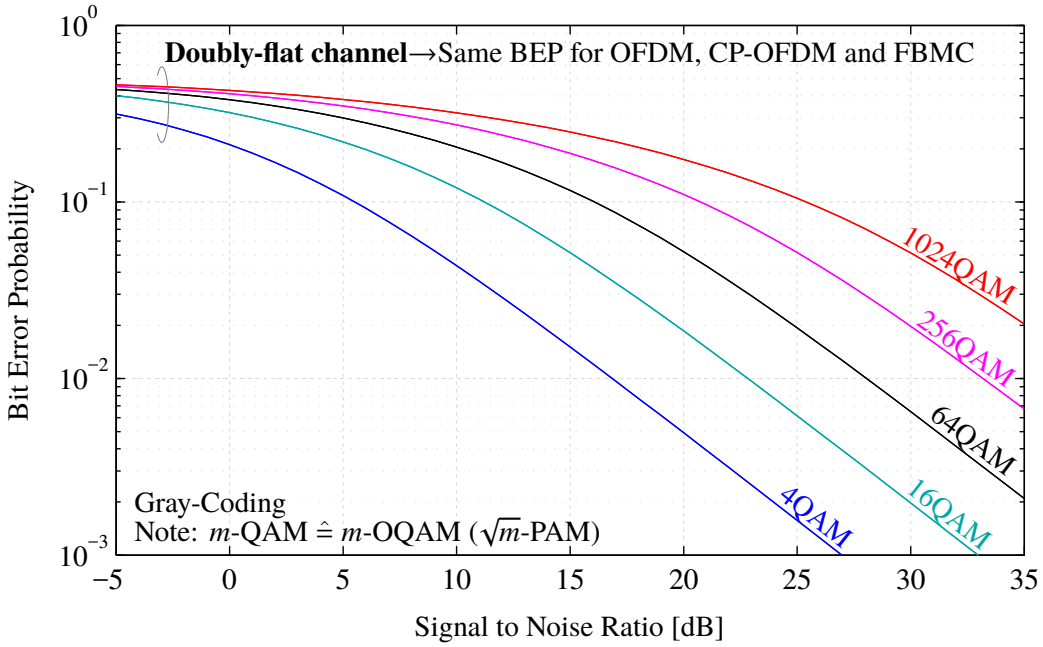

Figure 3.2. Doubly-flat fading represents an important special case because it also describes the BEP for doubly-selective channels, as long as the SNR is smaller than a certain threshold, see Figure 3.3. ©2017 IEEE, [32].

For higher modulation orders, similar expressions can be derived but they involve many terms so that I omit them at this point. Note that the SNR in (3.15) and (3.16) was already defined in Section 2.2, see (2.37). In particular, for the same bandwidth FL, the same SNR for OFDM and FBMC implies that the average transmit power $P_{\mathrm{S}} = \frac{1}{KT}\int_{-\infty}^{\infty}\mathbb{E}\{|s(t)|^2\}\,\mathrm{d}t$ is also the same for both modulation schemes, allowing a fair comparison.

Figure 3.2 plots the BEP over the SNR for the special case of a doubly-flat channel. The performance is independent of a specific modulation scheme but one should keep in mind that FBMC has lower out-of-band emissions than OFDM. Furthermore, for the same bandwidth FL, FBMC and OFDM without CP have the same bit rate while the bit rate for CP-OFDM is lower by a factor of $(1 + T_{\mathrm{CP}}F)$. Nonetheless, all modulation schemes use the same transmit power P_{S}, allowing a fair comparison. The special case of a doubly-flat channel can also be used to approximate the BEP in doubly-selective channels. One simply has to replace the SNR by the Signal-to-Interference plus Noise Ratio (SINR) in the BEP expressions of a doubly-flat channel. This corresponds to the assumption of Gaussian distributed interference and delivers a rough approximation of the true BEP. In Section 3.1.2, I will explain in detail how to calculate the interference power.

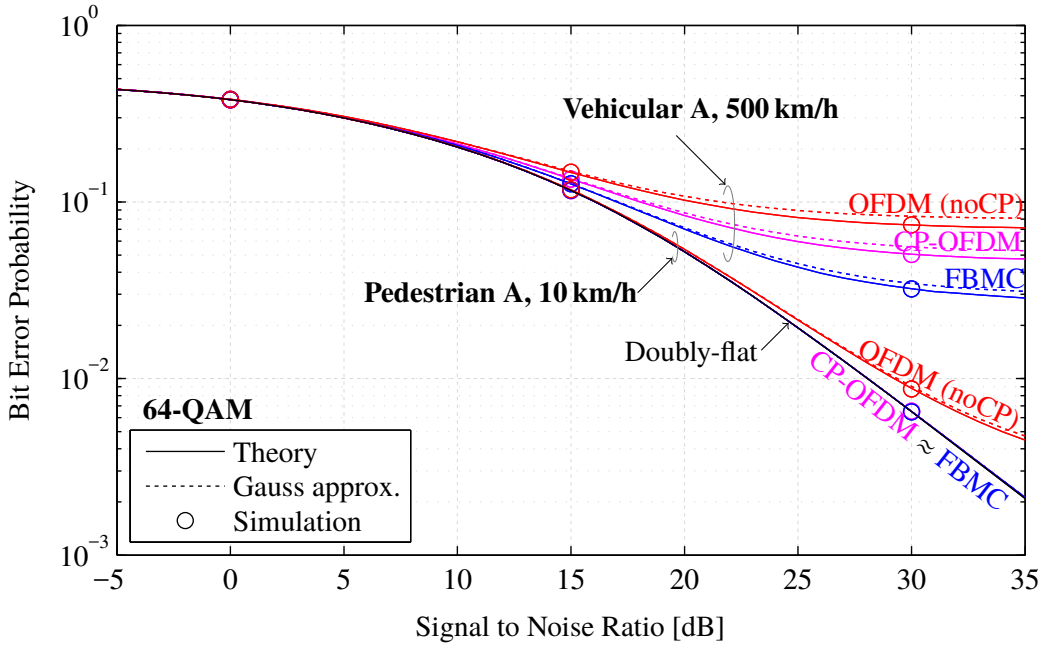

Figure 3.3. Simulations validate the BEP calculations. The interference is not Gaussian distributed, so that the Gaussian approximation only provides a rough estimate of the true BEP. Once the SNR is higher than the SIR, interference starts to dominate the noise, leading to a saturation effect. For a Vehicular A channel model at 500 km/h, OFDM without CP has an SIR of 17.5 dB, CP-OFDM 20 dB and FBMC 23 dB. ©2017 IEEE, [32].

Let me now numerically investigate the influence of time-variant multipath propagation onto the BEP for OFDM without CP, CP-OFDM and FBMC (Hermite prototype filter). For that, I consider a subcarrier spacing of $F = 15\,\mathrm{kHz}$, same as in LTE, a Jakes Doppler spectrum and two different channel models: Firstly, the Pedestrian A channel model which has a Root Mean Square (RMS) delay spread of 46 ns. Such small delay spread describes the reality of current (and future) mobile communication systems more accurately than channel models with a much higher delay spread because of various reasons [15]. Secondly, the Vehicular A channel model which has a relatively high RMS delay spread of 370 ns. Although I consider only these two channel models, it is worth mentioning that the downloadable MATLAB code allows for an arbitrary tapped delay line channel model, so that a large range of possible scenarios can be investigated. The sampling rate is chosen as small as possible, but high enough so that it fits approximately the predefined delay taps of the channel model. For a Pedestrian A channel model this leads to a sampling rate of 10.08 MHz and for a Vehicular A model to 2.94 MHz. The BEP is evaluated at the middle position and the number of subcarriers and the number of multicarrier symbols are chosen so that they include all significant interferers.

Figure 3.3 shows the BEP over the SNR. For a Pedestrian A channel model at low velocities, one-tap equalizers deliver an optimal performance for CP-OFDM and FBMC, but not necessarily for OFDM without CP. As long as the interference is dominated by noise, the BEP of a doubly-flat channel accurately describes the transmission system. For example, a Vehicular A channel model at 500 km/h leads to an SIR of 20 dB for CP-OFDM. As shown in Figure 3.3, the BEP severely starts to saturate at an SNR of 20 dB because interference becomes the dominant factor. As long as the SNR is approximately 10 dB lower than the SIR, noise completely dominates the interference which can thus be neglected. Even if the SNR approaches the SIR, only a small performance degeneration, equivalent to an SNR shift of approximately 3 dB, can be observed. The interference in case of a Vehicular A channel at 500 km/h is mainly dominated by the Doppler spread, so that FBMC (with a Hermite prototype filter) performs better than OFDM, although both modulation schemes suffer from interference. However, such high velocity scenarios will rarely happen and even if they do, an SIR of 20 dB is still high enough to obtain relatively high data rates. For a time-invariant channel, the BEP of CP-OFDM becomes the same as for doubly-flat fading. FBMC, on the other hand, is effected by a relatively high delay spread in a Vehicular A channel, so that it deviates from doubly-flat fading at very high SNR values (not shown in the Figure 3.3). However, for practical relevant SNR ranges smaller than 20 dB, this is no issue.

Figure 3.4 shows how the BEP depends on the velocity in case of zero noise and a Vehicular A channel model. For low velocities, CP-OFDM shows the lowest BEP because interference, caused by frequency-selectivity, can be completely eliminated at the expense of a lower bit rate. For velocities higher than 100 km/h, however, FBMC outperforms CP-OFDM because of a better robustness in time-variant channels.

3.1.2 Signal-to-Interference Ratio

As shown in Section 3.1.1, the SIR can be utilized to determine the point at which interference starts to dominate noise. Compared to the closed-form BEP expression, the SIR is much easier to handle, so that I will focus on the SIR in this section. So far, I have argued that in most cases, the channel induced interference can be neglected in FBMC systems. This is indeed true for all my testbed measurements conducted so far. In this section, I will formally derive an analytical SIR expression. Similar to my testbed measurements, I also conclude that the interference can be neglected in many cases, especially if the subcarrier spacing is chosen in an optimal way. The SIR for FBMC-OQAM systems was also calculated in [57, 89]. However, the authors of [89] calculated the SIR only for a given channel realization but did not include channel statistics and instead relied on simulations. Authors in [57]

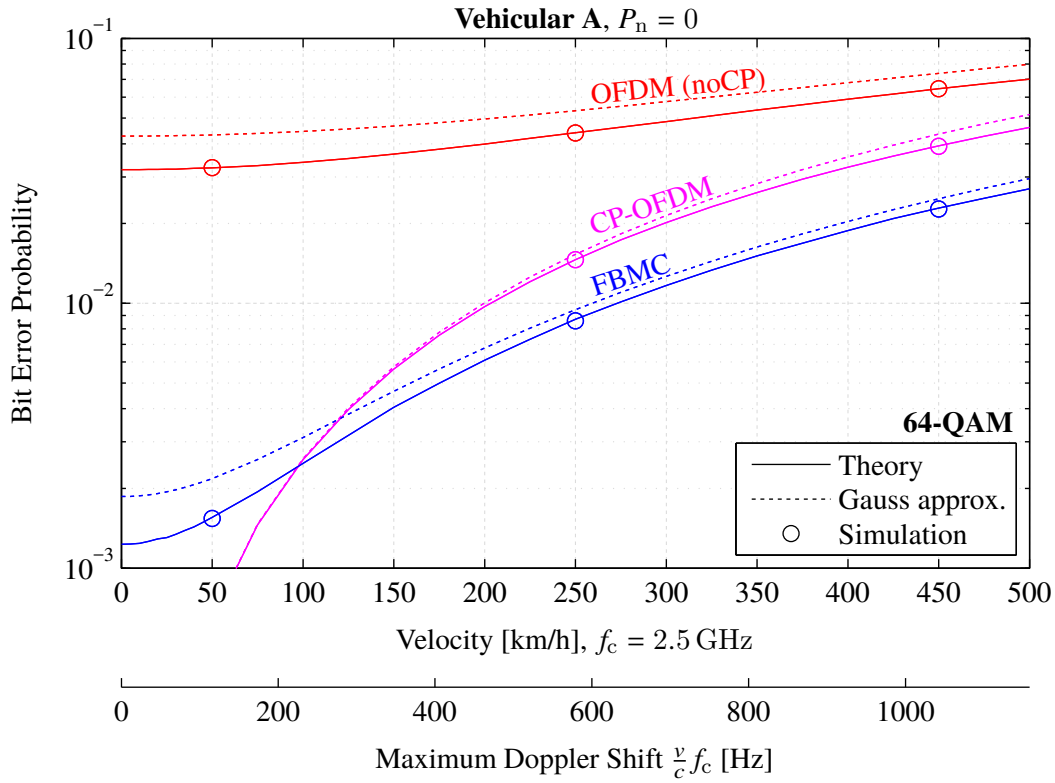

Figure 3.4. Similar to Figure 3.3, simulations validate the BEP calculations. The Gaussian interference approximation leads to relatively large errors. Note that FBMC outperforms OFDM for velocities larger than 100 km/h. ©2017 IEEE, [32].

utilized the ambiguity function to calculate the SIR. I, on the other hand, use a compact matrix description and compare the performance to OFDM.

The SIR in case of QAM transmissions can be straightforwardly calculated by employing my matrix notation. Similar to (3.9), I utilize the Kronecker product and evaluate only one received symbol, at subcarrier position l and time-position k, but additionally set the noise power to zero, leading to

$$y_{l,k} = \mathbf{q}_{l,k}^{\mathsf{H}} \, \mathbf{H} \, \mathbf{G} \, \mathbf{x} = \left((\mathbf{G} \, \mathbf{x})^{\mathsf{T}} \otimes \mathbf{q}_{l,k}^{\mathsf{H}} \right) \mathrm{vec}\{\mathbf{H}\}. \tag{3.17}$$

The SIR follows directly from (3.17) and can be expressed by (uncorrelated data symbols)

$$\mathrm{SIR}_{l,k}^{\mathrm{QAM}} = \frac{[\mathbf{\Gamma}]_{\overline{lk},\overline{lk}}}{\mathrm{tr}\{\mathbf{\Gamma}\} - [\mathbf{\Gamma}]_{\overline{lk},\overline{lk}}}, \tag{3.18}$$

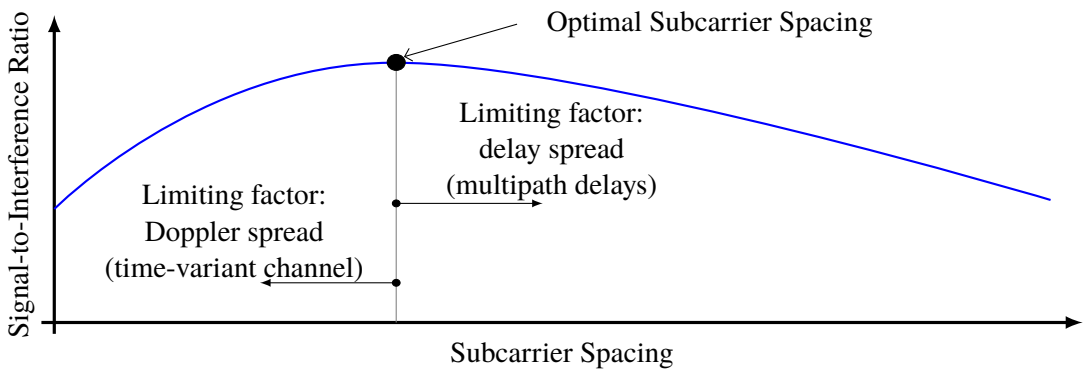

Figure 3.5. The SIR for different modulation schemes also depends on the subcarrier spacing. This dependency can be eliminated by considering an optimal subcarrier spacing, allowing a fair comparison.

with matrix $\mathbf{\Gamma} \in \mathbb{C}^{LK \times LK}$ given by

$$\mathbf{\Gamma} = \left(\mathbf{G}^{\mathsf{T}} \otimes \mathbf{q}_{l,k}^{\mathsf{H}}\right) \mathbf{R}_{\mathrm{vec}\{\mathbf{H}\}} \left(\mathbf{G}^{\mathsf{T}} \otimes \mathbf{q}_{l,k}^{\mathsf{H}}\right)^{\mathsf{H}}. \tag{3.19}$$

The correlation matrix $\mathbf{R}_{\mathrm{vec}\{\mathbf{H}\}} = \mathbb{E}\{\mathrm{vec}\{\mathbf{H}\}\mathrm{vec}\{\mathbf{H}\}^{\mathsf{H}}\}$ depends on the underlying channel model and has a major impact on the SIR. Note that $\overline{lk} = l + L(k-1)$ in (3.18) represents the $\overline{lk}$-th index of the vectorized symbol; see (2.26) for the underlying structure.

The SIR in OQAM transmissions cannot be calculated as easily as in QAM because OQAM utilizes phase compensation in combination with taking the real part. This is exactly what needs to be done to calculate the SIR,

$$\mathbf{\Gamma} = \mathbf{\Omega}\mathbf{\Omega}^{\mathsf{H}}, \tag{3.20}$$

$$[\tilde{\mathbf{\Omega}}_{\overline{lk}}]_{u,v} = [\mathbf{\Omega}]_{u,v} \frac{|[\mathbf{\Omega}]_{\overline{lk},v}|}{[\mathbf{\Omega}]_{\overline{lk},v}}, \qquad ; \text{for} \quad u, v = 1, 2, \ldots, LK \tag{3.21}$$

$$\tilde{\mathbf{\Gamma}}_{\overline{lk}} = \Re\{\tilde{\mathbf{\Omega}}_{\overline{lk}}\}\Re\{\tilde{\mathbf{\Omega}}_{\overline{lk}}\}^{\mathsf{H}}. \tag{3.22}$$

I perform a matrix decomposition of (3.19) according to (3.20). This delivers an auxiliary matrix $\mathbf{\Omega} \in \mathbb{C}^{LK \times LK}$ which is phase compensated based on the $\overline{lk}$-th row of $\mathbf{\Omega}$, see (3.21), leading to $\tilde{\mathbf{\Omega}}_{\overline{lk}} \in \mathbb{C}^{LK \times LK}$. As a final step, I combine the phase equalized auxiliary matrix, see (3.22), allowing me to express the SIR for OQAM by

$$\mathrm{SIR}_{l,k}^{\mathrm{OQAM}} = \frac{[\tilde{\mathbf{\Gamma}}_{\overline{lk}}]_{\overline{lk},\overline{lk}}}{\mathrm{tr}\{\tilde{\mathbf{\Gamma}}_{\overline{lk}}\} - [\tilde{\mathbf{\Gamma}}_{\overline{lk}}]_{\overline{lk},\overline{lk}}}. \tag{3.23}$$

In the numerical example of Section 3.1.1, FBMC outperforms CP -OFDM in high velocity scenarios. This, however, was only the case because interference from the Doppler spread dominated interference from the delay spread. By increasing the subcarrier spacing, the overall SIR could be improved, as illustrated in Figure 3.5. The big question is then, does FBMC still outperform CP-OFDM once both modulation schemes apply an optimal subcarrier spacing. This is, in particular, important for a fair comparison. Additionally, as 5G will allow such flexible subcarrier spacings, it also becomes a relevant factor for practical systems. I will thus consider an optimal subcarrier spacing in the sense of maximizing the SIR. As a rule of thumb, the subcarrier spacing should be chosen so that [23],

$$\frac{\sigma_t}{\sigma_f} \approx \frac{\tau_{\mathrm{rms}}}{\nu_{\mathrm{rms}}}, \tag{3.24}$$

where time-localization σ_t and frequency-localization σ_f is given by (2.17) for the Hermite pulse and by (2.20) for the PHYDYAS pulse. For FBMC-OQAM, the optimal subcarrier spacing can thus be expressed by:

$$F_{\mathrm{opt,Hermite}} \approx 0.71 \times \sqrt{\frac{\nu_{\mathrm{rms}}}{\tau_{\mathrm{rms}}}}, \tag{3.25}$$

$$F_{\mathrm{opt,PHYDYAS}} \approx 0.91 \times \sqrt{\frac{\nu_{\mathrm{rms}}}{\tau_{\mathrm{rms}}}}. \tag{3.26}$$

For a Jakes Doppler spectrum, the RMS Doppler spread is given by $\nu_{\mathrm{rms}} = \frac{1}{\sqrt{2}}\nu_{\max}$, where the maximum Doppler shift can be expressed by $\nu_{\max} = \frac{v}{c} f_{\mathrm{c}}$, with v the velocity, c the speed of light and f_{c} the carrier frequency. On the other hand, the RMS delay spread is $\tau_{\mathrm{rms}} = 46\,\mathrm{ns}$ for a Pedestrian A channel model and $\tau_{\mathrm{rms}} = 370\,\mathrm{ns}$ for a Vehicular A channel model [90]. Note that (3.24) represents only an approximation. The exact relation can be calculated, as for example done in [91] for the Gaussian pulse, and depends on the underlying channel model and prototype filter. However, for my chosen numerical parameters, the differences between the optimal SIR (exhaustive search) and the SIR obtained by applying the rule in (3.24) is less than 0.1 dB for FBMC-OQAM and less than 1 dB for FBMC-QAM. For the rest of this section, I always find the optimal subcarrier spacing in FBMC by exhaustive search.

As a reference, I also consider an optimal subcarrier spacing in CP-OFDM. The rule in (3.24), however, cannot be applied because the underlying rectangular pulse is not localized in frequency. Instead, I assume, for a fixed CP overhead of $\kappa = \frac{T_{\mathrm{CP}}}{T_0} = T_{\mathrm{CP}}F = TF - 1$, that the subcarrier spacing is chosen as high as possible while satisfying the condition of no Inter Symbol Interference (ISI), $T_{\mathrm{CP}} = \tau_{\max}$, so that the optimal subcarrier spacing for OFDM transforms to $F = \frac{\kappa}{\tau_{\max}}$. For a Jakes Doppler spectrum, the SIR can then be expressed by a

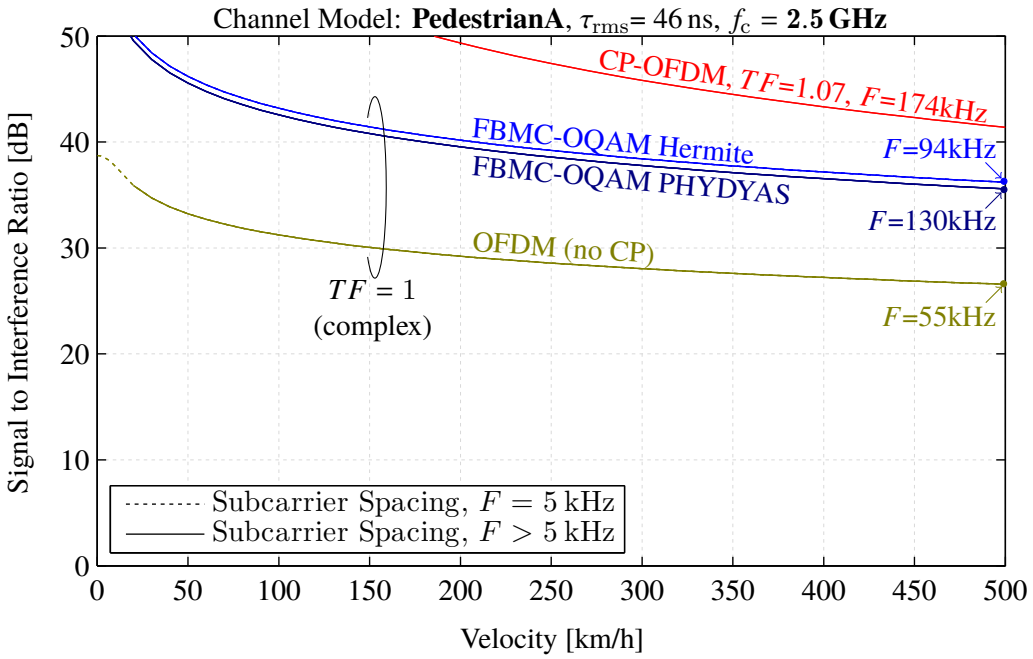

Figure 3.6. For a Pedestrian A channel model, the SIR is so high, that the channel induced interference can usually be neglected. It is dominated by noise. ©2017 IEEE, [1].

generalized hypergeometric function ${}_1F_2(\cdot)$ [92],

$$\text{SIR}_{\text{opt.,noISI}}^{\text{CP-OFDM}} = \frac{{}_1F_2\left(\frac{1}{2}; \frac{3}{2}, 2; -\left(\pi \frac{\nu_{\max}\tau_{\max}}{TF-1}\right)^2\right)}{1 - {}_1F_2\left(\frac{1}{2}; \frac{3}{2}, 2; -\left(\pi \frac{\nu_{\max}\tau_{\max}}{TF-1}\right)^2\right)}. \tag{3.27}$$

For example, LTE uses $\kappa = \frac{1}{14} \rightarrow TF = 1.07$. Besides the theoretical expression in (3.27), I also find the optimal subcarrier spacing through exhaustive search.

Figure 3.6 shows the SIR over velocity for a Pedestrian A channel model. FBMC exceeds OFDM without CP by approximately 10 dB. Furthermore, the Hermite filter performs better than the PHYDYAS filter, but only by approximately 0.7 dB. CP-OFDM performs best but also has a lower symbol density ($TF = 1.07$). Overall, the SIR is so high, that noise and other interference sources usually dominate the channel induced interference. Also, the limited symbol alphabet decreases the usefulness of high SNR values, as I will later show in Section 4.3.1 by real world throughput measurements.

Figure 3.7 shows a similar result as in Figure 3.6 but for a Vehicular A channel model. The SIR performance is worse than for Pedestrian A but still reasonably high. The SIR for CP-OFDM comes close to FBMC for high velocities, so that CP-OFDM with $TF = 1.07$ no longer provides a much higher SIR compared to FBMC. Note that I assume that the

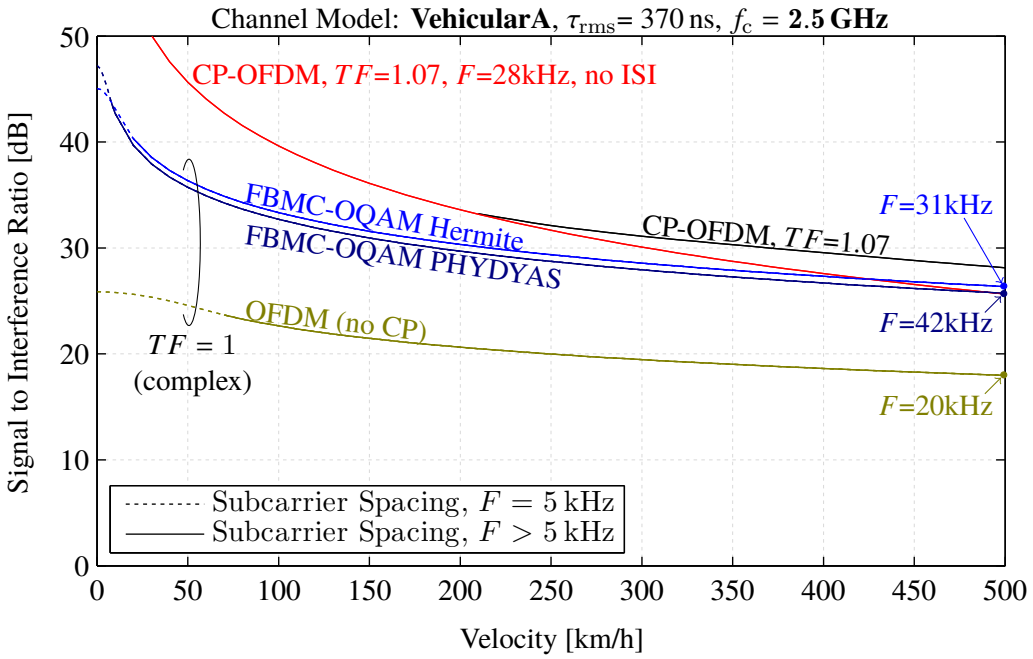

Figure 3.7. Similar to Figure 3.6, the interference can often be neglected, but now OFDM ($TF = 1.07$) and FBMC have a similar performance for high velocities scenarios. ©2017 IEEE, [1].

subcarrier spacing is lower bounded by $F \geq 5\,\text{kHz}$ in order to account for latency constraints, computational efficiency and real-world hardware effects. Figure 3.7 also shows that, in contrast to Figure 3.6, Equation (3.27) no longer is optimal for velocities higher than 200 km/h because the optimal subcarrier spacing obtained through exhaustive search leads to a higher SIR by allowing some small ISI (black line).

I now consider a carrier frequency of 60 GHz and the new Tapped Delay Line (TDL) channel model, proposed by 3GPP [93]. In contrast to the Pedestrian A and Vehicular A channel models, the delay taps are no longer fixed, but can be scaled to achieve a desired RMS delay spread. Figure 3.8 shows the SIR in case of a TDL-A channel model and the assumption of an RMS delay spread of 30 ns. Overall, the behavior is similar to Figure 3.7. In particular, for low velocities, distortions caused by frequency selectivity can be mitigated by decreasing the subcarrier spacing, assumed to be lower bounded by $F \geq 100\,\text{kHz}$. In contrast to the previous results, (3.27) no longer performs close to the optimum SIR (exhaustive search) because the TDL-A channel model has one extremely delayed tap with an extremely small power contribution. Such residual tap can usually be neglected. However, (3.27) assumes a perfect ISI free transmission, which is, in this case, highly suboptimal.

Figure 3.9 shows the SIR for a TDL-B channel model and an RMS delay spread of 900 ns, thus representing a doubly-selective channel with a very large delay spread. I expect that

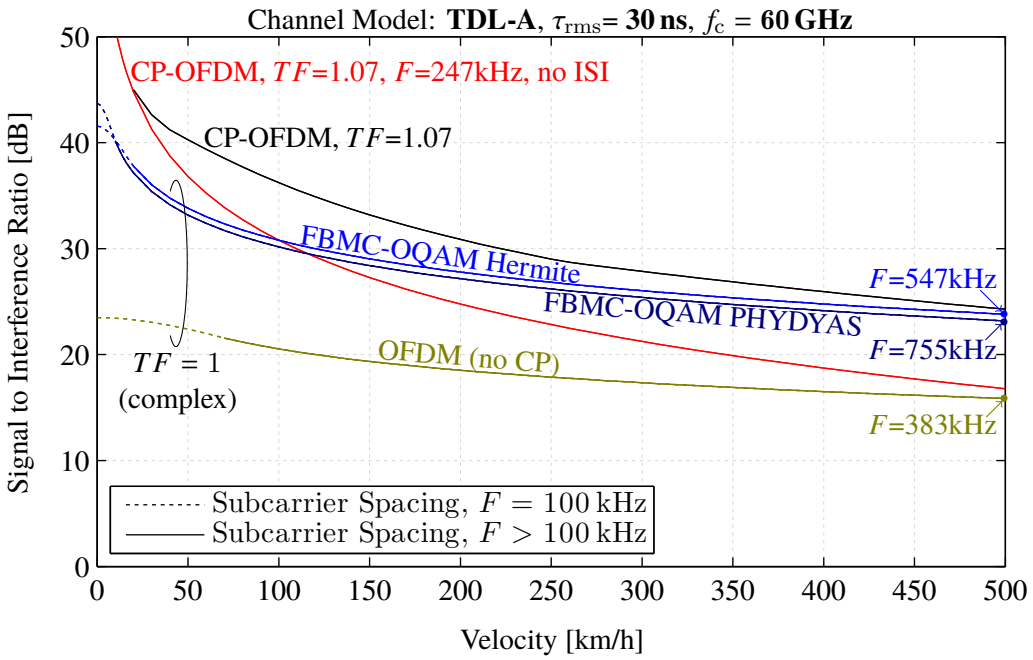

Figure 3.8. Even at a carrier frequency of 60 GHz, one-tap equalizers are often sufficient, especially if the RMS delay spread is relatively low. ©2017 IEEE, [1].

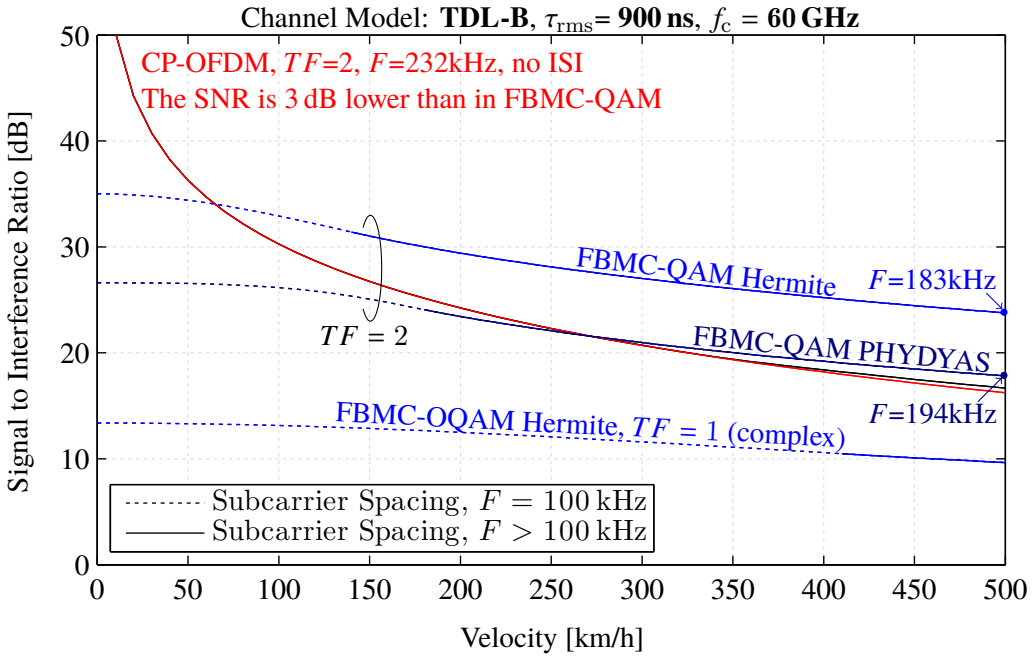

Figure 3.9. In the rare case of a very large delay spread, one might want to sacrifice spectral efficiency ($TF = 2$) in order to gain robustness. In such cases, FBMC-QAM even outperforms CP-OFDM (SIR and SNR). ©2017 IEEE, [1].

such extreme scenarios will rarely happen in reality and a system should therefore not be optimized for such extreme cases, but of course it should be able to cope with it. In FBMC, such harsh channel environments can easily be dealt with, simply by switching from an FBMC-OQAM transmission to an FBMC-QAM transmission, that is, setting some symbols $x_{l,k}$ to zeros. Thus, in order to gain robustness, one deliberately sacrifices spectral efficiency, $TF = 2$. It then turns out that FBMC performs even better than CP-OFDM. Additionally, the Hermite pulse strongly outperforms the PHYDYAS pulse because it has a better joint time-frequency localization. In FBMC-OQAM, this effect is somewhat lost because of the time-frequency squeezing. Note that it is not possible to transmit ISI free CP-OFDM with $TF = 1.07$ because it would require a subcarrier spacing of $F = \frac{1}{14\,\tau_{\max}} = 16\,\text{kHz} < 100\,\text{kHz}$, violating my lower bound.

Let me go back to the initial question, "Are One-Tap Equalizers Sufficient?". The correct answer to this question is, as almost always, "It depends". However, from a practical point of few, I think that the answer is "Yes, one-tap equalizers are sufficient in mobile communications". In most cases, the delay spread as well as the Doppler spread are so low, that the channel induced interference is dominated by noise, as depicted in Figure 3.6-3.9. Moving at 500 km/h will rarely happen. Also, a Jakes Doppler spectrum might not accurately model the true physical behavior. For example, in car-to-car communications, one might observe a half-bathtube shaped Doppler spectrum [94]. Furthermore, in trains scenarios, there might be a strong LOS path [95], leading to a fixed Doppler shift which can easily be compensated by the phase-locked loop. Feedback delays and repeated handovers are more problematic than a small, channel induced, interference. Even in the rare case of high interference, say an SIR of 20 dB, the data rate is still relatively high, see Section 4.3.1. By employing computational demanding equalizers, one has to sacrifice chip area. Furthermore, the power consumption and the costs increase. All those drawbacks, just for a small throughput improvement in a few rare cases are, in my opinion, not worth the effort.

3.2 Equalization in Doubly-Selective Channels

As discussed in Section 3.1, in almost all practical cases, the channel induced interference can be neglected compared to the noise, so that both, OFDM and FBMC, show the same performance in terms of Bit Error Ratio (BER) for a one-tap equalizer. However, in some rare cases, especially in high SNR regimes and if the usage of an optimal subcarrier spacing is not possible, interference may be dominant. Enhanced equalization methods can then improve the performance at the expense of increased computational complexity. Although I do not think that such equalizers are worth the effort in practical systems (at least in

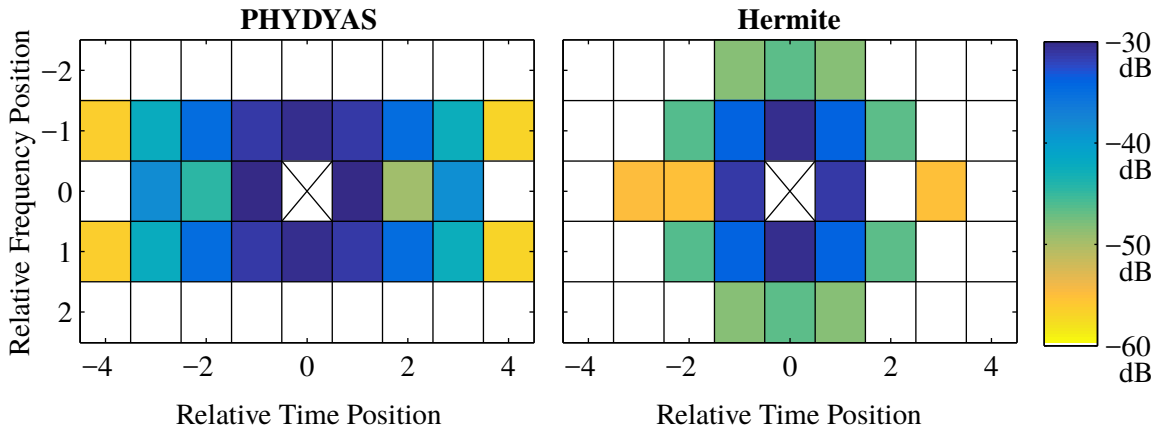

Figure 3.10. The interference contribution of neighboring symbols for the PHYDYAS prototype filter (left) and the Hermite prototype filter (right). Only a few symbols close to the symbol of interest have a significant contribution on the total interference. The SIR is 20 dB for the PHYDYAS pulse and 23 dB for the Hermite pulse. ©2017 IEEE, [37].

mobile communications), a lot of research has been focusing on exactly such equalizers. Most papers dealing with equalization in FBMC assume a time-invariant channel [18, 96–99]. Authors in [96] propose a parallel equalization scheme, requiring multiple parallel FFT blocks, while the equalization method in [97] requires a larger FFT. The authors of [100] apply the method of [96] on doubly-selective channels. In this thesis, I consider an equalization method that operates after a conventional FFT. MMSE equalization was proposed in [98] for a time-invariant channel and later extended in [99] to MIMO. Authors in [101] considered the same method as in [98], but applied on doubly-selective channels. All those papers [98, 99, 101] consider the interference contribution of neighboring subcarriers only in a statistical sense. However, from a conceptional point of view, there is no difference between interference coming from neighboring time symbols and interference coming from neighboring subcarriers. Thus, an equalizer which utilizes only neighboring time symbols, but ignores neighboring subcarriers, is in many cases not optimal. I thus propose a novel n-tap MMSE equalizer which, in contrast to [98, 99, 101], not only includes neighboring time symbols, but also utilizes neighboring subcarriers into the equalization process. I furthermore investigate a full block MMSE equalizer as well as a low-complexity interference cancellation scheme. Finally, I show that my equalization methods can be straightforwardly extended to MIMO systems.

To get a better understanding of the influence of doubly-selective channels in FBMC, I calculate how much interference neighboring symbols in time and frequency contribute to the total interference power. For that, I utilize a reshaped version of the diagonal elements of $\tilde{\mathbf{\Gamma}}_{\overline{lk}}$, see (3.22), and assume a subcarrier spacing of $F = 15\,\mathrm{kHz}$, a Vehicular A channel model

and a Jakes-Doppler spectrum with a maximum Doppler shift of 1.16 kHz (500 km/h for a carrier frequency of 2.5 GHz). Those parameters lead to a channel induced SIR of 20 dB for the PHYDYAS prototype filter. The left part of Figure 3.10 shows how much interference is generated by neighboring symbols in time and frequency for the PHYDYAS prototype filter. As illustrated, only a few close symbols contribute significantly to the SIR. The right part of Figure 3.10 shows the interference distribution for the Hermite prototype filter. The SIR is 23 dB and thus better than for the PHYDYAS filter. From Figure 3.10, I conclude that the underlying prototype filter has a huge impact on which neighboring symbols cause interference and that the distribution follows loosely the ambiguity function, see Figure 2.2.

Throughout this section, I assume the same channel model (Vehicular A, Jakes Doppler spectrum with a maximum Doppler shift of 1.16 kHz). The subcarrier spacing is set to $F = 15\,\mathrm{kHz}$ and the number of subcarriers to $L = 24$. For FBMC, I consider $K = 30$ time symbols and for OFDM $K = 14$ symbols (CP length of $4.7\,\mu\mathrm{s}$), leading to the same transmission time for both schemes ($KT = 1\,\mathrm{ms}$). The PAM modulation order is set to 16, equivalent to a 256-QAM signal constellation. Such high modulation order is necessary to see any influence of doubly-selectivity in practical systems. For example, for a 4-QAM signal constellation, the operating point is usually below an SNR of approximately 5 dB, so that an SIR of 20 dB has no influence. To be specific, channel coding would completely mitigate any channel induced interference with negligible coding overhead. For my channel parameters, one-tap equalizers might not be sufficient anymore if the SNR is high. Advanced equalization methods can then improve the performance at the expense of increased complexity.

3.2.1 MMSE

For the derivation of the MMSE equalizer, I utilize the same system model as already described in Section 2.2, see also (2.30),

$$\mathbf{y} = \mathbf{D}\,\mathbf{x} + \mathbf{n}, \tag{3.28}$$

where transmission matrix $\mathbf{D}$ helps to keep the notation compact and is defined as

$$\mathbf{D} = \mathbf{Q}^{\mathsf{H}}\,\mathbf{H}\,\mathbf{G}. \tag{3.29}$$

Note that $\mathbf{n} \sim \mathcal{CN}(\mathbf{0}, P_{\mathrm{n}}\,\mathbf{Q}^{\mathsf{H}}\mathbf{Q})$ denotes the Gaussian noise, same as in Section 2.2. A simple way to estimate the transmitted data symbols $\mathbf{x}$ in (3.28) would be the employment of a conventional (complex-valued) MMSE equalizer. Unfortunately, this does not work because such equalizer would also include the imaginary interference into the minimization problem,

leading to large detection errors. To avoid this problem, I stack real and imaginary part in a large vector, as suggested in [98]. The full block MMSE equalization of $\mathbf{y}$, see (3.28), can then be calculated by:

$$\hat{\mathbf{x}} = \begin{bmatrix} \Re\{\mathbf{D}\} \\ \Im\{\mathbf{D}\} \end{bmatrix}^{\mathsf{T}} \left(\begin{bmatrix} \Re\{\mathbf{D}\} \\ \Im\{\mathbf{D}\} \end{bmatrix} \begin{bmatrix} \Re\{\mathbf{D}\} \\ \Im\{\mathbf{D}\} \end{bmatrix}^{\mathsf{T}} + \boldsymbol{\Psi} \right)^{-1} \begin{bmatrix} \Re\{\mathbf{y}\} \\ \Im\{\mathbf{y}\} \end{bmatrix}, \tag{3.30}$$

with noise matrix $\boldsymbol{\Psi}$ given by

$$\boldsymbol{\Psi} = \frac{P_{\mathrm{n}}}{2} \begin{bmatrix} \Re\{\mathbf{Q}^{\mathsf{H}}\mathbf{Q}\} & -\Im\{\mathbf{Q}^{\mathsf{H}}\mathbf{Q}\} \\ \Im\{\mathbf{Q}^{\mathsf{H}}\mathbf{Q}\} & \Re\{\mathbf{Q}^{\mathsf{H}}\mathbf{Q}\} \end{bmatrix}. \tag{3.31}$$

Note that the matrix to be inverted in (3.30) usually has extremely small eigenvalues. This is caused by the time-frequency squeezing, similar as in Figure 2.5. In contrast to many other systems, noise matrix $\boldsymbol{\Psi}$ does not guarantee full rank because the noise matrix has a similar structure as $\mathbf{D}$ (in case of an AWGN channel, exactly the same). Thus, solving (3.30) is numerically very challenging and requires, for example, an eigendecomposition in combination with setting small eigenvalues to zero, as implicitly done in MATLAB by applying the pseudo inverse. However, there are two other main problems with the full block MMSE equalizer: Firstly, it has a high computational complexity. One has to invert a matrix of size $2LK \times 2LK$, too large for most practical applications. Secondly, a large delay is introduced because all symbols need to be received before equalization is possible. I therefore consider an n-tap MMSE equalizer which only includes a few neighboring symbols. Let me split the transmission model of (3.28) according to:

$$\mathbf{y}_{\mathcal{S}} = \mathbf{D}_{\mathcal{S}}\mathbf{x}_{\mathcal{S}} + \mathbf{D}_{\mathcal{S},\mathcal{R}}\mathbf{x}_{\mathcal{R}} + \mathbf{n}_{\mathcal{S}}. \tag{3.32}$$

Here, $\mathbf{y}_{\mathcal{S}} \in \mathbb{C}^{|\mathcal{S}|\times 1}$ is a subvector of $\mathbf{y}$ with $\mathcal{S}$ representing the considered subblock, that is, certain time-frequency positions, see Figure 3.11. For example, a subblock vector of size $|\mathcal{S}| = 5$ (5-tap) can be written as: $\mathbf{y}_{\mathcal{S}} = \begin{bmatrix} y_{l,k-2} & y_{l,k-1} & y_{l,k} & y_{l,k+1} & y_{l,k+2} \end{bmatrix}^{\mathsf{T}}$. Such subblock was used in [98] and only includes neighboring symbols in time but ignores neighboring subcarriers. In many cases, this is not optimal, especially in high velocity scenarios and for some specific prototype filters. My considered subblock vector, on the other hand, can be expressed by $\mathbf{y}_{\mathcal{S}} = \begin{bmatrix} y_{l,k-1} & y_{l-1,k} & y_{l,k} & y_{l+1,k} & y_{l,k+1} \end{bmatrix}^{\mathsf{T}}$, see Figure 3.11. Vector $\mathbf{x}_{\mathcal{S}} \in \mathbb{R}^{|\mathcal{S}|\times 1}$ in (3.32) represents the transmitted data symbols of the considered subblock, while $\mathbf{x}_{\mathcal{R}} \in \mathbb{R}^{|\mathcal{R}|\times 1}$ represents all other transmitted data symbols relevant for $\mathbf{y}_{\mathcal{S}}$. Only a few symbols outside the subblock have a significant contribution on $\mathbf{y}_{\mathcal{S}}$, so that

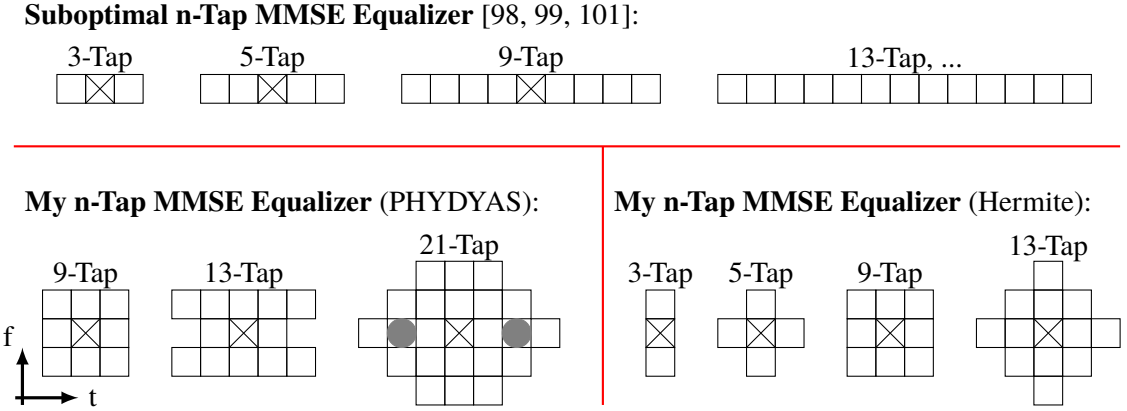

Figure 3.11. The n-tap equalizer utilizes n received symbols to estimate the transmitted data symbol at one time-frequency position (indicated by the crosses in the center). Authors in [98, 99, 101] employ only neighboring time symbols for the equalization process. This is, in many cases, not optimal. ©2017 IEEE, [37].

usually $|\mathcal{R}| << LK - |\mathcal{S}|$. The matrices $\mathbf{D}_{\mathcal{S}} \in \mathbb{C}^{|\mathcal{S}|\times|\mathcal{S}|}$ and $\mathbf{D}_{\mathcal{S},\mathcal{R}} \in \mathbb{C}^{|\mathcal{S}|\times|\mathcal{R}|}$ correspond to the correct elements of $\mathbf{D}$, so that (3.32) satisfies (3.28). Similar to (3.30), the $|\mathcal{S}|$-tap MMSE equalization of (3.32) becomes

$$\hat{\mathbf{x}}_{\mathcal{S}} = \begin{bmatrix} \Re\{\mathbf{D}_{\mathcal{S}}\} \\ \Im\{\mathbf{D}_{\mathcal{S}}\} \end{bmatrix}^{\mathsf{T}} \left(\mathbf{\Delta}_{\mathcal{S}} + \mathbf{\Delta}_{\mathcal{S},\mathcal{R}} + \mathbf{\Psi}_{\mathcal{S}} \right)^{-1} \begin{bmatrix} \Re\{\mathbf{y}_{\mathcal{S}}\} \\ \Im\{\mathbf{y}_{\mathcal{S}}\} \end{bmatrix} \tag{3.33}$$

with

$$\mathbf{\Delta}_{\mathcal{S}} = \begin{bmatrix} \Re\{\mathbf{D}_{\mathcal{S}}\} \\ \Im\{\mathbf{D}_{\mathcal{S}}\} \end{bmatrix} \begin{bmatrix} \Re\{\mathbf{D}_{\mathcal{S}}\} \\ \Im\{\mathbf{D}_{\mathcal{S}}\} \end{bmatrix}^{\mathsf{T}} \tag{3.34}$$

$$\mathbf{\Delta}_{\mathcal{S},\mathcal{R}} = \begin{bmatrix} \Re\{\mathbf{D}_{\mathcal{S},\mathcal{R}}\} \\ \Im\{\mathbf{D}_{\mathcal{S},\mathcal{R}}\} \end{bmatrix} \begin{bmatrix} \Re\{\mathbf{D}_{\mathcal{S},\mathcal{R}}\} \\ \Im\{\mathbf{D}_{\mathcal{S},\mathcal{R}}\} \end{bmatrix}^{\mathsf{T}} . \tag{3.35}$$

Noise matrix $\mathbf{\Psi}_{\mathcal{S}} \in \mathbb{C}^{2|\mathcal{S}|\times 2|\mathcal{S}|}$ in (3.33) is given by the submatrix of $\mathbf{\Psi} \in \mathbb{C}^{2LK\times 2LK}$, see (3.31), corresponding to the correct elements. Note that $\hat{\mathbf{x}}_{\mathcal{S}}$ in (3.33) delivers in total $|\mathcal{S}|$ estimates. However, I am only interested in the center position, as illustrated in Figure 3.11. The remaining elements are discarded. Thus, my equalization requires in total LK matrix inversions of size $2|\mathcal{S}| \times 2|\mathcal{S}|$. The computational complexity is usually lower then for the full block MMSE equalizer but still relatively high. In Section 3.2.2, I propose a low-complexity interference cancellation scheme. But first, I provide a numerical example of the MMSE equalizers.

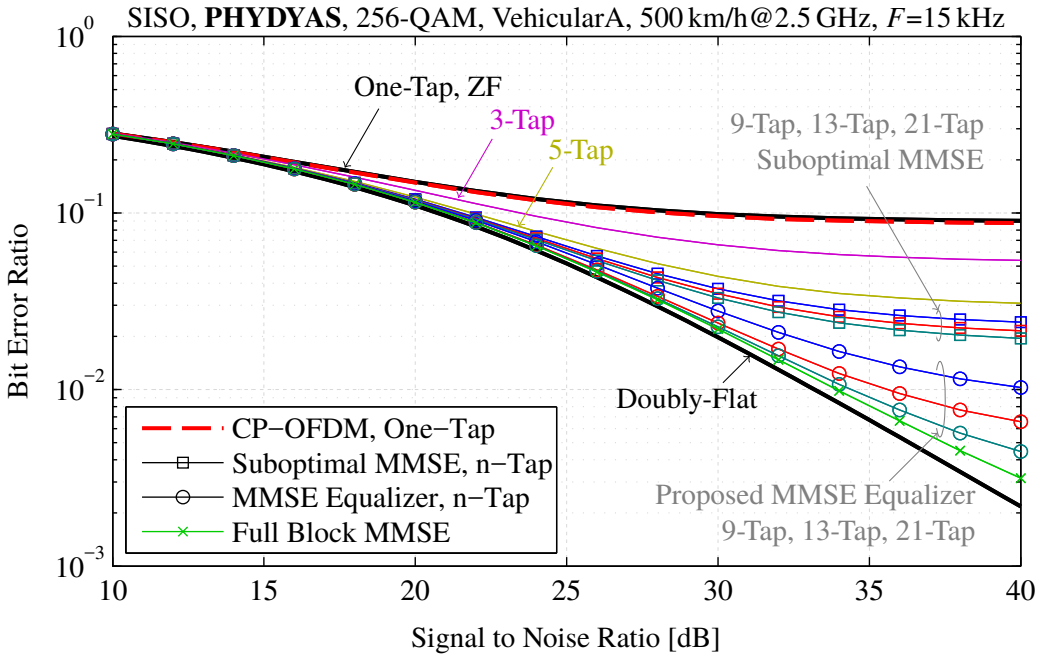

Figure 3.12. Considering only neighboring time symbols [98, 99, 101] is very inefficient. By utilizing neighboring subcarriers as well, see Figure 3.11, the performance of an n-tap equalizer can be greatly improved. ©2017 IEEE, [37].

Figure 3.12 shows how the BER depends on the SNR for the PHYDYAS prototype filter. As a reference, I also consider CP-OFDM. The upper black curve represent the performance for a one-tap equalizer while the lower black curve corresponds to a doubly-flat channel, see Figure 3.2 in Section 3.1. MMSE equalization will result in a performance between these two reference curves. Note that CP-OFDM slightly outperforms FBMC. The equalization method in [98], which uses only neighboring time symbols but ignores neighboring subcarriers, is suboptimal in this scenario. Increasing the number of taps from $|\mathcal{S}| = 5$-taps to $|\mathcal{S}| = 21$-taps only marginally improves the performance. On the other hand, with my equalization method, the performance increases significantly thanks to the employment of neighboring subcarriers. The 21-tap equalizer even comes close to the full block MMSE equalizer, see (3.30). For the 3-tap and 5-tap equalizer, it is sufficient to consider only neighboring time symbols. Figure 3.11 illustrates which symbols are utilized for the $|\mathcal{S}|$-tap equalizer. To determine the optimal subblock, I follow loosely the interference distribution of the one-tap equalizer, see Figure 3.10. However, this delivers not always the optimal solution as, for example, in case of the 21-tap equalizer.

Figure 3.13 shows the BER for the Hermite prototype filter. In contrast to the PHYDYAS filter, the Hermite filter outperforms CP-OFDM in case of a one-tap equalizer, as already

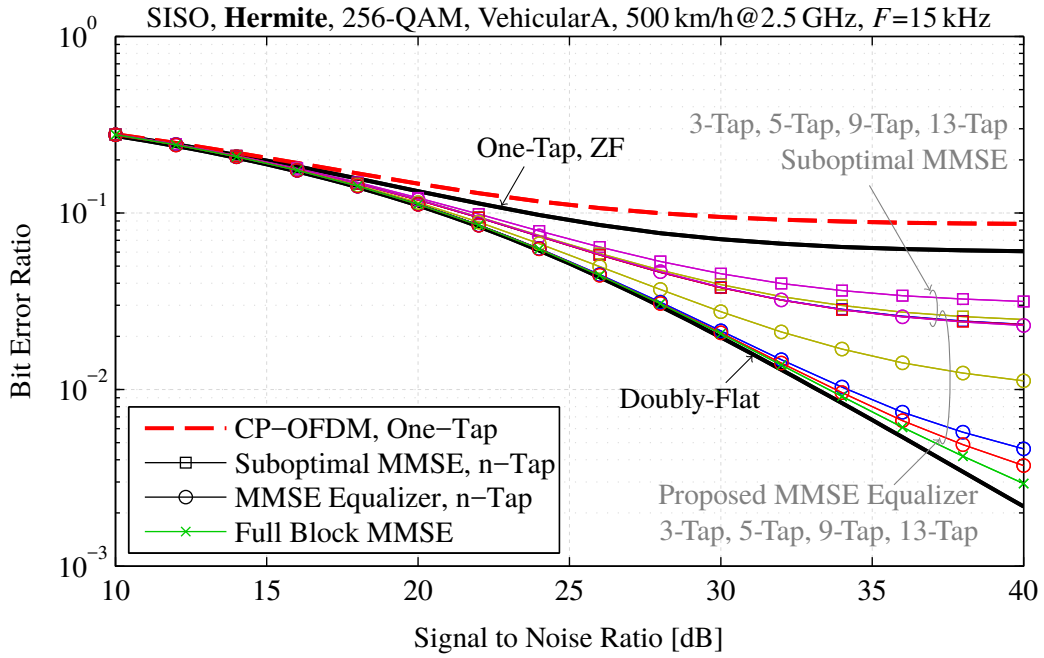

Figure 3.13. Compared to the PHYDYAS prototype filter, see Figure 3.12, the Hermite pulse shows better robustness in time-variant channels. ©2017 IEEE, [37].

observed in Section 3.1.1. Overall, the Hermite prototype filter is better suited for high velocity scenarios (for a fixed subcarrier spacing). In contrast to the PHYDYAS filter, even the 3-tap equalizer of [98] is suboptimal. The optimal 3-tap equalizer utilizes only neighboring subcarriers. The 13-tap equalizer already achieves a performance close to that of the full block MMSE equalizer.

The channel model and the prototype filter have a huge impact on which neighboring symbols should be used for the equalization process. For example, in a highly-frequency-selective, but time-invariant channel, it is usually not necessary to consider neighboring subcarriers for the PHYDYAS prototype filter. For the Hermite prototype filter, on the other hand, neighboring subcarriers have to be employed as well. Thus, for an optimal performance, one always has to check which symbols to include in the equalization process. Because the Hermite prototype filter performs better than the PHYDYAS prototype filter in high velocity scenarios, I consider only the Hermite prototype filter in Section 3.2.2 and Section 3.2.3.

3.2.2 Interference Cancellation

The MMSE equalizer has the big disadvantage of high computational complexity, even if only a small subblock is considered. This is, in particular, problematic in a time-variant channel, where the equalizer coefficients have to be calculated at every time instant. I therefore propose

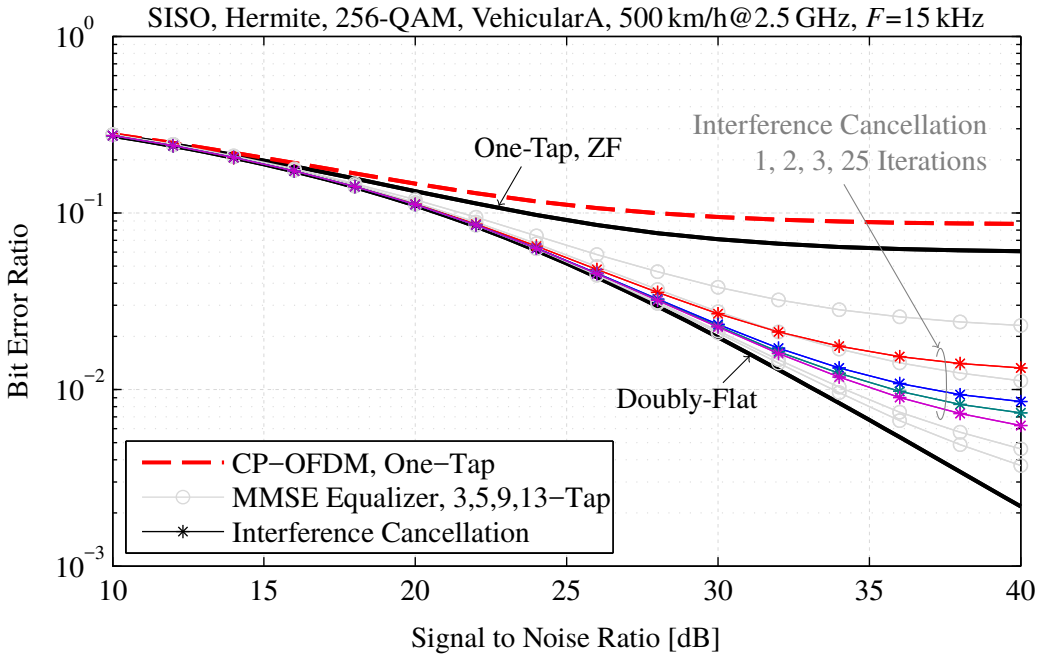

Figure 3.14. The main drawback of MMSE equalizers is the high computational complexity. A simple interference cancellation scheme can circumvent this limitation. For realistic SNR values smaller than 30 dB, the BER performs close to the optimum. ©2017 IEEE, [37].

a simple, yet effective, interference cancellation scheme. Similar as suggested in [102] for OFDM, one can cancel the interference by:

$$\mathbf{y}^{(i+1)} = \mathbf{y} - (\mathbf{D} - \mathrm{ddiag}\{\mathbf{D}\})\,\hat{\mathbf{x}}^{(i)}. \tag{3.36}$$

The superscript $(\cdot)^{(i)}$ denotes the i-th iteration and the $\mathrm{ddiag}\{\mathbf{D}\}$ operator generates a diagonal matrix with the same diagonal elements as $\mathbf{D}$. Thus $(\mathbf{D} - \mathrm{ddiag}\{\mathbf{D}\})$ represents all the off-diagonal elements of $\mathbf{D}$. The data estimates are obtained by one-tap equalization, see also (3.5), according to:

$$\hat{\mathbf{x}}^{(i)} = Q\left\{\mathrm{ddiag}\{\mathbf{D}\}^{-1}\,\mathbf{y}^{(i)}\right\}, \tag{3.37}$$

with $Q\{\cdot\}$ denoting the quantization operator, that is, nearest neighbor symbol detection. Note that quantization implicitly removes the imaginary interference of FBMC. My algorithm starts with $\hat{\mathbf{x}}^{(0)}$, representing the conventional (quantized) one-tap equalizer.

Figure 3.14 shows the BER over SNR for the interference cancellation scheme in (3.36) and (3.37). As a reference (grayed out), I also include the n-tap MMSE equalization from Section 3.2.1. The BER of interference cancellation lies between the 5-tap equalizer and the

9-tap equalizer. After 2 to 3 iterations, the performance no longer increases significantly. Thus, more than two to three iterations are not necessary, in particular if the computational complexity should be kept low. Although the cancellation scheme performs not as good as the MMSE equalizer in terms of BER, the performance is still very good, especially for practical relevant SNR values smaller than 30 dB.

Let me now discuss the computational complexity (per symbol) in more detail, where I assume that transmission matrix $\mathbf{D}$ is already known and does not need to be calculated. As shown in the right part of Figure 3.10, only eight neighboring symbols cause significant interference. Thus, for the first iteration, only nine multiplications (8 + one-tap equalizer) are needed. For the following iterations, a multiplication is only required if the estimated data symbol, $\hat{x}_{l,k}$, has changed. On the other hand, the computational complexity of a 5-tap MMSE equalizer is significantly higher. It requires a matrix inversion of size 10×10 together with additional multiplications, see (3.33).

3.2.3 Extension to MIMO

So far, I considered only a Single-Input and Single-Output (SISO) transmission, but the extension to MIMO is straightforward thanks to my matrix notation. One only needs bigger matrices. Of course, this further increases the computational complexity, making the practical implementation challenging. As a theoretical reference, however, the MMSE equalizer is quite useful. For a better illustration of the concept, I consider a 2×2 MIMO transmission system, which can be modeled similar as in (2.30):

$$\underbrace{\begin{bmatrix}\mathbf{y}_1\\ \mathbf{y}_2\end{bmatrix}}_{\mathbf{y}_\mathrm{M}} = \underbrace{\begin{bmatrix}\mathbf{Q}^\mathsf{H}\mathbf{H}_{1,1}\mathbf{G} & \mathbf{Q}^\mathsf{H}\mathbf{H}_{1,2}\mathbf{G}\\ \mathbf{Q}^\mathsf{H}\mathbf{H}_{2,1}\mathbf{G} & \mathbf{Q}^\mathsf{H}\mathbf{H}_{2,2}\mathbf{G}\end{bmatrix}}_{\mathbf{D}_\mathrm{M}} \underbrace{\begin{bmatrix}\mathbf{x}_1\\ \mathbf{x}_2\end{bmatrix}}_{\mathbf{x}_\mathrm{M}} + \begin{bmatrix}\mathbf{n}_1\\ \mathbf{n}_2\end{bmatrix}. \tag{3.38}$$

The subscript 1 and 2 now denote antenna 1 and antenna 2. Similar as in (3.30), I find the full block MMSE equalizer by:

$$\hat{\mathbf{x}}_\mathrm{M} = \begin{bmatrix}\Re\{\mathbf{D}_\mathrm{M}\}\\ \Im\{\mathbf{D}_\mathrm{M}\}\end{bmatrix}^\mathsf{T} \left(\begin{bmatrix}\Re\{\mathbf{D}_\mathrm{M}\}\\ \Im\{\mathbf{D}_\mathrm{M}\}\end{bmatrix} \begin{bmatrix}\Re\{\mathbf{D}_\mathrm{M}\}\\ \Im\{\mathbf{D}_\mathrm{M}\}\end{bmatrix}^\mathsf{T} + \mathbf{\Psi}_\mathrm{M} \right)^{-1} \begin{bmatrix}\Re\{\mathbf{y}_\mathrm{M}\}\\ \Im\{\mathbf{y}_\mathrm{M}\}\end{bmatrix} \tag{3.39}$$

with noise matrix $\mathbf{\Psi}_\mathrm{M} \in \mathbb{C}^{4LK \times 4LK}$ given by

$$\mathbf{\Psi}_\mathrm{M} = \frac{P_n}{2} \begin{bmatrix}\Re\{\mathbf{\Upsilon}\} & -\Im\{\mathbf{\Upsilon}\}\\ \Im\{\mathbf{\Upsilon}\} & \Re\{\mathbf{\Upsilon}\}\end{bmatrix} \quad \text{with} \quad \mathbf{\Upsilon} = \begin{bmatrix}\mathbf{Q}^\mathsf{H}\mathbf{Q} & \mathbf{0}\\ \mathbf{0} & \mathbf{Q}^\mathsf{H}\mathbf{Q}\end{bmatrix} \tag{3.40}$$

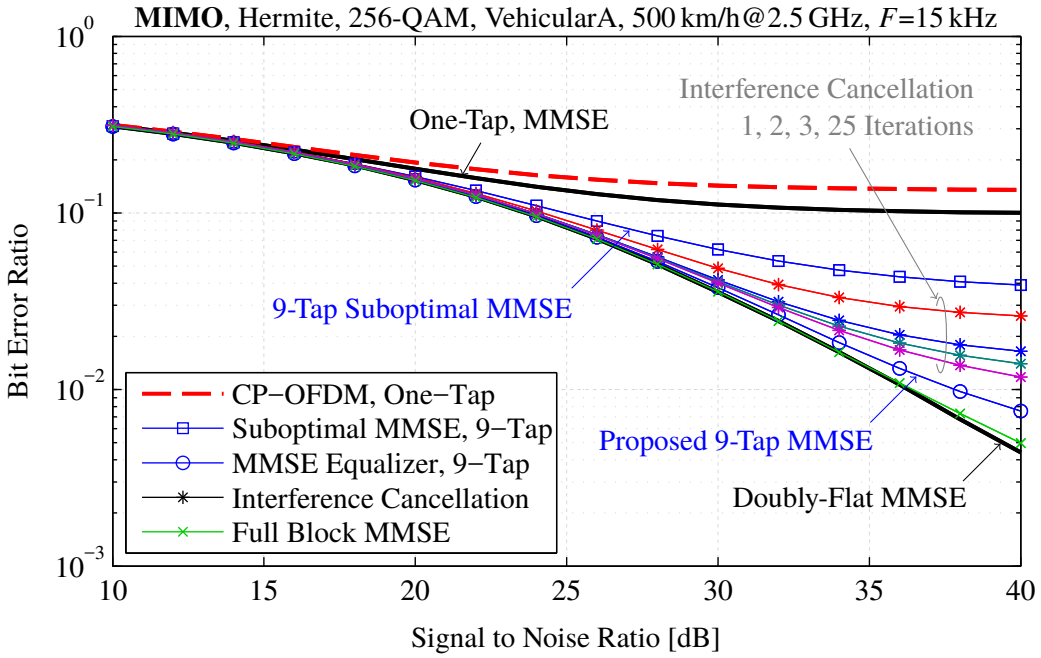

Figure 3.15. The matrix notation allows to straightforwardly extend the proposed equalization methods to MIMO. Overall, a similar behavior as in SISO is observed. Again, employing neighboring subcarriers improves the performance. ©2017 IEEE, [37].

One can also find the n-tap MIMO MMSE equalizer, similar as in (3.33), but applied on the system model in (3.38). To be consistent with SISO, I count, for an n-tap MIMO equalizer, only the number of taps per antenna. For example, a one-tap MMSE equalizer requires in total four multiplications for the equalization (ignoring the calculation of the equalizer matrix). The interference cancellation scheme in (3.36) can also be easily extended to MIMO. The one-tap ZF equalizer in (3.37) then becomes a one-tap MMSE equalizer.

Figure 3.15 shows the BER over the SNR for a 2×2 MIMO system. The behavior is similar to SISO. Considering only neighboring time symbols, but ignoring neighboring subcarriers, is highly suboptimal. Thus, my 9-tap equalizer performs much better than the 9-tap equalizer proposed in [98]. The interference cancellation scheme also performs relatively good, while at the same time the computational complexity is much lower compared to the MMSE equalization.

Chapter 4

Pilot-Aided Channel Estimation

In Section 3, I investigated channel equalization under perfect channel knowledge. In practical systems, however, the channel always has to be estimated before equalization is possible. In principle, one can distinguish between blind channel estimation [103–105], preamble based channel estimation [106–110] and pilot symbol aided channel estimation [111–113]. I will focus on the latter because the computational complexity as well as the overhead are relatively low and pilots allow a simple tracking of the channel in time. This also explains why pilot-aided channel estimation is employed in LTE. In this Section, I first explain the concept of pilot aided channel estimation. While in FBMC-QAM and block spread FBMC-OQAM, one can straightforwardly apply all channel estimation methods known in OFDM [114], this is not possible in conventional FBMC-OQAM because of the imaginary interference. To solve this issue, I investigate two methods to cancel the imaginary interference at the pilot positions, namely, auxiliary symbols and data spreading. Furthermore, I evaluate the performance in terms of measured throughput, achievable rate and theoretical BEP. Finally, I propose a novel channel estimation technique for doubly-selective channels. This chapter is mainly based on my publications [1, 30, 38, 40–42] and includes the following novel contributions:

- In Section 4.2.1, I propose a general method to choose auxiliary pilot symbols. In contrast to other contributions, my method allows closely spaced pilots and more than one auxiliary symbol per pilot. By, for example, choosing two auxiliary symbols per pilot, I am able to reduce the power offset so that the achievable rate increases for low to medium SNR ranges [42].

- In Section 4.2.2, I propose an algorithm for designing the coding matrix, required for the data spreading approach. Compared to other contributions, which consider only a spreading length of up to eight, my algorithm allows for an arbitrary spreading length [42].

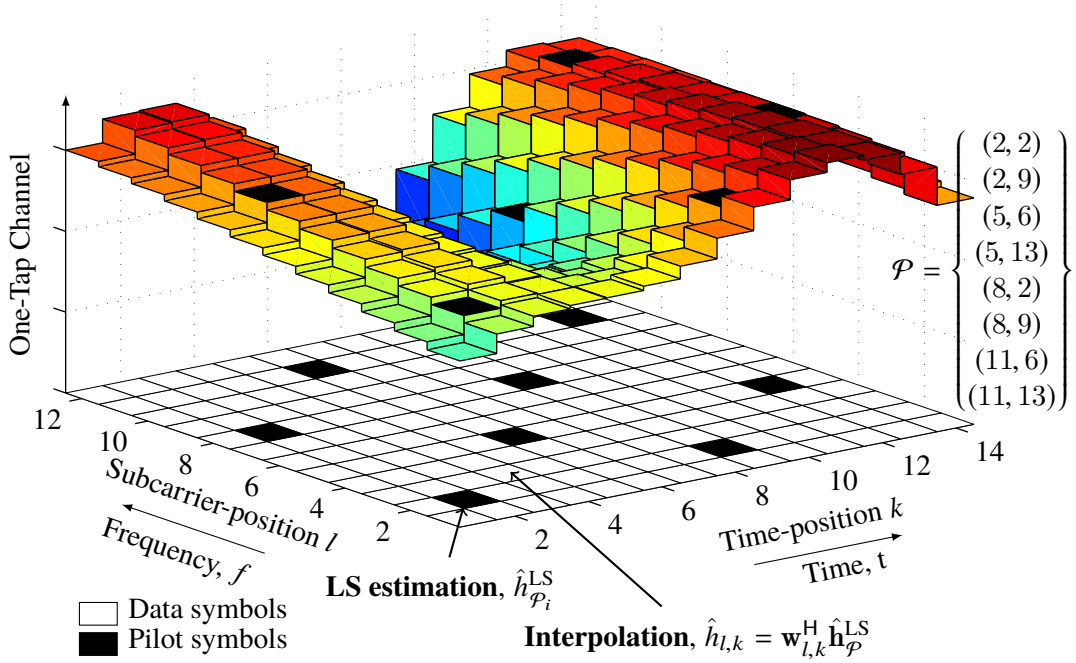

Figure 4.1. Pilot-symbol aided channel estimation consists of two basic steps: Firstly, a LS channel estimation at the pilot positions. Secondly, interpolation of those LS estimates to obtain the channel at the data positions. The pilot pattern in the figure is chosen according to the LTE standard.

- In Section 4.3, I provide a detailed performance comparison of the auxiliary symbol technique and the data spreading approach. In particular, in Section 4.3.1, I present real world throughput measurements, conducted with my testbed, together with the corresponding information theoretic bounds. In Section 4.3.2, I derive a closed-form expression for the BEP, including channel estimation errors, and discuss the optimal trade-off between pilot symbol power and data symbol power [1, 40, 41].

- In Section 4.4, I propose a novel channel estimation technique for doubly-selective channels. My method is based on MMSE interpolation and does not require clustered pilots or a basis expansion model. The content is partly based on [30, 38] but mainly consists of original work which was not yet submitted to any paper.

4.1 LS Estimation and Interpolation

The idea of pilot-aided channel estimation is quite simple. It consists of two basic steps, a LS channel estimation at the pilot positions and interpolation, as illustrated in Figure 4.1. Certain

"data" symbols, the so called pilots, are known a priory at the receiver. The LS estimation of the channel at the pilot positions $(l, k) \in \mathcal{P}$ can then be obtained by dividing the received symbols by the pilot symbols, that is,

$$\hat{h}^{\mathrm{LS}}_{\mathcal{P}_i} = \frac{y_{\mathcal{P}_i}}{x_{\mathcal{P}_i}}, \tag{4.1}$$

where $\mathcal{P}_i$ corresponds to the i-th pilot position, see Figure 4.1. Such LS channel estimation can be interpreted as sampling the transfer function at the pilot positions. The channel at the data positions, on the other hand, is estimated through interpolation of the LS estimates, that is,

$$\hat{h}_{l,k} = \mathbf{w}^{\mathsf{H}}_{l,k} \hat{\mathbf{h}}^{\mathrm{LS}}_{\mathcal{P}}, \tag{4.2}$$

where I stack all LS estimates from (4.1) in a vector $\hat{\mathbf{h}}^{\mathrm{LS}}_{\mathcal{P}} \in \mathbb{C}^{|\mathcal{P}|\times 1}$, according to

$$\hat{\mathbf{h}}^{\mathrm{LS}}_{\mathcal{P}} = \begin{bmatrix} \hat{h}^{\mathrm{LS}}_{\mathcal{P}_1} \\ \hat{h}^{\mathrm{LS}}_{\mathcal{P}_2} \\ \vdots \\ \hat{h}^{\mathrm{LS}}_{\mathcal{P}_{|\mathcal{P}|}} \end{bmatrix}. \tag{4.3}$$

Vector function $\mathbf{w}_{l,k} \in \mathbb{C}^{|\mathcal{P}|\times 1}$ in (4.2) describes an arbitrary linear interpolation method, for example, nearest neighbor interpolation, "straight line" interpolation, spline interpolation or linear MMSE interpolation. Although I call $\mathbf{w}_{l,k}$ interpolation, it may also describe extrapolation when the channel values are outside the pilot grid and, more generally, any linear combination of LS channel estimates. It is thus a very generic concept. For example, the linear MMSE channel interpolation (estimation) can be found by [38, 115],

$$\mathbf{w}^{\mathrm{LMMSE}}_{l,k} = \arg\min_{\mathbf{w}_{l,k}} \mathbb{E}\left\{ |h_{l,k} - \mathbf{w}^{\mathsf{H}}_{l,k} \hat{\mathbf{h}}^{\mathrm{LS}}_{\mathcal{P}}|^2 \right\} \tag{4.4}$$

$$= \mathbf{R}^{-1}_{\hat{\mathbf{h}}^{\mathrm{LS}}_{\mathcal{P}}} \mathbf{r}_{\hat{\mathbf{h}}^{\mathrm{LS}}_{\mathcal{P}}, h_{l,k}}, \tag{4.5}$$

with $\mathbf{R}_{\hat{\mathbf{h}}^{\mathrm{LS}}_{\mathcal{P}}} = \mathbb{E}\{\hat{\mathbf{h}}^{\mathrm{LS}}_{\mathcal{P}} (\hat{\mathbf{h}}^{\mathrm{LS}}_{\mathcal{P}})^{\mathsf{H}}\}$ denoting the correlation matrix and $\mathbf{r}_{\hat{\mathbf{h}}^{\mathrm{LS}}_{\mathcal{P}}, h_{l,k}} = \mathbb{E}\{\hat{\mathbf{h}}^{\mathrm{LS}}_{\mathcal{P}} h^*_{l,k}\}$ the correlation vector. Note that (4.5) follows directly from the orthogonal projection theorem [116]. If $\hat{\mathbf{h}}^{\mathrm{LS}}_{\mathcal{P}}$ and $h_{l,k}$ are zero mean, jointly complex Gaussian variables, as often assumed, the linear MMSE interpolation in (4.5) corresponds to the overall MMSE solution (linear and nonlinear).

The channel estimation in OFDM works exactly as illustrated in Figure 4.1. In particular, the complex orthogonality of OFDM guarantees that the LS channel estimation, see (4.1), is very accurate. The same holds true for FBMC-QAM and block spread FBMC-OQAM. However, in conventional FBMC-OQAM, the imaginary interference prevents a straightforward LS channel estimation, so that additional processing becomes necessary, see Section 4.2.

4.2 Canceling the Imaginary Interference

To provide a better understanding of the challenges in FBMC-OQAM and to describe possible solutions, I employ the same system model as in Section 2.2, see (2.31),

$$\mathbf{y} \approx \mathrm{diag}\{\mathbf{h}\}\,\bar{\mathbf{D}}\,\mathbf{x} + \mathbf{n}, \tag{4.6}$$

with back-to-back transmission matrix $\bar{\mathbf{D}}$ defined as,

$$\bar{\mathbf{D}} = \mathbf{Q}^{\mathrm{H}}\mathbf{H}\,\mathbf{G}\,\big|_{\mathbf{H}=\mathbf{I}_N} = \mathbf{Q}^{\mathrm{H}}\mathbf{G}. \tag{4.7}$$

The big challenge in FBMC-OQAM is the imaginary interference, described by the off-diagonal elements of $\bar{\mathbf{D}}$. The main idea of FBMC-OQAM is to equalize the phase followed by taking the real part in order to get rid of the imaginary interference. This, however, only works once the phase is known, thus only after channel estimation. The channel estimation itself has to be performed in the complex domain which is affected by the imaginary interference, leading to an SIR of 0 dB, too low for an accurate LS channel estimation in (4.1). Thus additional processing becomes necessary. A simple method for pilot aided channel estimation was proposed in [117], where one data symbol per pilot is sacrificed to cancel the imaginary interference at the pilot position. The authors of [118] proposed the name auxiliary symbol for such method. The big disadvantage of such method is the high power of the auxiliary symbols, worsening the PAPR and wasting signal power. Subsequently, different methods have been proposed to mitigate these harmful effects [42, 119–124]. From all those techniques, I think that the data spreading approach [119] is the most promising method because no energy is wasted, there is no noise enhancement, and the performance is close to OFDM. The idea of [119] is to spread data symbols over several time-frequency positions, close to the pilot symbol, in such a way, that the imaginary interference at the pilot position is canceled. The drawback is a slightly higher computational complexity because of de-spreading at the receiver. This complexity, however, can be reduced by a fast Walsh-Hadamard transform and by exploiting the limited symbol alphabet (at least at the transmitter). Another way of reducing the complexity is to combine the spreading approach with the auxiliary method, as

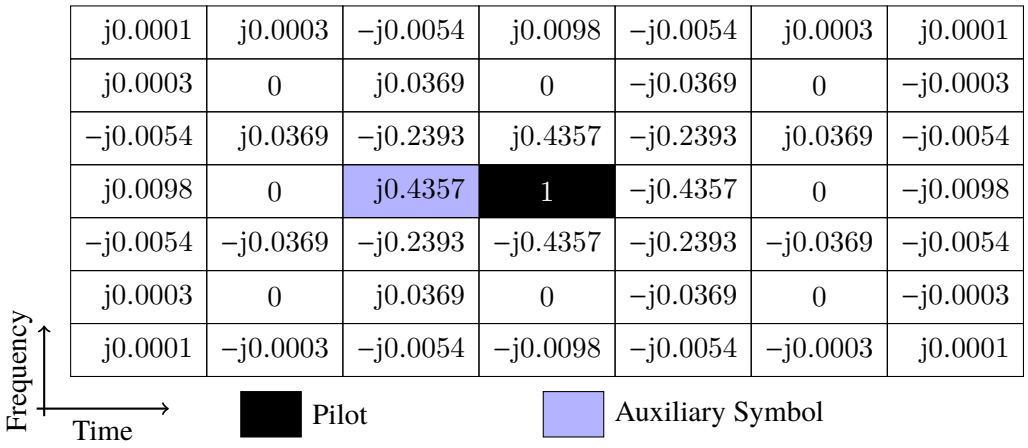

Figure 4.2. The imaginary interference weights in FBMC-OQAM (certain elements of $\bar{\mathbf{D}}$) for the Hermite prototype filter. Note that the interference weights are symmetric for the Hermite prototype filter. The auxiliary symbol is chosen so that it cancels the interference from all other neighboring symbols that affect the pilot. ©2016 IEEE, [42].

proposed in [125] (the performance becomes slightly worse because now energy is wasted). Moreover, for channels with a large delay spread and a large Doppler spread, the method in [125] seems promising because the spreading length is very short and closely spaced pilots are feasible. Note however, that also the classical spreading method performs well in doubly-selective channels [38]. In the following two sections, I will provide a detailed description of two interference cancellation techniques, namely the auxiliary symbol method and the data spreading approach.

4.2.1 Auxiliary Symbols

Figure 4.2 shows the interference weights of surrounding symbols for FBMC-OQAM (Hermite prototype filter). Those interference weights correspond to a reshaped version of an (arbitrary) row of $\bar{\mathbf{D}}$. For the most simple interference cancellation approach, one "data" symbol, the so called auxiliary symbol, is sacrificed to cancel the imaginary interference from all other symbols [117]. As indicated in Figure 4.2, the imaginary interference weight is smaller than one, here $0.4357 < 1$, implying that the auxiliary symbol power has to be increased to compensate for this loss. To be specific, the auxiliary symbol has to compensate the interference from all the surrounding symbols (excluding the auxiliary symbol), leading to a total interference power of $(1 - 0.4357^2) = 0.8102$. Additionally, the auxiliary symbol has to be multiplied by $\frac{1}{0.4357}$ to compensate for the loss caused by the interference weight. Thus, the auxiliary symbol power is $\frac{(1-0.4357^2)}{0.4357^2} = 4.27$ times higher than the data symbol power. In [42], I suggested the usage of two auxiliary symbols which split the cancellation job between

themselves, decreasing the power offset from 4.27 to $\frac{(1-2\times 0.4357^2)}{(2\times 0.4357)^2} = 0.82$. By extending this method to three and four auxiliary symbols, I am able to further decrease the power offset to 0.25 respectively 0.08. Of course, an increased number of auxiliary symbols per pilot also decreases the number of available data symbols. However, as I will show in Section 4.3.1, the saved power offsets the loss of data symbols and leads to an increased throughput for certain SNR ranges. Note that there exists two other important aspects related to the auxiliary symbol method . Firstly, the interference weight depends on the underlying prototype filter. While for the Hermite prototype filter the interference weight of the adjacent symbol in time is 0.4357, it is 0.5769 for the PHYDYAS prototype filter. Thus, the auxiliary symbol power offset for the PHDYAS filter is $\frac{(1-0.5769^2)}{0.5769^2} = 2$. Secondly, to keep the computational complexity as well as the latency low, not all interference terms are canceled. For example, if one cancels only the eight closest interferers, the power offset becomes $(3 \cdot 0.4357^2 + 4 \cdot 0.2393^2)/0.4357^2 = 4.21$, slightly less then canceling all interferers. Moreover, the residual interference leads to an interference power of $1 - (4 \cdot 0.4357^2 + 4 \cdot 0.2393^2) = 0.0116$ and thus an SIR of $19.4\,\mathrm{dB}$.

I will now utilize my matrix notation to express the cancellation condition in a more general way than suggested in [117, 118], allowing for an arbitrary number of auxiliary symbols per pilot and capturing also the interdependency of closely spaced pilot symbols (some authors, such as [126], claim that this is not possible). The imaginary interference at the pilot positions can be completely eliminated if the auxiliary symbols are chosen so that,

$$\mathbf{x}_{\mathcal{P}} = \begin{bmatrix} \bar{\mathbf{D}}_{\mathcal{P},\mathcal{P}} & \bar{\mathbf{D}}_{\mathcal{P},\mathcal{D}} & \bar{\mathbf{D}}_{\mathcal{P},\mathcal{A}} \end{bmatrix} \begin{bmatrix} \mathbf{x}_{\mathcal{P}} \\ \mathbf{x}_{\mathcal{D}} \\ \mathbf{x}_{\mathcal{A}} \end{bmatrix}, \tag{4.8}$$

which follows directly from my transmission system model in (4.6). Vector $\mathbf{x}_{\mathcal{P}} \in \mathbb{R}^{|\mathcal{P}|\times 1}$ denotes all those elements of $\mathbf{x}$ at the pilot positions. The same applies for $\mathbf{x}_{\mathcal{D}} \in \mathbb{R}^{|\mathcal{D}|\times 1}$ at the data positions and $\mathbf{x}_{\mathcal{A}} \in \mathbb{R}^{|\mathcal{A}|\times 1}$ at the auxiliary pilot positions. Similarly, matrix $\bar{\mathbf{D}}_{\mathcal{P},\mathcal{D}} \in \mathbb{C}^{|\mathcal{P}|\times|\mathcal{D}|}$ consists of those row elements and those column elements of $\bar{\mathbf{D}}$, corresponding to the pilot positions respectively data positions, that is, $\bar{\mathbf{D}}_{\mathcal{P},\mathcal{D}} = \mathbf{Q}_{\mathcal{P}}^{\mathsf{H}}\mathbf{G}_{\mathcal{D}}$. Again, the same is true for $\bar{\mathbf{D}}_{\mathcal{P},\mathcal{P}} \in \mathbb{C}^{|\mathcal{P}|\times|\mathcal{P}|}$ and $\bar{\mathbf{D}}_{\mathcal{P},\mathcal{A}} \in \mathbb{C}^{|\mathcal{P}|\times|\mathcal{A}|}$. If the number of auxiliary symbols is larger than the number of pilot symbols, that is, $|\mathcal{A}| > |\mathcal{P}|$, (4.8) has infinitely many solutions. One can then exploit this additional degree of freedom to spend as little energy as possible on auxiliary pilot symbols, leading to the following minimization problem:

$$\begin{aligned} &\underset{\mathbf{x}_{\mathcal{A}}}{\text{minimize}} \quad \|\mathbf{x}_{\mathcal{A}}\|^2 \\ &\text{subject to} \quad \bar{\mathbf{D}}_{\mathcal{P},\mathcal{A}}\,\mathbf{x}_{\mathcal{A}} = \left(\mathbf{I}_{|\mathcal{P}|} - \bar{\mathbf{D}}_{\mathcal{P},\mathcal{P}}\right)\mathbf{x}_{\mathcal{P}} - \bar{\mathbf{D}}_{\mathcal{P},\mathcal{D}}\,\mathbf{x}_{\mathcal{D}} \end{aligned}, \tag{4.9}$$

which can be solved by the Moore-Penrose pseudoinverse [116],

$$\mathbf{x}_{\mathcal{A}} = \bar{\mathbf{D}}^{\#}_{\mathcal{P},\mathcal{A}} \left(\mathbf{I}_{|\mathcal{P}|} - \bar{\mathbf{D}}_{\mathcal{P},\mathcal{P}} \right) \mathbf{x}_{\mathcal{P}} - \bar{\mathbf{D}}^{\#}_{\mathcal{P},\mathcal{A}} \bar{\mathbf{D}}_{\mathcal{P},\mathcal{D}} \mathbf{x}_{\mathcal{D}}, \tag{4.10}$$

with

$$\bar{\mathbf{D}}^{\#}_{\mathcal{P},\mathcal{A}} = \bar{\mathbf{D}}^{\mathsf{H}}_{\mathcal{P},\mathcal{A}} \left(\bar{\mathbf{D}}_{\mathcal{P},\mathcal{A}} \bar{\mathbf{D}}^{\mathsf{H}}_{\mathcal{P},\mathcal{A}} \right)^{-1}. \tag{4.11}$$

If the pilot symbols are spaced sufficiently far away from each other, $\bar{\mathbf{D}}_{\mathcal{P},\mathcal{P}}$ becomes an identity matrix, simplifying (4.10). Additionally, in case of one auxiliary symbol per pilot symbol, $\bar{\mathbf{D}}_{\mathcal{P},\mathcal{A}}$ becomes a diagonal matrix, further simplifying (4.10) and delivering the classical auxiliary symbol condition [117, 118]. Note that the auxiliary condition in (4.8) can also be expressed by a matrix according to

$$\mathbf{x} = \mathbf{C}_{\mathrm{a}} \begin{bmatrix} \mathbf{x}_{\mathcal{P}} \\ \mathbf{x}_{\mathcal{D}} \end{bmatrix}, \tag{4.12}$$

where matrix $\mathbf{C}_{\mathrm{a}} \in \mathbb{R}^{LK \times (LK - |\mathcal{A}|)}$ is mainly a one-to-one mapping of the data and pilot symbols to their corresponding positions. Only at the auxiliary symbol positions, the matrix becomes more evolved and is described by (4.10).

Let me denote the data symbol power by $P_{\mathcal{D}} = \mathbb{E}\{|x_{l,k}|^2\}$ for $(l,k) \in \mathcal{D}$, the pilot symbol power by $P_{\mathcal{P}} = \mathbb{E}\{|x_{l,k}|^2\}$ for $(l,k) \in \mathcal{P}$ and the (average) auxiliary symbol power by $P_{\mathcal{A}} = \frac{1}{|\mathcal{A}|} \operatorname{tr}\{\mathbb{E}\{\mathbf{x}_{\mathcal{A}} \mathbf{x}_{\mathcal{A}}^H\}\}$ with $\mathbf{x}_{\mathcal{A}}$ given by (4.10). The average transmitted symbol power can then be expressed by

$$P_x^{\mathrm{FBMC-OQAM}} = \frac{|\mathcal{D}|\, P_{\mathcal{D}} + |\mathcal{P}|\, P_{\mathcal{P}} + |\mathcal{A}|\, P_{\mathcal{A}}}{LK}, \tag{4.13}$$

and determines the SNR in (2.37) and (2.36).

4.2.2 Data Spreading

It is possible to spread $N_{\mathrm{s}} - 1$ data symbols over N_{s} time-frequency positions, close to the pilot, in such a way, that the imaginary interference is canceled at the pilot positions. This is illustrated in Figure 4.3. Note that only the interference from N_{s} neighboring time-frequency positions is canceled with this method, so that some residual interference remains.

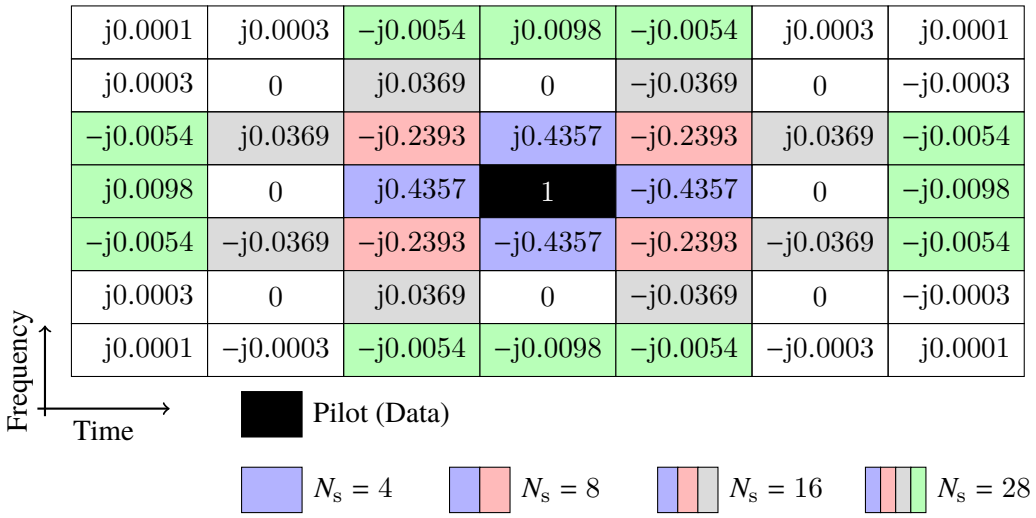

Figure 4.3. The imaginary interference weights in FBMC-OQAM (certain elements of $\bar{\mathbf{D}}$) for the Hermite prototype filter. $N_s - 1$ data symbols are spread over N_s time-frequency positions in such a way, that the imaginary interference is canceled at the pilot position. ©2016 IEEE, [42].

The data symbols $\tilde{\mathbf{x}}_{\mathcal{D}} \in \mathbb{R}^{(LK-2|\mathcal{P}|)\times 1}$ are precoded by matrix $\mathbf{C}_s \in \mathbb{R}^{LK\times(LK-|\mathcal{P}|)}$, so that the transmitted symbols $\mathbf{x}$ can be expressed as,

$$\mathbf{x} = \mathbf{C}_s \begin{bmatrix} \mathbf{x}_{\mathcal{P}} \\ \tilde{\mathbf{x}}_{\mathcal{D}} \end{bmatrix}. \tag{4.14}$$

Note that I utilize a tilde symbol to better point out that some data symbols no longer belong to a certain time-frequency position but are rather spread over several positions. Precoding matrix $\mathbf{C}_s$ must be designed so that the following two conditions are fulfilled,

$$\mathbf{Q}_{\mathcal{P}}^{\mathsf{H}} \mathbf{G} \mathbf{C}_s \begin{bmatrix} \mathbf{x}_{\mathcal{P}} \\ \tilde{\mathbf{x}}_{\mathcal{D}} \end{bmatrix} = \mathbf{x}_{\mathcal{P}} \tag{4.15}$$

$$\mathbf{C}_s^{\mathsf{T}} \mathbf{C}_s = \mathbf{I}_{LK-|\mathcal{P}|}. \tag{4.16}$$

The first condition (4.15) guarantees that the imaginary interference is canceled at the pilot positions, with $\mathbf{Q}_{\mathcal{P}} \in \mathbb{C}^{N\times|\mathcal{P}|}$ representing all column vectors of $\mathbf{Q}$ which correspond to the correct pilot positions. The second condition (4.16) implies that the received symbols can be decoded (despread) by $\mathbf{C}_s^{\mathsf{T}}$, that is,

$$\begin{bmatrix} \tilde{\mathbf{y}}_{\mathcal{P}} \\ \tilde{\mathbf{y}}_{\mathcal{D}} \end{bmatrix} = \mathbf{C}_s^{\mathsf{T}} \mathbf{y}, \tag{4.17}$$

where $\tilde{\mathbf{y}}_{\mathcal{D}}$ represents the received data symbols after despreading. Vector $\tilde{\mathbf{y}}_{\mathcal{P}}$, on the other hand, has no immediate use because the channel estimation is finished before decoding. Note that the noise statistics are the same as for the case without data spreading because of the orthogonality condition in (4.16). Furthermore, the spread data symbols no longer belong to a certain time-frequency position and are instead distributed over several time-frequency positions. This, however, only applies to data symbols close to the pilot. Data symbols farther away still belong to a certain time-frequency position, although this fact is somewhat hidden in (4.14). In doubly-selective channels, equalization might be necessary before decoding (despreading). However, in many cases, as for example in my testbed measurements, the channel is so flat in time and frequency, that the channel equalization can be performed after decoding (despreading).

In contrast to Section 4.2.1, I assume that the pilots are spaced sufficiently far away from each other, so that coding can be designed independently for different pilot positions. Thus, the challenge of finding $\mathbf{C}_{\mathrm{s}}$ can be simplified into finding a much smaller coding matrix $\widetilde{\mathbf{C}}_{\mathrm{s}} = \begin{bmatrix} \tilde{\mathbf{c}}_1 & \cdots & \tilde{\mathbf{c}}_{N_{\mathrm{s}}-1} \end{bmatrix} \in \mathbb{R}^{N_{\mathrm{s}} \times (N_{\mathrm{s}}-1)}$, which spreads $N_{\mathrm{s}} - 1$ data symbols over N_{s} time-frequency positions close to the pilot, see Figure 4.3. I follow loosely the approach suggested in [119]. The imaginary interference weights are stacked in a vector $\tilde{\mathbf{d}}_{\mathrm{I}} \in \mathbb{R}^{N_{\mathrm{s}} \times 1}$. For the i-th pilot, those weights correspond to the N_{s} largest elements (magnitude) of the i-th row of $\mathbf{Q}_{\mathcal{P}}^{\mathsf{H}}\mathbf{G}$. Furthermore, the elements with the same magnitude are clustered together, as shown in Figure 4.4. I assume M_{s} such cluster exists, each having either two, four or eight elements. By generating Hadamard matrices, dividing each row by the corresponding interference weight and canceling the column that is not orthogonal to the interference weights, I find $i = 1, 2, \ldots, N_{\mathrm{s}} - M_{\mathrm{s}}$ linearly independent coding vectors $\tilde{\mathbf{c}}_i \in \mathbb{R}^{N_{\mathrm{s}} \times 1}$ which are orthogonal to each other and to $\tilde{\mathbf{d}}_{\mathrm{I}}$. This process is illustrated in Figure 4.4. Although the authors in [119] provide general conditions for the remaining $M_{\mathrm{s}} - 1$ coding vectors, they give no detailed instructions on how to construct them. I thus propose the following algorithm:

1. Generate $j = (N_{\mathrm{s}} - M_{\mathrm{s}} + 1), (N_{\mathrm{s}} - M_{\mathrm{s}} + 2), \ldots, N_{\mathrm{s}} - 1$ vectors $\mathbf{v}_j \in \mathbb{R}^{N_{\mathrm{s}} \times 1}$ which consist of only two nonzero elements, located at the transition between two clusters, and chosen so that $\tilde{\mathbf{d}}_{\mathrm{I}}^T \mathbf{v}_j = 0$, see Figure 4.4.

2. Use Gram-Schmidt [116] orthogonalization to find the remaining $M_{\mathrm{s}} - 1$ coding vectors for $j = (N_{\mathrm{s}} - M_{\mathrm{s}} + 1), (N_{\mathrm{s}} - M_{\mathrm{s}} + 2), \ldots, N_{\mathrm{s}} - 1$:

$$\tilde{\mathbf{c}}_j = \mathbf{v}_j - \sum_{i=1}^{j-1} \frac{\mathbf{v}_j^T \tilde{\mathbf{c}}_i}{\tilde{\mathbf{c}}_i^T \tilde{\mathbf{c}}_i} \tilde{\mathbf{c}}_i. \tag{4.18}$$

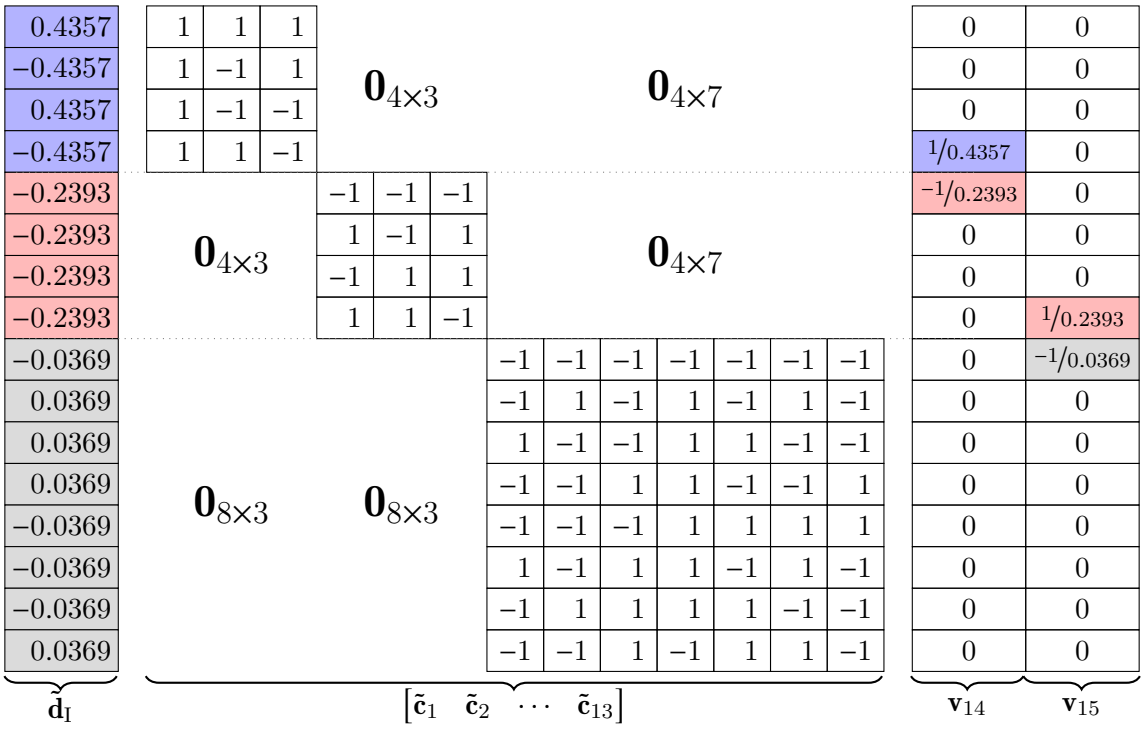

Figure 4.4. Illustration of the proposed algorithm for $N_{\mathrm{s}} = 16$ and $M_{\mathrm{s}} = 3$ clusters (indicated by the color). Vector $\tilde{\mathbf{d}}_{\mathrm{I}}$ represents the interference weights which can also be found in Figure 4.3. The key extension to [119, 125] are the vectors $\mathbf{v}_{14}$ and $\mathbf{v}_{15}$ which, in combination with Gram-Schmidt orthogonalization, allows to straightforwardly find the coding matrix $\widetilde{\mathbf{C}}_{\mathrm{s}}$. ©2016 IEEE, [42].

Note that (4.18) preserves orthogonality to the interference vector $\tilde{\mathbf{d}}_{\mathrm{I}}$, making such approach feasible. In order to keep the computational complexity low, the vectors $\mathbf{v}_j$ should combine always the clusters with the smallest number of elements for an increasing j. Once two clusters have been combined by vector $\mathbf{v}_j$, they form a new cluster. My proposed algorithm describes a general way of finding the coding matrix $\widetilde{\mathbf{C}}_{\mathrm{s}}$ and does not necessarily require orthogonal shortened "Hadamard" matrices. However, using them reduces the overall computational complexity. After normalizing each column of $\widetilde{\mathbf{C}}_{\mathrm{s}}$, the individual coding matrix $\widetilde{\mathbf{C}}_{\mathrm{s}}$ is mapped to the overall coding matrix $\mathbf{C}_{\mathrm{s}}$.

Similar as before, the average transmitted symbol power can be expressed by

$$P_x^{\mathrm{FBMC-OQAM}} = \frac{|\mathcal{D}|\, P_{\mathcal{D}} + |\mathcal{P}|\, P_{\mathcal{P}}}{LK}, \tag{4.19}$$

and determines the SNR in (2.37) and (2.36). Note, that $|\mathcal{D}| + |\mathcal{P}| = LK - |\mathcal{P}|$. Thus, a pilot power offset of $P_{\mathcal{P}}/P_{\mathcal{D}} = 2$ results in the same average transmit symbol power as for an FBMC system without channel estimation. Additionally, choosing $P_{\mathcal{P}}/P_{\mathcal{D}} = 2$ guarantees

Table 4.1. Additional computational complexity (per pilot) for the auxiliary symbol method (Aux.) and the data spreading approach (Spr.). ©2016 IEEE, [42].

	$N_\mathrm{s}=4$		$N_\mathrm{s}=8$		$N_\mathrm{s}=16$		$N_\mathrm{s}=28$	
	SIR=9 dB		**SIR=22 dB**		**SIR=35 dB**		**SIR=61 dB**	
	Spr.	Aux.	Spr.	Aux.	Spr.	Aux.	Spr.	Aux.
TX Multiplications	0	0	2	4	12	12	26	24
TX Summations	8	2	24	6	88	14	184	26
RX Multiplications	0	none	8	none	32	none	80	none
RX Summations	9	none	25	none	89	none	185	none

Note 1: Multiplications by -1 and 1/2 are considered as no complexity.
Note 2: A pilot to data power offset of $P_\mathcal{P}/P_\mathcal{D} = 2$ is assumed for the SIR calculations.
Note 3: A Hermite prototype filter is considered.

the same SNR for channel estimation (complex domain) and for data transmission (taking the real part reduces the noise power by a factor of two). This is the biggest advantage of the data spreading approach compared to the auxiliary symbol method: no energy is wasted.

4.3 Performance Evaluation

Before I compare the channel estimation methods in terms of achievable rate, measured throughput and BEP, let me investigate the computational complexity in more detail. Table 4.1 shows the additional computational complexity per pilot for a Hermite prototype filter. Multiplications are far more demanding than summations, so that the auxiliary symbol method and the data spreading approach have a similar complexity at the transmitter. However, the big disadvantage of data spreading is that it requires de-spreading at the receiver. Many papers claim that the data spreading approach is computationally very complex [120–122]. I do not agree with this assessment. For example, considering an LTE pilot pattern, see Figure 4.1, one has $|\mathcal{P}| = 8$ pilot symbols and $|\mathcal{D}| = 344$ data symbols (OQAM, no CP, $LK = 12 \times 30 = 360$). Thus, the auxiliary symbol method requires 344 multiplications for a one-tap equalizer. In contrast to that, the data spreading method requires $352 + 8 \times 32 = 608$ multiplications for an SIR of 35 dB, see Table 4.1, which is less than two times the complexity of the auxiliary symbol method. Thus the additional complexity is relatively small, in particular compared to other parts such as channel decoding. Additionally, one can combine the data spreading approach with the auxiliary symbol method, as proposed in [125], resulting in an intermediate complexity and only a small power offset. Table 4.1 also shows the SIR for a different number of considered interference terms N_s. I always consider a pilot to data power offset of $P_\mathcal{P}/P_\mathcal{D} = 2$, leading to the same SNR for channel estimation (complex

domain) and data detection (real domain), allowing a fair comparison. Many authors forget this crucial power offset, resulting in a poor BER performance.

4.3.1 Throughput

Let me start the discussion by explaining some theoretical bounds. The ergodic capacity [127] for one time-frequency position, see (3.1), is given by:

$$C_{\text{Gauss}} = \mathbb{E}_h\left\{\log_2\left(1 + |h|^2\,\text{SNR}\right)\right\}. \tag{4.20}$$

Such expression assumes Gaussian distributed data symbols, an unrealistic assumption. The data symbols are usually chosen from a fixed symbol alphabet, which is included in the Bit-Interleaved Coded Modulation (BICM) capacity [128, 129],

$$C_{\text{BICM}} = \mathbb{E}_h\left\{\max_{\mathcal{X}\in\{\tilde{\mathcal{X}}_1,\tilde{\mathcal{X}}_2,\ldots\}}\left(\log_2|\mathcal{X}| - \sum_{i=1}^{\log_2|\mathcal{X}|}\mathbb{E}_{b,y|h}\left[\log_2\frac{\sum\limits_{x\in\mathcal{X}}\text{pdf}_h(y|x)}{\sum\limits_{x\in\mathcal{X}_b^i}\text{pdf}_h(y|x)}\right]\right)\right\}, \tag{4.21}$$

where $\mathcal{X}$ is the symbol alphabet and $\mathcal{X}_b^i$ the subset of $\mathcal{X}$ whose label has the bit value $b \in \{0,1\}$ at position i. In contrast to [128], I also include an adaptive symbol alphabet $\{\tilde{\mathcal{X}}_1, \tilde{\mathcal{X}}_2, \ldots\} = \{4, 16, \ldots\}$-QAM. I could also include channel estimation in the BICM expressions [31, 130], but assuming perfect channel knowledge provides enough insights to understand the system. The achievable rate is then obtained by

$$R = \frac{|\mathcal{D}|\,C}{KT}, \tag{4.22}$$

where I account for the number of data symbols within one frame, that is, $|\mathcal{D}|$, and the frame duration, KT. The variable C can either be the true capacity, see (4.20), or the BICM capacity, see (4.21).

FBMC has a higher spectral efficiency than OFDM because of lower OOB emissions and no CP overhead. In order to validate this improvement and to show the feasibility of the channel estimation methods discussed so far, I measure an 1.4 MHz LTE like signal with the Vienna Wireless Testbed [40]. For OFDM, I assume a subcarrier spacing of $F = 15\,\text{kHz}$, $K = 14$ symbols and a CP length of 4.76 µs, resulting in a transmission time of $KT = 1\,\text{ms}$. FBMC also employs a subcarrier spacing of $F = 15\,\text{kHz}$ but uses $K = 30$ (real-valued symbols), leading to the same transmission time as OFDM, that is, $KT = 1\,\text{ms}$. Although LTE occupies 1.4 MHz, it only utilizes $L = 72$ subcarriers ($LF = 1.08\,\text{MHz}$). Because

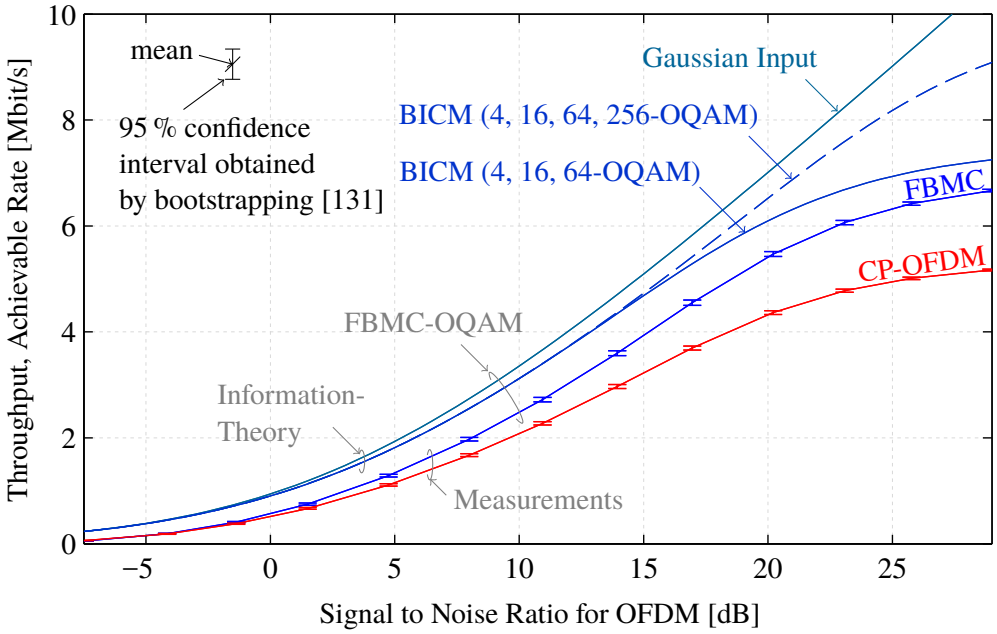

Figure 4.5. **Real-world testbed measurements** at 2.5 GHz show that FBMC has a higher throughput than OFDM (1.4 MHz LTE resembling SISO signal) because of a higher available bandwidth and no CP overhead. The channel estimation in FBMC is based on the data spreading approach. Note that the measured throughput performs close to the achievable rates based on information theory. ©2017 IEEE, [1].

of much lower OOB emissions in FBMC, I am able to increase the number of subcarriers to $L = 87$, corresponding to $LF = 1.305$ MHz and a power spectral density that is below 84 dB of its maximum value for frequencies outside the 1.4 MHz bandwidth. Note that the number of subcarriers must be a multiple of three to guarantee the same pilot density as in LTE. The pilot pattern is chosen according to the LTE standard, that is, a diamond-shaped pattern with a pilot density of $|\mathcal{P}|/(KTLF) = 0.044$, see Figure 4.1 for OFDM. In OFDM, the pilot symbol power is the same as the data symbol power, $P_{\mathcal{P}} = P_{\mathcal{D}}$, while in FBMC the pilot symbol power is increased by a factor of two, $P_{\mathcal{P}} = 2P_{\mathcal{D}}$, so that the channel estimation (complex domain) and the data transmission (real domain) experience the same SNR. I transmit my signal at a carrier frequency of 2.4955 GHz and obtain different channel realizations, corresponding to Rayleigh fading, by moving (and rotating) the receive antenna to 4096 different positions within a 4×4 wavelength grid. For the measured throughput, I use turbo coding in combination with 15 Channel Quality Indicator (CQI) values, corresponding to a specific modulation order and code rate, as defined in the LTE standard. I transmit the signal for all CQI values consecutively and choose at the receiver the highest possible

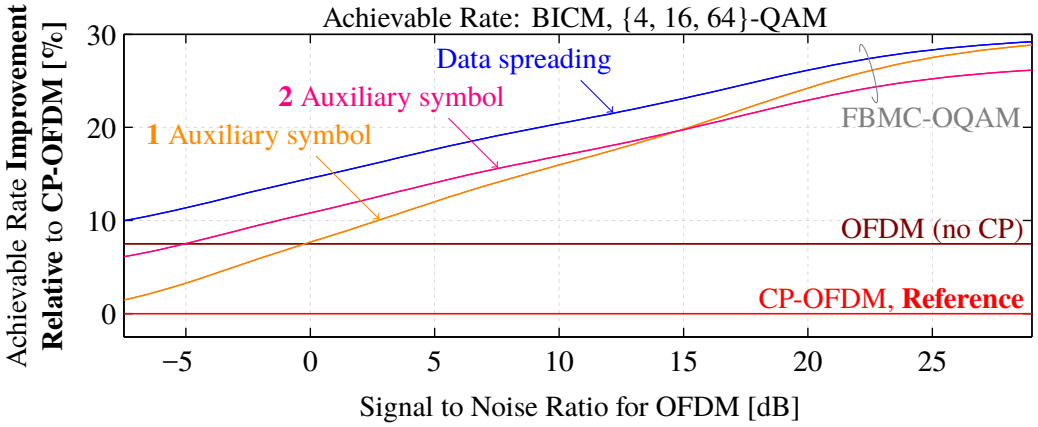

Figure 4.6. Achievable rate improvement relative to CP-OFDM. The data spreading approach shows the highest improvement because no energy is wasted. Two auxiliary symbols outperform one auxiliary symbols in low to medium SNR ranges because the power that is saved, offsets the loss in data symbols.

throughput, that is, the highest CQI value for which all data bits were detected correctly after turbo decoding.

Figure 4.5 shows the measured throughput as well as the theoretical bounds discussed so far (for Rayleigh fading). FBMC has a higher throughput than OFDM because of a higher usable bandwidth and no CP overhead. The channel estimation in Figure 4.5 is based on the data spreading approach in combination with a moving-block average interpolation, that is, all pilot estimates who are within a time-frequency range of 15 (complex-valued) time symbols and 12 subcarriers are averaged to obtain an estimate at the data position. Such interpolation method is possible because the channel is highly correlated in time and frequency. OFDM and FBMC have the same transmit power which leads to a 0.82 dB smaller SNR for FBMC compared to OFDM because the power is spread over a larger bandwidth, see (2.36). The measured throughput is only 2 dB worse than the theoretical BICM bound. Such differences can be explained by an imperfect coder, a limited code length, a limited number of code rates (I employ turbo coding [132] and 15-CQI values, same as in LTE) and channel estimation errors [133]. An important observation here is that the throughput saturates. If one increases the SNR from 0 dB to 10 dB, that is, by a factor of 10, then the throughput increases by approximately 300%. On the other hand, if the SNR is increased from 20 dB to 30 dB, also a factor of 10, the throughput only increases by 20%. Even by considering a symbol alphabet of up to 256-OQAM (BICM), the achievable rate only increases by 40%. Thus, a high SNR provides only a small throughput gain while power and hardware costs are significantly higher.

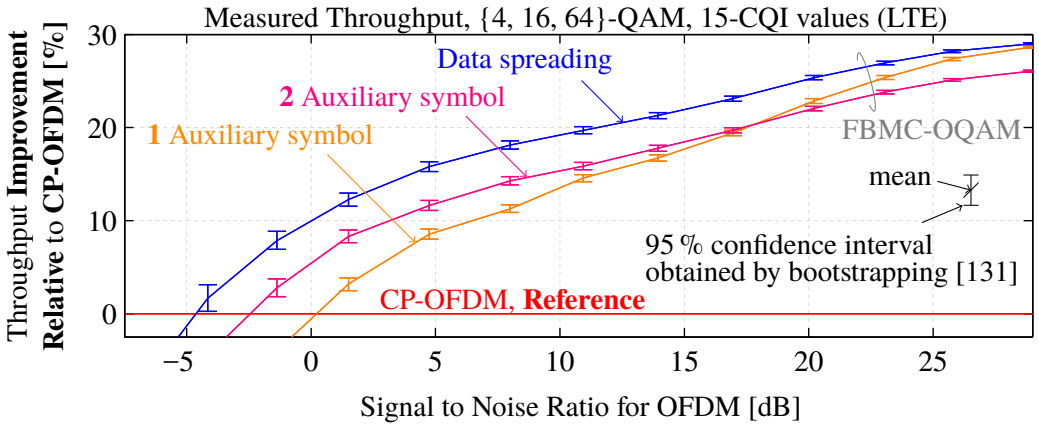

Figure 4.7. **Real-world testbed measurements** show that the throughput performs similarly as the achievable rate in Figure 4.6. Again, the data spreading approach performs best while two auxiliary symbols outperform one auxiliary symbols for low to medium SNR values. Note that only CP-OFDM is measured (the reference) but not OFDM without CP.

Figure 4.6 shows, for a doubly-flat channel, the improvement in achievable rate, see (4.21) and (4.22), relative to CP-OFDM. For example, at an SNR of 10 dB, FBMC based on data spreading has a 20% higher achievable rate than OFDM because of a higher bandwidth and no CP overhead. Overall, the data spreading approach performs best because no energy is wasted. Furthermore, two auxiliary symbols per pilot outperform one auxiliary symbol per pilot for SNR values smaller than 15 dB. To get a better understanding of Figure 4.6, let me investigate the SNR in more detail. The SNR definition in (2.36) and the average transmitted data symbol power for each method, see (4.13) and (4.19), implies that the SNR in FBMC based on data spreading is 0.82 dB smaller than in OFDM ($L_{\mathrm{OFDM}}/L_{\mathrm{FBMC}} = 72/87$). For the auxiliary method with one auxiliary symbol per pilot it is 1.22 dB (data symbol) and for two auxiliary symbols per pilot it is 0.88 dB (data symbol). Those SNR shifts are relevant for the achievable rate. In particular, FBMC has a lower SNR than OFDM but at the same time a higher bandwidth. In a low SNR regime, the received power has a relatively large impact on the achievable rate while in a high SNR regime the bandwidth is the dominant factor. This explains why the improvement of FBMC in Figure 4.6 increases with the SNR. Furthermore, it explains why two auxiliary symbols outperform one auxiliary symbol. The increased SNR of two auxiliary symbols is more important than the loss of the data symbols in low to medium SNR ranges. Note that it is also possible to employ more than two auxiliary symbols per pilot, as I have done in [40]. However, the potential improvement compared to two auxiliary symbols is relatively low. As shown in Figure 4.6, the relative improvement of OFDM without CP is constant over the SNR, because CP-OFDM and OFDM without CP have the same bandwidth and thus the same SNR.

Figure 4.7 shows the improvement of FBMC compared to OFDM for my real world throughput measurements, conducted with the Vienna Wireless Testbed. The results are similar as in Figure 4.6. Thus, the theoretical consideration based on the achievable rate accurately model the true physical behavior. Only for small SNR values, large differences can be observed because of a limited CQI in combination with the SNR shift between FBMC and OFDM. Again, data spreading performs best, while two auxiliary symbols outperform one auxiliary symbol for low to medium SNR values.

4.3.2 Bit Error Probability

In my opinion, the throughput is a more important performance metric than the uncoded BEP. Unfortunately, throughput simulations require channel coding which increases the simulation time and makes the overall evaluation relatively cumbersome. The uncoded BEP, on the other hand, can be simulated in a very simple way. Furthermore, the BEP is a more fundamental performance measure and allows an easy comparison to other papers. Thus, there are good reasons to consider the BEP, although possible effects on the throughput should be kept in mind. In Section 3.1.1, I already derived the BEP for perfect channel knowledge. In this section, I additionally include the effect of channel estimation into my BEP expressions. Although I could consider doubly-selective channels, similar as in Section 3.1.1, I assume a doubly-flat channel in order to focus on the important part, that is, the influence of channel estimation on the BEP. Note that doubly-flat fading also represents an important special case because it describes the performance for doubly-selective channels as long as the channel induced interference is dominated by noise, as already elaborated in Section 3.1.1. Furthermore, I assume a 4-QAM signal constellation in OFDM and a 2-PAM signal constellation in FBMC. Again, this simplification allows me to focus on the relevant factors. I also assume that the interpolation vector is chosen so that the following condition holds true, $\mathbf{w}_{l,k}^{\mathsf{H}}\mathbf{1}_{|\mathcal{P}|\times 1} = 1$, that is, the elements of $\mathbf{w}_{l,k}$ sum up to one. There are two main reasons for this assumption. Firstly, the interpolation should not cause any unnecessary phase rotations, so that, for doubly-flat fading, $\mathbf{w}_{l,k}^{\mathsf{H}}\mathbf{1}_{|\mathcal{P}|\times 1}$ has to be real-valued and greater than zero. Secondly, for a 4-QAM and 2-PAM signal constellation, only the phase of the estimated channel matters. The magnitude has no influence on the BEP, implying that $\mathbf{w}_{l,k}$ can be normalized by any real-valued number greater than zero. Choosing this number so that $\mathbf{w}_{l,k}^{\mathsf{H}}\mathbf{1}_{|\mathcal{P}|\times 1} = 1$ is fulfilled, allows me to express the BEP in a compact way.

The normalization of interpolation vector $\mathbf{w}_{l,k}$ and the assumption of doubly-flat fading imply that $\Im\{\mathbf{w}_{l,k}^{\mathsf{H}}\mathbf{1}_{|\mathcal{P}|\times 1}\} = \Im\{\mathbf{w}_{l,k}^{\mathsf{H}}\mathbf{r}_{\mathbf{h}_{\mathcal{P}},h_{l,k}}\} = 0$, allowing me to express the BEP in OFDM

by [34]:

$$\mathrm{BEP}_{l,k}^{\mathrm{OFDM}} = \Pr\left(\Re\left\{\frac{y_{l,k}}{\hat{h}_{l,k}}\right\} < 0 \middle| x_{l,k} = \sqrt{\frac{P_{\mathcal{D}}}{2}} + \mathrm{j}\sqrt{\frac{P_{\mathcal{D}}}{2}}\right). \tag{4.23}$$

Note that this BEP expression is similar as in Section 3.1.1 except that the perfectly known channel is now replaced with its estimate, that is, $h_{l,k} \rightarrow \hat{h}_{l,k}$. To apply Lemma 1, I need the second order statistics, which can easily be calculated by utilizing the perfect correlation property of a doubly-flat channel, $\mathbf{R}_{\mathbf{h}_{\mathcal{P}}} = \mathbf{1}_{|\mathcal{P}|\times|\mathcal{P}|}$ and $\mathbf{r}_{\mathbf{h}_{\mathcal{P}},h_{l,k}} = \mathbf{1}_{|\mathcal{P}|\times 1}$, as well as the normalization of the interpolation vector, $\mathbf{w}_{l,k}^{\mathsf{H}}\mathbf{1}_{|\mathcal{P}|\times 1} = 1$, leading to

$$\mathbb{E}\{y_{l,k}\hat{h}_{l,k}^{*}|x_{l,k}\} = x_{l,k} \tag{4.24}$$

$$\mathbb{E}\{|y_{l,k}|^2|x_{l,k}\} = |x_{l,k}|^2 + P_{\mathrm{n}} \tag{4.25}$$

$$\mathbb{E}\{|\hat{h}_{l,k}|^2\} = 1 + \|\mathbf{w}_{l,k}\|^2 \frac{P_{\mathrm{n}}}{P_{\mathcal{P}}}. \tag{4.26}$$

Finally, Lemma 1 together with (4.24)-(4.26) allows me to express the BEP in (4.23) by:

$$\mathrm{BEP}_{l,k}^{\mathrm{OFDM}} = \frac{1}{2} - \frac{1}{2\sqrt{2\left(1 + \|\mathbf{w}_{l,k}\|^2 \frac{P_{\mathrm{n}}}{P_{\mathcal{P}}}\right)\left(1 + \frac{P_{\mathrm{n}}}{P_{\mathcal{D}}}\right) - 1}}. \tag{4.27}$$

Besides data symbol power $P_{\mathcal{D}}$, pilot symbol power $P_{\mathcal{P}}$ and noise power P_{n}, the BEP also depends on the squared norm of the interpolation vector, given for nearest neighbor interpolation by $\|\mathbf{w}_{l,k}\|^2 = 1$ and for MMSE interpolation (doubly-flat fading) by $\|\mathbf{w}_{l,k}\|^2 = \frac{1}{|P|}$. In general, however, $\|\mathbf{w}_{l,k}\|^2$ depends on a specific time-frequency position, for example, linear interpolation (straight line) leads to $\|\mathbf{w}_{l,k}\|^2 < 1$, while linear extrapolation to $\|\mathbf{w}_{l,k}\|^2 > 1$. Note that the interpolation vector is normalized by $\mathbf{w}_{l,k}^{\mathsf{H}}\mathbf{1}_{|\mathcal{P}|\times 1} = 1$, so that $\mathbf{w}_{l,k}$ cannot take any arbitrary values. To be specific, $\|\mathbf{w}_{l,k}\|^2$ is lower bounded by $\|\mathbf{w}_{l,k}\|^2 \geq \frac{1}{|P|}$, where equality holds for the MMSE interpolation. Thus, MMSE interpolation delivers also the minimum BEP in (4.27). Note that this is not only true for a doubly-flat channel, but also for a doubly-selective channel (interference is treated as Gaussian noise), as I have shown in [34] by utilizing the generalized Rayleigh quotient.

In contrast to OFDM, the BEP in FBMC depends on all other symbols because of the imaginary interference. One can model the influence of the imaginary interference by a pseudo symbol $x'_{l,k}$, which not only includes the data symbol, but also the imaginary interference, as described in (4.6). Together with the law of total probability and auxiliary precoding matrix $\mathbf{C}_{\mathrm{a}}$, see (4.12), the BEP for FBMC in case of channel estimation based on

auxiliary symbols can be expressed by:

$$\mathrm{BEP}_{l,k}^{\mathrm{Aux.}} = \frac{1}{2^{|\mathcal{D}||\mathcal{P}|}} \sum_{\mathbf{x}_{\mathcal{D}} \in |\mathcal{X}|^{\mathcal{D}}} \sum_{\mathbf{x}_{\mathcal{P}} \in \mathcal{X}^{|\mathcal{P}|}} \Pr\left(\Re\left\{ \frac{y_{l,k}}{\hat{h}_{l,k}} \right\} < 0 \middle| x'_{l,k} = \sqrt{P_{\mathcal{D}}} + \mathrm{j}\, \Im\{\mathbf{q}_{l,k}^{\mathsf{H}} \mathbf{G}\} \mathbf{C}_{\mathrm{a}} \begin{bmatrix} \mathbf{x}_{\mathcal{P}} \\ \mathbf{x}_{\mathcal{D}} \end{bmatrix} \right). \tag{4.28}$$

A simple evaluation of (4.28) is computationally very challenging. However, because only a few symbols close to $x_{l,k}$ have a significant contribution to the BEP, it is possible to reduce the computational complexity by including only those closest symbols in the evaluation. Another method to reduce the computational complexity is a Monte Carlo evaluation, which I will use later for my numerical examples. Similar as in OFDM, I need the second order statistics to apply Lemma 1, which can be found by:

$$\mathbb{E}\{y_{l,k} \hat{h}_{l,k}^{*} | \mathbf{x}\} = x'_{l,k} + \mathbf{r}^{H}_{\mathbf{n}_{\mathcal{P}}, n_{l,k}} \mathrm{diag}(\mathbf{x}_{\mathcal{P}})^{-1} \mathbf{w}_{l,k} \tag{4.29}$$

$$\mathbb{E}\{|y_{l,k}|^2 | \mathbf{x}\} = |x'_{l,k}|^2 + P_{\mathrm{n}} \tag{4.30}$$

$$\mathbb{E}\{|\hat{h}_{l,k}|^2\} = 1 + \|\mathbf{w}_{l,k}\|^2 \frac{P_{\mathrm{n}}}{P_{\mathcal{P}}}. \tag{4.31}$$

Compared to OFDM, see (4.24)-(4.26), the only differences are the pseudo symbol, which includes the imaginary interference, and the correlation of the noise in (4.29). Applying Lemma 1 in (4.28), delivers immediately the desired BEP for FBMC. However, the exact closed-form solution is quite lengthy and does not provide any additional insights, so that I omit it at this point. Instead, I consider an approximation based on the following two assumptions. Firstly, the "random" imaginary interference, $\mathrm{j}\, \Im\{\mathbf{q}_{l,k}^{\mathsf{H}} \mathbf{G}\} \mathbf{C}_{\mathrm{a}} [\mathbf{x}_{\mathcal{P}} \;\; \mathbf{x}_{\mathcal{D}}]^{\mathsf{T}}$ is replaced by a fixed value of $\mathrm{j}\sqrt{P_{\mathcal{D}}}$. Secondly, the noise in (4.29) is uncorrelated. With those two assumptions, the BEP in (4.28) is well approximated by

$$\mathrm{BEP}_{l,k}^{\mathrm{Aux.,approx}} \approx \frac{1}{2} - \frac{1}{2\sqrt{2\left(1 + \frac{P_{\mathrm{n}}}{P_{\mathcal{P}}} \|\mathbf{w}_{l,k}\|^2\right)\left(1 + \frac{P_{\mathrm{n}}}{2P_{\mathcal{D}}}\right) - 1}}. \tag{4.32}$$

The only difference to the exact solution for OFDM, see (4.27), is the additional factor of two inside the right bracket. However, FBMC uses different data and pilot symbol powers when compared to OFDM. In particular, the data symbol power in FBMC (without channel estimation) is usually two times lower than that for OFDM. This implies that the BEP approximation for FBMC is the same as the exact solution for OFDM. However, auxiliary symbols are "wasted" energy, so that the approximated BEP in FBMC becomes slightly worse than the BEP for OFDM, that is, $\mathrm{BEP}_{l,k}^{\mathrm{Aux.,approx}} > \mathrm{BEP}_{l,k}^{\mathrm{OFDM}}$ (for all possible l, k, assuming the same interpolation method $\mathbf{w}_{l,k}$).

The calculation of the BEP for the data spreading approach works in a similar way as for the auxiliary method, but the received symbols in (4.28) have to be replaced by the decoded symbols from (4.17), that is, $y_{l,k} \rightarrow \tilde{y}_i$. Those decoded symbols, in general, no longer belong to a certain time-frequency position and are instead spread over several time-frequency positions, so that I replace the index (l, k) by i. Still, from a conceptional point of view nothing changes in the derivation of the BEP compared to the auxiliary method. Thus, I omit the derivation at this point and instead refer to my paper in [41]. Similar to the auxiliary method, one can find an approximation of the BEP which turns out to be exactly the same as in (4.32), except that the interpolation vector might be differently because of the spreading. Compared to the auxiliary method, however, no energy is wasted, so that, for a comparable interpolation method, $\mathrm{BEP}_{l,k}^{\mathrm{Spr.,approx}} = \mathrm{BEP}_{l,k}^{\mathrm{OFDM}} < \mathrm{BEP}_{l,k}^{\mathrm{Aux.,approx}}$ (for all possible l, k).

From the results so far, I identify three differences between OFDM and FBMC for the BEP in doubly-flat fading:

1. For OFDM, the imaginary part of the conditioned data symbol in the BEP expression is fixed and given by $\mathrm{j}\sqrt{\frac{P_{\mathcal{D}}}{2}}$, see (4.23), while for FBMC the imaginary part depends on the neighboring data symbols, that is, $\mathrm{j}\,\Im\{\mathbf{q}_{l,k}^{\mathsf{H}}\mathbf{G}\}\mathbf{C}_{\mathrm{a}}\,[\mathbf{x}_{\mathcal{P}}\ \ \mathbf{x}_{\mathcal{D}}]^{\mathsf{T}}$, and is thus a random variable, see (4.28).

2. The noise in FBMC is correlated, at least for symbols close to the pilots, see (4.29).

3. In the auxiliary symbol method (but not for the data spreading method), the data symbol power is lower than in OFDM, because auxiliary symbols are "wasted" energy.

In particular, the first point is interesting. It implies that, if the imaginary part in FBMC is relatively low, that is, $\mathrm{j}\,\Im\{\mathbf{q}_{l,k}^{\mathsf{H}}\mathbf{G}\}\mathbf{C}_{\mathrm{a}}\,[\mathbf{x}_{\mathcal{P}}\ \ \mathbf{x}_{\mathcal{D}}]^{\mathsf{T}} << \mathrm{j}\sqrt{P_{\mathcal{D}}}$, the BEP in FBMC is better than in OFDM because phase errors of the estimated channel have less impact on the BEP (ignoring any power offsets). On the other hand, if the imaginary interference is larger, any phase errors of the estimated channel will be amplified. Thus there are two opposite effects which influence the BEP in FBMC. A priori, it is not clear which of those effects is dominant. Let me therefore consider a numerical example for which I assume an LTE like pilot pattern, that is, eight pilot symbols within $TK = 1\,\mathrm{ms}$ and $FL = 180\,\mathrm{kHz}$, as illustrated in Figure 4.1 for CP-OFDM. Figure 4.8 shows how the BEP depends on the SNR. Overall there are only minor differences between OFDM and FBMC and the underlying interpolation method has a much greater influence. Still, a few small differences can be observed. Firstly, FBMC based on data spreading performs better than OFDM. Thus, the random imaginary interference in the BEP expression, $\mathrm{j}\,\Im\{\mathbf{q}_{l,k}^{\mathsf{H}}\mathbf{G}\}\mathbf{C}_{\mathrm{s}}\,[\mathbf{x}_{\mathcal{P}}\ \ \mathbf{x}_{\mathcal{D}}]^{\mathsf{T}}$, turns out to be advantageous compared to the fixed term in OFDM, $\mathrm{j}\sqrt{P_{\mathcal{D}}/2}$. However, the possible improvement in terms of BEP is

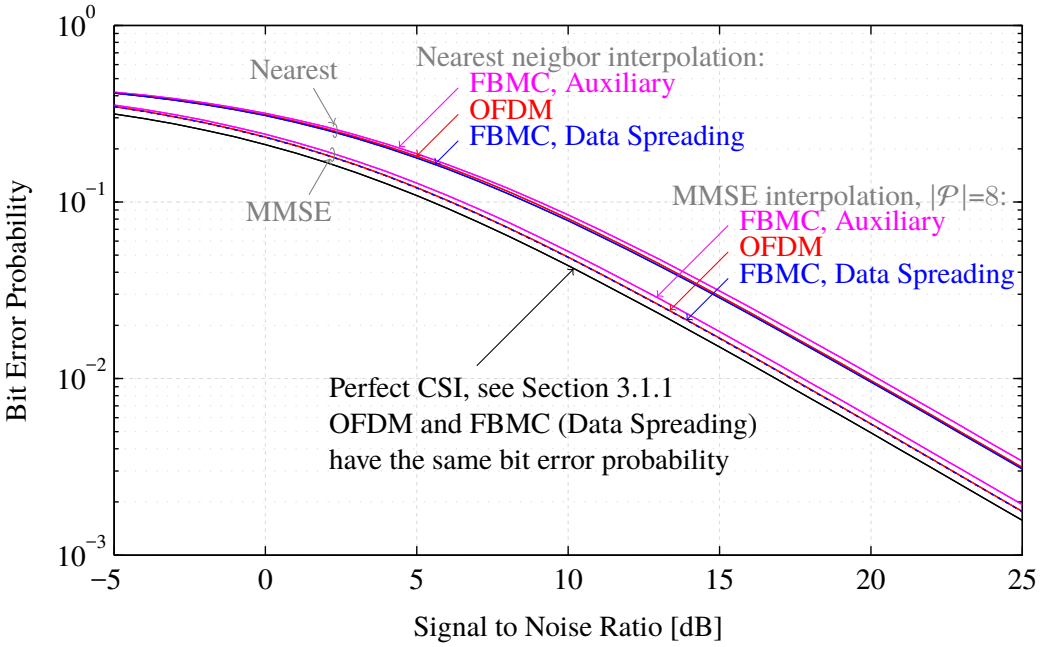

Figure 4.8. The BEP depends strongly on the channel estimation method, while the differences between FBMC and OFDM are very small. In contrast to many other papers, the auxiliary method shows a relatively good performance because the auxiliary symbol power is not only taken from the pilot, but also from the data symbols. ©2016 IEEE, [41].

less than 3% for nearest neighbor interpolation and less then 0.5 % for MMSE interpolation. The better the channel estimation, the closer are the BEP for FBMC and OFDM. In the limit of perfect channel knowledge, both BEP expressions are equal, as already investigated in Section 3.1.1. Note that the approximated BEP in FBMC, see (4.32), is the same as in OFDM, so that the reported differences between OFDM and FBMC (data spreading) also represent the approximation error. The second observation relates to FBMC based on auxiliary symbols. In principle, one has the same effect as for the data spreading approach, that is, the random imaginary interference term $\mathrm{j}\,\Im\{\mathbf{q}_{l,k}^{\mathsf{H}}\mathbf{G}\}\mathbf{C}_{\mathrm{a}}\,[\mathbf{x}_{\mathcal{P}}\ \ \mathbf{x}_{\mathcal{D}}]^{\mathsf{T}}$ is advantageous compared to the fixed term of OFDM. However, auxiliary symbols represent wasted energy, reducing the available power for the data symbols and the pilot symbols, so that the BEP for FBMC becomes worse than in OFDM. To be specific, for an MMSE interpolation, the BEP in FBMC is approximately 10 % worse than in OFDM and 9 % for a nearest neighbor interpolation. Of course, those differences also depend on the pilot density. If the pilot density is very low, the BEP for the auxiliary method will approach the BEP of the data spreading approach because the wasted energy becomes very small. My results indicate that the differences between FBMC (auxiliary symbols) and OFDM are relatively small. However, other papers report huge differences of approximately 100 % [120, 121]. Such poor

behavior can be explained by a reduced pilot symbol power because those papers assume that the additional auxiliary symbol power is solely taken from the pilots. I, on the other hand, assume that the additional auxiliary symbol power is equally taken from pilot symbols and data symbols, where the pilot-to-data power offset is two, leading to the same SNR for data transmission (real domain) and channel estimation (complex domain). Reducing the pilot symbol power below the data symbol power, as done in [120, 121], is quite problematic. To get a better understanding of this fact, let me consider the BEP expression in (4.27) for OFDM in case of nearest neighbor interpolation, $\|\mathbf{w}_{l,k}\|^2 = 1$. Then, the pilot symbol power has the same influence on the BEP as the data symbol power. However, there are usually much more data symbols than pilot symbols. Thus, it makes sense to slightly reduce the data symbol power and to distribute the available power to the pilot symbols. This increases the pilot symbol power significantly and is exactly the opposite of what authors in [120, 121] are doing. Let me formally derive an optimal pilot-to-data power offset which I define as

$$\kappa = \frac{P_{\mathcal{P}}}{P_{\mathcal{D}}}. \tag{4.33}$$

Inserting κ into (4.27) leads to the following minimization problem for OFDM:

$$\kappa_{\text{opt}}^{\text{OFDM}} = \arg\min_{\kappa} \left\{ \text{BEP}_{l,k}^{\text{OFDM}} \right\} \tag{4.34}$$

$$= \arg\min_{\kappa} \left\{ \frac{1}{2} - \frac{1}{2\sqrt{2\left(1 + \frac{\epsilon_{\mathcal{D}} + \epsilon_{\mathcal{P}}\kappa}{\text{SNR}\,\kappa}\|\mathbf{w}_{l,k}\|^2\right)\left(1 + \frac{\epsilon_{\mathcal{D}} + \epsilon_{\mathcal{P}}\kappa}{\text{SNR}}\right) - 1}} \right\} \tag{4.35}$$

$$= \sqrt{\frac{\epsilon_{\mathcal{D}}}{\epsilon_{\mathcal{P}}} \frac{\left(\frac{\epsilon_{\mathcal{D}}}{\text{SNR}} + 1\right)}{\left(\frac{\epsilon_{\mathcal{P}}}{\text{SNR}} + \frac{1}{\|\mathbf{w}_{l,k}\|^2}\right)}}. \tag{4.36}$$

Equation (4.35) can easily be solved by setting the first derivative to zero and solving with respect to κ. The optimal pilot-to-data power offset for OFDM depends on data symbol density $\epsilon_{\mathcal{D}} = \frac{|\mathcal{D}|}{KL}$, pilot symbol density $\epsilon_{\mathcal{P}} = \frac{|\mathcal{P}|}{KL}$, interpolation vector $\mathbf{w}_{l,k}$ and the SNR, as defined in Table 4.2. For the practical relevant case of $|\mathcal{D}| \geq |\mathcal{P}|$ and $\|\mathbf{w}_{l,k}\|^2 \leq 1$, the optimal pilot-to-data power offset is bounded by:

$$\sqrt{\frac{|\mathcal{D}|}{|\mathcal{P}|}\|\mathbf{w}_{l,k}\|^2} \leq \kappa_{\text{opt}}^{\text{OFDM}} \leq \frac{|\mathcal{D}|}{|\mathcal{P}|}, \tag{4.37}$$

which follows directly from SNR $\to \infty$ (left) and SNR $\to 0$ (right). Note that the SNR is often high enough so that the left part of (4.37) provides an accurate approximation of the

Table 4.2. Optimal (minimizes the BEP) pilot-to-data power offset κ_{opt}.

	OFDM	FBMC, Auxiliary	FBMC, Spreading
	$\epsilon_{\mathcal{D}} + \epsilon_{\mathcal{P}} = 1$	$\epsilon_{\mathcal{D}} + \epsilon_{\mathcal{P}} + \epsilon_{\mathcal{A}} = 1$	$\epsilon_{\mathcal{D}} + \epsilon_{\mathcal{P}} = 1 - \epsilon_{\mathcal{P}}$
SNR	$\frac{\lvert\mathcal{D}\rvert P_{\mathcal{D}} + \lvert\mathcal{P}\rvert P_{\mathcal{P}}}{LKP_{\text{n}}}$	$\frac{\lvert\mathcal{D}\rvert P_{\mathcal{D}} + \lvert\mathcal{P}\rvert P_{\mathcal{P}} + \lvert\mathcal{A}\rvert P_{\mathcal{A}}}{LK\frac{P_{\text{n}}}{2}}$	$\frac{\lvert\mathcal{D}\rvert P_{\mathcal{D}} + \lvert\mathcal{P}\rvert P_{\mathcal{P}}}{LK\frac{P_{\text{n}}}{2}}$
$\kappa_{\text{opt}} = \frac{P_{\mathcal{P}}}{P_{\mathcal{D}}}$	$\sqrt{\frac{\epsilon_{\mathcal{D}}}{\epsilon_{\mathcal{P}}} \frac{\left(\frac{\epsilon_{\mathcal{D}}}{\text{SNR}} + 1\right)}{\left(\frac{\epsilon_{\mathcal{P}}}{\text{SNR}} + \frac{1}{\lVert\mathbf{w}_{l,k}\rVert^2}\right)}}$	$\sqrt{\frac{\tilde{\epsilon}_{\mathcal{D}\mathcal{A}}}{\epsilon_{\mathcal{P}}} \frac{\left(\frac{\tilde{\epsilon}_{\mathcal{D}\mathcal{A}}}{\text{SNR}} + 1\right)}{\left(\frac{\epsilon_{\mathcal{P}}}{\text{SNR}} + \frac{1}{2\lVert\mathbf{w}_{l,k}\rVert^2}\right)}}$	$\sqrt{\frac{\epsilon_{\mathcal{D}}}{\epsilon_{\mathcal{P}}} \frac{\left(\frac{\epsilon_{\mathcal{D}}}{\text{SNR}} + 1\right)}{\left(\frac{\epsilon_{\mathcal{P}}}{\text{SNR}} + \frac{1}{2\lVert\mathbf{w}_{l,k}\rVert^2}\right)}}$

$$\epsilon_{\mathcal{D}} = \frac{\lvert\mathcal{D}\rvert}{KL}; \quad \epsilon_{\mathcal{P}} = \frac{\lvert\mathcal{P}\rvert}{KL}; \quad \epsilon_{\mathcal{A}} = \frac{\lvert\mathcal{A}\rvert}{KL}; \quad \tilde{\epsilon}_{\mathcal{D}\mathcal{A}} = \epsilon_{\mathcal{D}} + \bar{\kappa}_{\mathcal{A}\mathcal{D}}\,\epsilon_{\mathcal{A}}; \quad \bar{\kappa}_{\mathcal{A}\mathcal{D}} = \frac{P_{\mathcal{A}}}{P_{\mathcal{D}}}$$

Nearest neighbor: $\lVert\mathbf{w}_{l,k}\rVert^2 = 1$; MMSE: $\lVert\mathbf{w}_{l,k}\rVert^2 = \frac{1}{\lvert\mathcal{P}\rvert}$

optimal pilot-to-data power offset. For example, an LTE pilot pattern ($\lvert\mathcal{D}\rvert = 180 - 8 = 172$, $\lvert\mathcal{P}\rvert = 8$) leads to an optimal pilot-to-data power offset of 4.6 for nearest neighbor interpolation. Such power offset improves the BEP by approximately 30% which is equivalent to an SNR shift of 1.5 dB (for the same BEP). For an MMSE interpolation ($\lVert\mathbf{w}_{l,k}\rVert^2 = 1/8$), the optimal pilot-to-data power offset is 1.6. However, the possible improvement is only 2%, equivalent to an SNR shift of 0.07 dB.

In a similar way, one can also find the optimal pilot-to-data power offset for FBMC. However, instead of using the exact BEP solution, I utilize the approximation in (4.32) which is possible because the approximation error is relatively small. Table 4.2 shows the optimal pilot-to-data power offset. Note that the optimal pilot-to-data power offset is very similar to OFDM. In particular, for the data spreading approach, the optimal pilot-to-data power offset is exactly two times larger than in OFDM, that is, $\kappa_{\text{opt}}^{\text{FBMC,Spr.}} = 2\,\kappa_{\text{opt}}^{\text{OFDM}}$ (for comparable parameters). This can easily be checked in Table 4.2, where one has to keep in mind that $\lvert\mathcal{D}\rvert$ and K are two times higher in FBMC compared with OFDM because of the reduced time spacing.

4.4 Doubly-Selective Channel Estimation

So far, I mainly focused on scenarios with a low delay spread and a low Doppler spread because they are much more important in practice, as already discussed in Section 3.1. Yet, a lot of academic research is focused on highly double-selective channels because of its challenging nature, allowing to come up with innovative solutions. In this section, I also propose a doubly-selective channel estimation technique which, in contrast to most other proposed solutions, does not require clustered pilots and is thus complaint with the

LTE standard. However, I want to emphasize that I do not think that doubly-selective channel estimation and equalization are, in general, worth the effort. Note that the available literature about doubly-selective channel estimation in FBMC is very limited so that almost all references within this section refer to OFDM.

I employ the same system model as in Section 3.2, where the input-output relation can be described as

$$\mathbf{y} = \mathbf{D}\,\mathbf{x} + \mathbf{n}, \tag{4.38}$$

with transmission matrix $\mathbf{D}$ given by

$$\mathbf{D} = \mathbf{Q}^{\mathsf{H}}\,\mathbf{H}\,\mathbf{G}. \tag{4.39}$$

Most papers try to estimate the channel impulse response, that is, $\hat{\mathbf{H}}$. However, estimating the impulse response is quite problematic because in practical systems, the number of active subcarriers is always lower than the FFT size, that is $L < N_{\mathrm{FFT}}$. This implies that the channel transfer function at the zero subcarriers cannot be accurately estimated, preventing also an accurate estimation of the impulse response. By applying an inverse Fourier transform onto the channel transfer function of the L active subcarriers, one only obtains a pseudo impulse response, implicitly assuming a rectangular filter. In particular, the delay taps of the pseudo impulse response are no longer limited in time (within the symbol duration), even though the true impulse response might be. This is caused by the discontinuity of the channel transfer function at the edge subcarriers and becomes problematic for estimation methods which rely on the assumption that the delay taps are limited in time. Another aspect is the computational complexity. Even if one is able to accurately estimate the impulse response, the matrix multiplication in (4.39) still has to be evaluated, implying a huge computational burden. All those drawbacks can be avoided by directly estimating the transmission matrix, that is, $\hat{\mathbf{D}}$. To some extend, this is already happening in practical systems as the one-tap channel is usually estimated through interpolation, see Figure 4.1. Those one-tap channel coefficients correspond to the diagonal elements of $\hat{\mathbf{D}}$.

A recent method for doubly-selective channel estimation is based on compressed sensing [134], where the authors claim that conventional methods do not exploit the sparse nature of wireless channels. I do not completely agree with this statement because an MMSE channel estimation already exploits sparsity in the form of time-frequency correlation of the channel. Of course, the power delay profile and the Doppler spectral density must be known or accurately estimated for such estimation to work. Authors in [135] and [136] investigated MMSE channel estimation but considered only one OFDM symbol in time which requires

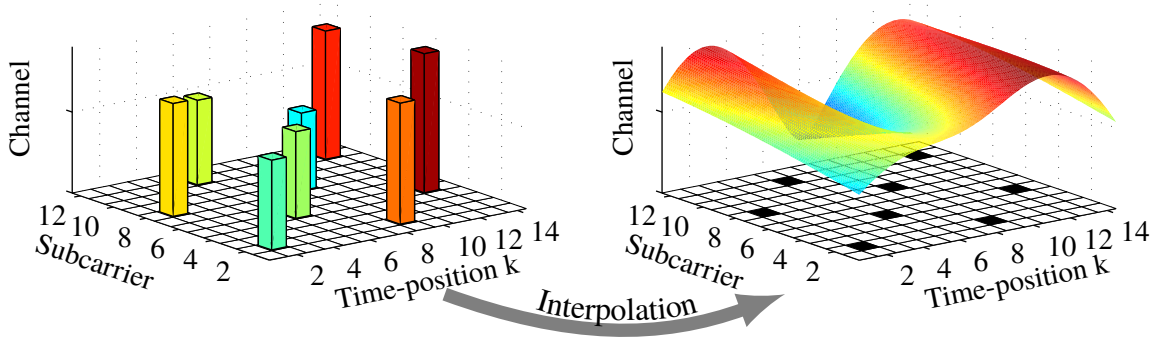

Figure 4.9. The LS channel estimates at the pilot positions are interpolated to estimate the time-variant transfer function. Note that FBMC transmission matrix $\mathbf{D}$ can be directly estimated without the detour of the time-variant transfer function.

clustered pilots. Many other authors employ a basis expansion model [137, 138] to estimate doubly-selective channels. Here, the time variation is modeled by a basis expansion, for example, an exponential basis [139], a polynomial basis [140], a Slepian basis [141] or an MMSE interpolation basis [142]. The main argument for a basis expansion model is that, estimating all $(LK)^2$ elements of $\hat{\mathbf{D}}$, out of just $|\mathcal{P}|$ pilot symbols, is very challenging, so that the number of unknown variables should be reduced. I do not completely agree with this assessment. Estimating all elements of $\hat{\mathbf{D}}$ can easily be achieved by exploiting the time-frequency correlation of the channel. This becomes especially useful if not only one OFDM/FBMC symbol is considered, as most other authors do, but several symbols in time jointly, that is, $K > 1$. The main idea is illustrated in Figure 4.9. The "sampled" time-variant transfer function (at the pilot positions) is interpolated, delivering an accurate estimate of the full time-variant transfer function. This is possible because of a high correlation in time and frequency. Compared to the conventional channel interpolation, see Figure 4.1, one not only estimates the one-tap channel, but rather interpolates the whole transfer function and thus includes the time-frequency variations within one symbol. Of course, it is computationally more efficient to directly estimate $\hat{\mathbf{D}}$ without the detour of the channel transfer function, whereby the underlying correlation is preserved. One element of transmission matrix $\hat{\mathbf{D}}$, at row position $\overline{l_1 k_1} = l_1 + L(k_1 - 1)$ and column position $\overline{l_2 k_2} = l_2 + L(k_2 - 1)$, can be estimated by

$$[\hat{\mathbf{D}}]_{\overline{l_1 k_1}, \overline{l_2 k_2}} = \tilde{\mathbf{w}}^{\mathsf{H}}_{l_1,k_1,l_2,k_2} \hat{\mathbf{h}}^{\mathrm{LS}}_{\mathcal{P}}, \tag{4.40}$$

where $\tilde{\mathbf{w}}_{l_1,k_1,l_2,k_2} \in \mathbb{C}^{|\mathcal{P}|\times 1}$ represents a weighting vector and $\hat{\mathbf{h}}^{\mathrm{LS}}_{\mathcal{P}} \in \mathbb{C}^{|\mathcal{P}|\times 1}$ the LS channel estimates at the pilot positions, see (4.3). In contrast to Section 4.1, I not only estimate the

one-tap channel coefficients, that is, the diagonal elements, $[\hat{\mathbf{D}}]_{\overline{lk},\overline{lk}} = \hat{h}_{l,k}$, but rather the whole transmission matrix, including the off-diagonal elements. Note that, for $l = l_1 = l_2$ and $k = k_1 = k_2$, the weighting vector in (4.40) is the same as the interpolation vector in (4.2), that is, $\tilde{\mathbf{w}}_{l,k,l,k} = \mathbf{w}_{l,k}$. Equation (4.40) can also be written as

$$\hat{\mathbf{D}} = \sum_{i=1}^{|P|} \mathbf{\Theta}_i \, \hat{h}^{\mathrm{LS}}_{\mathcal{P}_i}, \tag{4.41}$$

where $\mathbf{\Theta}_i \in \mathbb{C}^{LK \times LK}$ represents a weighting matrix for which the $\overline{l_1 k_1}$-th row and $\overline{l_2 k_2}$-th column element is given by the i-th element of $\tilde{\mathbf{w}}^{\mathsf{H}}_{l_1,k_1,l_2,k_2}$. Note that $\mathbf{\Theta}_i$ is a sparse matrix. For example, in case of an FBMC design based on a Hermite prototype filter, each row of $\mathbf{\Theta}_i$ only has nine relevant elements, see Figure 3.10, leading to a matrix density of $\frac{9}{LK} << 1$. Thus, the computational complexity of my channel estimation method is relatively very low. One only has to multiply $|\mathcal{P}|$ sparse matrices with a scalar followed by $|\mathcal{P}| - 1$ sparse matrix summations.

The interpolation method has a major influence on the estimation accuracy. Authors in [143] interpolate the estimated impulse responses of several OFDM symbols linearly, whereas the authors in [144] utilize a LS polynomial fitting and the authors in [145] a LS discrete prolate spheroidal fitting. I, on the other hand, employ an MMSE interpolation which is the best possible channel estimation method in terms of minimum Mean Squared Error (MSE). By utilizing the orthogonal projection theorem, the MMSE weighting vector in (4.40) can be calculated by

$$\tilde{\mathbf{w}}^{\mathrm{LMMSE}}_{l_1,k_1,l_2,k_2} = \mathbf{R}^{-1}_{\hat{\mathbf{h}}^{\mathrm{LS}}_{\mathcal{P}}} \mathbf{r}_{\hat{\mathbf{h}}^{\mathrm{LS}}_{\mathcal{P}},[\mathbf{D}]_{\overline{l_1 k_1},\overline{l_2 k_2}}}, \tag{4.42}$$

with $\mathbf{R}_{\hat{\mathbf{h}}^{\mathrm{LS}}_{\mathcal{P}}} \in \mathbb{C}^{|\mathcal{P}| \times |\mathcal{P}|}$ denoting the correlation matrix of the LS estimates at the pilot positions and $\mathbf{r}_{\hat{\mathbf{h}}^{\mathrm{LS}}_{\mathcal{P}},[\mathbf{D}]_{\overline{l_1 k_1},\overline{l_2 k_2}}} \in \mathbb{C}^{|\mathcal{P}| \times 1}$ the correlation vector between the LS channel estimates at the pilot positions and one element of transmission matrix $\mathbf{D}$. Very often, the biggest challenge is to find the required correlation matrices. Thanks to my superior matrix notation, however, finding those matrices becomes a trivial task. The correlation between the LS channel estimates at the pilot positions can be calculated by

$$\mathbf{R}_{\hat{h}^{\mathrm{LS}}_{\mathcal{P}_i}} = \frac{1}{P_{\mathcal{P}}} \mathrm{tr}\left\{ \left(\mathbf{C}_{\mathrm{a}}^{\mathsf{T}} \mathbf{G}^{\mathsf{T}} \otimes \mathbf{q}^{\mathsf{H}}_{\mathcal{P}_i} \right) \mathbf{R}_{\mathrm{vec}\{\mathbf{H}\}} \left(\mathbf{C}_{\mathrm{a}}^{\mathsf{T}} \mathbf{G}^{\mathsf{T}} \otimes \mathbf{q}^{\mathsf{H}}_{\mathcal{P}_i} \right)^{\mathsf{H}} \right\} + \frac{P_{\mathrm{n}}}{P_{\mathcal{P}}} \mathbf{q}^{\mathsf{H}}_{\mathcal{P}_i} \mathbf{q}_{\mathcal{P}_i}. \tag{4.43}$$

$$\mathbf{R}_{\hat{h}^{\mathrm{LS}}_{\mathcal{P}_i},\hat{h}^{\mathrm{LS}}_{\mathcal{P}_j}} = \left(\mathbf{g}^{\mathsf{T}}_{\mathcal{P}_i} \otimes \mathbf{q}^{\mathsf{H}}_{\mathcal{P}_i} \right) \mathbf{R}_{\mathrm{vec}\{\mathbf{H}\}} \left(\mathbf{g}^{\mathsf{T}}_{\mathcal{P}_j} \otimes \mathbf{q}^{\mathsf{H}}_{\mathcal{P}_j} \right)^{\mathsf{H}} \quad \text{for} \quad i \neq j. \tag{4.44}$$

The auto-correlation in (4.43) and the cross-correlation in (4.44) build up the overall correlation matrix $\mathbf{R}_{\hat{\mathbf{h}}^{\mathrm{LS}}_{\mathcal{P}}} \in \mathbb{C}^{|\mathcal{P}|\times|\mathcal{P}|}$. To simplify the notation, I assume that the imaginary interference cancellation matrix $\mathbf{C}_{\mathrm{a}}$ also includes any power-offsets. Furthermore, $\mathbf{C}_{\mathrm{a}}$ can be the precoding matrix of the data spreading approach, that is, $\mathbf{C}_{\mathrm{s}}$. Similar as before, the correlation between the LS channel estimate at the i-th pilot position and one element of transmission matrix $\mathbf{D}$, can be calculated by

$$\mathbf{r}_{\hat{h}^{\mathrm{LS}}_{\mathcal{P}_i},[\mathbf{D}]_{\overline{l_1k_1},\overline{l_2k_2}}} = \left(\mathbf{g}^{\mathsf{T}}_{\mathcal{P}_i} \otimes \mathbf{q}^{\mathsf{H}}_{\mathcal{P}_i}\right) \mathbf{R}_{\mathrm{vec}\{\mathbf{H}\}} \left(\mathbf{g}^{\mathsf{T}}_{l_2,k_2} \otimes \mathbf{q}^{\mathsf{H}}_{l_1,k_1}\right)^{\mathsf{H}}, \tag{4.45}$$

and builds up correlation vector $\mathbf{r}_{\hat{\mathbf{h}}^{\mathrm{LS}}_{\mathcal{P}},[\mathbf{D}]_{\overline{l_1k_1},\overline{l_2k_2}}} \in \mathbb{C}^{|\mathcal{P}|\times 1}$. With (4.43)-(4.45) one has all the necessary tools to calculate the MMSE weighting vector in (4.42), that is, $\tilde{\mathbf{w}}^{\mathrm{LMMSE}}_{l_1,k_1,l_2,k_2}$. One might think that my channel estimation method is unrealistic because the correlation matrices are not known in practical systems. While it is indeed hard to find the true correlation matrices, a rough approximation can easily be found and is often sufficient to obtain a close to optimal performance. For example, testbed measurements at 400 km/h validate that my MMSE channel estimation works in real world testbed scenarios [30]. To measure at such high velocities, the Vienna Wireless Testbed was augmented by a rotation wheel unit [45, 146]. To calculate the required correlation matrices, I assumed a frequency flat channel (13 subcarriers) and a uniform Doppler spectral density. The maximum Doppler shift was then estimated by matching the theoretical interference power (for a uniform Doppler spectral density) to the measured interference power (exploiting the zero subcarriers). The measurement results in [30] indicate that my channel estimation method, see (4.40) and (4.42), performs close to perfect channel knowledge, although some additional iterative steps are necessary. Thus, in contrast to almost all other works related to time-variant channel estimation, my method was already proven to work in real world testbed scenarios.

Besides the challenge of doubly-selective channel estimation, channel equalization is also important and was already discussed in Section 3.2. I will now combine channel estimation and equalization in an iterative way. The channel equalization is based on interference cancellation because it offers the best performance complexity trade-off, see Section 3.2. My iterative interference mitigation scheme works as follows, where the superscript $(\cdot)^{(\mathrm{i})}$ denotes the i-th iteration step:

1. MMSE channel estimation of transmission matrix $\hat{\mathbf{D}}^{(0)}$, see (4.40)-(4.45).
2. One-tap equalization and quantization, $\hat{x}^{(0)}_{l,k} = Q\left\{y^{(0)}_{l,k}/\hat{h}^{(0)}_{l,k}\right\}$, with $\hat{\mathbf{h}}^{(0)} = \mathrm{diag}\{\hat{\mathbf{D}}^{(0)}\}$.
3. Initialize with $\mathrm{i} = 0$.

4. Interference cancellation, $\mathbf{y}^{(\mathrm{i}+1)} = \mathbf{y} - (\hat{\mathbf{D}}^{(\mathrm{i})} - \mathrm{diag}\{\hat{\mathbf{D}}^{(\mathrm{i})}\})\,\hat{\mathbf{x}}^{(\mathrm{i})}$

5. Improved estimation of transmission matrix $\hat{\mathbf{D}}^{(\mathrm{i}+1)}$, enabled by reduced interference at the pilot positions.

6. Improved one-tap equalization and quantization $\hat{x}_{l,k}^{(\mathrm{i}+1)} = Q\left\{y_{l,k}^{(\mathrm{i}+1)} / \hat{h}_{l,k}^{(\mathrm{i}+1)}\right\}$

7. Repeat Step 4 to Step 6. In my simulations, I considered $\mathrm{i} = 0, 1, ..., 4$.

Note that the underlying correlation in (4.43) does not take the power reduction of the interference after cancellation into account because non-linearities make the analytical calculation very challenging. To circumvent this problem, I employ a slightly mismatched MMSE estimation. For iteration step $\mathrm{i} = 0, 1, 2$, I consider the correlation as described in (4.43) while for iteration step $\mathrm{i} = 3$ and $\mathrm{i} = 4$, I assume that interference was perfectly canceled, so that the matrix product $\mathbf{C}^{\mathsf{T}}\mathbf{G}^{\mathsf{T}}$ in (4.43) transforms to $\mathbf{C}^{\mathsf{T}}\mathbf{G}^{\mathsf{T}} \rightarrow \sqrt{P_{\mathcal{P}}}\,\mathbf{g}_{\mathcal{P}_i}^{\mathsf{T}}$. The computational complexity of my interference mitigation technique is relatively low once the MMSE weighting vector is calculated. Let me ignore the computational complexity of the imaginary interference cancellation method (auxiliary symbols/data spreading) because it was already discussed in Section 4.2. I assume that each row of matrix $\mathbf{D}$ has nine relevant interference terms. Furthermore, approximately $|\mathcal{P}| = 10$ pilots are needed for an accurate channel estimation. A conventional one-tap equalization together with MMSE channel estimation then requires in total 11 multiplications per data symbol. On the other hand, my interference cancellation scheme requires $91 + 99\mathrm{i}$ multiplications for i iterations. For example, four iterations require in total 487 multiplications, implying that the computational complexity is approximately 45 times higher that for a conventional one-tap equalizer. Of course, one can reduce this complexity by reducing the number of iterations, the number of considered interference terms, or the number of pilot symbols. Thus, there exists a performance-complexity trade-off.

Let me now discuss the improvement of my interference cancellation scheme compared with conventional one-tap equalization. I assume an FBMC transmission with a Hermite prototype filter and channel estimation based on the data spreading approach, see Section 4.2.2. The parameters are chosen similarly as for the channel equalization in Section 3.2. I consider a diamond-shaped pilot pattern, same as in LTE, that is, $|\mathcal{P}| = 32$ pilots are distributed over a time-frequency resource of $KT = 2\,\mathrm{ms}$ and $LF = 360\,\mathrm{kHz}$. The total overhead is given by $\frac{TF|\mathcal{P}|2}{KTLF} = 4.4\%$, where the factor of two inside the equation can be explained by the data spreading approach which requires to sacrifice one additional time-frequency position per pilot. To improve the channel estimation accuracy, I employ a pilot-to-data power offset of four, so that the data symbol SNR is 0.19 dB smaller than the overall SNR.

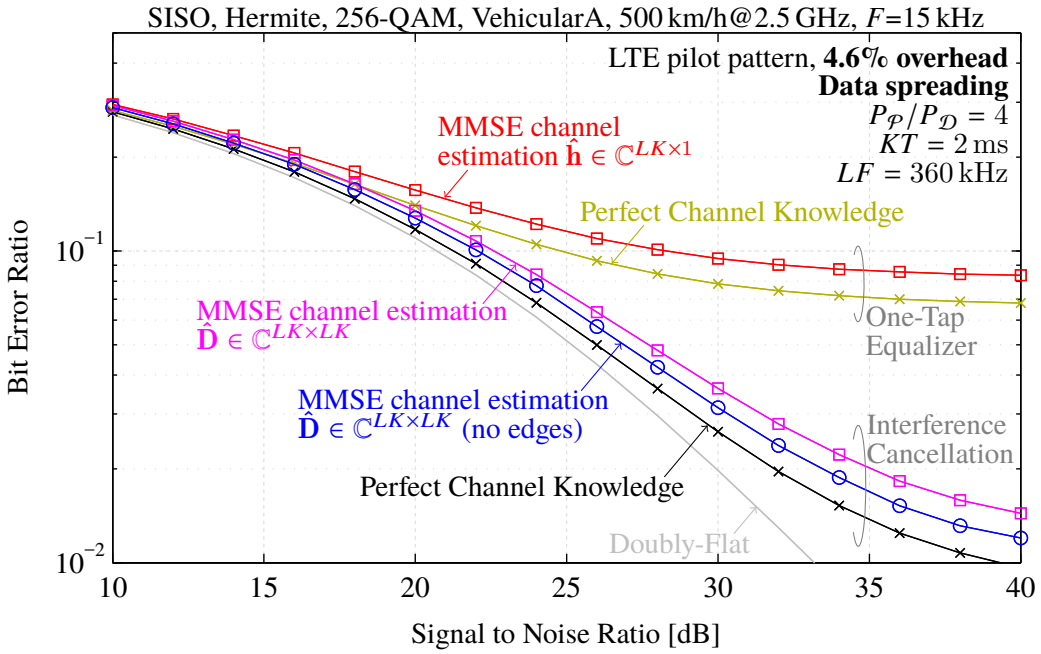

Figure 4.10. The proposed doubly-selective channel estimation method performs close to perfect channel knowledge. Compared with Figure 3.14, the BER is slightly worse, even for perfect channel knowledge, because of spreading of the data symbols and the pilot-to-data power offset, leading to a lower data symbol SNR.

Figure 4.10 shows the BER over the SNR. Compared to Section 3.2, the performance for perfect channel knowledge is slightly worse due the SNR shift of the data symbols and the spreading. A one-tap equalizer performs poorly once interference starts to dominate the noise. By employing my interference cancellation scheme, the performance can be significantly improved. Overall, MMSE channel estimation is very accurate and only slightly worse than perfect channel knowledge. In particular, my doubly-selective channel estimation technique performs close to perfect channel knowledge (only a small SNR shift of approximately 1 dB for the "no edges" curve). For the "no edges" MMSE channel estimation curve in Figure 4.10, I ignore extrapolation, that is, time-frequency positions close to the edges are excluded. One can imagine a sliding block with an inner and an outer block where only the inner block is evaluated for the BER while the outer block only contributes to the channel estimation.

Figure 4.11 shows the BER over SNR for channel estimation based on auxiliary symbols. I employ four auxiliary symbols per pilot so that the channel induced interference at the pilot positions is relatively low, while at the same time the required overhead is the same as in LTE, that is, $\frac{TF(|\mathcal{P}|+|\mathcal{A}|)}{KTLF} = 11.1\%$ for FBMC and $\frac{LFT_{\mathrm{CP}}K+|\mathcal{P}|}{KTLF} = 11.1\%$ for OFDM. Furthermore, I consider a pilot-to-data power offset of 4.685, which guarantees that the data symbol SNR is the same as the overall SNR. This is possible because the auxiliary symbol power is close

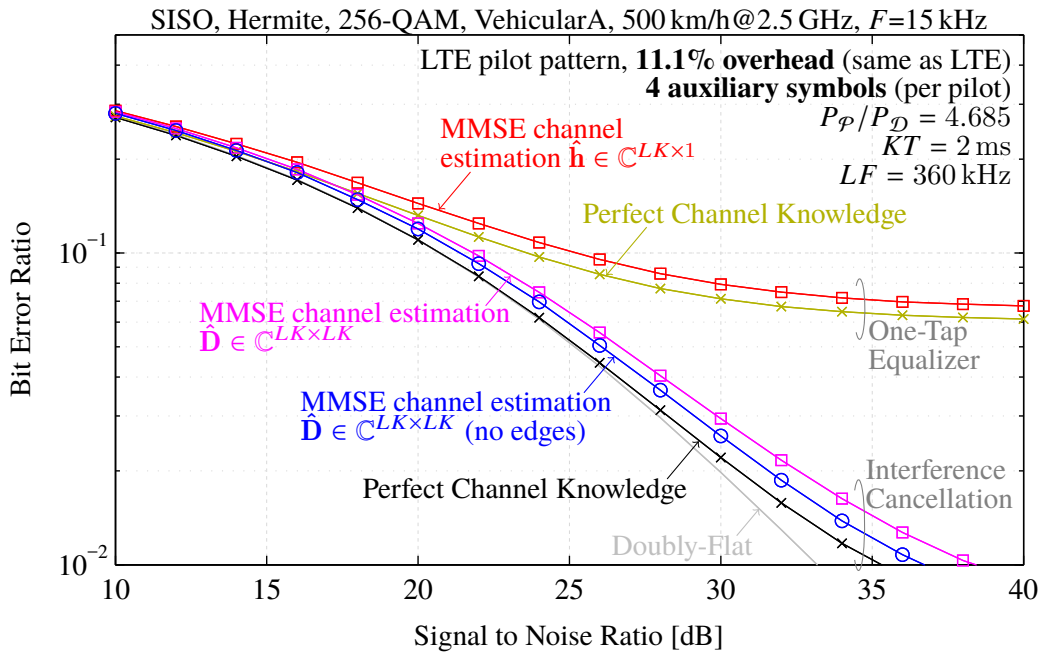

Figure 4.11. The proposed doubly-selective channel estimation method performs close to the theoretical bound of doubly-flat fading. In terms of BER, four auxiliary symbols show a better performance than the spreading approach in Figure 4.10. However, this comes at the expense of an increased overhead.

to zero so that the available power can be distributed to the pilots. With those settings, the BER for perfect channel knowledge in Figure 4.11 is the same as in Figure 3.14. Again, my MMSE channel estimation scheme performs close to perfect channel knowledge, validating its capability to deal with doubly-selective channels.

My proposed interference cancellation scheme can be considered as a first step and can be further improved. For example, one could optimize the pilot density or the pilot-to-data power offset. Other possible improvements are soft information bits or decoding at each iteration step. A detailed discussion of all those possible improvements, however, is beyond the scope of this work, in particular because I do not think that doubly-selective channel estimation and equalization are usually worth the effort.

Chapter 5

Block Spread FBMC-OQAM: Restoring Complex Orthogonality

The loss of complex orthogonality is the main obstacle in FBMC-OQAM and seriously hampers some important transmission techniques, such as channel estimation [42], Alamouti's space-time-block-code [69] or maximum likelihood MIMO detection [70]. In particular the limited MIMO compatibility is a major issue [147], preventing a widespread application of FBMC. Most papers which combine MIMO and FBMC have some serious drawbacks, such as [148] which relies on channel knowledge at the transmitter or [149, 150] which require high computational complexity. On the other hand, there exists many practical solutions for channel estimation in FBMC, as already discussed in Chapter 4. However, all those solutions merely deal with the imaginary interference, but not truly solve the underlying problem, that is, the loss of complex orthogonality.

In this section, I investigate a method which restores complex orthogonality in FBMC-OQAM. This is enabled by adding an additional code dimension (besides time and frequency), so that all methods known in OFDM can be straightforwardly employed in FBMC. In contrast to conventional FBMC, the data symbols no longer belong to a certain time-frequency position, but are rather spread over several time or frequency positions. Such spreading increases the sensitivity to doubly-selective channels. However, if the delay spread and the Doppler spread are sufficiently low, channel induced interference can still be neglected. In future wireless systems, such condition will often be fulfilled, making block spread FBMC-OQAM an interesting modulation scheme.

This chapter is mainly based on my publications [1, 27, 36, 39] and includes the following novel contributions:

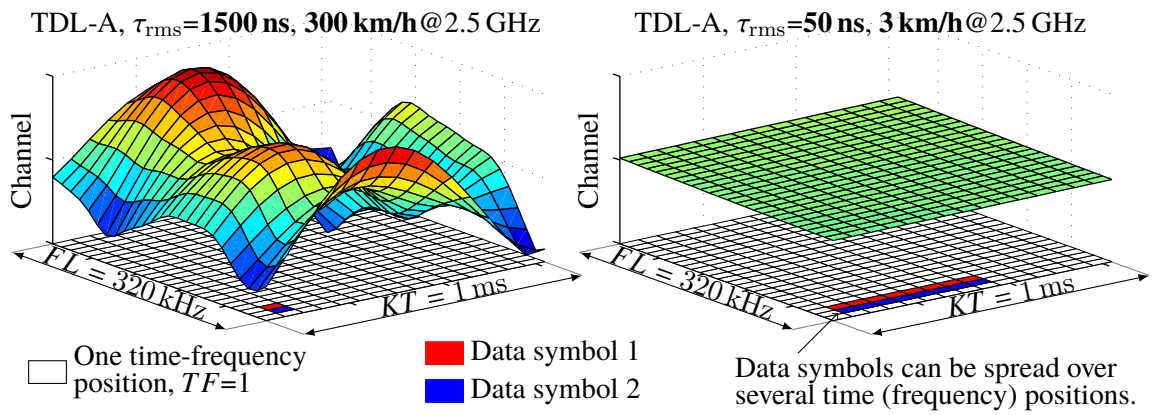

Figure 5.1. In conventional multicarrier systems, each data symbol only occupies a small time-frequency resource of approximately $TF = 1$. This is advantageous in highly double-selective channels (left part of the figure) because the transmission can still be modeled by one-tap channels. However, in a more realistic scenario (right part of the figure), data symbols can be spread over several time (or frequency) positions while keeping all the advantages of conventional multicarrier systems. In FBMC, such spreading is beneficial because the additional code dimension allows to restore complex-orthogonality.

- In Section 5.1, I present the basic idea of block spread FBMC-OQAM. Furthermore, I derive the optimal spreading matrix and explain why Walsh–Hadamard spreading is a more practical solution. Finally, I discuss two possible interpretations of the spreading approach (code dimension, changing the basis pulses) [1, 36, 39].
- In Section 5.2, I provide a detailed discussion of Walsh–Hadamard spreading in time. Compared to [69, 71], I investigate the interference between different blocks and propose the usage of guard symbols. Furthermore, I allow for a time-variant channel and derive closed-form SIR expressions. Finally, I validate the applicability of my block spread FBMC transmission scheme by real world testbed measurements [27, 39]
- In Section 5.3, I discuss Walsh–Hadamard spreading in frequency. Again, I consider a doubly-selective channel and propose a block frequency spreading approach, similar to Section 5.2, but now in frequency instead of time [36].

5.1 Introduction

The left part of Figure 5.1 shows a channel with a very large delay spread and a very large Doppler spread. In such scenarios, it is advantageous that each data symbol only occupies a small time-frequency resource of approximately $TF = 1$, so that the transmission can be

modeled by a one-tap channel. This has many advantages, such as, simple equalization, a straightforward employment of MIMO techniques and efficient scheduling of multiple users. However, such highly double-selective channel will rarely happen in practice. A much more realistic scenario is depicted in the right part of Figure 5.1, corresponding to a low delay spread and a low Doppler spread. For such channel, there is no reason why one data symbol should only occupy a small time-frequency resource of $TF = 1$. Instead, one data symbol can be spread over several time-frequency positions. Because the channel is approximately flat within such spreading interval, all the beneficial properties of conventional multicarrier systems are preserved. Of course, the channel is only flat over a certain bandwidth and a certain period of time, so that several transmission blocks must be concatenated to achieve a desired bandwidth and transmission time. Furthermore, to keep the data rate high, several data symbols occupy the same time-frequency resources. Those symbols are differentiated by their spreading sequences.

Spreading is very beneficial in FBMC because it allows to solve the problem of the imaginary interference. For example, authors in [151] proposed a block-Alamouti scheme (over time) which can be seen as special kind of spreading (distributing symbols in time). The same method was recently applied by [152] in the frequency domain. However, a better method is Walsh–Hadamard spreading [69] because it restores complex orthogonality, so that it not only works for Alamouti transmissions (as in [151, 152]), but additionally allows to straightforwardly employ all other methods known in OFDM, such as channel estimation, other space-time-block codes or low-complexity maximum likelihood symbol detection. Similar to Walsh–Hadamard spreading, authors in [70] suggested FFT spreading in time to restore (quasi)-orthogonality. However, I prefer Walsh–Hadamard spreading because it has a much lower computational complexity and perfectly restores complex orthogonality within one block.

Let me describe the spreading approach in more detail. In a first step, I assume an AWGN channel, that is, $\mathbf{H} = \mathbf{I}_N$, so that (2.30) transforms to

$$\mathbf{y} = \mathbf{Q}^{\mathsf{H}}\mathbf{G}\,\mathbf{x} + \mathbf{n}. \tag{5.1}$$

Note that (5.1) describes a block transmission of L subcarriers and K symbols in time. Several of those blocks must be concatenated in time and frequency to achieve a desired bandwidth and transmission time. In block spread FBMC, complex-valued data symbols $\tilde{\mathbf{x}} \in \mathbb{C}^{\frac{LK}{2}\times 1}$, are precoded by a coding/spreading matrix $\mathbf{C} \in \mathbb{C}^{LK\times\frac{LK}{2}}$, so that the transmitted symbols $\mathbf{x} \in \mathbb{C}^{LK\times 1}$ are obtained by

$$\mathbf{x} = \mathbf{C}\,\tilde{\mathbf{x}}. \tag{5.2}$$

Note that, a priori, the size of $\mathbf{C}$ and $\tilde{\mathbf{x}}$ is unknown. I will explain later in this section why the size was chosen that way. The received data symbols $\tilde{\mathbf{y}} \in \mathbb{C}^{\frac{LK}{2}\times 1}$ are obtained by decoding the received symbols according to

$$\tilde{\mathbf{y}} = \mathbf{C}^{\mathsf{H}}\,\mathbf{y}. \tag{5.3}$$

To restore complex orthogonality, the coding matrix has to be chosen so that the following condition is fulfilled,

$$\mathbf{C}^{\mathsf{H}}\,\mathbf{Q}^{\mathsf{H}}\mathbf{G}\,\mathbf{C} = \mathbf{I}_{LK/2}. \tag{5.4}$$

As already mentioned in Section 2.2, it is possible to satisfy (5.4) by utilizing an eigenvalue decomposition $\mathbf{Q}^{\mathsf{H}}\mathbf{G} = \mathbf{G}^{\mathsf{H}}\mathbf{G} = \mathbf{U}\mathbf{\Lambda}\mathbf{U}^{\mathsf{H}}$, so that coding matrix $\mathbf{C} \in \mathbb{C}^{LK\times\frac{LK}{2}}$ can be calculated by

$$\mathbf{C} = \mathbf{U}\begin{bmatrix} \Lambda_1^{-1/2} & 0 & 0 \\ 0 & \ddots & 0 \\ 0 & 0 & \Lambda_{LK/2}^{-1/2} \\ 0 & \dots & 0 \\ \vdots & \vdots & \vdots \\ 0 & \dots & 0 \end{bmatrix}, \tag{5.5}$$

where Λ_i represents the i-th eigenvalue (sorted) of $\mathbf{Q}^{\mathsf{H}}\mathbf{G}$ and $\mathbf{U}$ the corresponding eigenvector matrix. As shown in Figure 2.5, the eigenvalues for $K \to \infty$ and $L \to \infty$ are given by $\Lambda_1 = \Lambda_2 = \cdots = \Lambda_{LK/2} = 2$ and $\Lambda_i = 0$ for $i > \frac{LK}{2}$. Thus, (5.5) implicitly applies the water-filling algorithm [73], so that $\mathbf{C}$ becomes the optimal spreading matrix in terms of maximizing the information rate. In particular, it shows that the optimal size of the spreading matrix is $LK \times \frac{LK}{2}$ and that any matrix, $\mathbf{C} \in \mathbb{C}^{LK\times\frac{LK}{2}}$, which satisfies (5.4), is optimal for $K \to \infty$ and $L \to \infty$ (the SNR is always the same). Once K and L are bounded, the spreading matrix in (5.5) no longer correspond to the optimum. The optimal spreading matrix can then be found by applying the water-filling algorithm, where the column size of the matrix will usually be larger than $\frac{LK}{2}$. However, a spreading matrix of size $LK \times \frac{LK}{2}$, which satisfies (5.4), still performs close to the optimum, as indicated by the eigenvalues in Figure 2.5. For example, for $L = 36$ and $K = 30$, the suboptimal spreading matrix performs only 3.6% worse in terms of achievable rate than the optimal spreading matrix (water filling) for SNR values smaller than 20 dB. Furthermore, the optimal spreading matrix requires different code rates for layers close to the eigenvalue of $\Lambda_{LK/2}$. This increases the overall complexity while the possible improvement is rather low, so that, employing a suboptimum spreading matrix, such as (5.5), makes sense in practical systems. Note that precoding reduces the average transmit power by a factor of two, that is, $\mathrm{tr}\left\{\mathbf{G}\mathbf{C}\mathbf{C}^{\mathsf{H}}\mathbf{G}^{\mathsf{H}}\right\} = \mathrm{tr}\left\{\mathbf{C}^{\mathsf{H}}\mathbf{G}^{\mathsf{H}}\mathbf{G}\mathbf{C}\right\} = \frac{LK}{2} = \frac{1}{2}\mathrm{tr}\left\{\mathbf{G}^{\mathsf{H}}\mathbf{G}\right\}$. Thus, for the same SNR, the data symbol power has to be increased by a factor of two. This

is in agreement with my observation that the power of complex-valued data symbols is twice as large as the power of real-valued data symbols, employed in FBMC-OQAM, as already discussed in Section 2.2. It is also interesting that the noise after de-spreading is white, $\tilde{\mathbf{n}} \sim \mathcal{CN}(\mathbf{0}, P_{\mathrm{n}}\,\mathbf{I}_{LK/2})$, even though the spreading matrix itself is not necessarily semi-unitary. The reason behind this is again the orthogonalization condition in (5.4), implying that $\mathbf{R}_{\tilde{\mathbf{n}}} = \mathbf{C}^{\mathsf{H}}\mathbf{R}_{\mathbf{n}}\mathbf{C} = \mathbf{C}^{\mathsf{H}}\mathbf{Q}^{\mathsf{H}}\mathbf{Q}\mathbf{C} = P_{\mathrm{n}}\,\mathbf{I}_{LK/2}$.

The spreading matrix in (5.5) was my first approach to restore complex orthogonality in FBMC. I later realized that a related concept, based on Walsh–Hadamard matrices, was already proposed in [69, 71]. While the spreading matrix in (5.5) provides analytical insights, it is not very practical because of the high computational complexity and the fact that the spreading is performed in both, time and frequency, which only works for a doubly-flat channel. Walsh–Hadamard spreading, on the other hand, is a much more practical solution because it requires almost no additional complexity and the spreading is performed in only one direction, either in time, see Section 5.2, or in frequency, see Section 5.3. Thus, the channel only has to be flat in one dimension. Authors of [71] left the question open whether it is possible to find a spreading matrix that has more than $\frac{LK}{2}$ columns while still satisfying (5.4). My investigations in (5.5) show that this is not possible (ignoring any edge effects which become negligible for a large number of K and L). A small disadvantage of Walsh–Hadamard spreading is the fact that the spreading length has to be a power of two[1]. This makes the integration into existing systems problematic but has almost no impact if a system is designed from scratch. The big advantage of Walsh–Hadamard spreading, on the other hand, is that only additions but no multiplications are needed. Thus, the additional computational complexity is very low. Moreover, a fast Walsh–Hadamard transform can be used, further reducing the computational complexity. For example, spreading in time only requires $\log_2(K) - 1$ extra additions/subtractions per data symbol at the transmitter and $\log_2(K)$ extra additions/subtractions per data symbol at the receiver. For spreading in frequency, it is $\log_2(L) - 1$ respectively $\log_2(L)$. Because the Hermite prototype filter has better localization in time than the PHYDYAS filter, I employ the Hermite prototype filter for spreading in time so that one guard symbol is usually sufficient to separate different transmission blocks. The same applies in reversed order for spreading in frequency, that is, I employ the PHYDYAS prototype filter.

In principle, there exist two interpretations of my proposed spreading scheme.

1. Code dimension: on top of a conventional FBMC-OQAM system, a code dimension is added (besides time and frequency), allowing to restore complex orthogonality.

[1]Restoring complex orthogonality in FBMC requires that the spreading length is a power of two [71]. Conventional Hadamard matrices must not necessarily be a power of two.

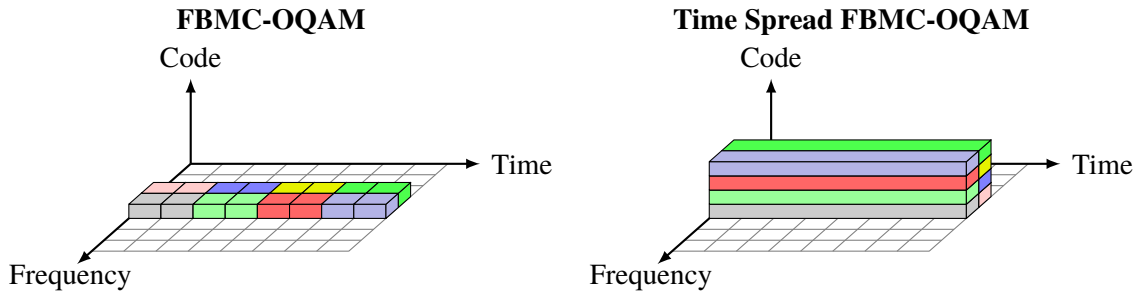

Figure 5.2. In conventional FBMC-OQAM, each time-frequency position can only carrier real-valued symbols, so that two time slots are required to transmit one complex-valued symbol (thus the name offset-QAM). In block spread FBMC-OQAM, complex-valued symbols are spread over several time slots, allowing to restore complex orthogonality in FBMC-OQAM. Illustration: $L = 2$, $K = 8$. ©2016 IEEE, [39].

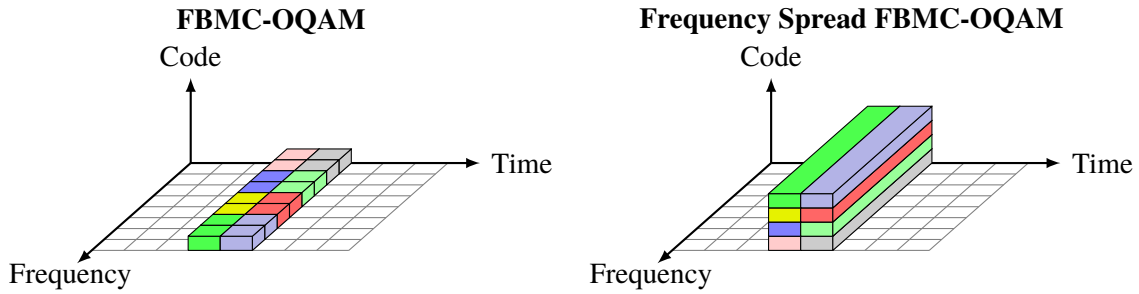

Figure 5.3. Similar to Figure 5.2, one can equivalently spread in frequency. Note that there is no reason why the "offset" in FBMC-OQAM should be in time (as usually assumed in literature). Instead, the offset can equivalently be applied in frequency, so that the left part and the right part of the figure are consistent. Illustration: $L = 8$, $K = 2$.

2. Transformed basis pulses: data symbols are no longer modulated by the basis pulses in $\mathbf{G}$ but by the transformed basis pulses, given by, $\tilde{\mathbf{G}} = \mathbf{GC} = \begin{bmatrix} \tilde{\mathbf{g}}_1 & \tilde{\mathbf{g}}_2 & \dots & \tilde{\mathbf{g}}_{LK/2} \end{bmatrix}$.

The first interpretation is illustrated in Figure 5.2-5.3 and corresponds to the mathematical description in (5.2) and (5.3), that is, symbols are transmitted over a rectangular time-frequency grid. In conventional FBMC-OQAM, two time-frequency positions are required to transmit one complex-valued data symbol. In block spread FBMC, on the other hand, complex-valued data symbols are spread over several time-frequency positions, allowing to restore complex orthogonality. Some data symbols occupy the same time-frequency resources. For those symbols, different code words guaranteed complex orthogonality. In time spread FBMC, one can easily add subcarriers without losing complex orthogonality. Concatenating blocks in the time, however, causes interference, so that guard symbols might become necessary, see Section 5.2. The same applies in reversed order for frequency

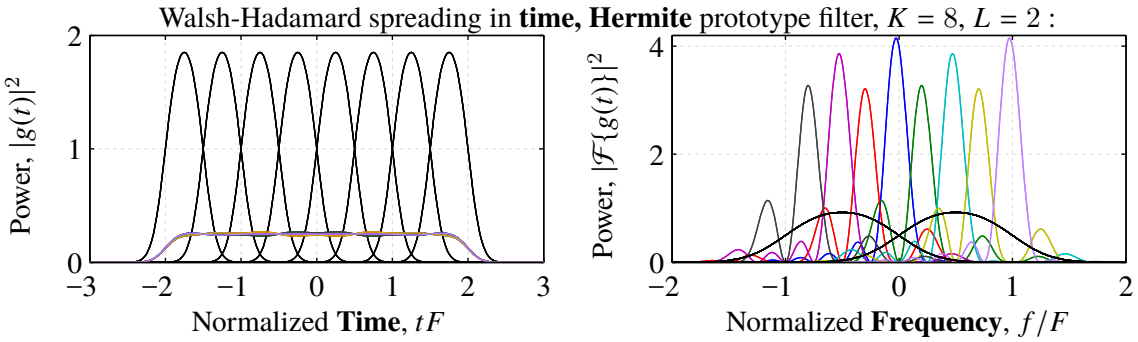

Figure 5.4. The black curves correspond to the basis pulses of conventional FBMC-OQAM and represent the power in time, $|g_{l,k}(t)|^2$, and in frequency, $|\mathcal{F}\{g_{l,k}(t)\}|^2$. The colored curves, on the other hand, represent the "new" basis pulses, that is, $|\tilde{g}_i(t)|^2$ and $|\mathcal{F}\{\tilde{g}_i(t)\}|^2$. In contrast to the conventional basis pulses, the new basis pulses are not only orthogonal in the real domain, but also in the complex domain.

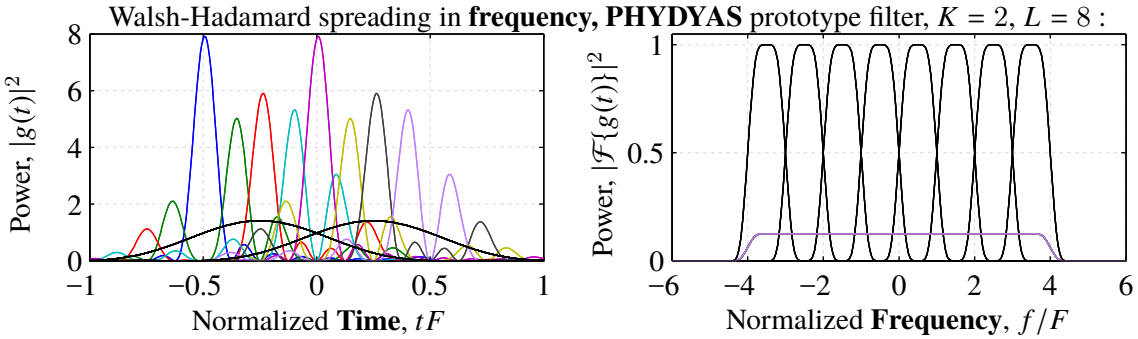

Figure 5.5. The power distribution in time and frequency for conventional basis pulses (black) and the new basis pulses (colored). Similar to Figure 5.4, but for spreading in frequency and the PHYDYAS prototype filter.

spreading, that is, an additional block can easily be added in time while adding frequency blocks causes interference, see Section 5.3. Note that the guard symbols slightly reduce the spectral efficiency.

The second interpretation of my block spread FBMC-OQAM transmission scheme is illustrated in Figure 5.4-5.5 and shows the power in time and frequency of the conventional basis pulses (black curve) and the transformed basis pulses (colored curves). I start my discussion with the conventional FBMC-OQAM basis pulses (black), see (2.2). The left part of Figure 5.4-5.5 represents the power distribution in time, that is, $|g_{l,k}(t)|^2$ while the right part describes the power distribution in frequency, that is, $|\mathcal{F}\{g_{l,k}(t)\}|^2$, with $\mathcal{F}\{\cdot\}$ denoting the Fourier transform. As already mentioned in Section 2.1, the basis pulses of conventional multicarrier systems are just time and frequency shifted versions of the prototype filter. This

implies that the power distribution in time has the same shape for all the basis pulses and the only difference is that those pulses are shifted by $T = \frac{1}{2F}$. The same applies in the frequency domain, where the frequency shift is given by F. Let me now discuss the more interesting part, that is, the transformed basis pulses (colored curves). Same as before, the left part of Figure 5.4-5.5 shows the power distribution in time, that is, $|\tilde{g}_i(t)|^2$, while the right part shows the power distribution in frequency, $|\mathcal{F}\{\tilde{g}_i(t)\}|^2$. In contrast to conventional FBMC, the underlying prototype filters are now unsymmetrical and no longer the same for all basis pulses. Furthermore, the main power of those pulses is concentrated within a small area (the peaks) but the side lobes are much higher than for a typical FBMC systems.

Frequency spreading can also be interpreted as a single carrier transmission scheme. To achieve a desired bandwidth, several such single carrier blocks must be transmitted in parallel. This is the same as in my block spread FBMC-OQAM transmission scheme. In particular, both methods require a small guard band to improve the SIR, see Section 5.3. Still block spread FBMC-OQAM has some advantages compared with conventional single carrier schemes, such as, low complexity signal generation, flexible time-frequency assignment, block wise processing and, in case of a doubly-selective channel, simple one-tap equalization (although some advantages of block spread FBMC might be lost in such scenarios).

In a similar way, time spread FBMC can be compared to windowed OFDM. For this, I consider spreading over K FBMC symbols in time, so that the transmission time is $\frac{K}{2F}$ (seconds). To obtain the same transmission time in windowed OFDM, one could reduce the subcarrier spacing by a factor of $\frac{K}{2}$. A potential window overhead is then relatively small, comparable to the overhead of block spread FBMC, see Section 5.2. For such a setup, FBMC still has better spectral properties than windowed OFDM, but the differences between those two modulation schemes become very small. However, time spread FBMC has some additional advantages over windowed OFDM (reduced subcarrier spacing). For example, the common phase error caused by phase noise can be better dealt with. One only has to equalize the phase before de-spreading. This is especially useful if all receive chains of a MIMO system have the same phase error. Then, all the advantages of block spread FBMC can be preserved. However, if the time variations are caused by the channel, this is no longer possible so that windowed OFDM and block spread FBMC show a similar performance degeneration.

5.2 Walsh–Hadamard Spreading in Time

In a first step, I propose a coding matrix that satisfies the orthogonality condition in (5.4) and, at the same time, is based on a fast Walsh–Hadamard transform, so that the additional computational complexity becomes very low. As explained in Section 5.1, the ratio between

the row dimension and the column dimension must be $2:1$. Thus, spreading in time can be modeled by the matrices $\mathbf{C}_{t'} \in \mathbb{R}^{K\times\frac{K}{2}}$ and $\mathbf{C}_{t''} \in \mathbb{R}^{K\times\frac{K}{2}}$ where one has to alternate between spreading with $\mathbf{C}_{t'}$ and $\mathbf{C}_{t''}$ for adjacent subcarriers. The spreading matrix itself is found by taking every second column out of a sequency ordered [153] Walsh-Hadamard matrix $\boldsymbol{\mathcal{H}} \in \mathbb{R}^{K\times K}$, that is,

$$\begin{aligned}[\mathbf{C}_{t'}]_{k,m} &= [\boldsymbol{\mathcal{H}}]_{k,2m-1} \\ [\mathbf{C}_{t''}]_{k,m} &= [\boldsymbol{\mathcal{H}}]_{k,2m}\end{aligned} \quad ; \text{for} \quad k = 1,2,\ldots,K;\ m = 1,2,\ldots,\frac{K}{2}. \tag{5.6}$$

To find the overall spreading matrix $\mathbf{C} \in \mathbb{R}^{LK\times\frac{LK}{2}}$, one has to map the individual spreading matrices $\mathbf{C}_{t'}$ and $\mathbf{C}_{t''}$ to the correct subcarrier positions. For my vectorized system model, see (2.26), this leads to,

$$\mathbf{C} = \mathbf{C}_{t'} \otimes \mathbf{I}_{L/2} \otimes \begin{bmatrix} 1 & 0 \\ 0 & 0 \end{bmatrix} + \mathbf{C}_{t''} \otimes \mathbf{I}_{L/2} \otimes \begin{bmatrix} 0 & 0 \\ 0 & 1 \end{bmatrix}. \tag{5.7}$$

It can easily be checked through numerical evaluations that (5.7) satisfies the complex orthogonalization condition in (5.4). Note that the matrices $\left[\begin{smallmatrix} 1 & 0 \\ 0 & 0 \end{smallmatrix}\right]$ and $\left[\begin{smallmatrix} 0 & 0 \\ 0 & 1 \end{smallmatrix}\right]$ in (5.7) are necessary to alternate between spreading with $\mathbf{C}_{t'}$ and $\mathbf{C}_{t''}$ for adjacent subcarriers.

So far, I considered only a block transmission of L subcarriers and K symbols in time. In theory, K can approach infinity. However, as symbols are spread over K time slots, this is not practical because of latency constraints and the fact that the channel varies over time, destroying orthogonality. Indeed, the concept of block spread FBMC-OQAM is based on concatenating several blocks. For analytical investigations, it is sufficient to assume three transmit blocks and to analyze the performance in block 2. The first block is characterized by transmit matrix $\mathbf{G}_1$, the second block by $\mathbf{G}_2$ and the third block by $\mathbf{G}_3$. Those transmit matrices are almost the same except that they are time shifted by KT from each other, see Figure 5.6. Note that $\mathbf{G}_1$, $\mathbf{G}_2$ and $\mathbf{G}_3$ must all have the same column dimension and can, for example, be generated by a larger transmit matrix $\mathbf{G}$ with $3K$ symbols in time, followed by splitting this matrix into three pieces. The overall transmit signal can then be written as

$$\mathbf{s} = \begin{bmatrix} \mathbf{G}_1 & \mathbf{G}_2 & \mathbf{G}_3 \end{bmatrix} \begin{bmatrix} \mathbf{x}_1 \\ \mathbf{x}_2 \\ \mathbf{x}_3 \end{bmatrix}, \tag{5.8}$$

where $\mathbf{x}_1 \in \mathbb{C}^{LK\times 1}$ represents the transmitted symbols of the first block, $\mathbf{x}_2$ of the second block and $\mathbf{x}_3$ of the third block. As shown in Figure 5.6, these blocks overlap slightly. In conventional FBMC, such overlapping has no influence on the performance because of the

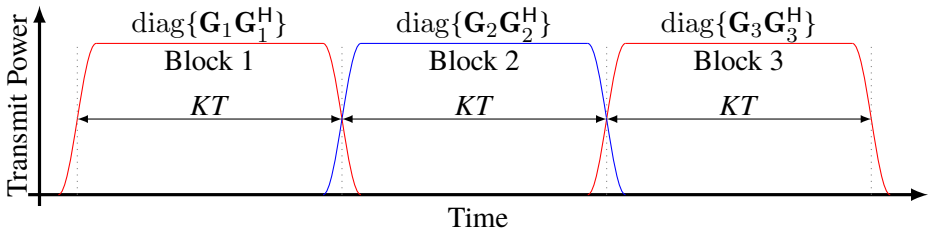

Figure 5.6. Neighboring blocks cause interference. In conventional FBMC-OQAM, such interference can be completely eliminated by taking the real part. In block spread FBMC-OQAM, however, this interference remains, see Figure 5.7, and affects the performance if the interference power is higher than the noise power. ©2016 IEEE, [39].

real orthogonality condition, that is $\Re\{\mathbf{Q}_2^{\mathsf{H}}\mathbf{G}_1\} = \Re\{\mathbf{Q}_2^{\mathsf{H}}\mathbf{G}_3\} = \mathbf{0}_{LK}$, where $\mathbf{Q}_2 = \mathbf{G}_2$ denotes the receive matrix for block 2. Unfortunately, orthogonality no longer holds true if time spreading is applied within one transmission block. By neglecting noise, the received data symbols of block 2 can be calculated by

$$\tilde{\mathbf{y}}_2 = \mathbf{C}^{\mathsf{H}}\mathbf{Q}_2^{\mathsf{H}}\,\mathbf{s} \tag{5.9}$$

$$= \tilde{\mathbf{x}}_2 + \mathbf{C}^{\mathsf{H}}\mathbf{Q}_2^{\mathsf{H}}\mathbf{G}_1\mathbf{C}\,\tilde{\mathbf{x}}_1 + \mathbf{C}^{\mathsf{H}}\mathbf{Q}_2^{\mathsf{H}}\mathbf{G}_3\mathbf{C}\,\tilde{\mathbf{x}}_3. \tag{5.10}$$

The first term in (5.10) represents the signal power while the second and third term the undesired interference. The SIR of block 2 can thus be expressed by

$$\mathrm{SIR}_2 = \frac{\frac{KL}{2}}{||\mathbf{C}^{\mathsf{H}}\mathbf{Q}_2^{\mathsf{H}}\mathbf{G}_1\mathbf{C}||_{\mathsf{F}}^2 + ||\mathbf{C}^{\mathsf{H}}\mathbf{Q}_2^{\mathsf{H}}\mathbf{G}_3\mathbf{C}||_{\mathsf{F}}^2}, \tag{5.11}$$

with $||\cdot||_{\mathsf{F}}$ denoting the Frobenius norm.

Figure 5.7 shows the SIR over spreading length K. As long as the SNR is much smaller than the SIR, block interference can be neglected because the interference is dominated by noise. Interference between blocks occurs only at the boarder region, so that, by increasing spreading length K, the SIR can be improved because the interference is spread over a higher number of symbols. However, if a short spreading length is desired, the interference might be too high. By inserting a guard slot in time, the SIR can be increased at the expense of spectral efficiency. Such efficiency loss, $\eta = \frac{1}{K+1}$, is relatively small and decreases for an increasing spreading length K. As a reference, I also consider an LTE like OFDM system which has an efficiency loss of $\eta = 6.67\%$, caused by the CP. The overall spectral efficiency loss, however, is higher than 6.67% because OFDM requires large guard bands, especially compared with FBMC, see Section 2.4.

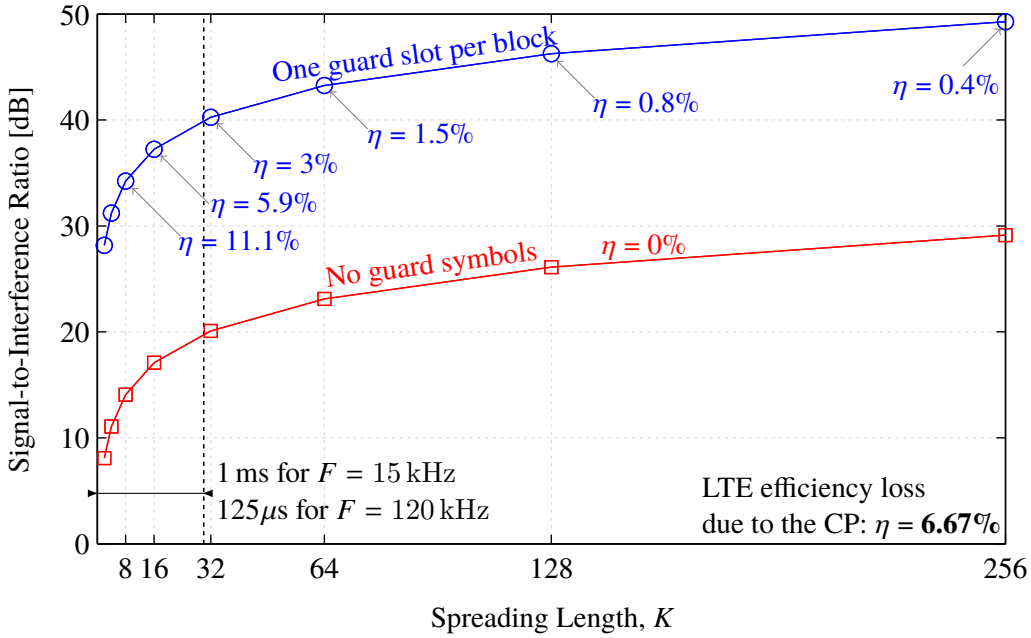

Figure 5.7. Overlapping between blocks, see Figure 5.6, causes interference. By including a guard slot, the SIR can be increased by approximately 20 dB at the loss of spectral efficiency, that is, $\eta = \frac{1}{K+1}$. Note that the spreading length has to be a power of two because of the Walsh-Hadamard structure. ©2016 IEEE, [39].

Let me now include doubly-selective channels into my model by a time-variant convolution matrix $\mathbf{H}$, see Section 2.2. Again, I neglect noise, so that the received data symbols at subcarrier position $l = 1, 2, \ldots, L$ and code position $m = 1, 2, \ldots, \frac{K}{2}$ for transmission block 2 can be expressed by:

$$\tilde{y}_{l,m,2} = \mathbf{c}_{l,m}^{\mathsf{H}} \mathbf{Q}_2^{\mathsf{H}} \mathbf{H} \begin{bmatrix} \mathbf{G}_1\mathbf{C} & \mathbf{G}_2\mathbf{C} & \mathbf{G}_3\mathbf{C} \end{bmatrix} \begin{bmatrix} \tilde{\mathbf{x}}_1 \\ \tilde{\mathbf{x}}_2 \\ \tilde{\mathbf{x}}_3 \end{bmatrix} \tag{5.12}$$

$$= \left(\begin{bmatrix} \tilde{\mathbf{x}}_1 \\ \tilde{\mathbf{x}}_2 \\ \tilde{\mathbf{x}}_3 \end{bmatrix}^{\mathsf{T}} \begin{bmatrix} \mathbf{G}_1\mathbf{C} & \mathbf{G}_2\mathbf{C} & \mathbf{G}_3\mathbf{C} \end{bmatrix}^{\mathsf{T}} \otimes \mathbf{c}_{l,m}^{\mathsf{H}} \mathbf{Q}_2^{\mathsf{H}} \right) \mathrm{vec}\{\mathbf{H}\}, \tag{5.13}$$

where $\mathbf{c}_{l,m} \in \mathbb{R}^{LK \times 1}$ denotes the $l + L(m-1)$-th column vector of $\mathbf{C}$ and corresponds to subcarrier position l and code position m. Similar as in Section 3.1.2, the Kronecker product in (5.13) helps to simplify statistical investigations. With (5.13), the signal plus interference

power $\mathrm{P}_{\mathrm{S+I}_{l,m,2}} = \mathbb{E}\{|\tilde{y}_{l,m,2}|^2\}$ can be straightforwardly calculated by

$$\mathrm{P}_{\mathrm{S+I}_{l,m,2}} = \mathrm{tr}\left\{\left(\begin{bmatrix}\mathbf{G}_1\mathbf{C} & \mathbf{G}_2\mathbf{C} & \mathbf{G}_3\mathbf{C}\end{bmatrix}^{\mathsf{T}} \otimes \mathbf{c}_{l,m}^{\mathsf{H}}\mathbf{Q}_2^{\mathsf{H}}\right)\mathbf{R}_{\mathrm{vec}\{\mathbf{H}\}}\left(\begin{bmatrix}\mathbf{G}_1\mathbf{C} & \mathbf{G}_2\mathbf{C} & \mathbf{G}_3\mathbf{C}\end{bmatrix}^{\mathsf{T}} \otimes \mathbf{c}_{l,m}^{\mathsf{H}}\mathbf{Q}_2^{\mathsf{H}}\right)^{\mathsf{H}}\right\} \tag{5.14}$$

where $\mathbf{R}_{\mathrm{vec}\{\mathbf{H}\}} = \mathbb{E}\{\mathrm{vec}\{\mathbf{H}\}\mathrm{vec}\{\mathbf{H}\}^{\mathsf{H}}\}$ denotes the correlation matrix of the vectorized convolution matrix and can easily be calculated for a given power delay profile and a given power spectral density. Similar to (5.14), the signal power (without interference) can be found by

$$\mathrm{P}_{\mathrm{S}_{l,m,2}} = \left(\mathbf{c}_{l,m}^{\mathsf{T}}\mathbf{G}_2^{\mathsf{T}} \otimes \mathbf{c}_{l,m}^{\mathsf{H}}\mathbf{Q}_2^{\mathsf{H}}\right)\mathbf{R}_{\mathrm{vec}\{\mathbf{H}\}}\left(\mathbf{c}_{l,m}^{\mathsf{T}}\mathbf{G}_2^{\mathsf{T}} \otimes \mathbf{c}_{l,m}^{\mathsf{H}}\mathbf{Q}_2^{\mathsf{H}}\right)^{\mathsf{H}}, \tag{5.15}$$

so that the average SIR for block 2 becomes:

$$\mathrm{SIR}_2 = \frac{\sum_{l=1}^{L}\sum_{m=1}^{\frac{K}{2}} \mathrm{P}_{\mathrm{S}_{l,m,2}}}{\sum_{l=1}^{L}\sum_{m=1}^{\frac{K}{2}} \left(\mathrm{P}_{\mathrm{S+I}_{l,m,2}} - \mathrm{P}_{\mathrm{S}_{l,m,2}}\right)}. \tag{5.16}$$

If the channel is approximately frequency flat within one subcarrier (supported by my measurements) and for a Jakes Doppler spectrum, Figure 5.8 shows how the SIR depends on the velocity. For a flat fading channel, the performance depends only on the normalized maximum Doppler shift, that is, $f_\mathrm{c}\frac{v}{c}\frac{1}{F}$, with f_c being the carrier frequency, v the velocity and c the speed of light. Note that I consider one guard slot per block, so that, for a velocity of zero, the same SIR as the blue curve in Figure 5.7 is achieved. The smaller the spreading length, the less effect has a time-variant channel. Therefore, both curves in Figure 5.8 intersect at some point.

The main reason for block spread FBMC is to enable MIMO transmissions in FBMC with approximately the same MIMO complexity as in OFDM. To validate my spreading approach, I conduct real world testbed measurements at a carrier frequency of 2.5 GHz [39] and 60 GHz [27]. Let me start with the description of my 2.5 GHz measurement setup. The signal is transmitted at a carrier frequency of $f_\mathrm{c} = 2.4955\,\mathrm{GHz}$ with $L = 12$ subcarriers and a subcarrier spacing of $F = 15\,\mathrm{kHz}$, leading to a transmission bandwidth of $FL = 180\,\mathrm{kHz}$. The sampling rate is $f_\mathrm{s} = 200\,\mathrm{MHz}$ (determined by the hardware), so that the FFT size becomes $\lceil\frac{f_\mathrm{s}}{F}\rceil = 13334$, where most FFT points are set to zero. Similar as in Figure 5.6, I consider three transmit blocks but evaluate the performance only for block 2. For FBMC, one block consists of $K = 32$ FBMC symbols and a zero time slot, leading to a transmission time

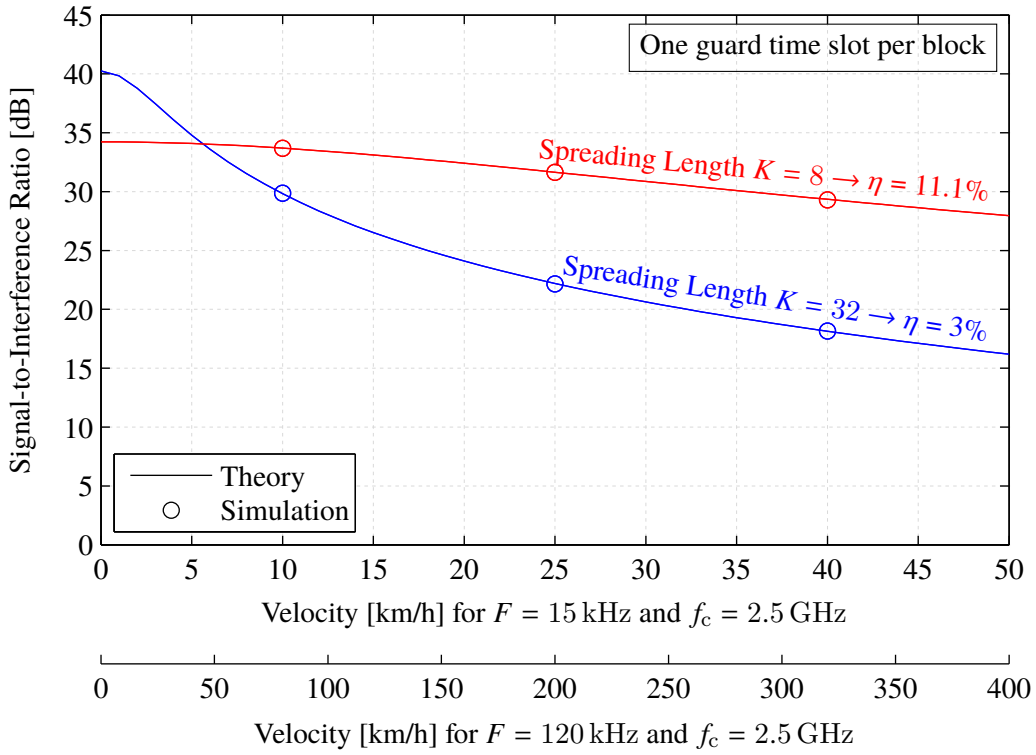

Figure 5.8. A high velocity reduces the SIR because time spread FBMC-OQAM implicitly assumes a time-invariant channel. Note that the robustness can be improved by increasing the subcarrier spacing or by reducing the spreading length. The theoretical SIR expression in (5.16) is validated by simulations. ©2016 IEEE, [39].

of $(K+1)T = 1.1\,\mathrm{ms}$ per block. I also apply spreading in the time domain, as described in this section, so that for each transmission block, 16 symbols per subcarrier are available. For OFDM, the CP length is set to $T_{\mathrm{CP}} = 2.085\,\mu\mathrm{s}$, approximately half the length of that in LTE, and the number of time symbols per block is set to $K = 16$, leading to the same transmission time as in FBMC, that is, $K(1/F + T_{\mathrm{CP}}) = 1.1\,\mathrm{ms}$. Thus, the bit rate is the same for FBMC and OFDM, allowing a fair comparison, although one should keep in mind that FBMC has better spectral properties so that a higher number of subcarriers could be used. Note that the SNR in FBMC is 0.13 dB higher than in OFDM because the zero time slots require no power. In real world transmissions, channel estimation is always necessary, which I perform by pilot symbol aided channel estimation, similar as in LTE, that is, a diamond shaped pilot pattern with eight pilot symbols per antenna, see Section 4.1. Because the channel is highly correlated in time and frequency, I average over all eight channel estimates, improving the channel estimation accuracy. At the pilot positions of antenna 1, antenna 2 must transmit zero symbols in order to avoid interference. The same applies in reversed order. Thus, I lose 16 data

symbols for the channel estimation, so that, for 16-QAM, 704 bits are transmitted per antenna (spatial multiplexing). The receiver is located indoor while the transmitter is 150 m away, on the rooftop of the opposite building, see Figure 1.3. Different MIMO channel realizations are obtained by relocating the static receive antennas to 1024 positions within a 4×4 wavelength grid. For 2×2 spatial multiplexing, I transmit independent bit streams at both antennas simultaneously. At the receiver, I employ ML MIMO detection, assuming perfect channel knowledge and Gaussian distributed noise, so that my detection only approximates the true ML performance. Note that ML detection is not feasible in conventional FBMC-OQAM since too many possibilities have to be calculated because of the imaginary interference [70]. The second considered transmission scheme is 2×1 Alamouti's space-time block code [69] which achieves full diversity at rate one. Besides my measurements at 2.5 GHz, I also measure at 60 GHz. The parameters are chosen similar to my 2.5 GHz measurements, except that the subcarrier spacing is set to $F = 500\,\mathrm{kHz}$ and the number of subcarriers is increased to $L = 48$, leading to a transmission bandwidth of $FL = 24\,\mathrm{MHz}$. Note that such a high subcarrier spacing is proposed for mmWave transmissions [154] and implicitly reduces the latency. Thus, even though I spread data symbols in time, the overall transmission time is less than 40 μ, satisfying the low-latency condition of 100 μs [78]. More details on my mmWave measurement setup can be found in [27].

Figure 5.9 shows the measured BER over SNR for my 2.5 GHz measurement as well as my 60 GHz measurement. FBMC and OFDM show the same BER performance but FBMC has much better spectral properties. The measurement results validate that my block spread FBMC-OQAM transmission scheme works in real world testbed scenarios.

5.3 Walsh–Hadamard Spreading in Frequency

Again, I start my discussion with the calculation of spreading matrix $\mathbf{C} \in \mathbb{R}^{LK \times \frac{LK}{2}}$. Similar as in Section 5.2, frequency spreading matrix $\mathbf{C}_f \in \mathbb{R}^{L \times \frac{L}{2}}$ can be found by taking every second column out of a sequency ordered [153] Walsh-Hadamard matrix $\boldsymbol{\mathcal{H}} \in \mathbb{R}^{L \times L}$, that is,

$$[\mathbf{C}_f]_{l,m} = [\boldsymbol{\mathcal{H}}]_{l,2m-1} \qquad ; \text{for} \quad l = 1, 2, \ldots, L;\ m = 1, 2, \ldots, \frac{L}{2}. \tag{5.17}$$

In contrast spreading in time, however, there is no need to alternate between two matrices, so that one frequency spreading matrix is sufficient. Matrix $\mathbf{C}_f$ in (5.17) could be equivalently defined by $[\boldsymbol{\mathcal{H}}]_{l,2m}$. Utilizing the underlying structure of my notation (vectorization) and the

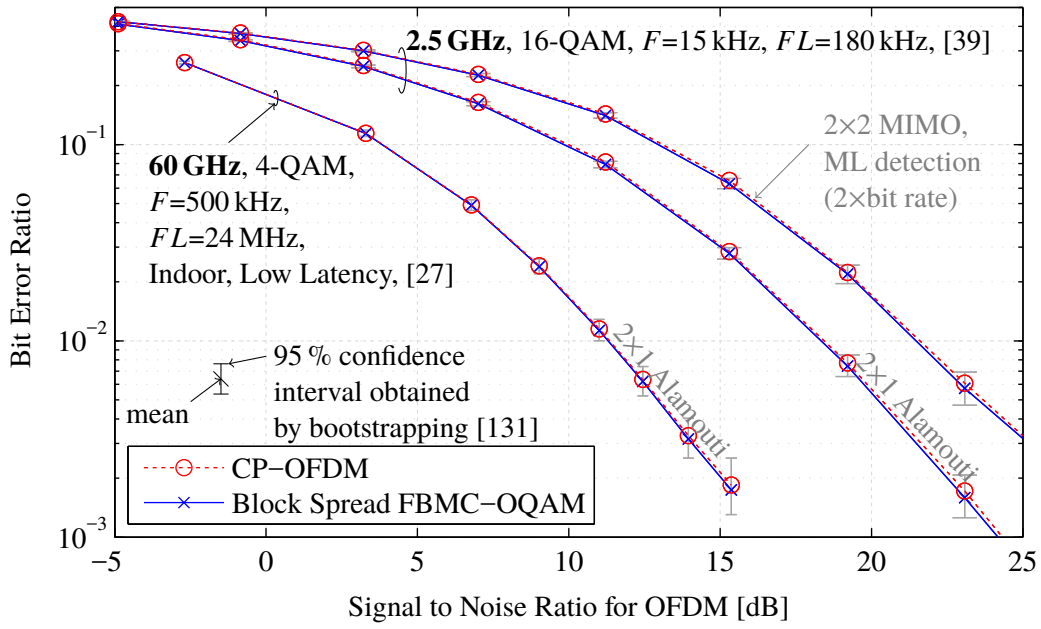

Figure 5.9. **Real-world testbed measurements** show that MIMO works in FBMC once symbols are spread in time. The spreading process itself has low computational complexity because a fast Walsh-Hadamard transformation can be used. FBMC and OFDM experience both the same BER, but FBMC has lower OOB emissions. ©2017 IEEE, [1].

fact that I spread over frequency only, allows me to express spreading matrix $\mathbf{C} \in \mathbb{R}^{LK \times \frac{LK}{2}}$ by,

$$\mathbf{C} = \mathbf{I}_K \otimes \mathbf{C}_f, \tag{5.18}$$

where Kronecker product $\otimes$ together with identity matrix $\mathbf{I}_K$ map coding matrix $\mathbf{C}_f$ to the correct time slot.

Similar as in Section 5.2, I am interested in the performance over doubly-selective channels. From a mathematical point of view, the SIR calculation is exactly the same as in Section 5.2, see (5.14)-(5.16). Only the interpretation of transmit matrix $\mathbf{G}_1$ and $\mathbf{G}_3$ is differently. They now represent a frequency-shift by FL instead of a time-shift by KT. Furthermore, the index changes slightly, that is, (l, m) transforms to (m, k), reflecting that coding is performed in the frequency domain and not in the time domain. As already elaborated throughout this thesis, I expect a low delay spread for future wireless communication systems, enabled by beamforming, higher carrier frequencies and smaller cell sizes. This is important for my frequency spreading approach because efficient one-tap equalization only works for a low delay spread. To cover a large range of possible scenarios, I include three different Rayleigh fading channel models in my performance evaluation. Firstly, the Vehicular A channel model

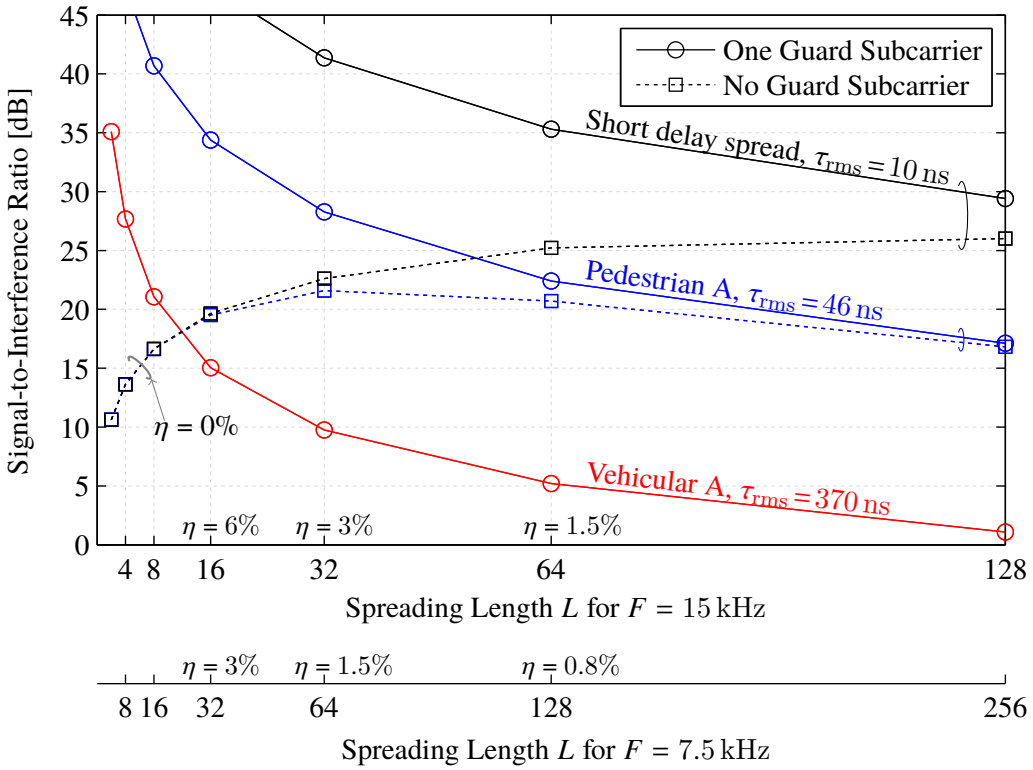

Figure 5.10. The interference can be neglected if the SIR is approximately 10 dB higher than the SNR. A guard subcarrier increases the SIR significantly, especially for a short spreading length. The higher the spreading length, the higher the spectral efficiency. However, a high spreading length also leads to a large, channel induced, interference. ©2017 IEEE, [36].

with a relatively large delay spread of 370 ns. Secondly, the Pedestrian A channel model with a moderate delay spread of 46 ns. Thirdly, a short delay spread of 10 ns for which I assume three equally spaced taps. These taps are 100 ns apart and the power of each tap is 20 dB lower then the previous tap. Such short delay spread represents, for example, an indoor scenario [25]. For those channel models, Figure 5.10 shows the SIR over spreading length L. Here, I assume a time invariant channel. In many practical cases, the SNR is below 20 dB. Thus, for a short delay spread (10 ns), one can easily spread over $L = 128$ subcarriers, leading to an almost negligible time-frequency efficiency loss of $\eta = \frac{1}{L+1} = 0.8\%$. For a Pedestrian A channel model, spreading over $L = 32$ subcarriers is feasible, leading to $\eta = 3\%$. Only for a high delay spread, my method is suboptimal because of the large overhead required for a sufficiently high SIR. As a reference, I also include the SIR in case of no guard subcarriers (dotted line). In some cases, especially for low to medium SNR ranges, one does not need a guard subcarrier, that is, $\eta = 0\%$.

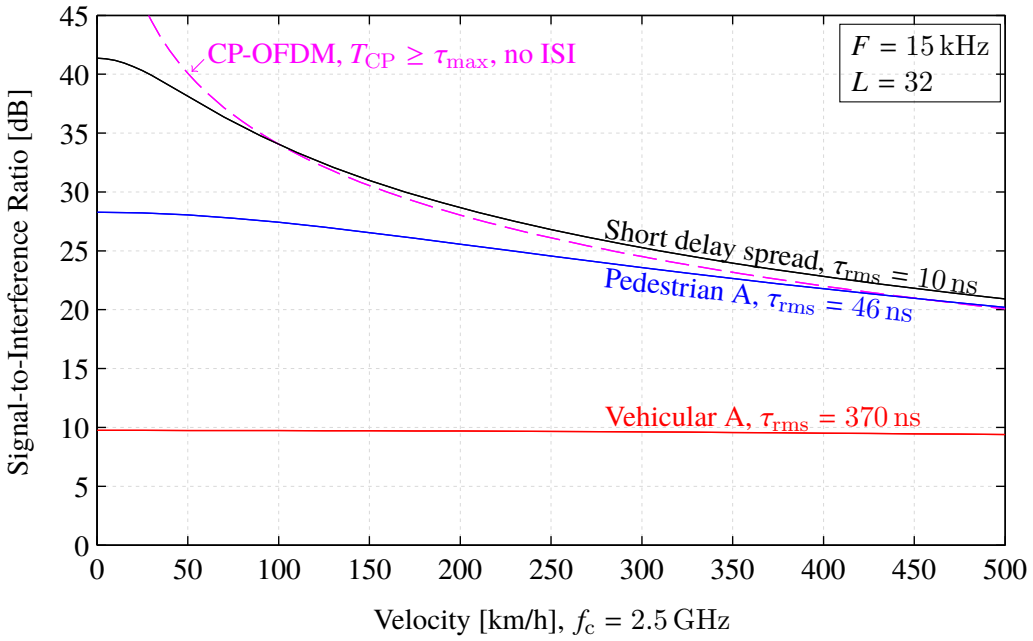

Figure 5.11. A time-variant channel causes additional interference. For high velocities, FBMC shows approximately the same SIR as OFDM. Thus, OFDM no longer performs better in terms of SIR but still has poorer spectral properties. The SIR for velocity zero can be found in Figure 5.7. ©2017 IEEE, [36].

Figure 5.11 shows how the SIR depends on the velocity. Even high velocities, such as 200 km/h, generate only small additional interference, so that the SIR remains sufficiently high for a short delay spread and a Pedestrian A channel model. Compared to the time-spreading approach, discussed in Section 5.2, frequency spreading provides higher robustness in time-variant channels. As a reference, I also include the SIR for conventional CP-OFDM.

In contrast to Section 5.2, I validate my transmission scheme by means of simulations instead of measurements, allowing a high degree of freedom in terms of channel parameters. I assume a Pedestrian A channel model and a Jakes Doppler spectrum (velocity 100 km/h at 2.5 GHz). The subcarrier spacing is set to $F = 15\,\mathrm{kHz}$ and the symbol alphabet is chosen from a 16-QAM signal constellation. For FBMC, I assume a spreading length of $L = 32$ and a total of $N_{\mathrm{B}} = 16$ frequency blocks. This leads to a transmission bandwidth of $F(L+1)N_{\mathrm{B}} = 7.92\,\mathrm{MHz}$. OFDM employs the same bandwidth, that is 528 subcarriers. Note, however, that in practice, OFDM requires an additional guard band because of the poor spectral behavior. The transmission time for both methods is the same and given by $KT = 1\,\mathrm{ms}$. The zero guard subcarrier in FBMC leads to a slightly higher SNR compared to OFDM, but only by $(L+1)/L = 1.03$ which has almost no influence.

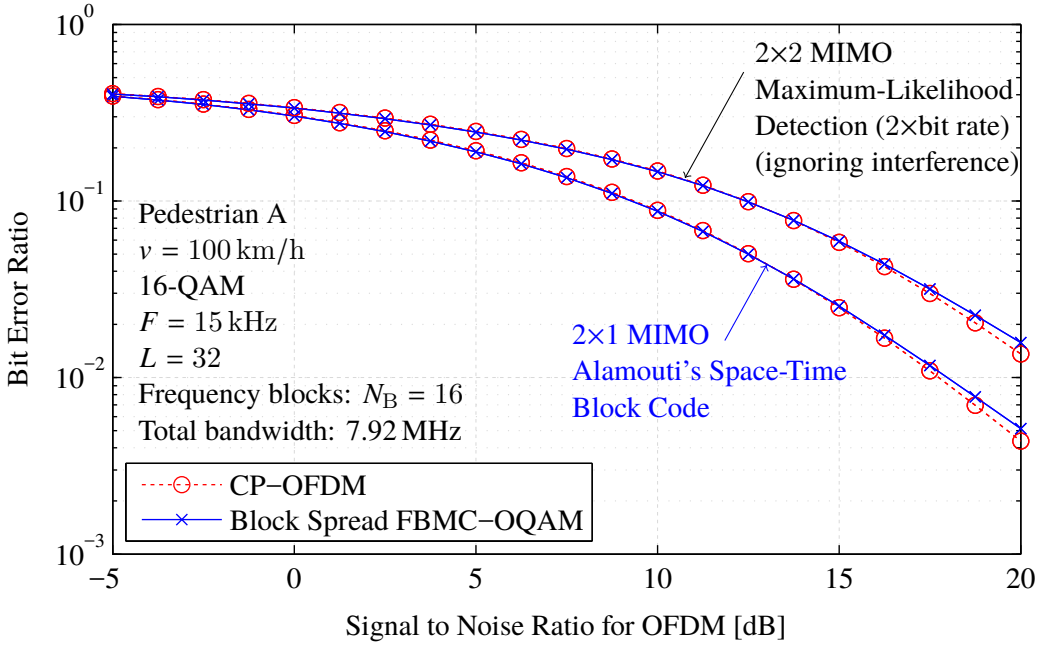

Figure 5.12. Simulations validate that the proposed block spread FBMC-OQAM transmission scheme has approximately the same BER as OFDM. However, FBMC has the additional advantage of a higher spectral efficiency because of lower OOB emissions. Only for high SNR values, the channel induced interference becomes noticeable, see also Figure 5.11. ©2017 IEEE, [36].

Similar as in Section 5.2, I consider a 2×1 Alamouti transmission scheme as well as spatial multiplexing with ML symbol detection. To keep the computational complexity low, my ML detection ignores any channel induced interference and thus represents a slightly mismatched ML detection. Figure 5.12 shows that FBMC has almost the same BER performance as OFDM, but the additional advantage of much better spectral properties. Only for high SNR values, small deviations between OFDM and FBMC are observable. This can be explained by the channel induced interference which leads to an SIR of approximately 27 dB, see Figure 5.11. Such interference, however, has no influence for low to medium SNR values. Only for high SNR values, the spreading length might need to be reduced in order to improve robustness.

Chapter 6

Pruned DFT Spread FBMC-OQAM: Reducing the PAPR

The superior spectral properties of FBMC are lost if nonlinearities become dominant [1, 55]. Thus, the concept of sharp digital filters to enable a flexible time-frequency allocation, see Figure 1.1 and Section 2.4, only works as long as FBMC operates in the linear regime. In multicarrier systems, this is hard to achieve because of a poor PAPR, caused by the overlapping structure of subcarriers in time, essentially leading to Gaussian distributed samples. The poor PAPR is one of the main disadvantages of multicarrier systems. To reduce the PAPR in OFDM, several techniques have been suggested, such as, selective mapping [155] or partial transmit sequences [156]. Those methods can be extended to FBMC, as demonstrated, for example, in [157–159]. However, all those techniques require a high computational complexity and side information. Those drawbacks explain why they are not employed in practical systems. Instead, LTE uses SC-FDMA in the uplink [160], essentially, a DFT precoded OFDM system. The same technique will also be included in 5G [7]. The advantages of SC-FDMA compared with other PAPR reduction techniques are a relatively low computational complexity and that no side information is necessary. The disadvantages, compared with pure OFDM, are a slightly lower throughput and a slightly higher computational complexity.

Simply combining FBMC and a DFT, as done in SC-FDMA for OFDM, performs poorly in FBMC [161–163]. To improve the performance, authors in [161] propose precoding by a filter bank instead of a DFT. While such method reduces the PAPR, it still does not perform as good as SC-FDMA and has the additional disadvantages of a higher computational complexity and an increased overhead. To overcome those limitations, I propose a novel modulation scheme based on a pruned DFT in combination with one-tap scaling. My proposed technique has the same PAPR as SC-FDMA but requires no CP and has much better

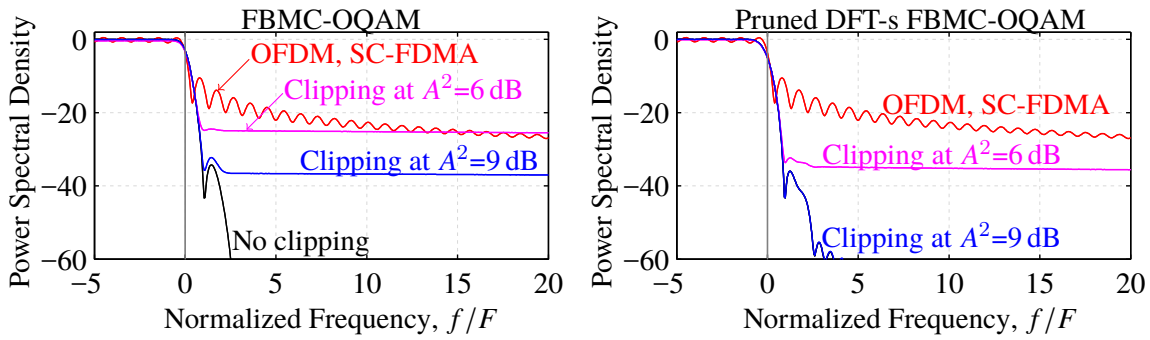

Figure 6.1. Nonlinearities, such as clipping, destroy the superior spectral properties of FBMC. Thus, a flexible time-frequency allocation, as illustrated in Figure 1.1, is not possible anymore. To overcome this limitation, I propose a novel transmission scheme, pruned DFT spread FBMC-OQAM, which is less sensitive to nonlinearities.

spectral properties. Furthermore, my method restores complex orthogonality and allows for low latency transmissions. Compared to pure SC-FDMA, the computational complexity is only two times higher. This chapter is mainly based on my publication in [33], currently under review, and contains the following novel contributions:

- In Section 6.1, I describe the basic idea of pruned DFT spread FBMC and discuss its relationship to other transmission techniques.
- In Section 6.2, I provide a comprehensive mathematical description of pruned DFT spread FBMC. Furthermore, I propose the usage of CP subcarriers. Such overhead is usually not necessary, but might be needed if the spreading length is small.
- Finally, in Section 6.3, I compare my method to OFDM, SC-FDMA and conventional FBMC in terms of PAPR and throughput.

6.1 Introduction

To get a better understanding of how nonlinearities affect the PSD, I consider a simple clipping example. Here, the real part of the signal is clipped to a fixed value of $\pm A\sqrt{\bar{P}_S/2}$ as soon as the signal is larger/smaller than a certain threshold, that is, $\Re\{s(t)\} \gtrless A\sqrt{\bar{P}_S/2}$. The same applies for the imaginary part. The left part of Figure 6.1 shows that clipping destroys the superior spectral properties of conventional FBMC. This is a major problem because one of the biggest advantages of FBMC is lost. Thus, having a low PAPR is a crucial aspect for all filter based modulation schemes. The right part of Figure 6.1 shows the PSD of my

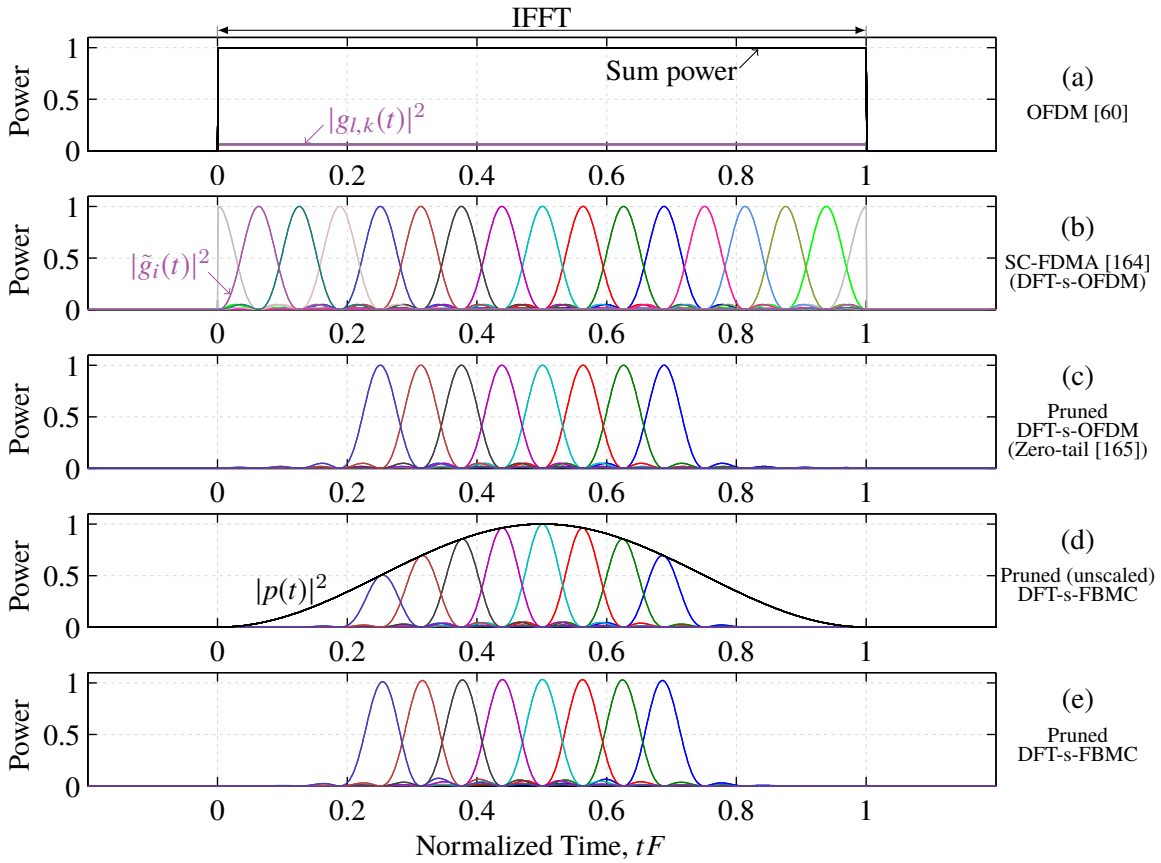

Figure 6.2. Power of the underlying basis pulses in time, that is, $|g_{l,k}(t)|^2$ and $|\tilde{g}_i(t)|^2$; (a) conventional OFDM, $N_{\mathrm{FFT}} = 1024$, $L = 16$; (b) conventional SC-FDMA, that is, precoding by DFT matrix $\mathbf{W}_L$; (c) only $L/2 = 8$ basis pulses, close to the center, are utilized, that is, $\mathbf{W}_L$ is replaced by a pruned DFT matrix, $\widetilde{\mathbf{W}}_{L\times L/2}$; (d) multiply by a window/prototype filter $p(t)$, so that OFDM transforms into FBMC; (e) one-tap scaling of the basis pulses so that the transmit power is approximately constant over time.

pruned DFT spread FBMC transmission scheme. My method performs much better than conventional FBMC. The possible improvement in terms of OOB emissions is 10 dB for $A^2 = 6\,\mathrm{dB}$ and 35 dB for $A^2 = 9\,\mathrm{dB}$.

The basic idea of my transmission scheme can be best explained with the underlying basis pulses. Figure 6.2 shows the power of those basis pulses and illustrates a step by step construction of my method, starting from a conventional OFDM system. Figure 6.2 (a) represents an OFDM transmission for $N_{\mathrm{FFT}} = 1024$, $L = 16$ and $K = 1$. The underlying basis pulses are rectangular functions which are shifted in frequency, see (2.12). However, in terms of transmit power, a frequency shift has no influence. All the basis pulses are added together with some random weights (the data symbols), so that, according to the central limit theorem, the signal distribution at one time position approaches a Gaussian distribution. This

explains the poor PAPR performance of OFDM. In SC-FDMA, see Figure 6.2 (b), DFT precoding by $\mathbf{W}_L$ transforms the basis pulses of a conventional OFDM system in such a way, that a single carrier transmission is emulated. In particular, the basis pulses are more localized in time and even though they still overlap in time, the signal distribution at one time position is mainly determined by 1-2 basis pulses. Thus, as long as the data symbols are not Gaussian distributed, but chosen from a limited signal constellation such as QAM, the PAPR will be better than in OFDM. Unfortunately, SC-FDMA has the same poor OOB emissions as OFDM. This can easily be deduced by considering the transmitted signal at the edge positions, that is, $tF = 0$ and $tF = 1$. Similar as in OFDM, the underlying rectangular pulse cuts through the signal so that, at the edges, the signal value abruptly jumps to zero without a smooth transition. Only basis pulses close to the edge positions are affected by this cutting effect. Thus, setting the basis pulses at the edges to zero, reduces the OOB emissions and is indeed the basic idea of zero-tail DFT-spread-OFDM [165, 166]. However, authors in [165, 166] remove only a few basis pulses to keep the overhead low. I, on the other hand, remove $\frac{L}{2}$ basis pulses from the set, that is, DFT spreading matrix $\mathbf{W}_L$ is replaced by a pruned DFT matrix $\widetilde{\mathbf{W}}_{L\times L/2}$. In contrast to zero-tail DFT-spread-OFDM, however, my method does not impose any overhead because I also reduce the time spacing by a factor of two, as typically done in FBMC-OQAM. The result of my approach is shown in Figure 6.2 (c). The reason why I remove exactly $\frac{L}{2}$ basis pulses is motivated by my observation in Section 5.1, which provides a theoretical background on the optimal spreading matrix and, in particular, its size. To combat multipath delays, zero-tail DFT-spread-OFDM utilizes the zero-tail overhead in a similar way as the CP in OFDM, reducing the spectral efficiency. Again, I choose a different approach, namely, I transform the OFDM system into an FBMC system, so that the influence of multipath propagation becomes very low and can usually be neglected, see Section 3.1.2. As shown in Section 2.3, an OFDM system can easily be transformed into an FBMC system simply by multiplying the IFFT output with a prototype filter $p(t)$, as illustrated in Figure 6.2 (d). In the last step, the individual basis pulses are scaled so that the sum transmit power is approximately constant over the transmission time. This final step completes my novel pruned DFT spread FBMC transmission scheme, see Figure 6.2 (e). To keep the illustration in Figure 6.2 simple, I consider a root-raised cosine pulse in time (roll-off factor one, time length $\frac{1}{F}$). However, in Section 6.2- 6.3, I employ a truncated Hermite pulse of length $1.56\frac{1}{F}$ (seconds). In particular, the IFFT output has to be repeated so that it covers the full length of the prototype filter, as already explained in Section 2.3.

With respect to other modulation schemes, my method is related to zero-tail DFT-spread-OFDM [165, 166] and FFT-FBMC [70, 167], although the differences are still severe. Compared to zero-tail DFT-spread-OFDM, my method does not need any overhead and has

much better spectral properties. Compared to FFT-FBMC, I spread in frequency instead of time, include one-tap scaling, employ a modified prototype filter, and focus on the PAPR performance as well as the latency. Furthermore, the channel may vary within the spreading interval while FFT-FBMC relies on a time invariant channel. FFT-FBMC is therefore more closely related to block spread FBMC, see Chapter 5. The key difference between pruned DFT spread and block spread FBMC is that in pruned DFT spread FBMC, data symbols are spread over the whole bandwidth, while for block spread FBMC the bandwidth is split into smaller chunks. These small chunks can then be equalized by a simple one-tap equalizer, so that Alamouti's space-time block code and ML MIMO detection becomes feasible. In pruned DFT spread FBMC, on the other hand, ML detection is often not possible. However, this is not a big problem because the focus lies on a low PAPR. Furthermore, SC-FDMA has the same drawback. The advantages and possible disadvantages of my novel pruned DFT spread FBMC transmission scheme, can be summarized as follows:
Advantages:

- Low PAPR, same as in SC-FDMA.
- Low OOB emissions, comparable to FBMC.
- Low latency, only slightly higher than in OFDM.
- Complex orthogonality is restored, therefore an efficient multi-user uplink transmission is possible.
- Maximum symbol density, $TF = 1$ (complex), same as in FBMC.
- Low-complexity one-tap equalizers can be used.
- Relatively high robustness in doubly-selective channels.

Possible disadvantages:

- Slightly higher computational complexity, approximately two times that of SC-FDMA.
- Only quasi-orthogonal, that is, some small residual interference remains. This, however, is usually not a problem. Furthermore, a frequency CP can reduce this interference.
- Low-complexity ML MIMO detection only works if the channel is approximately flat within the spreading interval (same problem as in SC-FDMA).
- Throughput is slightly lower than in multicarrier systems because of the spreading (same problem as in SC-FDMA).

6.2 Mathematical Details of the Novel Approach

I will now mathematically describe my pruned DFT spread FBMC transmission scheme in more detail. I stack all basis pulses, belonging to time-position k, into matrix $\mathbf{G}_k \in \mathbb{C}^{N \times L}$, according to

$$\mathbf{G}_k = \begin{bmatrix} \mathbf{g}_{1,k} & \dots & \mathbf{g}_{L,k} \end{bmatrix}. \tag{6.1}$$

The overall transmit signal can then be modeled, similar as in Section 2.2, by

$$\mathbf{s} = \sum_{k=1}^{K} \mathbf{G}_k \mathbf{x}_k = \mathbf{G}\,\mathbf{x}, \tag{6.2}$$

where $\mathbf{x}_k = [x_{1,k} \quad \dots \quad x_{L,k}]^{\mathsf{T}} \in \mathbb{C}^{L \times 1}$ consists of all data symbols belonging to time-position k. The overall transmission system is described by, see (2.31),

$$\mathbf{y} \approx \mathrm{diag}\{\mathbf{h}\}\, \mathbf{Q}^{\mathsf{H}} \mathbf{G}\, \mathbf{x} + \mathbf{n}. \tag{6.3}$$

Similar as in Section 5.3, I spread $L/2$ complex valued data symbols, $\tilde{\mathbf{x}}_k \in \mathbb{C}^{\frac{L}{2} \times 1}$, over L subcarriers, so that the transmitted symbols for FBMC at time position k become:

$$\mathbf{x}_k = \mathbf{C}_f\, \tilde{\mathbf{x}}_k, \tag{6.4}$$

with $\mathbf{C}_f \in \mathbb{C}^{L \times \frac{L}{2}}$ denoting the frequency spreading matrix. In contrast to conventional FBMC, the transmitted symbols are now complex-valued. Note that the size of spreading matrix $\mathbf{C}_f$ is optimal, as already discussed in Section 5.1. The received data symbols $\tilde{\mathbf{y}}_k \in \mathbb{C}^{\frac{L}{2} \times 1}$ are obtained by one-tap equalization of the received symbols with $\mathbf{e}_k \in \mathbb{C}^{L \times 1}$, followed by despreading according to

$$\tilde{\mathbf{y}}_k = \mathbf{C}_f^{\mathsf{H}}\, \mathrm{diag}\{\mathbf{e}_k\}^{-1}\, \mathbf{y}_k. \tag{6.5}$$

For the derivation of spreading matrix $\mathbf{C}_f$, I assume an AWGN channel, $\mathbf{H} = \mathbf{I}_N$, for which no equalization is necessary. The ultimate goal is to restore complex orthogonality, that is,

$$\mathbf{C}_f^{\mathsf{H}} \mathbf{Q}_k^{\mathsf{H}} \mathbf{G}_k \mathbf{C}_f \approx \mathbf{I}_{L/2}. \tag{6.6}$$

The approximation symbol in (6.6) indicates that some small residual interference remains so that the system is only quasi orthogonal. However, in many practical cases, this has no impact on the performance. In a first step, I assume that the spreading and despreading is

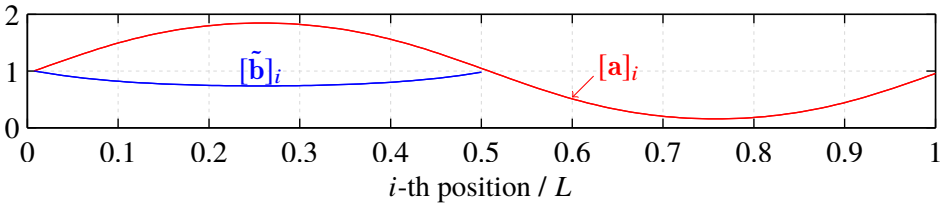

Figure 6.3. Equalizing $L/2$ largest elements of $\mathbf{a}$ delivers the scaling values $\tilde{\mathbf{b}}$. These scaling values guarantee that the transmit power is approximately constant over time. Note that element $[\mathbf{a}]_i$ corresponds to the i-th column vector of $\mathbf{W}$.

performed by a DFT matrix $\mathbf{W} \in \mathbb{C}^{L\times L}$, so that the left part of (6.6) can be rewritten as:

$$\mathbf{a} = \mathrm{diag}\{\mathbf{W}^{\mathsf{H}}\mathbf{Q}_k^{\mathsf{H}}\mathbf{G}_k\mathbf{W}\}, \tag{6.7}$$

with $\mathbf{a} \in \mathbb{R}^{L\times 1}$ denoting an auxiliary vector. Figure 6.3 shows how $[\mathbf{a}]_i$ depends on position i. Note that element $[\mathbf{a}]_i$ corresponds to the i-th column vector of $\mathbf{W}$. The main idea of my transmission scheme is to utilize only those column vectors of $\mathbf{W}$, which correspond to the $\frac{L}{2}$ largest elements of $\mathbf{a}$. This means only the first $\frac{L}{2}$ column vectors of $\mathbf{W}$ are employed. Furthermore, I perform pre-equalization of $[\mathbf{a}]_i$. The final spreading matrix $\mathbf{C}_f \in \mathbb{C}^{L\times\frac{L}{2}}$ can then be expressed by

$$\mathbf{C}_f = \widetilde{\mathbf{W}}\,\mathrm{diag}\{\tilde{\mathbf{b}}\}, \tag{6.8}$$

with pruned DFT matrix $\widetilde{\mathbf{W}} \in \mathbb{C}^{L\times\frac{L}{2}}$ and scaling vector $\tilde{\mathbf{b}} \in \mathbb{R}^{\frac{L}{2}\times 1}$ given by:

$$[\tilde{\mathbf{b}}]_i = \sqrt{\frac{1}{[\mathbf{a}]_i}} \quad ; \text{for} \quad i = 1, 2, \ldots, \frac{L}{2}, \tag{6.9}$$

$$\widetilde{\mathbf{W}} = \mathbf{W}\begin{bmatrix}\mathbf{I}_{\frac{L}{2}}\\ \mathbf{0}_{\frac{L}{2}}\end{bmatrix}. \tag{6.10}$$

The whole transmission system is depicted in Figure 6.4. The gray areas indicate the novel parts. To be specific, I spread and de-spread data symbols with $\mathbf{C}_f$ and employ a truncated Hermite prototype filter, that is, a conventional Hermite prototype filter, see (2.15), for which the pulse is set to zero after the first zero-crossing. This leads to a pulse length of $1.56\frac{1}{F}$ (seconds) where $O = 1.56$ also represents the overlapping factor in FBMC. Note that other prototype filters are also possible and there exists a trade-off between OOB emissions and latency.

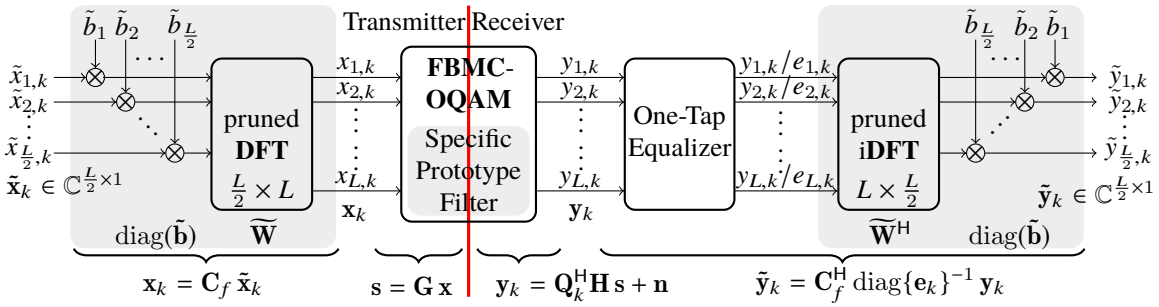

Figure 6.4. Block diagram of pruned DFT spread FBMC-OQAM at time position k. The gray boxes highlight the novel parts, that is, precoding by $\mathbf{C}_f$, a modified prototype filter (truncated Hermite) and decoding by $\mathbf{C}_f^{\mathsf{H}}$.

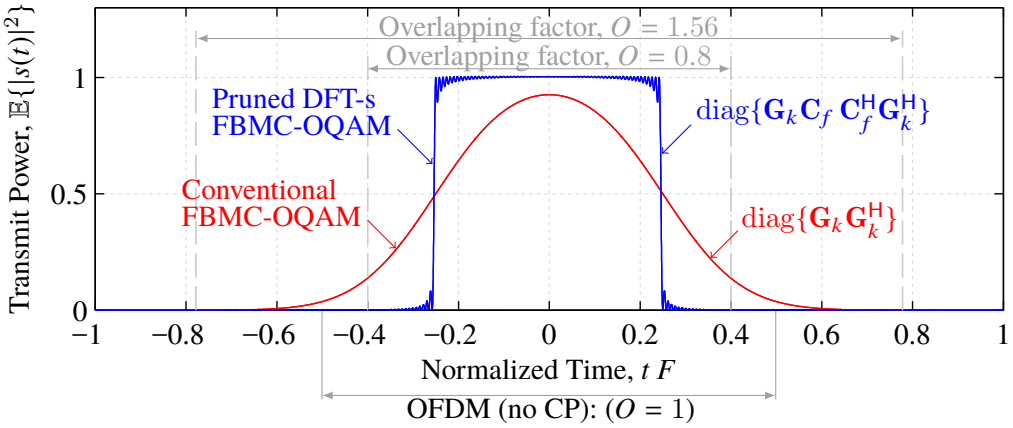

Figure 6.5. Precoding matrix $\mathbf{C}_f$ shapes the average transmit power, that is, the diagonal elements of $\mathbb{E}\{\mathbf{s}_k\mathbf{s}_k^{\mathsf{H}}\} = \mathbf{G}_k\mathbf{C}_f\,\mathbf{C}_f^{\mathsf{H}}\mathbf{G}_k^{\mathsf{H}}$, achieving an almost perfect rectangular shape with many beneficial properties.

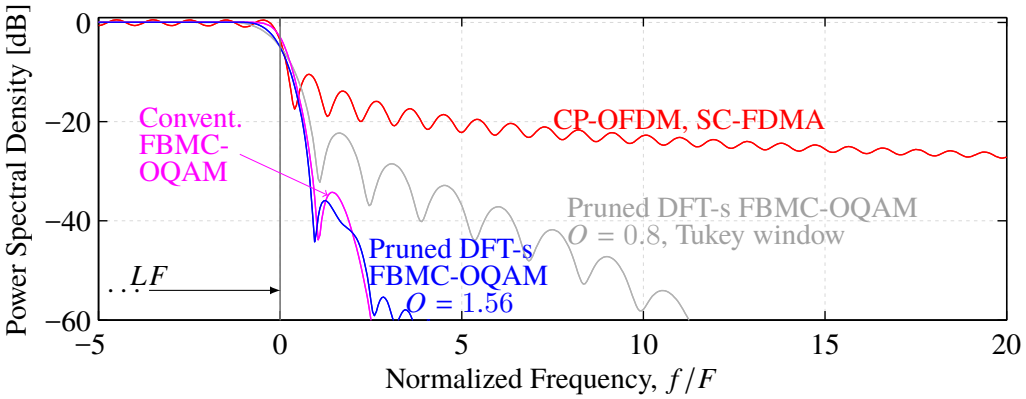

Figure 6.6. The superior spectral properties of FBMC are preserved in pruned DFT Spread FBMC-OQAM. Decreasing the overlapping factor, see Figure 6.5, reduces the latency but also leads to poorer OOB emissions. Thus, there is a trade-off.

Figure 6.5 shows the expected transmit power for one time-position (ignoring other symbols in time). In conventional FBMC, there exists a large overlapping of symbols in time. In pruned DFT spread FBMC, on the other hand, precoding by $\mathbf{C}_f$ shapes the transmitted signal in such a way, that the overlapping in time is very low. This is very important for low-latency transmissions and to keep the computational complexity low. Furthermore, an efficient multi-user uplink transmission becomes feasible because phase synchronous transmission, an unrealistic assumption and a major problem in conventional FBMC uplink, is no longer necessary. The latency can be further reduced by decreasing the overlapping factor in combination with windowing. However, this comes at the expense of higher OOB emissions, as shown in Figure 6.6. Still, the OOB emissions are much better than in OFDM. For an overlapping factor of $O = 1.56$, the OOB emissions of my method are comparable to conventional FBMC transmissions and much better than in OFDM. Note that a similar precoding effect, as shown in Figure 6.5, was also observed in FFT-FBMC [167], but in the frequency domain instead of the time domain.

Let me now discuss the latency in more detail. The transmission time of one FBMC symbol depends on the overlapping factor and requires $\frac{O}{F}$ (seconds). However, one FBMC symbol only carries half the information of that of an OFDM symbol. Thus, one might need to include the second symbol, leading to an additional delay of $T = \frac{0.5}{F}$, that is, the time spacing. For example, an overlapping factor of $O = 0.8$ implies that the first half of the information is received 20% faster than in OFDM (no CP) while the second half needs 30% longer.

The computational complexity of my transmission scheme is approximately two times higher than in conventional SC-FDMA. To be specific, the computational complexity relative to SC-FDMA at the transmitter can be approximated by

$$\frac{C_{\mathrm{pDFTsFBMC}}}{C_{\mathrm{SCFDMA}}} \approx \frac{2\left(\frac{L}{2} + L\log\frac{L}{2} + N_{\mathrm{FFT}}\,\log N_{\mathrm{FFT}} + ON_{\mathrm{FFT}}\right)}{L\,\log L + N_{\mathrm{FFT}}\,\log N_{\mathrm{FFT}}} \approx 2. \tag{6.11}$$

The term $N_{\mathrm{FFT}}\,\log N_{\mathrm{FFT}}$ corresponds to the IFFT, required for both, FBMC and OFDM. Additionally, FBMC requires element-wise multiplication by the prototype filter, see Section 2.3, leading to an additional complexity of ON_{FFT}. Furthermore, DFT spreading in SC-FDMA has a complexity of $L\,\log L$, while the pruned DFT in combination with one-tap scaling requires $\frac{L}{2} + L\log\frac{L}{2}$. Finally, the reduced time-spacing in FBMC implies that all the calculations have to be applied two times as often as in SC-FDMA (no CP).

Although I shape the transmit signal in time by $\mathbf{C}_f$, see Figure 6.5, there still exists some residual interference between blocks. Furthermore, only quasi orthogonality is restored within one block. To quantify those effects, I calculate the SIR. The pruned DFT spread

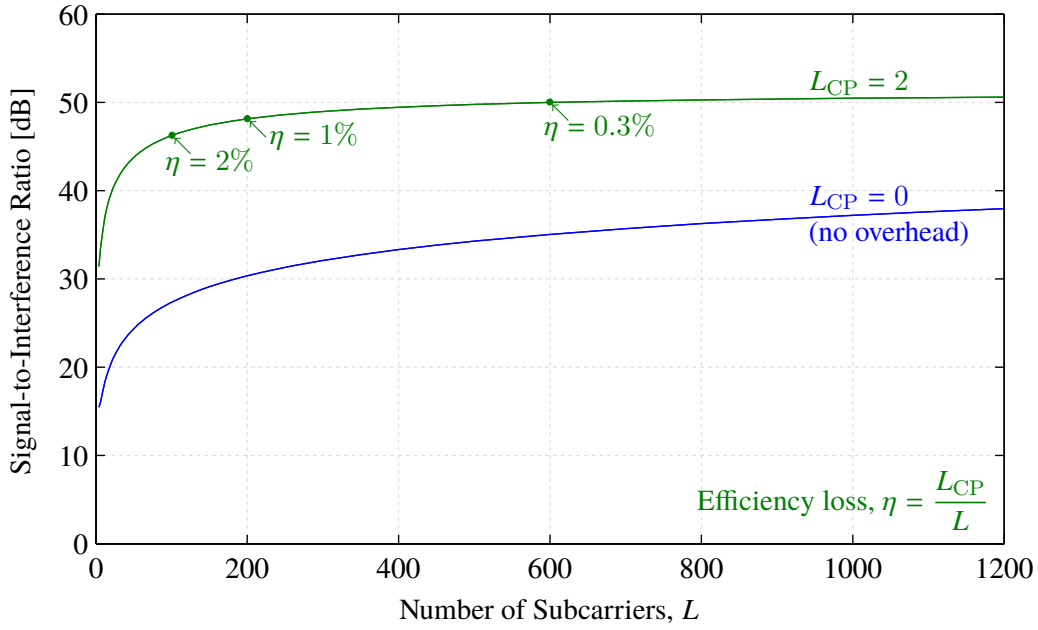

Figure 6.7. The SIR is so high, that interference can usually be neglected. Only if the number of subcarriers is very small, a frequency CP might be necessary, slightly reducing the spectral efficiency.

FBMC transmission matrix can be expressed by

$$\widetilde{\mathbf{D}} = (\mathbf{I}_K \otimes \mathbf{C}_f)^{\mathsf{H}} \, \mathbf{Q}^{\mathsf{H}} \mathbf{G} \, (\mathbf{I}_K \otimes \mathbf{C}_f), \tag{6.12}$$

and describes the input-output relation $\tilde{\mathbf{y}} = \widetilde{\mathbf{D}} \, \tilde{\mathbf{x}}$ in case of zero noise, $\mathbf{n} = \mathbf{0}_{N\times 1}$. The Kronecker product in (6.12) maps the frequency spreading matrix to the correct time-positions. Utilizing (6.12), the SIR can be straightforwardly calculated by

$$\mathrm{SIR} = \frac{\sum_{i=1}^{\frac{L}{2}K} |[\widetilde{\mathbf{D}}]_{i,i}|^2}{\sum_{i=1}^{\frac{L}{2}K} \sum_{j=1}^{\frac{L}{2}K} |[\widetilde{\mathbf{D}}]_{i,j}|^2 - \sum_{i=1}^{\frac{L}{2}K} |[\widetilde{\mathbf{D}}]_{i,i}|^2}. \tag{6.13}$$

The blue curve in Figure 6.7 shows the SIR over the number of subcarriers. For a large number of subcarriers, the SIR is so high, that the interference is usually dominated by noise. However, sometimes a higher SIR might be required. This can easily be accomplished with a frequency CP/suffix, that is, a cyclical extension of the signal in the frequency domain. The drawback is a small reduction in spectral efficiency. The CP at the transmitter can be modeled by matrix $\mathbf{T}_{\mathrm{CP}} \in \mathbb{C}^{L\times(L-L_{\mathrm{CP}})}$ and the CP reduction at the receiver by $\mathbf{R}_{\mathrm{CP}} \in \mathbb{C}^{L\times(L-L_{\mathrm{CP}})}$. For

example, a frequency CP of length $L_{\mathrm{CP}} = 2$ leads to

$$\mathbf{T}_{\mathrm{CP}} = \begin{bmatrix} 0 & 0 & \cdots & 0 & 1 \\ & & \mathbf{I}_{L-2} & & \\ 1 & 0 & \cdots & 0 & 0 \end{bmatrix}; \qquad \mathbf{R}_{\mathrm{CP}} = \begin{bmatrix} 0 & \cdots & 0 \\ & \mathbf{I}_{L-2} & \\ 0 & \cdots & 0 \end{bmatrix}, \tag{6.14}$$

and guarantees that $x_{1,k} = x_{L-1,k}$ and $x_{L,k} = x_{2,k}$. Compared to the previous coding matrix, see (6.8), the new matrices $\mathbf{C}_{\mathrm{f,TX}} \in \mathbb{C}^{L \times \frac{L-L_{\mathrm{CP}}}{2}}$ and $\mathbf{C}_{\mathrm{f,RX}} \in \mathbb{C}^{L \times \frac{L-L_{\mathrm{CP}}}{2}}$ change according to:

$$\mathbf{C}_{\mathrm{f,TX}} = \mathbf{T}_{\mathrm{CP}}\, \widetilde{\mathbf{W}}\, \mathrm{diag}\{\tilde{\mathbf{b}}\} \tag{6.15}$$

$$\mathbf{C}_{\mathrm{f,RX}} = \mathbf{R}_{\mathrm{CP}}\, \widetilde{\mathbf{W}}\, \mathrm{diag}\{\tilde{\mathbf{b}}\}. \tag{6.16}$$

Furthermore, pruned DFT matrix $\widetilde{\mathbf{W}} \in \mathbb{C}^{(L-L_{\mathrm{CP}}) \times \frac{L-L_{\mathrm{CP}}}{2}}$ and scaling vector $\mathbf{b} \in \mathbb{R}^{\frac{L-L_{\mathrm{CP}}}{2} \times 1}$ now also have different dimensions. The process of finding $\widetilde{\mathbf{W}}$ and $\mathbf{b}$, however, is the same as described in (6.6)-(6.10). Figure 6.7 shows that a frequency CP can significantly improve the SIR while the efficiency loss, given by $\eta = \frac{L_{\mathrm{CP}}}{L}$, is relatively small.

6.3 Performance Evaluation

Figure 6.8 shows the Complementary Cumulative Distribution Function (CCDF) of the PAPR. A simple DFT spread FBMC transmission scheme, as propose in [161], performs poorly. In contrast to that, my method performs as good as SC-FDMA. By including a frequency CP, the PAPR can be further improved at the expense of spectral efficiency.

In the following simulations, I utilize the 3GPP 38.900 TDL-A channel model [93, Section 7.7.3]. For such channel model, Figure 6.9 shows the throughput, that is, turbo coding in combination with an adaptive modulation and coding scheme, similar as in LTE. The detection is based on a one-tap MMSE-MIMO equalizer, where"one-tap" means a per time-frequency position equalization. Although not shown directly, SC-FDMA without CP is severely effected by the long delay spread while the delay spread has almost no influence on my pruned DFT spread FBMC transmission scheme. Of course, SC-FDMA with CP is also not effected by the long delay spread because of the CP. However, in contrast to my transmission scheme, SC-FDMA is severely effected by the high velocity. This explains why in Figure 6.9, my method performs much better than SC-FDMA. Of course, some of the improvement also comes from the fact that my scheme does not need a CP. Conventional FBMC performs best because the log likelihood ratios include the fading states, whereas spreading destroys this information (for a low complexity detection). Note that I ignore guard subcarriers in my considerations here. Thus, the true performance of FBMC compared

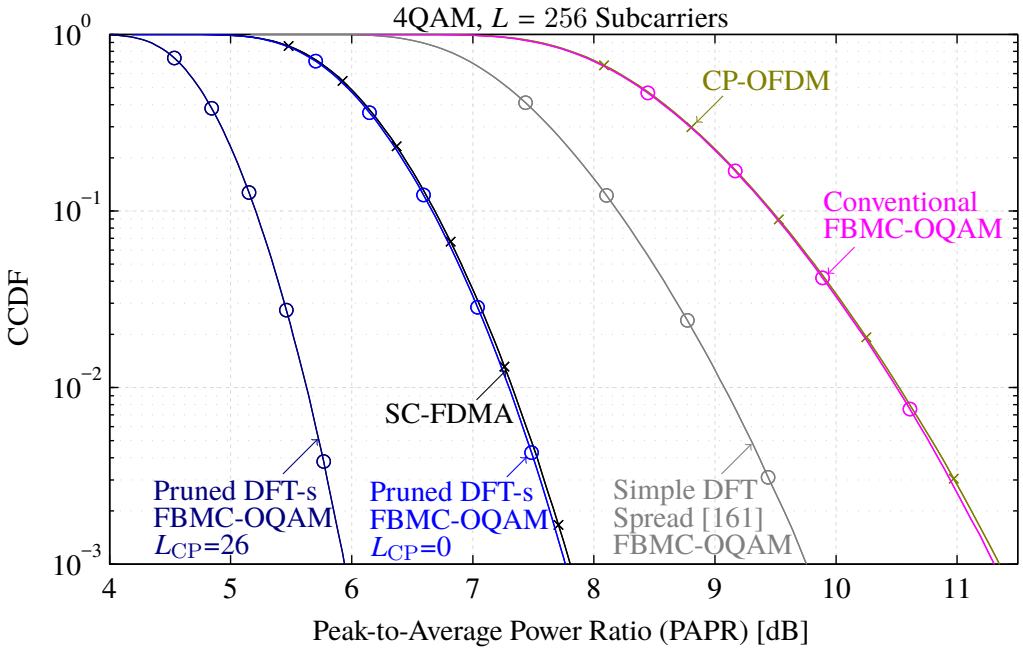

Figure 6.8. Pruned DFT spread FBMC-OQAM has the same PAPR as SC-FDMA but the additional advantages of a higher throughput and much lower OOB emissions. By employing a frequency CP, the PAPR can be further improved at the expense of spectral efficiency.

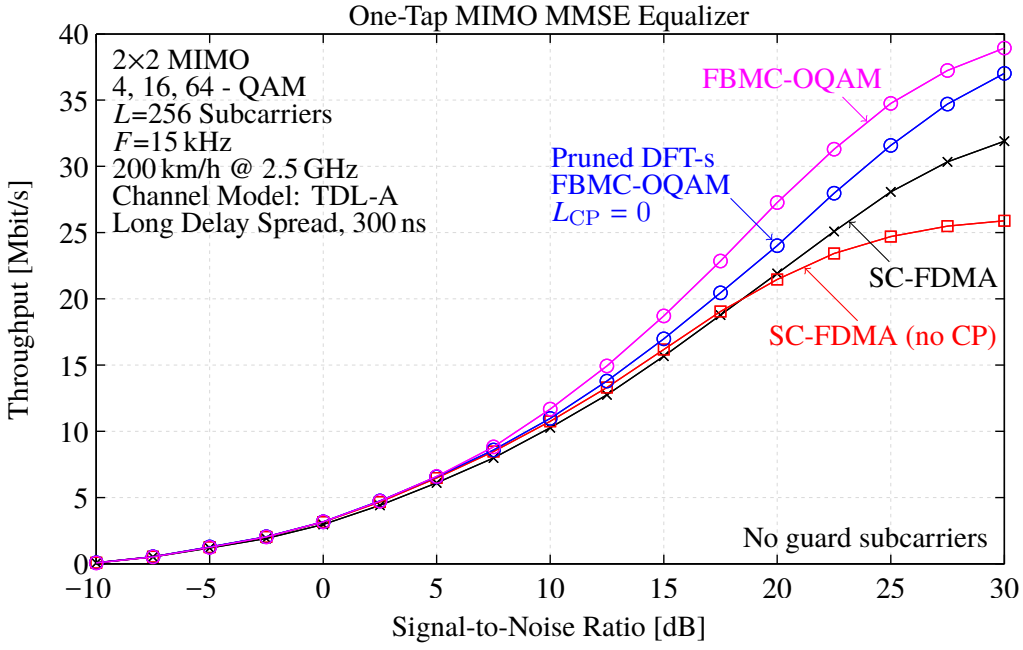

Figure 6.9. Pruned DFT spread FBMC-OQAM performs much better than SC-FDMA. Conventional FBMC-OQAM performs best because the channel decoder can exploit different fading states, while spreading destroys this information.

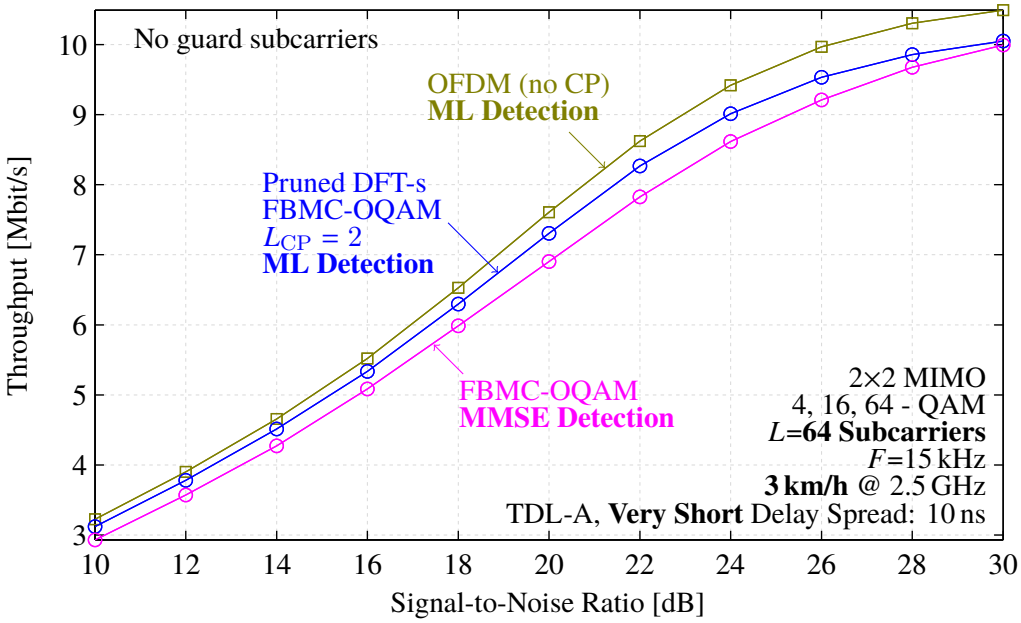

Figure 6.10. In contrast to conventional FBMC-OQAM, ML-MIMO detection is feasible in pruned DFT spread FBMC-OQAM, leading to a higher throughput. OFDM performs best because no CP is necessary. However, once guard subcarriers are included, pruned DFT spread FBMC will outperform OFDM.

to OFDM is even better than illustrated in Figure 6.9 because fewer guard subcarriers are needed.

Figure 6.10 shows the throughput for a very short delay spread and a small number of subcarriers, as I expect, for example, in indoor Machine to Machine (M2M) communications. The channel is approximately flat within the transmission bandwidth, allowing to de-spread before equalization, leading to a similar scenario as discussed in Chapter 5. In particular, low complexity ML detection becomes possible because pruned DFT spread FBMC restores complex orthogonality. This is not the case in conventional FBMC, so that ML detection is not feasible. Still, my method performs slightly worse than OFDM because of the frequency CP, required as the number of subcarriers is relatively small. However, once guard subcarriers are included, my method will outperform even OFDM.

Chapter 7

Conclusions

Future wireless systems will have to support a large range of different use cases within the same band. This is difficult in legacy CP-OFDM because of the poor OOB emissions. There exists methods to reduce the OOB emissions in OFDM, such as windowing and filtering, but they are only efficient if the number of subcarriers is high. Not all possible use cases envisioned for future wireless systems will employ such a high number of subcarriers, so that FBMC becomes an efficient alternative to OFDM, because it has much better spectral properties. Although FBMC has many advantages, it also requires some special treatment because of the intrinsic imaginary interference. In this thesis, I have shown that many challenges associated with FBMC, such as channel estimation and MIMO, can be efficiently dealt with. Furthermore, in contrast to most other papers, my proposed solutions are validated by real world testbed measurement and a downloadable MATLAB code supports reproducibility.

I employ a matrix-based system model which greatly simplifies analytical evaluations. Even highly sophisticated concepts, such as doubly-selective channel estimation and equalization, become very easy to handle. Additionally, my matrix notation helps in understanding that there is, from a conceptional point of view, no difference between the signal generation in windowed OFDM and FBMC. Thus, the overly complicated polyphase description is not needed to find an efficient IFFT based implementation.

One-tap equalizers are in most practical cases sufficient for FBMC once the subcarrier spacing is matched to the channel. I have shown this by deriving closed-form solutions for the BEP and the SIR. Thus, sophisticated equalization methods are usually not worth the effort and their usefulness is often overstated in literature. Still, for the sake of completeness, I have also proposed enhanced equalization methods, namely, an MMSE equalizer and a low-complexity interference cancellation scheme. Thanks to my matrix notation, those equalizers can be straightforwardly extended to MIMO transmission systems.

Channel estimation is always required in practical systems and therefore an integral part of my thesis. I have discussed different methods to cancel the imaginary interference at the pilot positions. By applying two auxiliary symbols instead of one, as usually done in literature, I am able to improve the throughput for low to medium SNR values because the saved power offsets the loss of data symbols. I have also formulated general conditions for the auxiliary symbols, enabling closely spaced pilots. Many authors claim that the BER in case of auxiliary symbols performs poorly when compared to OFDM. This is not true once a fair power distribution between pilot and data symbols is considered, especially if the pilot-to-data power offset is optimized. My testbed measurements have shown that the data spreading approach performs best, at the expense of a higher computational complexity, which, however, is still manageable. I have further improved the data spreading approach by proposing an algorithm that allows spreading over arbitrary many time-frequency positions. For highly double-selective channels, I have proposed a novel channel estimation technique which performs close to perfect channel knowledge and outperforms existing methods in the sense that clustered pilots and basis expansions are not necessary. In the context of OFDM, the feasibility of my approach was even validated by real world testbed measurements at velocities of up to 400 km/h.

By spreading data symbols in time or frequency, complex orthogonality can be restored in FBMC-OQAM, allowing to straightforwardly employ all methods known in OFDM. I have derived the optimal spreading matrix and proposed two different interpretations of such spreading, either in the code dimension, or by transforming the basis pulses. Although the optimal spreading matrix provides analytical insights, a more practical solution is based on Walsh-Hadamard spreading because it requires almost no additional complexity and performs close to the optimum. Because different spreading blocks interfere with each other, I have proposed the usage of guard symbols. This slightly reduces the spectral efficiency but improves the SIR. The underlying assumption of block spread FBMC is a flat channel within the spreading interval. In mildly-selective channels, this assumption is often true, as I have shown by deriving closed-form SIR expressions. The feasibility of my block spread FBMC transmission scheme was validated by real world testbed measurements at a carrier frequency of 2.5 GHz as well as 60 GHz.

One of the most important contributions of this thesis is pruned DFT spread FBMC, which has the remarkable properties of a low PAPR, low latency transmissions and a high spectral efficiency. Pruned DFT spread FBMC outperforms SC-FDMA in almost all aspects. It is more robust in doubly-selective channels, requires no CP and has much lower OOB emissions. If the channel is approximately flat within the transmission bandwidth, pruned DFT spread FBMC even outperforms conventional FBMC-OQAM in terms of throughput

because low-complexity ML-MIMO detection becomes feasible. Potential applications of my scheme include uplink transmissions in wireless communications as well as M2M communications, where the good time-frequency localization guarantees that no sophisticated synchronization between users is necessary.

Open Issues

Although this thesis provides a comprehensive overview of FBMC and covers a large range of different topics, not all possible aspects are included. In this subsection, I will give a short overview of possible future research directions.

So far, I only considered average performances. In terms of user experience, however, it is often more important to have a steady performance without large fluctuations. In this sense, the deep fading states in Figure 1.5 are problematic. This is even more true if the channel is relatively flat in time and frequency, as I have argued throughout this thesis, implying that there is no inherent channel induced diversity anymore. One then has to rely on technical methods to prevent deep fading states, such as beamforming, cyclic delay diversity or space time block codes. The effect of those techniques in the context of FBMC and, in particular, on my prosed solutions, should be investigated in more detail.

My testbed offers a much higher hardware quality than typically installed in low-cost devices. Thus, many hardware challenges were never an issue in my measurements. Time-frequency synchronization errors, non-linearities and phase noise should be investigated in more detail. With respect to phase noise, it should be possible to extend my proposed solutions for doubly selective channels to phase noise.

I briefly mentioned that there exist some similarities between block spread FBMC and single-carrier transmissions (spreading in frequency) as well as windowed OFDM with reduced subcarrier spacing (spreading in time). However, a comprehensive and quantitative comparison is still an open topic.

While pruned DFT spread FBMC is a promising new technique, further research is necessary to fully exploit its potential. Because there are many similarities to conventional SC-FDMA, I expect that many methods known in SC-FDMA can be straightforwardly employed in pruned DFT spread FBMC. However, some techniques, such as Alamouti's space time block code, might require some special treatment.

Appendix A

A.1 Why A Matrix Description?

Many authors employ a discrete-time filter representation to describe multicarrier systems. However, in my opinion, such description is rather cumbersome because it transforms a simple system into something unnecessarily complicated. I therefore utilize a matrix notation with many beneficial properties. Let me start my argument with a simple example. Suppose the data symbols are modulated by prototype filter $p[n]$. At the receiver, a matched filter is employed, so that the received symbols $y[k]$ can be expressed by:

$$y[k] = (r[n] \star p^*[-n])_{\downarrow N_{\mathrm{FFT}}/2}, \tag{A.1}$$

where $\star$ denotes the convolution and $\downarrow N_{\mathrm{FFT}}/2$ down-sampling by $N_{\mathrm{FFT}}/2$. Assuming that the prototype filter has a length of $N_{\mathrm{FFT}}O$, the convolution in (A.1) requires in total $\frac{1}{2}N_{\mathrm{FFT}}^2 O$ multiplications for each detected symbol. However, down-sampling implies that many results of the convolution are discarded. Thus, there is no point in calculating them in the first place. I therefore consider a more practical vector description,

$$y_k = \mathbf{p}^{\mathsf{H}}\,\mathbf{r}_k, \tag{A.2}$$

where $\mathbf{r}_k \in \mathbb{C}^{N_{\mathrm{FFT}}O\times 1}$ simply stacks the appropriate received samples $r[n]$ in a vector. The evaluation in (A.2) no longer includes any unnecessary calculations and only requires $N_{\mathrm{FFT}}O$ multiplications. In my opinion, a filter represenation is only benefical in the continuous-time domain. Here, physics does the convolution, so that no additional calculations are necessary. Furthermore, the underlying integral would require a vector of size $N_{\mathrm{FFT}}O \to \infty$ in (A.2), not possible in practice. However, just because a concept is useful in the continuous-time domain does not mean it should also be employed in the discrete-time domain. This simple fact motivates my matrix notation. In multicarrier systems, the advantages of my matrix

notation become even more prominent. Authors in [149] utilize the following convolution based system model (ignoring noise and with a slight abuse of notation):

$$y_l[k] = \sum_{l'=1}^{L} x_{l'}[k] \star \left(g_{l'}[n] \star h[n] \star q_l^*[-n] \right)_{\downarrow N_{\mathrm{FFT}}/2} . \tag{A.3}$$

I, on the other hand, employ the following simple matrix description, see Section 2.2,

$$y_{l,k} = \mathbf{q}_{l,k}^{\mathsf{H}} \mathbf{H}\, \mathbf{G}\, \mathbf{x}. \tag{A.4}$$

In contrast to (A.3), my matrix notation does not require any convolutions or down-sampling, making it much easier to handle. Furthermore, I write both, subcarrier index l and time-position k, in a subscript to better point out that time and frequency are, from a mathematical point of view, completely equivalent. If a signal processing algorithm works in one domain, it also works in the other domain, as already discussed in Section 3.2 in the context of channel equalization. By treating time and frequency differently, one might miss some crucial aspects of multicarrier transmissions. Another advantage of my matrix notation is that a time-variant channel is modeled by a sparse matrix $\mathbf{H}$. This is very beneficial for simulations because sparse matrix multiplications are efficiently implemented in most numerical programs, such as MATLAB, reducing the simulation time. Also, my matrix notation tremendously helps in finding an efficient IFFT based signal generation algorithm. For example, the polyphase representation in [74] is rather lengthy and unnecessarily complicated. In contrast to that, my windowed based description in Figure 2.7 is much easier to understand.

Some authors evaluate (A.3) explicitly, leading to a similar description I employ. However, those authors do not utilize my matrix notation and instead rely on many summation, which is, in my opinion, rather cumbersome to use. For example, authors in [167] needed several pages to calculate the PSD. With my matrix notation, this is a matter of two equations, that is, (2.33) together with correlation matrix $\mathbf{R}_{\mathbf{x}} = \mathbf{C}\mathbf{C}^{\mathsf{H}}$. Another example is the calculation of the SIR. Authors in [89] provided a rather lengthy and cumbersome evaluation of the SIR. Furthermore, they only considered the SIR conditioned on a fixed channel but did not include channel statistics. With my matrix notation, calculating the SIR becomes trivial, as discussed in Section 3.1.2. Similar to [89], my matrix notation also allows to investigate inter-carrier-interference and inter-symbol-interference separately, simply by considering the corresponding submatrices of $\mathbf{G}$. The only drawback of my matrix notation in the context of SIR calculations is that the required correlation matrix $\mathbf{R}_{\mathrm{vec}\{\mathbf{H}\}}$ has dimension $N^2 \times N^2$, which is rather large. Even though $\mathbf{R}_{\mathrm{vec}\{\mathbf{H}\}}$ is sparse, it still requires a large amount of memory. Either the sampling rate or the number of symbols in time must then be reduced so

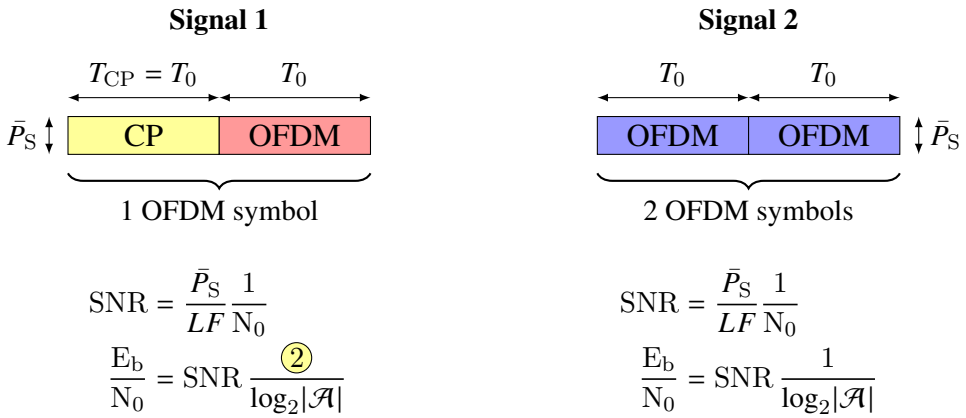

Figure A.1. To better illustrate the underlying problem with $\mathrm{E_b/N_0}$, two extreme cases of OFDM are considered, that is, OFDM for which the CP is as long as the useful symbol duration and OFDM without a CP. The SNR is the same for both signals, see also (2.36). However, Signal 2 has twice the data rate, so that the same SNR implies a 3 dB shift in $\mathrm{E_b/N_0}$ between the two signals.

that the allocated memory becomes reasonable small. Another approach is to split the whole transmission system into smaller submatrices and to processed them individually (with some overlapping).

A.2 $\mathrm{E_b/N_0}$: A Problematic Normalization

In order to compare different modulation schemes, one has to find a meaningful metric. Many authors, such as [119], use the BER over $\mathrm{E_b/N_0}$ to compare FBMC with CP-OFDM. However, in my opinion, $\mathrm{E_b/N_0}$ has some serious drawbacks. To understand why, let me consider a simple example. I assume there exists two signals, as illustrated in Figure A.1. Signal 1 consists of one OFDM symbol for which the CP is as long as the useful symbol duration. Signal 2 consists of two OFDM symbols (without CP). Both signals occupy the same time duration. For a fair comparison, I always consider the same average transmit power $\bar{P}_{\mathrm{S}}$. This leads to the same SNR, see Section 2.2, and therefore the same BER performance in an AWGN channel, see Figure A.2 (a). However, Signal 2 has twice the data rate. The idea in $\mathrm{E_b/N_0}$ is to account for such different data rates, but a simple power normalization is not a good solution because the symbol power affects the throughput only logarithmically. Let me explain this in more detail. The same $\mathrm{E_b/N_0}$ implies that the transmit power for Signal 1 is 3 dB lower. Thus, the BEP over $\mathrm{E_b/N_0}$ is also 3 dB shifted, as shown in Figure A.2 (b). One might now think that, by increasing the transmit power of Signal 1 by 3 dB, both systems will perform equally good because the same BEP for a given energy per bit is achieved. However,

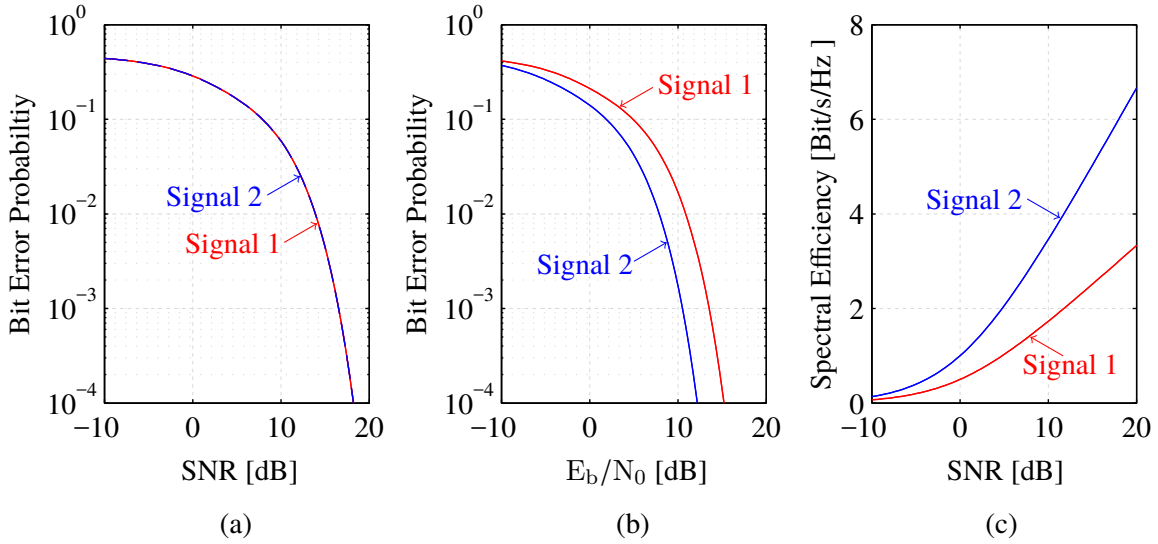

Figure A.2. Subplot (a) and (b) show the BEP for 16-QAM in an AWGN channel. The meaning of Signal 1 and Signal 2 is illustrated in Figure A.1. The power normalization $\mathrm{E_b}/\mathrm{N_0}$ might be misleading because the power affects the rate only logarithmically, as can be concluded from subplot (c).

this is wrong, as can be deduced from Figure A.2 (c) which shows the spectral efficiency for an AWGN channel, see (4.20) for $h = 1$. Consider for example an initial SNR of 10 dB. Increasing the SNR of Signal 1 by 3 dB, leads only to a small throughput improvement, still much lower than the throughput of Signal 2. The transmit power of Signal 1 has to be increased by more than 10 dB to achieve the same performance as in Signal 2. Thus, in my opinion, the BER over $\mathrm{E_b}/\mathrm{N_0}$ might be misleading. Instead of $\mathrm{E_b}/\mathrm{N_0}$, I suggest to always use the same average transmit power $\bar{P}_\mathrm{S}$ on the x-axis when comparing different modulation schemes. Of course, this can also be included implicitly by the SNR, as in this thesis. If the data rates are different, it is, in my option, better to include this as a side note rather than some artificial power normalization.

A.3 Bit Error Probability: Doubly-Flat Rayleigh, 4-QAM

Table A.1 provides a compact comparison of the BEP for OFDM and FBMC, calculated in Section 3.1.1 and Section 4.3.2. In case of perfect channel knowledge, there is no difference between OFDM and FBMC. For imperfect channel knowledge, on the other hand, there are some small differences between OFDM and FBMC, mainly caused by different power distributions, especially for the auxiliary symbol method. However, those differences are

Table A.1. Bit Error Probability for OFDM and FBMC in case of perfect channel knowledge and imperfect channel knowledge (channel estimation). Valid for a 4-QAM signal constellation in case of a doubly-flat Rayleigh channel.

	Bit Error Probability	
	OFDM	FBMC
Perfect Chan. Know.[1]	$\frac{1}{2} - \frac{1}{2\sqrt{1+2\frac{1}{\mathrm{SNR}}}}$	$\frac{1}{2} - \frac{1}{2\sqrt{1+2\frac{1}{\mathrm{SNR}}}}$
Chan. Est.[2,3]	$\frac{1}{2} - \frac{1}{2\sqrt{2\left(1+\lVert\mathbf{w}_{l,k}\rVert^2\frac{P_\mathrm{n}}{P_\mathcal{P}}\right)\left(1+\frac{P_\mathrm{n}}{P_\mathcal{D}}\right)-1}}$ $\mathrm{SNR} = \frac{\lvert\mathcal{D}\rvert P_\mathcal{D} + \lvert\mathcal{P}\rvert P_\mathcal{P}}{LKP_\mathrm{n}}$	$\approx \frac{1}{2} - \frac{1}{2\sqrt{2\left(1+\frac{P_\mathrm{n}}{P_\mathcal{P}}\lVert\mathbf{w}_{l,k}\rVert^2\right)\left(1+\frac{P_\mathrm{n}}{2P_\mathcal{D}}\right)-1}}$ $\mathrm{SNR}_{\mathrm{Aux.}} = \frac{\lvert\mathcal{D}\rvert P_\mathcal{D} + \lvert\mathcal{P}\rvert P_\mathcal{P} + \lvert\mathcal{A}\rvert P_\mathcal{A}}{LK\frac{P_\mathrm{n}}{2}}$ $\mathrm{SNR}_{\mathrm{Spr.}} = \frac{\lvert\mathcal{D}\rvert P_\mathcal{D} + \lvert\mathcal{P}\rvert P_\mathcal{P}}{LK\frac{P_\mathrm{n}}{2}}$

[1] The BEP is exactly the same for OFDM and FBMC.
[2] For FBMC, the BEP represents only an approximation, see Section 4.3.2.
[3] Perfect channel knowledge is obtained by $\lVert\mathbf{w}_{l,k}\rVert^2 = 0$, $|\mathcal{P}| = |\mathcal{A}| = 0$ and $|\mathcal{D}| = LK$.

so small that they can often be neglected. Note that the BEP in Table A.1 for FBMC (channel estimation) represents only an approximation. The exact expression must include the imaginary interference, as discussed in Section 4.3.2.

Appendix B

B.1 List of Symbols

The notation is, in general, consistent throughout the thesis. However, sometimes it is necessary to slightly change it in order to improve readability.

Mathematical Notation

Notation	Description
$(\cdot)^{\mathsf{H}}$	Hermitian of a matrix.
$(\cdot)^{\mathsf{T}}$	Transposed of a matrix.
$\otimes$	Kronecker product.
$\circ$	Element-wise Hadamard product.
$\|\| \cdot \|\|$	Euclidean norm.
$\|\| \cdot \|\|_{\mathsf{F}}$	Frobenius norm.
$(\cdot)^*$	Conjugate complex.
$\| \cdot \|$	Scalar: absolute value; Set: cardinality.
$\hat{}$	Estimation ("hat" symbol).
$\overline{lk}$	Short notation: $\overline{lk} = l + L(k-1)$ due to the vectorized structure.
$\mathfrak{R}\{\cdot\}$	Real part.
$\mathfrak{I}\{\cdot\}$	Imaginary part.
$\mathbb{E}\{\cdot\}$	Expectation.
$\Pr\{\cdot\}$	Probability.
$\mathcal{Q}\{\cdot\}$	Nearest neighbor detection.

Set Symbols

Notation	Description
$\mathcal{X}$	Symbol alphabet, usually a QAM or PAM signal constellation.
$\mathcal{S}$	Set of (l, k), corresponding to the signal subblock (equalization).
$\mathcal{R}$	Set of (l, k), corresponding to the residual interference (equalization).
$\mathcal{A}$	Set of (l, k), corresponding to the auxiliary pilot positions (channel estimation).
$\mathcal{D}$	Set of (l, k), corresponding to the data positions (channel estimation).
$\mathcal{P}$	Set of (l, k), corresponding to the pilot positions (channel estimation).

Matrix/Vector Notation

Variable	Dimension	Description
$\mathbf{M}$	$\mathbb{C}^{m_1 \times m_2}$	Matrix, upper-case bold.
$\mathbf{v}$	$\mathbb{C}^{v \times 1}$	Vector, lower-case bold.
s, S	$\mathbb{C}$	Scalar, non-bold.
$[\mathbf{M}]_{i,j}$	$\mathbb{C}$	i-th row element and j-th column element of matrix $\mathbf{M}$.
$[\mathbf{v}]_i$	$\mathbb{C}$	i-th element of vector $\mathbf{v}$.
$\mathbf{M}_{\mathcal{S},\mathcal{R}}$	$\mathbb{C}^{\lvert\mathcal{S}\rvert \times \lvert\mathcal{R}\rvert}$	Submatrix of $\mathbf{M}$ (Set $\mathcal{S}$: row position; Set $\mathcal{R}$: column position)[1].
$\mathbf{v}_{\mathcal{S}}$	$\mathbb{C}^{\lvert\mathcal{S}\rvert \times 1}$	Subvector of $\mathbf{v}$ (positions are chosen from set $\mathcal{S}$).
$\mathbf{M}_{\mathcal{P}}$	$\mathbb{C}^{m_1 \times \lvert\mathcal{P}\rvert}$	Submatrix of $\mathbf{M}$ (column positions are chosen from set $\mathcal{P}$)[1].
$\mathbf{v}_{\mathcal{P}_i}$	$\mathbb{C}^{v \times 1}$	Vector $\mathbf{v}_{l,k}$, corresponding to the i-position of set $\mathcal{P}$.
$\mathbf{I}_m$	$\mathbb{R}^{m \times m}$	Identity matrix.
$\mathbf{0}_{m_1 \times m_2}$	$\mathbb{R}^{m_1 \times m_2}$	All zero matrix.
$\mathbf{1}_{m_1 \times m_2}$	$\mathbb{R}^{m_1 \times m_2}$	All one matrix.
$\mathbf{R}_{\mathbf{v}_1,\mathbf{v}_2}$	$\mathbb{C}^{v_1 \times v_2}$	Correlation matrix between vector $\mathbf{v}_1$ and $\mathbf{v}_2$, that is, $\mathbb{E}\{\mathbf{v}_1 \mathbf{v}_2^{\mathsf{H}}\}$.
$\mathbf{r}_{\mathbf{v},s}$	$\mathbb{C}^{v \times 1}$	Correlation vector between vector $\mathbf{v}$ and scalar s, that is, $\mathbb{E}\{\mathbf{v} s^*\}$.
$\mathbf{W}_m$	$\mathbb{C}^{m \times m}$	DFT matrix of size m.
$\mathrm{vec}\{\mathbf{M}\}$	$\mathbb{C}^{m_1 m_2 \times 1}$	Vectorization operator.
$\mathrm{diag}\{\mathbf{M}\}$	$\mathbb{C}^{m \times 1}$	Take the diagonal elements out of a square matrix $\rightarrow$ vector.
$\mathrm{diag}\{\mathbf{v}\}$	$\mathbb{C}^{v \times v}$	Put the vector elements of $\mathbf{v}$ in a diagonal matrix.
$\mathrm{ddiag}\{\mathbf{M}\}$	$\mathbb{C}^{m \times m}$	Double diagonal operator.
$\mathrm{tr}\{\mathbf{M}\}$	$\mathbb{C}$	Trace operator.

[1] Does not apply to Greek letters.

Upper-Case Symbols

Variable	Dimension	Description
F	$\mathbb{R}$	Frequency-spacing (subcarrier spacing) [Hz].
T	$\mathbb{R}$	Time-spacing [s].
T_0	$\mathbb{R}$	Time-scaling parameter [s].
T_{CP}	$\mathbb{R}$	Cyclic prefix duration in OFDM [s].
$A(\tau, \nu)$	$\mathbb{C}$	Ambiguity function, see (2.5).
O	$\mathbb{R}$	Overlapping factor in FBMC.
K	$\mathbb{N}^+$	Number of symbols in time (per block).
L	$\mathbb{N}^+$	Number of subcarriers (per block).
N	$\mathbb{N}^+$	Total number of samples in time, see (2.23).
N_{FFT}	$\mathbb{N}^+$	FFT size
N_{s}	$\mathbb{N}^+$	Spreading length (channel estimation).
$\mathbf{C}_{\mathrm{a}}$	$\mathbb{R}^{LK\times(LK-\lvert\mathcal{A}\rvert)}$	Precoding matrix (channel estimation, auxiliary symbols).
$\mathbf{C}_{\mathrm{s}}$	$\mathbb{R}^{LK\times(LK-\lvert\mathcal{P}\rvert)}$	Precoding matrix (channel estimation, data spreading).
$\mathbf{C}$	$\mathbb{C}^{LK\times\frac{LK}{2}}$	Precoding/spreading matrix.
$\mathbf{C}_t$	$\mathbb{R}^{K\times\frac{K}{2}}$	Precoding/spreading matrix in time.
$\mathbf{C}_f$	$\mathbb{R}^{L\times\frac{L}{2}}$	Precoding/spreading matrix in frequency.
$\mathbf{D}$	$\mathbb{C}^{LK\times LK}$	Transmission matrix, see (3.29).
$\bar{\mathbf{D}}$	$\mathbb{C}^{LK\times LK}$	Transmission matrix for $\mathbf{H} = \mathbf{I}_N$, see (4.7).
$\mathbf{G}$	$\mathbb{C}^{N\times LK}$	Transmit basis pulse matrix, see (2.24).
$\mathbf{H}$	$\mathbb{C}^{N\times N}$	Time-variant convolution matrix, see (2.29).
$\mathbf{Q}$	$\mathbb{C}^{N\times LK}$	Receive basis pulse matrix, see (2.28).
N_0	$\mathbb{R}$	Noise spectral density.
P_{n}	$\mathbb{R}$	White Gaussian noise power in the time domain.
$\bar{P}_{\mathrm{S}}$	$\mathbb{R}$	Average transmit signal power in time, see (2.34).
P_x	$\mathbb{R}$	Transmitted symbol power.
$P_{\mathcal{A}}$	$\mathbb{R}$	Auxiliary symbol power.
$P_{\mathcal{D}}$	$\mathbb{R}$	Data symbol power.
$P_{\mathcal{P}}$	$\mathbb{R}$	Pilot symbol power.

Lower-Case Symbols

Variable	Dimension	Description
k	$\mathbb{N}$	Time position.
l	$\mathbb{N}$	Subcarrier position.
f_s	$\mathbb{R}$	Sampling rate [Hz].
$g_{l,k}(t)$	$\mathbb{C}$	Transmit basis pulse, see (2.2).
$\tilde{g}_i(t)$	$\mathbb{C}$	New transmit basis pulse, transformed by $\mathbf{C}$.
$p(t)$	$\mathbb{R}$	Prototype filter.
$s(t)$	$\mathbb{C}$	Transmitted signal.
$\mathbf{g}_{l,k}$	$\mathbb{C}^{N\times 1}$	Transmit basis pulse, see (2.22).
$\mathbf{s}$	$\mathbb{C}^{N\times 1}$	Transmitted signal.
$\mathbf{q}_{l,k}$	$\mathbb{C}^{N\times 1}$	Receive basis pulse.
$h_{l,k}$	$\mathbb{C}$	One-tap channel.
$n_{l,k}$	$\mathbb{C}$	Gaussian noise.
$x_{l,k}$	$\mathbb{C}$	Transmitted symbol.
$y_{l,k}$	$\mathbb{C}$	Received symbol (after demodulation, but before equalization).
$\mathbf{h}$	$\mathbb{C}^{LK\times 1}$	One-tap channel in vectorized form.
$\mathbf{n}$	$\mathbb{C}^{LK\times 1}$	Gaussian distributed noise (colored) in vectorized form.
$\mathbf{x}$	$\mathbb{C}^{LK\times 1}$	Transmitted symbols in vectorized form, see (2.26).
$\tilde{\mathbf{x}}$	$\mathbb{C}^{\frac{LK}{2}\times 1}$	Transmitted (data) symbols before precoding.
$\mathbf{y}$	$\mathbb{C}^{LK\times 1}$	Received symbols in vectorized form.
$\tilde{\mathbf{y}}$	$\mathbb{C}^{\frac{LK}{2}\times 1}$	Received (data) symbols after decoding by $\mathbf{C}^{\mathsf{H}}$.
$\hat{h}^{\mathrm{LS}}_{\mathcal{P}_i}$	$\mathbb{C}$	LS channel estimation at pilot position i, see (4.1).
$\hat{\mathbf{h}}^{\mathrm{LS}}_{\mathcal{P}}$	$\mathbb{C}^{\lvert\mathcal{P}\rvert\times 1}$	LS channel estimates (pilot, vectorized), see (4.3).
$\mathbf{w}_{l,k}$	$\mathbb{C}^{\lvert\mathcal{P}\rvert\times 1}$	Interpolation (extrapolation) vector for channel estimation.
$\tilde{\mathbf{w}}_{l_1,k_1,l_2,k_2}$	$\mathbb{C}^{\lvert\mathcal{P}\rvert\times 1}$	Weighting vector for doubly-selective channel estimation.

Greek Symbols

Variable	Description
τ_rms	RMS delay spread.
ν_rms	RMS Doppler spread.
$\theta_{l,k}$	Symbol-wise phase shift in FBMC.

B.2 List of Abbreviations

3G	Third Generation
3GPP	3rd Generation Partnership Project
4G	Fourth Generation
5G	Fifth Generation
AWGN	Additive White Gaussian Noise
BEP	Bit Error Probability
BER	Bit Error Ratio
BICM	Bit-Interleaved Coded Modulation
CCDF	Complementary Cumulative Distribution Function
CDF	Cumulative Distribution Function
CDMA	Code Division Multiple Access
CMT	Cosine Modulated Multitone
CP	Cyclic Prefix
CQI	Channel Quality Indicator
DAC	Digital-to-Analog-Converter
DFT	Discrete Fourier Transform
DVB-T	Digital Video Broadcasting - Terrestrial
eMBB	enhanced Mobile Broadband
eMTC	enhanced Machine Type Communications
FBMC	Filter Bank Multicarrier Modulation
FFT	Fast Fourier Transform
f-OFDM	filtered-OFDM
IFFT	Inverse Fast Fourier Transform
ISI	Inter Symbol Interference
LOS	Line-Of-Sight
LS	Least Squares
LTE	Long Term Evolution
M2M	Machine to Machine
MIMO	Multiple-Input and Multiple-Output
ML	Maximum Likelihood
MMSE	Minimum Mean Squared Error
MSE	Mean Squared Error
NLOS	Non-Line-Of-Sight
OFDM	Orthogonal Frequency Division Multiplexing
OOB	Out-Of-Band

OQAM	Offset Quadrature Amplitude Modulation
PAM	Pulse-Amplitude Modulation
PAPR	Peak-to-Average Power Ratio
pdf	probability density function
PSD	Power Spectral Density
QAM	Quadrature Amplitude Modulation
RMS	Root Mean Square
RX	Receiver
SC-FDMA	Single Carrier - Frequency-Division Multiple Access
SINR	Signal-to-Interference plus Noise Ratio
SIR	Signal-to-Interference Ratio
SISO	Single-Input and Single-Output
SMT	Staggered Multitone
SNR	Signal-to-Noise Ratio
TDL	Tapped Delay Line
TX	Transmitter
UFMC	Universal Filtered Multi-Carrier
URLLC	Ultra-Reliable Low Latency Communications
WOLA	Weighted Overlap and Add
ZF	Zero-Forcing
ZP	Zero-Padding

B.3 List of Figures

B.4 List of Tables

Bibliography

[1] R. Nissel, S. Schwarz, and M. Rupp, "Filter bank multicarrier modulation schemes for future mobile communications," *IEEE Journal on Selected Areas in Communications*, vol. 35, no. 8, pp. 1768–1782, 2017.

[2] 3GPP, "TSG RAN; study on scenarios and requirements for next generation access technologies; (release 14)." http://www.3gpp.org/DynaReport/38913.htm, Oct. 2016.

[3] S. Schwarz and M. Rupp, "Society in motion: Challenges for LTE and beyond mobile communications," *IEEE Commun. Mag., Feature Topic: LTE Evolution*, vol. 54, no. 5, 2016.

[4] F. Schaich, T. Wild, and R. Ahmed, "Subcarrier spacing-how to make use of this degree of freedom," in *IEEE Vehicular Technology Conference (VTC Spring)*, pp. 1–6, 2016.

[5] X. Zhang, M. Jia, L. Chen, J. Ma, and J. Qiu, "Filtered-OFDM-enabler for flexible waveform in the 5th generation cellular networks," in *IEEE Global Communications Conference (GLOBECOM)*, pp. 1–6, 2015.

[6] S. Schwarz, T. Philosof, and M. Rupp, "Signal processing challenges in cellular assisted vehicular communications," *IEEE Signal Processing Magazine*, vol. 34, pp. 47–59, March 2017.

[7] 3GPP, "TSG RAN; study on new radio access technology; physical layer aspects; (release 14)." http://www.3gpp.org/DynaReport/38802.htm, Mar. 2017.

[8] J. G. Andrews, S. Buzzi, W. Choi, S. V. Hanly, A. Lozano, A. C. Soong, and J. C. Zhang, "What will 5G be?," *IEEE Journal on Selected Areas in Communications*, vol. 32, no. 6, pp. 1065–1082, 2014.

[9] G. Wunder, P. Jung, M. Kasparick, T. Wild, F. Schaich, Y. Chen, S. Brink, I. Gaspar, N. Michailow, A. Festag, *et al.*, "5GNOW: non-orthogonal, asynchronous waveforms for future mobile applications," *IEEE Communications Magazine*, vol. 52, no. 2, pp. 97–105, 2014.

[10] P. Banelli, S. Buzzi, G. Colavolpe, A. Modenini, F. Rusek, and A. Ugolini, "Modulation formats and waveforms for 5G networks: Who will be the heir of OFDM?: An overview of alternative modulation schemes for improved spectral efficiency," *IEEE Signal Process. Mag.*, vol. 31, no. 6, pp. 80–93, 2014.

[11] 3GPP, "TSG RAN; study on new radio access technology; (release 14)." http://www.3gpp.org/DynaReport/38912.htm, Sept. 2016.

[12] 3GPP, "TSG RAN; study on new radio access technology; radio interface protocol aspects; (release 14)." http://www.3gpp.org/DynaReport/38804.htm, Mar. 2017.

[13] Qualcomm Incorporated, "Waveform candidates," in *3GPP TSG-RAN WG1 84b*, (Busan, Korea), April 2016.

[14] F. Schaich, T. Wild, and Y. Chen, "Waveform contenders for 5G-suitability for short packet and low latency transmissions," in *IEEE Vehicular Technology Conference (VTC Spring)*, pp. 1–5, 2014.

[15] H. Asplund, K. Larsson, and P. Okvist, "How typical is the "typical urban" channel model?," in *IEEE Vehicular Technology Conference*, pp. 340–343, 2008.

[16] L. Bernadó, T. Zemen, F. Tufvesson, A. F. Molisch, and C. F. Mecklenbräuker, "Delay and doppler spreads of nonstationary vehicular channels for safety-relevant scenarios," *IEEE Transactions on Vehicular Technology*, vol. 63, no. 1, pp. 82–93, 2014.

[17] S. Payami and F. Tufvesson, "Delay spread properties in a measured massive MIMO system at 2.6 GHz," in *IEEE International Symposium on Personal, Indoor, and Mobile Radio Communications (PIMRC)*, pp. 53–57, Sept 2013.

[18] M. Caus and A. I. Pérez-Neira, "Transmitter-receiver designs for highly frequency selective channels in MIMO FBMC systems," *IEEE Transactions on Signal Processing*, vol. 60, no. 12, pp. 6519–6532, 2012.

[19] H. Bölcskei, "Orthogonal frequency division multiplexing based on offset QAM," in *Advances in Gabor analysis*, pp. 321–352, Springer, 2003.

[20] D. Mattera, M. Tanda, and M. Bellanger, "Filter bank multicarrier with PAM modulation for future wireless systems," *Signal Processing*, vol. 120, pp. 594–606, 2016.

[21] M. Bellanger, D. Mattera, and M. Tanda, "MIMO techniques in the frequency domain with FBMC-PAM," in *European Conference on Networks and Communications (EuCNC)*, pp. 345–349, 2016.

[22] M. Bellanger, D. Mattera, and M. Tanda, "Asynchronous uplink access with FBMC-PAM for future wireless systems," in *IEEE Wireless Communications and Networking Conference (WCNC)*, pp. 1–6, 2017.

[23] B. Farhang-Boroujeny, "OFDM versus filter bank multicarrier," *IEEE Signal Processing Magazine*, vol. 28, pp. 92–112, May 2011.

[24] B. Farhang-Boroujeny, "Filter bank multicarrier modulation: A waveform candidate for 5G and beyond," *Advances in Electrical Engineering*, vol. 2014, December 2014.

[25] E. Zöchmann, M. Lerch, S. Caban, R. Langwieser, C. Mecklenbräuker, and M. Rupp, "Directional evaluation of receive power, Rician K-factor and RMS delay spread obtained from power measurements of 60 GHz indoor channels," in *IEEE Topical Conference on Antennas and Propagation in Wireless Communications (APWC)*, pp. 1–4, 2016.

[26] S. Caban, J. A. García-Naya, and M. Rupp, "Measuring the physical layer performance of wireless communication systems," *IEEE Instrumentation & Measurement Magazine*, vol. 14, no. 5, pp. 8–17, 2011.

[27] R. Nissel, E. Zöchmann, M. Lerch, S. Caban, and M. Rupp, "Low-latency MISO FBMC-OQAM: It works for millimeter waves!," in *IEEE International Microwave Symposium*, Honolulu, Hawaii, June 2017.

[28] M. Lerch, S. Caban, M. Mayer, and M. Rupp, "The Vienna MIMO testbed: Evaluation of future mobile communication techniques.," *Intel Technology Journal*, vol. 4, pp. 58–69, 2014.

[29] R. Nissel, M. Lerch, and M. Rupp, "Experimental validation of the OFDM bit error probability for a moving receive antenna," in *IEEE Vehicular Technology Conference (VTC)*, Vancouver, Canada, Sept 2014.

[30] R. Nissel and M. Rupp, "Doubly-selective MMSE channel estimation and ICI mitigation for OFDM systems," in *IEEE International Conference on Communications (ICC)*, London, UK, June 2015.

[31] R. Nissel, S. Caban, and M. Rupp, "Closed-Form capacity expression for low complexity BICM with uniform inputs," in *IEEE International Symposium on Personal, Indoor and Mobile Radio Communications (PIMRC)*, pp. 678–682, Hong Kong, P.R. China, aug 2015.

[32] R. Nissel and M. Rupp, "OFDM and FBMC-OQAM in doubly-selective channels: Calculating the bit error probability," *IEEE Communications Letters*, vol. 21, no. 6, pp. 1297–1300, 2017.

[33] R. Nissel and M. Rupp, "Pruned DFT spread FBMC-OQAM: Low-PAPR, low latency, high spectral efficiency," *Submitted to IEEE Transactions on Communications*, 2018.

[34] R. Nissel, M. Lerch, M. Šimko, and M. Rupp, "Bit error probability for pilot-symbol-aided OFDM channel estimation in doubly-selective channels," in *International ITG Workshop on Smart Antennas (WSA)*, Erlangen, Germany, Mar 2014.

[35] R. Nissel and M. Rupp, "Dynamic spectrum allocation in cognitive radio: Throughput calculations," in *IEEE International Black Sea Conference on Communications and Networking (BlackSeaCom 2016)*, Varna, Bulgaria, June 2016.

[36] R. Nissel, J. Blumenstein, and M. Rupp, "Block frequency spreading: A method for low-complexity MIMO in FBMC-OQAM," in *IEEE Workshop on Signal Processing Advances in Wireless Communications (SPAWC)*, Hokkaido, Japan, July 2017.

[37] R. Nissel, M. Rupp, and R. Marsalek, "FBMC-OQAM in doubly-selective channels: A new perspective on MMSE equalization," in *IEEE Workshop on Signal Processing Advances in Wireless Communications (SPAWC)*, Hokkaido, Japan, July 2017.

[38] R. Nissel, E. Zöchmann, and M. Rupp, "On the influence of doubly-selectivity in pilot-aided channel estimation for FBMC-OQAM," in *IEEE Vehicular Technology Conference (VTC Spring)*, Sydney, Australia, June 2017.

[39] R. Nissel and M. Rupp, "Enabling low-complexity MIMO in FBMC-OQAM," in *IEEE Globecom Workshops (GC Wkshps)*, Washington DC, USA, Dec 2016.

[40] R. Nissel, S. Caban, and M. Rupp, "Experimental evaluation of FBMC-OQAM channel estimation based on multiple auxiliary symbols," in *IEEE Sensor Array and Multichannel Signal Processing Workshop (SAM)*, Rio de Janeiro, Brazil, July 2016.

[41] R. Nissel and M. Rupp, "Bit error probability for pilot-symbol aided channel estimation in FBMC-OQAM," in *IEEE International Conference on Communications (ICC)*, Kuala Lumpur, Malaysia, May 2016.

[42] R. Nissel and M. Rupp, "On pilot-symbol aided channel estimation in FBMC-OQAM," in *IEEE International Conference on Acoustics, Speech and Signal Processing (ICASSP)*, pp. 3681–3685, Shanghai, China, March 2016.

[43] R. Nissel, "Symbol detection in high speed channels," in *The Vienna LTE-Advanced Simulators: Up and Downlink, Link and System Level Simulation*, pp. 39–60, Singapore: Springer-Verlag, 2016.

[44] R. Nissel, "Dynamic spectrum allocation in mobile communication," Master's thesis, Department of Economics, University of Vienna, 2015.

[45] S. Caban, R. Nissel, M. Lerch, and M. Rupp, "Controlled OFDM measurements at extreme velocities," in *Extreme Conference on Communication and Computing (ExtremeCom 2014)*, 2014.

[46] E. Zöchmann, R. Langwieser, S. Caban, M. Lerch, S. Pratschner, R. Nissel, C. Mecklenbräuker, and M. Rupp, "A millimeter wave testbed for repeatable high velocity measurements," in *European Wireless 2017*, pp. 358–362, 2017.

[47] T. Nguyen, R. Nissel, S. Le, M. Wuilpart, and P. Megret, "Equalization-enhanced phase noise suppression advantage of CO-FBMC over RGI CO-OFDM," in *Conference on Lasers and Electro-Optics (CLEO)*, 2017.

[48] E. Zöchmann, M. Lerch, S. Pratschner, R. Nissel, S. Caban, and M. Rupp, "Associating spatial information to directional millimeter wave channel measurements," in *IEEE Vehicular Technology Conference (VTC Fall)*, 2017.

[49] J. Blumenstein, R. Marsalek, T. Gotthans, R. Nissel, and M. Rupp, "On mutual information of measured 60 GHz wideband indoor MIMO Channels:Time Domain singular values," in *IEEE International Symposium on Personal, Indoor, and Mobile Radio Communications (PIMRC)*, Oct. 2017.

[50] IEEE Signal Processing Society, "IEEE transactions on signal processing: Reproducible research." http://signalprocessingsociety.org/publications-resources/ieee-transactions-signal-processing. Accessed: 2017-10-19.

[51] P. Vandewalle, J. Kovacevic, and M. Vetterli, "Reproducible research in signal processing," *IEEE Signal Processing Magazine*, vol. 26, no. 3, 2009.

[52] R. W. Chang, "Synthesis of band-limited orthogonal signals for multichannel data transmission," *Bell System Technical Journal*, vol. 45, no. 10, pp. 1775–1796, 1966.

[53] B. Saltzberg, "Performance of an efficient parallel data transmission system," *IEEE Transactions on Communication Technology*, vol. 15, no. 6, pp. 805–811, 1967.

[54] S. Weinstein and P. Ebert, "Data transmission by frequency-division multiplexing using the discrete fourier transform," *IEEE Transactions on Communication Technology*, vol. 19, pp. 628–634, October 1971.

[55] A. Sahin, I. Guvenc, and H. Arslan, "A survey on multicarrier communications: Prototype filters, lattice structures, and implementation aspects," *IEEE Communications Surveys Tutorials*, vol. 16, pp. 1312–1338, December 2012.

[56] G. Matz, D. Schafhuber, K. Grochenig, M. Hartmann, and F. Hlawatsch, "Analysis, optimization, and implementation of low-interference wireless multicarrier systems," *IEEE Transactions on Wireless Communications*, vol. 6, no. 5, pp. 1921–1931, 2007.

[57] M. Fuhrwerk, J. Peissig, and M. Schellmann, "Channel adaptive pulse shaping for OQAM-OFDM systems," in *IEEE European Signal Processing Conference (EUSIPCO)*, pp. 181–185, 2014.

[58] H. G. Feichtinger and T. Strohmer, *Gabor analysis and algorithms: Theory and applications*. Springer Science & Business Media, 2012.

[59] M. Vetterli, J. Kovačević, and V. K. Goyal, *Foundations of signal processing*. Cambridge University Press, 2014.

[60] Y. G. Li and G. L. Stuber, *Orthogonal frequency division multiplexing for wireless communications*. Springer Science & Business Media, 2006.

[61] A. F. Molisch, *Wireless communications*, vol. 34. John Wiley & Sons, 2012.

[62] H. Nam, M. Choi, S. Han, C. Kim, S. Choi, and D. Hong, "A new filter-bank multicarrier system with two prototype filters for QAM symbols transmission and reception," *IEEE Transactions on Wireless Communications*, vol. 15, no. 9, pp. 5998–6009, 2016.

[63] Y. H. Yun, C. Kim, K. Kim, Z. Ho, B. Lee, and J.-Y. Seol, "A new waveform enabling enhanced QAM-FBMC systems," in *IEEE International Workshop on Signal Processing Advances in Wireless Communications (SPAWC)*, pp. 116–120, 2015.

[64] C. Kim, Y. H. Yun, K. Kim, and J.-Y. Seol, "Introduction to QAM-FBMC: from waveform optimization to system design," *IEEE Communications Magazine*, vol. 54, no. 11, pp. 66–73, 2016.

[65] R. Haas and J.-C. Belfiore, "A time-frequency well-localized pulse for multiple carrier transmission," *Wireless Personal Communications*, vol. 5, no. 1, pp. 1–18, 1997.

[66] M. Bellanger, D. Le Ruyet, D. Roviras, M. Terré, J. Nossek, L. Baltar, Q. Bai, D. Waldhauser, M. Renfors, T. Ihalainen, *et al.*, "FBMC physical layer: a primer," *PHYDYAS, January*, 2010.

[67] M. G. Bellanger, "Specification and design of a prototype filter for filter bank based multicarrier transmission," in *IEEE International Conference on Acoustics, Speech, and Signal Processing*, vol. 4, pp. 2417–2420, 2001.

[68] S. Mirabbasi and K. Martin, "Design of prototype filter for near-perfect-reconstruction overlapped complex-modulated transmultiplexers," in *IEEE International Symposium on Circuits and Systems*, 2002.

[69] C. Lélé, P. Siohan, and R. Legouable, "The Alamouti scheme with CDMA-OFDM/OQAM," *EURASIP Journal on Advances in Signal Processing*, vol. 2010, Article ID 703513, pp. 1–13, 2010.

[70] R. Zakaria and D. Le Ruyet, "A novel filter-bank multicarrier scheme to mitigate the intrinsic interference: application to MIMO systems," *IEEE Transactions on Wireless Communications*, vol. 11, no. 3, pp. 1112–1123, 2012.

[71] C. Lélé, P. Siohan, R. Legouable, and M. Bellanger, "CDMA transmission with complex OFDM/OQAM," *EURASIP Journal on Wireless Communications and Networking*, vol. 2008, Article ID 748063, pp. 1–12, 2008.

[72] G. Matz, H. Bolcskei, and F. Hlawatsch, "Time-frequency foundations of communications: Concepts and tools," *IEEE Signal Processing Magazine*, vol. 30, no. 6, pp. 87–96, 2013.

[73] E. Telatar, "Capacity of multi-antenna gaussian channels," *Transactions on Emerging Telecommunications Technologies*, vol. 10, no. 6, pp. 585–595, 1999.

[74] P. Siohan, C. Siclet, and N. Lacaille, "Analysis and design of OFDM/OQAM systems based on filterbank theory," *IEEE Transactions on Signal Processing*, vol. 50, no. 5, pp. 1170–1183, 2002.

[75] M. Terre, "FBMC modulation / demodulation." Matlab Central: https://www.mathworks.com/matlabcentral/, 2014. Accessed: 2017-10-19.

[76] Q. Bodinier, F. Bader, and J. Palicot, "Coexistence in 5G: Analysis of cross-interference between OFDM/OQAM and legacy users," in *IEEE Globecom Workshops (GC Wkshps)*, 2016.

[77] C. Thein, M. Fuhrwerk, and J. Peissig, "About the use of different processing domains for synchronization in non-contiguous FBMC systems," in *IEEE International Symposium on Personal, Indoor, and Mobile Radio Communications (PIMRC)*, pp. 791–795, Sept 2013.

[78] G. P. Fettweis, "The tactile internet: Applications and challenges," *IEEE Vehicular Technology Magazine*, vol. 9, no. 1, pp. 64–70, 2014.

[79] A. Goldsmith, *Wireless communications*. Cambridge university press, 2005.

[80] S. Weiss, S. R. Dooley, R. W. Stewart, and A. K. Nandi, "Adaptive equalization in oversampled subbands," in *Asilomar Conference on Signals, Systems and Computers*, vol. 1, pp. 389–393 vol.1, Nov 1998.

[81] S. Weiss, M. Hadef, M. Konrad, and M. Rupp, "Blind chip-rate equalisation for DS-CDMA downlink receiver," in *Asilomar Conference on Signals, Systems Computers*, vol. 2, pp. 1283–1287 Vol.2, Nov 2003.

[82] M. Hadef, S. Weiss, and M. Rupp, "Adaptive blind multiuser DS-CDMA downlink equaliser," *Electronics Letters*, vol. 41, no. 21, pp. 1184–1186, 2005.

[83] M. Rupp, "Robust design of adaptive equalizers," *IEEE Transactions on Signal Processing*, vol. 60, no. 4, pp. 1612–1626, 2012.

[84] M. Rupp and J. A. Garcia-Naya, "Equalizers in mobile communications," *IEEE Instrumentation Measurement Magazine*, vol. 15, no. 3, pp. 32–42, 2012.

[85] L. Rugini and P. Banelli, "BER of OFDM systems impaired by carrier frequency offset in multipath fading channels," *IEEE Transactions on Wireless Communications*, vol. 4, no. 5, pp. 2279–2288, 2005.

[86] T. Wang, J. G. Proakis, E. Masry, and J. R. Zeidler, "Performance degradation of OFDM systems due to Doppler spreading," *IEEE Transactions on Wireless Communications*, vol. 5, no. 6, pp. 1422–1432, 2006.

[87] R. J. Baxley, B. T. Walkenhorst, and G. Acosta-Marum, "Complex Gaussian ratio distribution with applications for error rate calculation in fading channels with imperfect CSI," in *IEEE GLOBECOM*, 2010.

[88] M. Russell and G. L. Stuber, "Interchannel interference analysis of OFDM in a mobile environment," in *IEEE Vehicular Technology Conference*, pp. 820–824, 1995.

[89] L. Zhang, P. Xiao, A. Zafar, A. ul Quddus, and R. Tafazolli, "FBMC system: an insight into doubly dispersive channel impact," *IEEE Transactions on Vehicular Technology*, vol. 66, no. 5, pp. 3942–3956, 2017.

[90] ITU, "Recommendation ITU-R M.1225: Guidelines for Evaluation of Radio Transmission Technologies for IMT-2000," tech. rep., ITU, 1997.

[91] F.-M. Han and X.-D. Zhang, "Wireless multicarrier digital transmission via Weyl-Heisenberg frames over time-frequency dispersive channels," *IEEE Transactions on Communications*, vol. 57, no. 6, 2009.

[92] P. Robertson and S. Kaiser, "The effects of Doppler spreads in OFDM(A) mobile radio systems," in *IEEE Vehicular Technology Conference (VTC Fall)*, pp. 329–333, 1999.

[93] 3GPP, "TSG RAN; study on channel model for frequency spectrum above 6GHz; (release 14)." http://www.3gpp.org/DynaReport/38900.htm, Dec. 2016.

[94] T. Blazek, M. Ashury, C. F. Mecklenbräuker, D. Smely, and G. Ghiaasi, "Vehicular channel models: A system level performance analysis of tapped delay line models," in *International Conference on ITS Telecommunications (ITST)*, pp. 1–8, May 2017.

[95] F. Kaltenberger, A. Byiringiro, G. Arvanitakis, R. Ghaddab, D. Nussbaum, R. Knopp, M. Bernineau, Y. Cocheril, H. Philippe, and E. Simon, "Broadband wireless channel measurements for high speed trains," in *IEEE International Conference on Communications (ICC)*, pp. 2620–2625, IEEE, 2015.

[96] X. Mestre and D. Gregoratti, "Parallelized structures for MIMO FBMC under strong channel frequency selectivity.," *IEEE Trans. Signal Processing*, vol. 64, no. 5, pp. 1200–1215, 2016.

[97] M. Bellanger, "FS-FBMC: An alternative scheme for filter bank based multicarrier transmission," in *IEEE International Symposium on Communications Control and Signal Processing (ISCCSP)*, 2012.

[98] D. S. Waldhauser, L. G. Baltar, and J. A. Nossek, "MMSE subcarrier equalization for filter bank based multicarrier systems," in *IEEE Workshop on Signal Processing Advances in Wireless Communications*, pp. 525–529, 2008.

[99] A. Ikhlef and J. Louveaux, "Per subchannel equalization for MIMO FBMC/OQAM systems," in *IEEE Pacific Rim Conference on Communications, Computers and Signal Processing*, 2009.

[100] F. Rottenberg, X. Mestre, D. Petrov, F. Horlin, and J. Louveaux, "Parallel equalization structure for MIMO FBMC-OQAM systems under strong time and frequency selectivity," *IEEE Transactions on Signal Processing*, vol. 65, pp. 4454–4467, Sept 2017.

[101] L. Marijanovic, S. Schwarz, and M. Rupp, "MMSE equalization for FBMC transmission over doubly-selective channels," in *Thirteenth International Symposium on Wireless Communication Systems*, (Poznan, Poland), pp. 1–6, September 2016.

[102] A. F. Molisch, M. Toeltsch, and S. Vermani, "Iterative methods for cancellation of intercarrier interference in OFDM systems," *IEEE Transactions on Vehicular Technology*, vol. 56, no. 4, pp. 2158–2167, 2007.

[103] H. Bolcskei, P. Duhamel, and R. Hleiss, "A subspace-based approach to blind channel identification in pulse shaping OFDM/OQAM systems," *IEEE Transactions on Signal Processing*, vol. 49, no. 7, pp. 1594–1598, 2001.

[104] B. Muquet, M. De Courville, and P. Duhamel, "Subspace-based blind and semi-blind channel estimation for OFDM systems," *IEEE Transactions on signal processing*, vol. 50, no. 7, pp. 1699–1712, 2002.

[105] C. Shin, R. W. Heath, and E. J. Powers, "Blind channel estimation for MIMO-OFDM systems," *IEEE Transactions on Vehicular Technology*, vol. 56, no. 2, pp. 670–685, 2007.

[106] E. G. Larsson, G. Liu, J. Li, and G. B. Giannakis, "Joint symbol timing and channel estimation for OFDM based WLANs," *IEEE Communications Letters*, vol. 5, pp. 325–327, Aug 2001.

[107] C. Lélé, J.-P. Javaudin, R. Legouable, A. Skrzypczak, and P. Siohan, "Channel estimation methods for preamble-based OFDM/OQAM modulations," *European Transactions on Telecommunications*, vol. 19, no. 7, pp. 741–750, 2008.

[108] D. Katselis, E. Kofidis, A. Rontogiannis, and S. Theodoridis, "Preamble-based channel estimation for CP-OFDM and OFDM/OQAM systems: A comparative study," *IEEE Trans. Signal Process.*, vol. 58, no. 5, pp. 2911–2916, 2010.

[109] E. Kofidis, D. Katselis, A. Rontogiannis, and S. Theodoridis, "Preamble-based channel estimation in OFDM/OQAM systems: a review," *Signal Processing*, vol. 93, no. 7, pp. 2038–2054, 2013.

[110] D. Kong, D. Qu, and T. Jiang, "Time domain channel estimation for OQAM-OFDM systems: algorithms and performance bounds," *IEEE Transactions on Signal Processing*, vol. 62, no. 2, pp. 322–330, 2014.

[111] Y. Li, "Pilot-symbol-aided channel estimation for OFDM in wireless systems," *IEEE transactions on vehicular technology*, vol. 49, no. 4, pp. 1207–1215, 2000.

[112] S. Coleri, M. Ergen, A. Puri, and A. Bahai, "Channel estimation techniques based on pilot arrangement in OFDM systems," *IEEE Transactions on broadcasting*, vol. 48, no. 3, pp. 223–229, 2002.

[113] X. Dong, W.-S. Lu, and A. C. Soong, "Linear interpolation in pilot symbol assisted channel estimation for OFDM," *IEEE transactions on wireless communications*, vol. 6, no. 5, 2007.

[114] M. K. Ozdemir and H. Arslan, "Channel estimation for wireless OFDM systems," *IEEE Communications Surveys & Tutorials*, vol. 9, no. 2, pp. 18–48, 2007.

[115] P. Hoeher, S. Kaiser, and P. Robertson, "Two-dimensional pilot-symbol-aided channel estimation by Wiener filtering," in *IEEE International Conference on Acoustics, Speech, and Signal Processing (ICASSP)*, vol. 3, pp. 1845–1848, IEEE, 1997.

[116] T. K. Moon and W. C. Stirling, *Mathematical methods and algorithms for signal processing*, vol. 1. Prentice Hall New York, 2000.

[117] J.-P. Javaudin, D. Lacroix, and A. Rouxel, "Pilot-aided channel estimation for OFDM/OQAM," in *IEEE Vehicular Technology Conference (VTC)*, vol. 3, pp. 1581–1585, 2003.

[118] T. H. Stitz, T. Ihalainen, A. Viholainen, and M. Renfors, "Pilot-based synchronization and equalization in filter bank multicarrier communications," *EURASIP Journal on Advances in Signal Processing*, vol. 2010, p. 9, 2010.

[119] C. Lélé, R. Legouable, and P. Siohan, "Channel estimation with scattered pilots in OFDM/OQAM," in *IEEE Workshop on Signal Processing Advances in Wireless Communications (SPAWC)*, pp. 286–290, 2008.

[120] B. Yu, S. Hu, P. Sun, S. Chai, C. Qian, and C. Sun, "Channel estimation using dual-dependent pilots in FBMC/OQAM systems," *IEEE Communications Letters*, vol. 20, pp. 2157–2160, Nov 2016.

[121] J.-M. Choi, Y. Oh, H. Lee, and J.-S. Seo, "Interference-dependent pair of pilots for channel estimation in FBMC systems," in *IEEE International Symposium on Broadband Multimedia Systems and Broadcasting*, pp. 1–4, 2016.

[122] J.-M. Choi, Y. Oh, H. Lee, and J.-S. Seo, "Pilot-aided channel estimation utilizing intrinsic interference for FBMC/OQAM systems," *IEEE Transactions on Broadcasting*, 2017.

[123] C. Lélé, "Iterative scattered-based channel estimation method for OFDM/OQAM," *EURASIP Journal on Advances in Signal Processing*, vol. 2012, no. 1, p. 42, 2012.

[124] J. Bazzi, P. Weitkemper, and K. Kusume, "Power efficient scattered pilot channel estimation for FBMC/OQAM," in *International ITG Conference on Systems, Communications and Coding*, pp. 1–6, VDE, 2015.

[125] W. Cui, D. Qu, T. Jiang, and B. Farhang-Boroujeny, "Coded auxiliary pilots for channel estimation in FBMC-OQAM systems," *IEEE Transactions on Vehicular Technology*, vol. 65, pp. 2936–2946, May 2016.

[126] X. He, Z. Zhao, and H. Zhang, "A pilot-aided channel estimation method for FBMC/OQAM communications system," in *International Symposium on Communications and Information Technologies (ISCIT)*, pp. 175–180, IEEE, 2012.

[127] D. Tse and P. Viswanath, *Fundamentals of wireless communication*. Cambridge university press, 2005.

[128] G. Caire, G. Taricco, and E. Biglieri, "Bit-interleaved coded modulation," *IEEE Transactions on Information Theory*, vol. 44, no. 3, pp. 927–946, 1998.

[129] A. G. i Fàbregas, A. Martinez, and G. Caire, *Bit-interleaved coded modulation*. Now Publishers Inc, 2008.

[130] C. Novak and G. Matz, "Low-complexity MIMO-BICM receivers with imperfect channel state information: Capacity-based performance comparison," in *IEEE Workshop on Signal Processing Advances in Wireless Communications (SPAWC)*, (Marrakech, Morocco), June 2010.

[131] B. Efron and R. J. Tibshirani, *An introduction to the bootstrap*. CRC press, 1994.

[132] H. Zarrinkoub, *Understanding LTE with MATLAB: from mathematical modeling to simulation and prototyping*. John Wiley & Sons, 2014.

[133] S. Schwarz, M. Simko, and M. Rupp, "On performance bounds for MIMO OFDM based wireless communication systems," in *Signal Processing Advances in Wireless Communications SPAWC*, (San Francisco, CA), pp. 311 –315, June 2011.

[134] G. Taubock, F. Hlawatsch, D. Eiwen, and H. Rauhut, "Compressive estimation of doubly selective channels in multicarrier systems: Leakage effects and sparsity-enhancing processing," *IEEE Journal of Selected Topics in Signal Processing*, vol. 4, no. 2, pp. 255–271, 2010.

[135] C. Sgraja and J. Lindner, "Estimation of rapid time-variant channels for OFDM using Wiener filtering," in *IEEE International Conference on Communications (ICC)*, vol. 4, pp. 2390–2395 vol.4, May 2003.

[136] C. Shin, J. Andrews, and E. Powers, "An efficient design of doubly selective channel estimation for OFDM systems," *IEEE Transactions on Wireless Communications*, vol. 6, pp. 3790–3802, October 2007.

[137] Z. Tang, R. C. Cannizzaro, G. Leus, and P. Banelli, "Pilot-assisted time-varying channel estimation for OFDM systems," *IEEE Transactions on Signal Processing*, vol. 55, no. 5, pp. 2226–2238, 2007.

[138] F. Hlawatsch and G. Matz, *Wireless communications over rapidly time-varying channels*. Academic Press, 2011.

[139] G. B. Giannakis and C. Tepedelenlioglu, "Basis expansion models and diversity techniques for blind identification and equalization of time-varying channels," *Proceedings of the IEEE*, vol. 86, no. 10, pp. 1969–1986, 1998.

[140] D. K. Borah and B. Hart, "Frequency-selective fading channel estimation with a polynomial time-varying channel model," *IEEE Transactions on Communications*, vol. 47, no. 6, pp. 862–873, 1999.

[141] T. Zemen and C. F. Mecklenbrauker, "Time-variant channel estimation using discrete prolate spheroidal sequences," *IEEE Transactions on signal processing*, vol. 53, no. 9, pp. 3597–3607, 2005.

[142] W.-G. Song and J.-T. Lim, "Pilot-symbol aided channel estimation for OFDM with fast fading channels," *IEEE Transactions on Broadcasting*, vol. 49, no. 4, pp. 398–402, 2003.

[143] Y. Mostofi and D. C. Cox, "ICI mitigation for pilot-aided OFDM mobile systems," *Wireless Communications, IEEE Transactions on*, vol. 4, no. 2, pp. 765–774, 2005.

[144] H. Hijazi and L. Ros, "Polynomial estimation of time-varying multipath gains with intercarrier interference mitigation in OFDM systems," *IEEE Transactions on Vehicular Technology*, vol. 58, no. 1, pp. 140–151, 2009.

[145] M. Simko, C. Mehlführer, T. Zemen, and M. Rupp, "Inter-carrier interference estimation in MIMO OFDM systems with arbitrary pilot structure," in *IEEE Vehicular Technology Conference (VTC Spring)*, 2011.

[146] S. Caban, J. Rodas, and J. A. García-Naya, "A methodology for repeatable, off-line, closed-loop wireless communication system measurements at very high velocities of up to 560 km/h," in *IEEE Instrumentation and Measurement Technology Conference (I2MTC)*, pp. 1–5, IEEE, 2011.

[147] A. A. Zaidi, J. Luo, R. Gerzaguet, A. Wolfgang, R. J. Weiler, J. Vihriala, T. Svensson, Y. Qi, H. Halbauer, Z. Zhao, *et al.*, "A preliminary study on waveform candidates for 5G mobile radio communications above 6 GHz," in *IEEE Vehicular Technology Conference (VTC Spring)*, pp. 1–6, 2016.

[148] M. Payaró, A. Pascual-Iserte, and M. Nájar, "Performance comparison between FBMC and OFDM in MIMO systems under channel uncertainty," in *IEEE European Wireless Conference (EW)*, pp. 1023–1030, 2010.

[149] A. I. Pérez Neira, M. Caus, Z. Rostom, D. Le Ruyet, E. Kofidis, M. Haardt, X. Mestre, and Y. Cheng, "MIMO signal processing in offset-QAM based filter bank multicarrier systems," *IEEE transactions on signal processing*, vol. 64, no. 21, pp. 5733–5762, 2016.

[150] P. Chevalier, D. L. Ruyet, and R. Chauvat, "Maximum likelihood Alamouti receiver for filter bank based multicarrier transmissions," *ITG-Fachbericht-WSA 2016*, 2016.

[151] M. Renfors, T. Ihalainen, and T. H. Stitz, "A block-Alamouti scheme for filter bank based multicarrier transmission," in *European Wireless Conference (EW)*, 2010.

[152] D. Na and K. Choi, "Intrinsic ICI-free Alamouti coded FBMC," *IEEE Communications Letters*, vol. 20, no. 10, pp. 1971–1974, 2016.

[153] J. Manz, "A sequency-ordered fast Walsh transform," *IEEE Transactions on Audio and Electroacoustics*, vol. 20, no. 3, pp. 204–205, 1972.

[154] Z. Pi and F. Khan, "An introduction to millimeter-wave mobile broadband systems," *IEEE Communications Magazine*, vol. 49, pp. 101–107, June 2011.

[155] R. W. Bauml, R. F. Fischer, and J. B. Huber, "Reducing the peak-to-average power ratio of multicarrier modulation by selected mapping," *Electronics letters*, vol. 32, no. 22, pp. 2056–2057, 1996.

[156] S. H. Muller and J. B. Huber, "OFDM with reduced peak-to-average power ratio by optimum combination of partial transmit sequences," *Electronics letters*, vol. 33, no. 5, pp. 368–369, 1997.

[157] A. Skrzypczak, J.-P. Javaudin, and P. Siohan, "Reduction of the peak-to-average power ratio for the OFDM/OQAM modulation," in *IEEE Vehicular Technology Conference, (VTC Spring)*, vol. 4, pp. 2018–2022, IEEE, 2006.

[158] D. Qu, S. Lu, and T. Jiang, "Multi-block joint optimization for the peak-to-average power ratio reduction of FBMC-OQAM signals," *IEEE Transactions on Signal Processing*, vol. 61, no. 7, pp. 1605–1613, 2013.

[159] C. Ye, Z. Li, T. Jiang, C. Ni, and Q. Qi, "PAPR reduction of OQAM-OFDM signals using segmental PTS scheme with low complexity," *IEEE Transactions on Broadcasting*, vol. 60, no. 1, pp. 141–147, 2014.

[160] S. Sesia, M. Baker, and I. Toufik, *LTE-the UMTS long term evolution: from theory to practice*. John Wiley & Sons, 2011.

[161] T. Ihalainen, A. Viholainen, T. H. Stitz, M. Renfors, and M. Bellanger, "Filter bank based multi-mode multiple access scheme for wireless uplink," in *IEEE European Signal Processing Conference (EUSIPCO)*, pp. 1354–1358, 2009.

[162] C. H. Yuen, P. Amini, and B. Farhang-Boroujeny, "Single carrier frequency division multiple access (SC-FDMA) for filter bank multicarrier communication systems," in *IEEE International Conference on Cognitive Radio Oriented Wireless Networks (CROWNCOM)*, pp. 1–5, 2010.

[163] D. Na and K. Choi, "Low PAPR FBMC," *IEEE Transactions on Wireless Communications*, 2017, accepted for publication.

[164] H. G. Myung, J. Lim, and D. J. Goodman, "Single carrier FDMA for uplink wireless transmission," *IEEE Vehicular Technology Magazine*, vol. 1, no. 3, pp. 30–38, 2006.

[165] G. Berardinelli, F. M. Tavares, T. B. Sorensen, P. Mogensen, and K. Pajukoski, "Zero-tail DFT-spread-OFDM signals," in *IEEE Globecom Workshops (GC Wkshps)*, pp. 229–234, IEEE, 2013.

[166] G. Berardinelli, K. I. Pedersen, T. B. Sorensen, and P. Mogensen, "Generalized DFT-spread-OFDM as 5G waveform," *IEEE Communications Magazine*, vol. 54, no. 11, pp. 99–105, 2016.

[167] R. Zakaria and D. Le Ruyet, "Theoretical analysis of the power spectral density for FFT-FBMC signals," *IEEE Communications Letters*, vol. 20, no. 9, pp. 1748–1751, 2016.